UNIVERSITY OF SOUTHAMPTON

FACULTY OF ENGINEERING AND THE ENVIRONMENT

National Centre for Advanced Tribology (nCATS)

Nano-scale tribocorrosion of CoCrMo biomedical alloys

by

Vanesa Martínez Nogués

Academic Supervisory Team:
Dr. Richard B. Cook
Dr. Martin Stolz
Prof. Robert J. K. Wood

Thesis for the Degree of Doctor of Philosophy

April 2016

UNIVERSITY OF SOUTHAMPTON

ABSTRACT

FACULTY OF ENGINEERING AND THE ENVIRONMENT

National Centre for Advanced Tribology

Thesis for the Degree of Doctor of Philosophy

NANO-SCALE TRIBOCORROSION OF CoCrMo BIOMEDICAL ALLOYS

Vanesa Martínez Nogués

Tribocorrosion plays a significant role in the performance and failure of implantable metallic devices. The damage caused by tribocorrosion has been reported previously in several implantable devices such as disk replacements, bone plates, the interface between the fixation cement and the metallic stem in cemented hip arthroplasties and also in the taper-trunnion contact area of hip replacements. The origin of the tribocorrosion processes is produced at the nanoscale as a result of the micromotion between hard single asperities and the metallic components at their contacting interfaces. Hard particles cause deformation and wear of the surfaces and depassivation, opening new metallic areas to corrosive attack. The combination of both processes produces the liberation of metallic ions and metal debris responsible for adverse reactions within the body, causing pain and the need for implant revision.

Significant research has been undertaken to understand the wear-corrosion mechanisms at the macro and micro scale. The focus has been on different experimental conditions and the effects of the environment (protein-phosphate contents or pH), the role played by the microstructure of CoCrMo alloys and the contact conditions or the wear mode (sliding, fretting, scratching). However, no work has been undertaken into the interaction of plastic deformation and corrosion mechanisms at the nano-scale. For a better understanding of the combined effects of the corrosion and the deformation processes, a new electrochemistry cell was designed in combination with the nanoindenter system to simulate a single asperity in contact with a metallic surface. Four CoCrMo alloys with different manufacturing and thermal histories were analysed to

obtain a deformation-corrosion map which summarizes their scratch-corrosion performance at the nano-scale.

The microstructure, chemical composition and mechanical properties of the Forged, As Cast (AC), As Cast thermal treated (AC-TT) and As Cast with low carbon content (AC-LC) Co based alloys were studied. Grain size, carbide morphology, carbon content and crystallographic phases present were analysed by metallographic preparation, Scanning Electron Microscopy (SEM) observations and Electron Backscattered Diffraction (EBSD) techniques respectively. Hardness (*H*) and Young's Modulus (*E*) were calculated by indentation and nano-indentation techniques. Static corrosion behaviour of the four alloys immersed in 0.9 wt.% NaCl solution was studied using open circuit potential (OCP) and potentiodynamic (PD) polarization experiments to understand the corrosion mechanisms affecting the alloys without the interference of the plastic deformation and to estimate the minimum stabilization time required to reach a steady potential to be used in the nano-scratch corrosion experiments.

The deformation processes under fretting, reciprocating sliding and scratch experiments in dry conditions were also characterized by measuring tangential friction forces, coefficient of friction and plastic deformation values. Post experimental surface analysis was performed to analyse the oxide layer formation and the wear scar morphology.

The four CoCrMo alloys were tested under several loading conditions using the new electrochemistry cell performing single scratch-corrosion experiments. The results demonstrated that the crystallographic orientation of the grains produced characteristic deformation features. These features were directly linked to the repassivation times and current densities and were governing the deformation corrosion processes at the nano-scale and the liberation of metallic ions.

This work establishes a novel experimental technique that gives a better understanding of the deformation-corrosion processes occurring at the nano-scale in CoCrMo alloys. In addition the results obtained will be useful to help interpret the failure mechanisms observed in retrieved implants and improve the design and development of new materials and material pairing selection for future implants. Moreover the technique developed as part of this work can be extended not just to biomedical applications but also to any other applications in the materials science field where passivated metals are used in a corrosive environment and single asperity contacts act to deform metallic surfaces.

Contents

List of tables

List of figures

Declaration of authorship

I, Vanesa Martínez Nogués

Declare that this thesis and the work presented in it are my own and has been generated by me as the result of my own original research.

Nano-scale tribocorrosion of CoCrMo biomedical alloys

I confirm that:

- This work was done wholly or mainly while in candidature for a research degree at this University;
- Where any part of this thesis has previously been submitted for a degree or any other qualification at this University or any other institution, this has been clearly stated;
- Where I have consulted the published work of others, this is always clearly attributed;
- Where I have quoted from the work of others, the source is always given. With the exception of such quotations, this thesis is entirely my own work;
- I have acknowledged all main sources of help;
- Where the thesis is based on work done by myself jointly with others, I have made clear exactly what was done by others and what I have contributed myself;
- Part of this work has been submitted to the next conference proceeding or to scientific journals:

  - Nano-scale wear characterization of CoCrMo biomedical alloys.
    V.Martinez-Nogues, J.M. Nesbitt, R.J.K. Wood, .B.Cook.
    Journal: Tribology International, Volume: 93(2016) 563-572.
    http://dx.doi.org/10.1016/j.triboint.2015.03.037

- Nano-scale wear of CoCrMo alloys as biomedical materials. V.Martinez-Nogues, J.C.Walker, R.F.J Wood, J.M.Nesbitt, R.B.Cook
  20th Internation Conference on Wear of Materials.Toronto (Canada). 12-16th April 2015.Contribution: Poster

- Nano-scale fretting of biomedical materials: validation of a new nanointerferometer measurement system.
  V.Martinez-Nogues, R.J.K. Wood, J.M. Nesbitt, C.Maul, R.B.Cook.
  41st Leeds-Lyon Symposium on Tribology: Integrated Tribology.Leeds (UK). 7-9th September 2014. Contribution: Oral

- Analysis of the scratch corrosion behaviour of CoCrMo alloys at the nano-scale.
  V.Martinez-Nogues, R.J.K. Wood, R.B.Cook
  Aceppted for oral presentation at the 3rd International Conference on Biotribology (ICoBT 2016). London (UK). 11-14th September 2016

- Specific grain orientation influence in the deformation-corrosion behaviour of CoCrMo biomedical materials.
  V.Martinez-Nogues, R.J.K. Wood, R.B.Cook
  Intended to be submitted to Acta Biomateralia in the next months.

Signed: Vanesa Martínez Nogués

Date: Southampton 15/06/2016

Acknowledgements

First and foremost I want to thank my advisor Dr Richard Cook. It has been an honor to be his first Ph.D. student. He has taught me, both consciously and unconsciously, how good experimental work is done. I appreciate all his contributions of time, ideas, and funding to make my Ph.D. experience productive and stimulating. The joy and enthusiasm he has for his research was contagious and motivational for me, even during the tougher times of the Ph.D. I am also thankful to him for his interest, suggestions and comments done to correct this dissertation and make it happen.

I would also like to thank the two members of my oral examination, Professor Brian Mellor and Dr. Benjamin Beake, for their time and insightful questions.

Thanks to Dr. Russ Alberts for all his support and help during the first years of my PhD, his patience and enthusiasm for his research was inspiring. To all the nCATS members which provide technical support and interesting discussions and scientific support during coffee mornings specially Prof. Robert Wood, Julian Wharton, Liam Goodes, Terry Harvey and John Walker. To Dave Beckett and Heather Porter for all their help in the materials preparation laboratory. Also I am grateful to the group's administrative assistant Sue Berger who kept everything organized and was always there ready to help with all the paper work.

Also thanks to John Nesbitt and Christian Maul at Redlux Ltd. and James Murray at University of Nottingham for their help with the interferometric measurements.

I gratefully acknowledge the funding sources that made my Ph.D. work possible. I was funded by the EPRSC Award and my work was also supported by the University of Southampton.

My time at Southampton was made enjoyable in large part due to the many friends that became a part of my life. I am grateful for the time spent with my office mates, especially Natalya, Stefania, Jahnaby, Jim, Kasia and Viktoria for all the laughs and food discussions to support the stressful times. To Pawee for the endless hours helping me with the microscope and EBSD analysis. To Jorge for

been my personal trainer and the suffering hours in the gym. To my Italian friends: Stefania and Paolo, Davide and Irene, Danielle, Stefano, Federico and Otti and Mirko, and our trips and excursions all over. To my first friends here: Valentina, Asim, Asad and Waqar for their immense hospitality and their nice Pakistani dinners that made me cry at the beginning but with time I'm holding all the spiciness. Thanks also to my colleagues from University of Zaragoza: Maria Jose, Lola and Patxi who always believed I was worthy for doing a PhD. To my University friends in Zaragoza for their encouragement every time I visited them and our trip to Scotland. I will always remember it. To my best friends: Cristina, Maria, Silvia and Teresa, to be all together soon.

Lastly, I would like to thank my family for all their love and encouragement. To my parents who rose me believing that hard work is always worthy and supported me in all my projects. Be far from you during this years has been the hardest part. To my grandmother who was always excited about talking to me on the computer although she couldn't understand how was it possible. "Yaya", you will be always in my heart. To Alex to be the most supportive, encouraging, and patient boyfriend during the final stage of this Ph.D. The wait for our trip to Iceland will be worthy. Thank you.

"Finalmente, me gustaría agradecer a mi familia por su amor y apoyo. A mis padres que me criaron creyendo que el trabajo duro siempre es recompensado y siempre me han apoyado en todos mis proyectos. Haber estado lejos de vosotros durante estos años ha sido sin duda la parte más difícil. A mi abuela que siempre estaba impaciente para hablar conmigo cuando conectábamos el ordenador a pesar que nunca entendió como podía verme por la pantalla estando tan lejos. Yaya, siempre te recordare. Para Alex, por ser el novio más paciente y darme aliento y apoyo durante la última etapa de este doctorado. La espera para nuestro viaje a Islandia merecerá la pena. Muchas gracias a todos"

List of Abbreviations

AC: as cast
AC-LC: as cast low carbon content
AC-TT: as cast thermal treated
AFM: atomic force microscopy
ALVAL: Aseptic Lymphocyte-Dominated Vasculitis-Associated Lesion
ARMD: Adverse Reaction to Metal Debris
ASTM: American Society for Testing and Materials
bcc: body centered cubic
BMI: Body Mass Index
CoC: Ceramic On Ceramic
CoCrMo: Cobalt-Chromium-Molybdenum
COF: coefficient of friction
CoM: Ceramic on Metal
CoP: Ceramic On Polymer
CRSS: critical resolved shear stress
DNA: deoxyribonucleic acid
E: Young Modulus
EBSD: electron backscatter diffraction
EHL: elastohydrodynamic lubrication
EIS: electrochemical impedance spectroscopy
EN: electrochemical noise
fcc: face center cubic
FIB-SIMS: focus ion beam- ion mass spectrometry
GNB: geometrically necessary boundary dislocations
GND: geometrically necessary dislocations
GSR: Gross Slip Regime
H: Hardness
HB: Brinell Hardness
hcp: hexagonal close packed
HIP: hot isostatic pressing

HK: Knoop Hardness
HV: Vickers Hardness
ICP-OES: inductively couple plasma optical emission spectroscopy
IPF: inverse pole figures
IR: infrared spectroscopy
ISE: indentation size effect
ISO: International Standard Organization
MACC: Mechanically Assisted Crevice Corrosion
MoM: Metal on Metal
MoP: Metal On Polymer
MSR: Mixed Slip Regime
OCP: open circuit potential
PBS: phosphate buffered saline
PD: potentiodynamic polarization
PE: Polyethylene
PF: pole figures
PMMA: polymethyl methacrylate
PSR: Partial Slip Regime
PVC: polyinyl chloride
RMS: Root Mean Square
SEM: scanning electron microscopy
SFE: stacking fault energy
SIT: strain induced transformation
SSD: statistically stored dislocations
TCR: tribochemical reaction
THA: total hip arthoplasty
THA: Total Hip Arthroplasty
UHMWPE: Ultra High Molecular Weight Polyethylene
XLPE: Cross Linked Polyethylene
XPS: X-ray photoelectron spectroscopy

Symbols

β: Tafel slope
δ: displacement amplitude
η_{op}: overpotential
λ: fluid film thickness ratio
λ_c: profile filter-roughness
λ_f: profile filter--waviness
ν: Poison ratio
μ: coefficient of friction
$: dollar
γ: fcc phase
ε: hcp phase
σ: tensile stress
σ_o: stress yield constant
σ_y: stress yield
τ: repassivation constant
τ_R: resolved shear stress
τ_c: critical shear stress
ϕ: angle between slip plane normal and stress direction
ρ: density
μ: coefficient of friction
$2a$: contact width
$2D$: displacement
A: fretting energy ratio
A_n: true contact area
ΔG: increment of free energy
ΔH: increment of enthalpy
ΔS: increment of entrophy
a: radius of contact Hertz equation
A_p: projected area
A_s: surface area
b_a: anodic slope
b_c: catodic slope
CR: corrosion rate
D: diffusion rate
d: Vickers hardness diagonal
D_0: diffusion coefficient
D_{f0}: fretting initial contact depth
D_f: fretting final contact depth
D_{total}: scratch depht + pile up depth
$D_{pile\text{-}up}$: pile up depht
$D_{scratch}$: scratch depht
E^*: reduced modulus
e: fretting ratio
E: Young´s modulus
E^*: combined modulus
E_b: breakdown potential
E_{corr}: corrosion potential
E_{couple}: galvanic corrosion potential
E_r:reduced modulus
E_d: dispersed energy
E_p: passivation potential
E_t: total energy
EW: equivalent weight
F_n: applied normal force
F_f: frictional force
F_o: contact load scratch
F_N: normal load scratch
F: Faraday's constant
H: hardness
h_a: penetration depth
h_t: total penetration depth
h_c: contact penetration depth
h_r: residual penetration depth
h_{min}: minimum film thickness
H_{IT}: indentation hardness

$H_{IT\text{-}nano}$: nanoindentation hardness
H_v: Vickers hardness
I_c: corrosion current
i_o: exchange current density
i_{corr}: corrosion current density
I_{couple}: galvanic corrosion current
i_p: passivation current
I_{peak}: peak current
I_{max}: maximum current
I_∞: baseline current
k_y: Hall Petch equation constant
l_n : evaluation length
l_r: sampling length
L: applied load indentation
M: Schmid factor
M_r: molar mass
M_w: molecular weight
N: normal load
N_c: number of cycles
p: penetration depth
P: indenter load
P_c: spatial roughness parameter
P_m: average contact pressure
P_o: maximum contact pressure
P_t: profile roughness parameter
Q_a: activation energy
Q: charge
Q_f: tangential force
R: impedance real component
R: Universal gas constant
R_a: arithmetic average roughness
R_i: indenter radius
R_p: polarization resistance
R_q: root mean square surface roughness
R_{q1}: root mean square surface roughness surface 1
R_{q2}: root mean square surface roughness surface 2
R_t: total roughness
R_{sk}: statistical roughness parameter
S: contact stiffness
t: implantation time
T: absolute temperature
U_0: running in friction coefficient
U_{steady}: steady state friction coefficient
V: volumetric wear
w: scratch widht
$wt\%$: weight percentage
W_t: waviness roughness parameter
W_m: current flow under OCP
X: impedance imaginary component
Z: number of electrons
Z_w: impedance

Units

°C: degree Celsius
µm/point: micrometer per point
µm/s: micrometre per second
µm/y: micrometre per year
µm: micrometre
µJ: microJoule
µJ/cycle; microJoule per cyle
A/cm^2: area per square cm
A: ampere
C: Culoumb
cm: centimetre
cm^2: square centimetre
data/µs: data per micro second
data/s: data per second
g/cm^3: gram per cubic cm
g/mol: gram per mol
GPa: giga Pascal
Hz: Hertz
J: Joule
kg: kilogram
m/s: metre per second
mL: millilitre
mm/y : millimetre per year
mm: millimetre
mN/ s: milliNewton per second
mN: milliNewton
mol
MPa: mega Pascal
mV/s: milliVolt per second
mV: milliVolt
N: Newton
n: number of repetitions/cycles
nA: nano ampere
nA/µm^2: nano Ampere per micro square metre
nJ : nanoJoule
nJ/cycle: nanoJoule per cycle
nm: nanometre
nm^2: square nm
Pa: Pascal
s: second
V/dec: volt per decade
V: volt
Ώ: Ohm

1 Introduction

1.1 Background

Total hip arthroplasty is one of the most common surgical procedures in orthopaedics. It is a successful, safe and cost-effective medical treatment to restore functionality to the hip joint and pain-free mobility in patients suffering from degenerative joint diseases, such as osteoarthritis, or trauma injuries. The total number of hip procedures entered into the National Joint Registry during 2014 was 83125, an increase of 20% over 2009 [1]. Business Wire (20Dec 2013) [2] reported that the Total Hip Replacement market is estimated to reach a value of $7.1 billion by 2019, due not only to the growth of the global elderly population, but also the climbing number of younger patients in need of the procedure. This increasing trend is shown in Figure 1.1 [1].

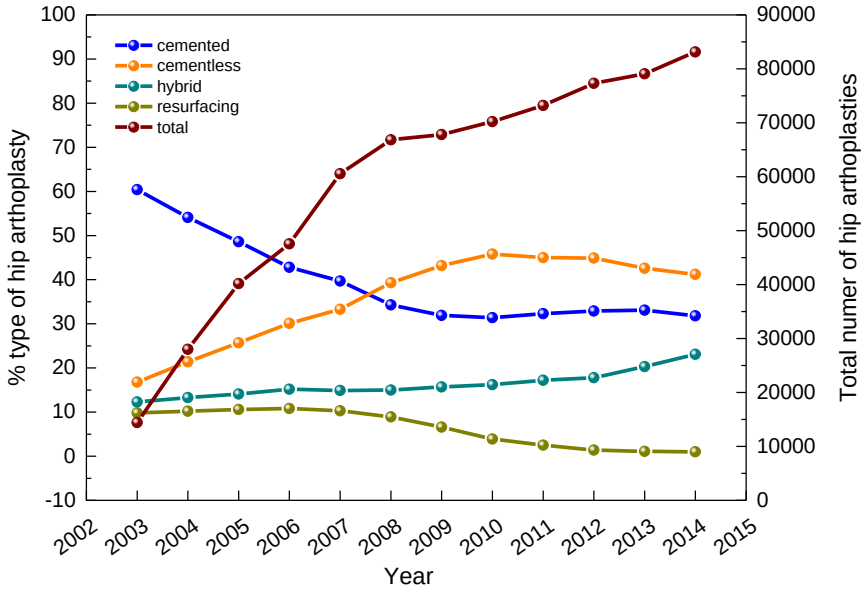

Figure 1.1 Evolution from 2003 to 2014 of the percentage of different types of hip implants and total number of hip replacements [1]

The in-vivo service life of an implant is critical for hip replacements, particularly for younger active individuals where their life span is expected to extend beyond the service life of the implant components.

Since the first hip was implanted in a human body, several materials, bearing couple combinations, designs, tolerances, manufacturing process and surgery techniques have been used. Some of the first materials used were ivory, glass or stainless steel. The first generation of metal on metal hip implants (McKee-Farrar,[3]) were introduced in the 1950's. Although it was a relatively crude monoblock design, the final results were quite promising, with implants surviving for extended periods over 20 years. Retrieval studies [4] reported high wear rates, metallic wear particles production and osteolysis, mainly due to poor design and improper implantation techniques. In an attempt to solve some of the problems caused by metal on metal (MoM) implants, John Charnley developed a metal on polyethylene-based implant that was so successful it displaced the use of other bearing materials. The earliest ceramic (alumina) implants were also implanted during this time period, but due to inadequate mechanical properties caused by poor manufacturing there were unacceptably high rates of fracture [5].

However, after several decades, the patient demographic undergoing hip replacement changed, with a larger population of younger more active individuals requiring joint replacement. Standard polyethylene vs. metal implants started to show high wear rates, 0.1 mm per year, and particle

production leading to early bone osteolysis [6]. This issue prompted the medical community to think again about hard bearing surfaces pairings such as metal on metal or ceramic on ceramic. A second generation of metal on metal implants and ceramic on ceramic then emerged. The sphericity, clearance, surface roughness, implant designs, materials and manufacturing processes were improved, promoting better lubrication and reducing the wear rate, therefore increase their life span. Despite the modifications mentioned above, MoM retrievals still showed wear rates similar to the first generation [7], with certain designs failing at alarming rates, creating uncertainty about their safety and effectiveness of the artificial hip joints.

One of the main concerns with MoM implants is the body's reaction to high levels of Co and Cr metal ions and metallic wear debris released from the joints. The Adverse Reaction to Metal Debris (ARMD) [8], or Aseptic Lymphocyte-Dominated Vasculitis-Associated Lesion (ALVAL) [9], can cause a great deal of pain to the patient but also trigger tissue necrosis. The diagnosis of ARMD and ALVAL will necessitate urgent revision surgery and removal of the joint. If left undiagnosed the levels of tissue necrosis, can result in complex revision surgery, the need of special revision implants and bone grafts.

In light of the link between ARMD and ALVAL with released particles and ions, it is important to understand their origin and the mechanisms by which they are produced. Metal debris was thought to be generated solely from the bearing articulation; however joint registries around the globe demonstrated that there were other possible sources of material loss which could be affecting implant performance. There are several interfaces in hip implants where fretting, with different amplitudes, can occur, as indicated with yellow arrows in Figure 1.2:

- Articular surfaces: femoral head-articular surface (sliding tribocorrosion)
- Taper-trunnion interfaces: < 100 μm
- Femoral stem – cement interface (10-60 μm)

The femoral stem-cement/bone interface and the taper-trunnion junction, known as trunnionosis [10], have been identified as sources of particles and metal ion release [11-14]. The mechanism of loss at both interfaces is caused by micromotion between the contacting surfaces, resulting in a combination of wear and corrosion processes, termed generally as tribocorrosion although it is often referred to as mechanically assisted crevice corrosion [15] for the taper-trunnion interface. The magnitude of stress is dependent on the normal loading, the friction coefficient and surface roughness. The continuous repetition of the asperity contact between both surfaces causes the fracture of the oxide layer, that combined with high surface contact stresses and localized electrochemical dissolution leads to an accelerated removal of the material and the nucleation of small cracks and the breaking away of particulate debris.

Scratches at the micro and the nano-scale have been reported in clinical and in vitro studies [13, 16] on the metallic femoral stems due to the interaction of hard particles (radiopacifier particles embedded in the fixation cement) which stand out from the cement interacting with the femoral stem and starting the wear-corrosion process.

This study will focus on the interface between the cemented femoral stems and the cement mantle used to fix the implant to the femur. The novel technique developed will enable the controlled study of the deformation and electrochemical processes which occur in these interfaces. A better understanding of the underlying deformation and corrosion mechanisms occurring in CoCrMo alloys with different manufacturing processes and thermal treatment history will allow an improvement in the future design of new alloys which can be used in a manner which minimises the risk to the patient.

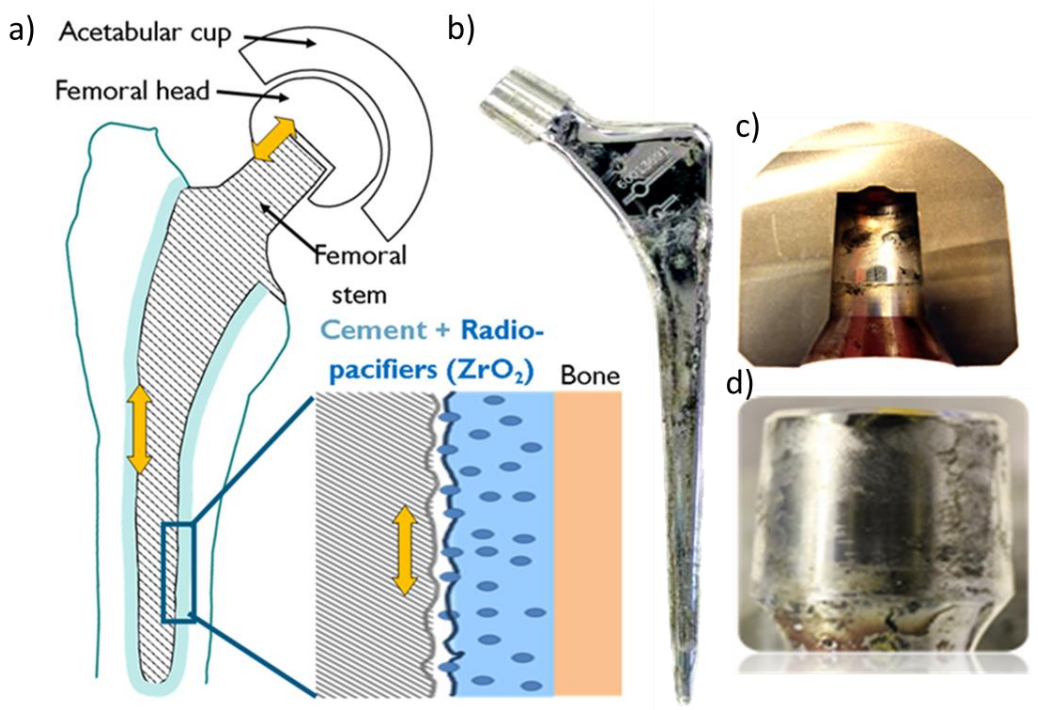

Figure 1.2 Examples of fretting corrosion in retrievals from implanted hips: a) Diagram showing the areas where fretting corrosion can occurs in a hip implant [17], b) Exeter femoral stem with signs of corrosion in the femoral contact area, c)Taper interface from a cross-sectioned femoral head and d) Trunnion interface from a femoral stem

1.2 Aim and objectives of this study

The aim of this study is to develop a novel technique able to reproduce the tribocorrosion damage occurring at the nano-scale where hard single asperities scratch and damage the metallic femoral stem in cemented hip implants.

The specific objectives of the work are:

- To analyse the specific microstructure, chemical composition and crystallographic structure of four CoCrMo alloys obtained from different hip implant components.

- To characterize the mechanical properties, hardness (H) and Young's Modulus (E), of the CoCrMo alloys. Hardness has been related as a key parameter related with wear resistance properties. In addition hardness to Young´s modulus ratios: H/E and H^3/E^2 were also calculated since they are linked to the deformation relative to yielding and the alloys resistance to plastic deformation respectively.

- To determine the corrosion behaviour of the Co-based alloys under static conditions to be used as a baseline for the analysis of the tribocorrosion synergism and to determine the minimum stabilization time required for the scratch-corrosion experiments. Potential and current differences between the alloys will give an understanding of the galvanic effects of pairing metal-metal surfaces in biological environments.

- To establish a testing protocol capable of determining the deformation and wear resistance properties of the alloys in dry conditions. Intermittent fretting, reciprocating sliding and single scratch experiments were used to quantify the severity of the plastic deformation produced at the nano-scale in dry conditions. Single scratch experiments were chosen to simulate a single asperity contact scratching the metallic femoral stem surface.

- The development of a new electrochemistry cell which allows the monitoring of the transient currents and potential changes during scratch experiments in NaCl solution. To correlate the corrosion parameters (repassivation times and current densities), the plastic deformation levels and the effects of the crystallographic orientation to understand the synergism between deformation and corrosion at the nano-scale on Co-based alloys.

1.3 Thesis structure

The thesis is divided in 4 main parts containing 8 chapters. It starts with an introduction on the topic to assess the problem under study and a literature review where the relevant subject areas and the state of the art of the field are reviewed.

The second part of the study, Chapter 3, describes the materials and the methodology used to characterize the different alloys together with detailed experimental techniques to investigate their nano-wear behaviour in dry conditions, their corrosion response in static conditions and the relationship between the deformation and corrosion mechanisms. The most relevant section in this chapter is related with the novel design and development of the new electrochemistry cell which allows monitoring the corrosion parameters at the same time the scratches were produced on the CoCrMo alloys at the nano-scale. Additional techniques to characterize the surfaces after the experiments and measuring levels of plastic deformation such as scanning electron microscopy (SEM), atomic force microscopy (AFM) or white light interferometry are also described.

The experimental results obtained during this work are covered in part 3, which is divided in 3 chapters: Chapter 4, 5 and 6. The first section of Chapter 4 describes the microstructural characterization for the four different alloys used in the thesis to know extensively which materials are used. The phases presented, grain size, carbon content and carbide morphology will be determined to analyse their influence in the tribological and corrosion properties evaluated later. Section 4.2 goes through the mechanical properties, E_r and H, which were obtained by indentation and nanoindentation techniques to characterize them at the macro, micro and nano-scale. Mechanical properties are needed to understand how the manufacturing process, thermal process and carbon content affect the different CoCrMo alloys under study. The last section of Chapter 4 presents the static corrosion properties of the CoCrMo alloys, including results obtained from open circuit potential measurements (OCP) and potentiodynamic polarization (PD). The reason for these static corrosion experiments is to know the behaviour of the different alloys immersed in a NaCl solution without any load applied and see if there are differences as a result of their microstructural features. The results will be also used to establish the minimum stabilization time required before the tribocorrosion experiments.

Chapter 5 presents and discusses the results obtained from the dry nano-scale wear and scratch experiments done on the specimens. The purpose of this chapter is to summarize the preliminary steps that were done before choosing the most appropriate experiment to simulate the single contact asperity between the femoral stem and the hard particles in the cement in dry conditions. Comparison

of the coefficients of friction (COF) measurements during the running in and the steady state periods and dispersed energy values were described. Nano-wear scars measurements were carried using two standards systems: AFM and nanoindenter system and a new white light interferometry system was validated with the last two ones. Finally nano-wear scars morphology was compared using optical and SEM microscopy pictures at different loads.

Finally, chapter 6, analyses the deformation and corrosion processes observed from the nano-scale scratch-corrosion experiments. Currents were monitored while the scratch tests were occurring to obtain a current-time plot which was used to calculate the total current dispersed during the experiments. The real area affected in the nano-scratch experiments was measured by white light interferometry and current density values were calculated and compared between samples for a different load range. Nano-scratches were observed by SEM microscopy and deformation mechanisms of the four alloys under a single scratch were evaluated. The specific deformation mechanisms and repassivation kinetics were correlated to the grain orientation of each sample.

The last two chapters will discuss the results obtained during the study detailing the main conclusions obtained from the thesis and the novel contributions added to the existing knowledge in the field. The last section of chapter 8 will be dedicated to describe the future work plans.

2
Literature review

This chapter presents a review of the literature surrounding the main research topics for the present investigation. The focus of this literature review is to outline the current knowledge about the deformation and corrosion mechanisms and the tribocorrosion processes that affect medical grade CoCrMo alloys at different scale levels focusing on the femoral stem-cement mantle interface.

2.1 Cobalt-based alloys used for hip replacements

All CoCrMo alloys usually contain Cr (~ 26-30 wt %), Mo (~5-7 wt%), some Ni (1 wt% wt% maximum in order to minimize concerns related to possible Ni sensitivity), other residual other residual trace elements (Mn, Fe,Si, N) and C (either low-C ~ 0.05wt% or high-C high-C ~0.25wt%). The specific effects of each alloying element are summarised in

in

Table 2.1. A detailed summary of all the available CoCrMo alloys and their compositions are shown in Table 2.2. Although in low concentration, the carbon content has a significant effect on the alloy. It is responsible for the generation of carbides, which strengthen the material and affect the wear and the corrosion resistance [18, 19] and play a key role in the alloy microstructure and its mechanical properties.

Table 2.1 Effects of alloying elements in CoCrMo alloys

Element	Effect on the alloy
Cr	Improves oxidation and corrosion resistance by forming a passive oxide film, strengthens by formation of Cr_7C_3 within the hcp zones and $Cr_{23}C_6$ carbides/ Stabilize the hcp phase by reducing the stacking fault energy of the crystal structure.
Mo	Solid solution strengthener, also strengthens by formation of Co_3M intermetallic compound and Co_6C carbide/ Stabilize the hcp phase by reducing the stacking fault energy of the crystal structure.
Ni	Stabilizes fcc phase and improves forgeability. High content, at temperatures between 425 and 650 creates a two-phase fcc (γ) + hcp (ε) equilibrium microstructure. Improves the fatigue crack growth resistance by increasing the SFE
C	Strengthens by formation of MC, M_7C_3, $M_{23}C_6$ and M_6C carbides M represents either Co, Cr or Mo/ stabilizes the fcc phase
N	Increases M_6C carbide formation over $M_{23}C_6$, improving the mechanics of the alloy but reducing its ductility because of concentration of carbides in grain boundaries [20]
W / Si	Stabilizes the hcp phase
Mn / Fe	Stabilizes the fcc phase

2.1.1 Cast CoCrMo

Cast CoCrMo alloys are made by investment casting procedures (lost wax process). The high carbon content alloys are the most wear resistant, due to the presence of $M_{23}C_6$, M_7C_3 and M_6C carbides, that form within the structure during solidification, where M can be either Co or Cr. Depending on the solidification path the carbides will have different structures and can either grow at the grain boundaries (intergranular carbides) or in the matrix (dendritic carbides). Carbides improve alloy wear resistance due to the localized hardening of the matrix. Alloys can be treated thermally by homogenization or sintering which result in the partial or total dissolution of the carbides conferring different mechanical and corrosion properties to the as cast alloys [21]. Sintering is a post treatment used for some components of hip replacements such as acetabular cups to create porous rough surfaces from metal powders on the areas in contact with the bone to improve their osteointegration and a proper implant fixation.

The alloy solidifies between 1450 and 1350°C depending on its exact composition, [22]and forms a typical as-cast, cored structure on solidification with the major phase being face-center cubic (fcc) austenite designated as either γ or α-phase in the literature, with interdendritic zones rich in Cr, Mo, and C. The γ-phase which has a hexagonal close-packed (hcp) structure forms via an allotropic diffusionless martensitic phase transformation when the temperature drops below 970 °C, although is normally lower, around 870 °C, because Cr and Co stabilize the fcc phase. The phase transformation from fcc to hcp is however slow and a metastable fcc phase is usually retained at room temperature. If thermal treatment is continued, stacking faults are formed within the fcc or hcp phases microstructure.

Solution annealing treatments result in partial homogenization of the cored structure enough to give acceptable ductility and to keep their wear resistance. However, the major disadvantage of the cast and solution annealed CoCrMo alloys is their relatively low mechanical properties resulting from their coarse grain structure (> hundreds of microns and up to the millimetre size range) and casting defects such as porosity. In addition, the carbides that are retained after the solution anneal, can be detrimental for their wear resistance since they are less stable than the bulk carbides and can be easier pulled out from the matrix. In addition the can create sites for easy crack initiation and crack propagation. They might also decrease the corrosion resistance acting as galvanic cells due to the Cr gradient between the carbides and their surrounding areas.

2.1.2 Wrought CoCrMo

The wrought alloy in its forged condition shows a fine grained fcc matrix with a dispersion of small hcp platelets. The volume fraction of the hcp phase can be modified by different post thermal treatments [23]. The lower carbon content version, maximum content 0.05 wt.%, results in fewer and smaller carbides throughout the structure improving the alloys formability but reducing its wear resistance. The high carbon version, maximum content 0.25wt.%, is available and used, but requires a very close control of the forging and re-annealing stages of manufacture. The result is a fine-grained and strain-hardened alloy with the additional benefit that the finely distributed carbides provide a better wear resistance than forged alloys with larger carbides.

Hot forging of CoCrMo billets can result in significantly higher mechanical properties than the as cast alloys. Billets are heated to temperatures between 1000 and 1150°C. Re-annealing at stages during the forging process is used in order to prevent edge cracking during deformation and to break up larger carbides formed during solidification. A lower temperature final forging operation, as

with the stainless steel alloys, is used to achieve a degree of strain hardening of the alloy and a final component with desirable mechanical properties. The yield, ultimate and fatigue strengths are significantly higher than for the high-C, cast alloy. This is a result of the much finer grain size, the increase in stacking faults and hcp band formation, and strain hardening due to the lower temperature working operation.

Fine-grained, high-C bar stock can also be formed using a powder metallurgy processing route known as hot isostatic pressing (HIP)[24, 25]. By this method, the powders formed represent very rapidly solidified "micro-castings" so that while retaining carbides, these are small and finely distributed throughout the atomized powder. After atomization, the powders are then consolidated to full density by placement in a suitable containment vessel that is evacuated, sealed and hot isostatically pressed or hot forged, to form full density CoCrMo alloy. During the period at elevated temperature, some grain coarsening occurs but it is limited because of the grain growth inhibition effect of the finely distributed carbides. Strengthening of the alloy is possible by the addition of La or Al before the atomization resulting in the generation of finely dispersed La and Al oxide particles. Theses oxides inhibit the grain growth during the sintering annealing treatment used in the implant processing when a porous surface coating is added [26].

Table 2.2 Composition (wt%) of CoCrMo alloys used for orthopaedic implants

ASTM	Cr	Mo	Ni	Fe	C	Si	Mn	W	P	S	Other
F 75-92	27-30	5-7	1	0.75	0.35max	1	1	0.2	0.02	0.01	0.25N;0.3Al;0.01B
F799 (low C)	26-30	5-7	1	0.75	0.05	1	1				0.25N
F799 (high C)	26-30	5-7	1	0.75	0.25	1	1				0.25N-oxides of La and La
F 1537-94	26-30	5-7	1	0.75	0.35	1	1				
F 563	18-22	3-4	15-25	4-5	0.05	0-1	1	3-4		0.01	0.50-3.5Ti
F 562 (MP35N)	19-21	9-10.5	33-37	1	0.025max	0.15	0.15		0.015	0.01	1.0Ti
F 90	19-21		9-11	3	0.05-0.15	0.4	1.0-2.0	14-16	0.04	0.03	
F1058 (Elgiology)	19-21	6-8	14-16	Bal	0.15	1.2	1.0-2.0		0.015	0.015	0.10Be;39.0-41Co

2.2 Corrosion of CoCrMo alloys

The electrochemical properties of metallic implants are characterized by their chemical composition, crystal structure, conductivity and galvanic effects between the phases present at the alloy surface and the environment where the metal is immersed.

2.2.1 Metal interface and interactions with the environment

Corrosion occurs when anodic and cathodic reactions take place. When a metal in immersed in a liquid environment the charge on its surface will be re-distributed at the interface as its shown in Figure 2.1a and is defined as the electrical double layer. Cathodic reactions consist of the reduction of the oxidising agent, and the anodic reaction is the oxidation of the metal releasing electrons into the metal. Figure 2.1b illustrates the metal reaction in a liquid environment involving both reactions. For the cathodic reaction there is a mass transfer in the diffusion layer from the electrolyte towards the metal surface crossing the electrical double layer and a charge transfer from the metal surface to the electrolyte that finish in the solution as reaction products from the reaction.

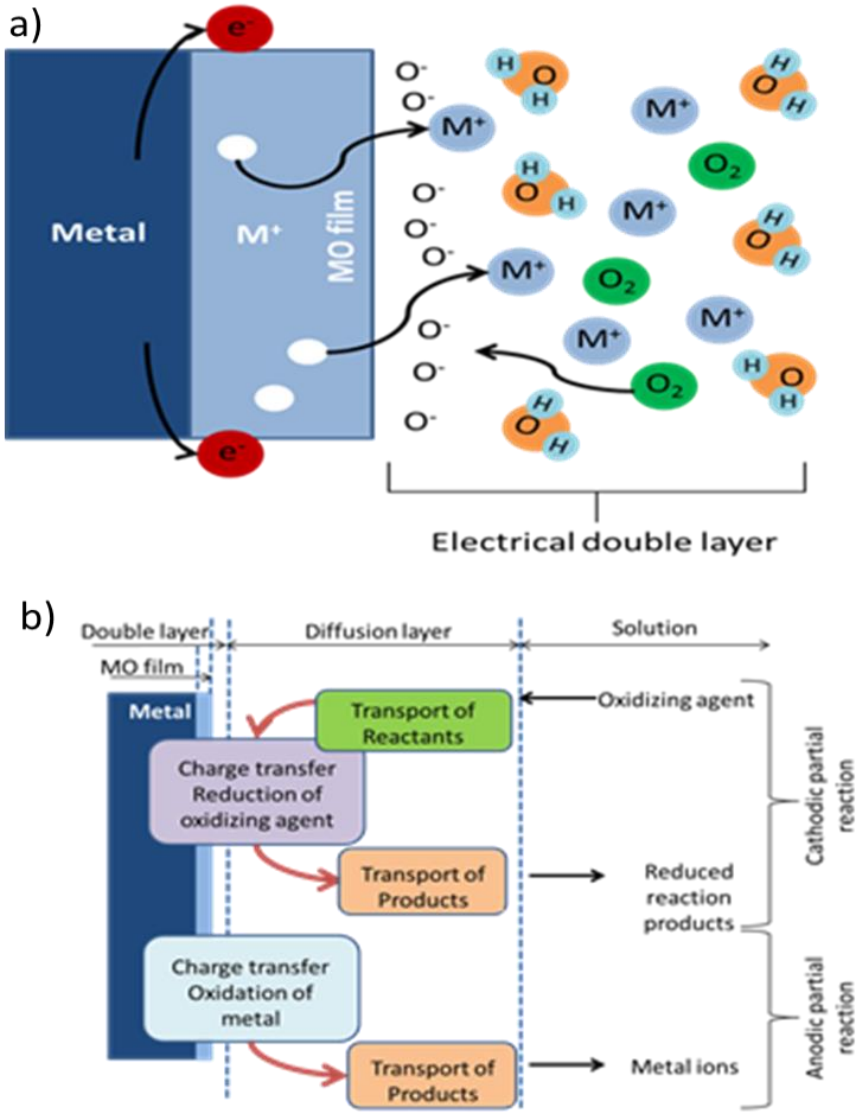

Figure 2.1 a) First reaction of the metallic surface when is in contact with the electrolyte b) Flow diagram of cathodic and anodic reaction for metals immersed in an electrolyte

For the anodic reaction there is a charge transfer from the oxidation of the metal producing the liberation of metallic ions into the solution. The positively charged metal atoms leave the surface and migrate into the surrounding liquid. The dissolved oxygen in the body fluids reacts with the charged metal ions and lead to the anodic processes. The main cathodic reactions depending on the environment, acidic or neutral /alkaline, are as follows according to Equation 2.1 to Equation 2.4:

Cathodic reactions			
Acidic conditions	Oxygen reduction	$O_2+4H^++4e^-\rightarrow 2H_2O$	Equation 2.1
	Proton reduction	$2H^++2e^-\rightarrow H_2$	Equation 2.2
Neutral or alkaline conditions	Oxygen reduction	$O_2+2H_2O+4e^-\rightarrow 4OH^-$	Equation 2.3
	Water reduction	$2H_2O+2e^-\rightarrow H_2+2OH^-$	Equation 2.4

In the case of CoCrMo, its anodic reactions depend on the nature of the surrounding medium and particularly on its pH and phosphate-protein concentration. In acid conditions, pH below 5, Co and Cr will go into solution as ions, following Equation 2.5 and Equation 2.6, whereas in neutral or alkaline environments the anodic reaction will form Co and Cr oxides as expressed by Equation 2.7 and Equation 2.8 respectively, repassivating the surface[27].

Anodic reactions		
Acidic conditions	$Co \rightarrow Co^{2+} + 2e^-$	Equation 2.5
	$Cr \rightarrow Cr^{3+} + 3e^-$	Equation 2.6
Neutral or alkaline conditions	$2Co + O_2 \rightarrow 2CoO$	Equation 2.7
	$4Cr + 3O_2 \rightarrow 2Cr_2O_3$	Equation 2.8

2.2.2 Passivation-depassivation processes and repassivation kinetics

From an electrochemical point of view, all metals currently used for orthopaedic implants can be oxidised by body fluids and become protected against further corrosion by an oxide layer, which in the case of CoCrMo is about 1.8nm thick [28]. The oxide layer prevents the metal surface from coming into contact with the environment. The formation of the oxide layer is known as the passivation process and the layer is usually formed by insoluble oxides such as Cr_2O_3 ,CrO and MoO_3 for Co based alloys and TiO_2 for Ti alloys, which act as a kinetic barrier to further oxidation.

Their corrosion resistance depends on the stability of the oxidised surface layer. Any change of pH or composition of the electrolyte, or damage due to motion

and mechanical processes might initiate the depassivation processes [15] when the oxide layer is removed.

The repassivation process takes place after the initial passive film damage due to the oxide reforming, mainly Cr_2O_3, according to Equation2.9, which suppresses the corrosion process by reforming the barrier until it depassivates again.

$$4Cr^{3+} + 3O_2 + 12e^- = 2\,Cr_2O_3 \qquad \text{Equation2.9}$$

The rate of repassivation is dependent on the reaction kinetics and is related to the amount of corrosion product released into the surrounding environment [29]. Different models to study the depassivation/ repassivation and peak current of metals/alloys in tribo-corrosion systems have been developed [17, 30-33], however, the complexity of the damaged area resulting from the different tribosystems and the multiple chemical and contact conditions make it difficult to compare between them.

2.2.3 Modes of corrosion

Corrosion can be classified as general corrosion, which involves the uniform dissolution of the metal surface or localised corrosion when corrosion happens in specific sites on the metal surface such as pits or inclusions. The localised corrosion can cause high local dissolution rates resulting in high rates of penetration and liberation of metallic ions. The main localised types of corrosion are pitting, crevice corrosion, intergranular corrosion, galvanic corrosion and fretting corrosion.

Pitting corrosion is observed on passive metals in the presence of certain anions (in particular chloride) when the potential exceeds a critical value producing pits in the metal's surface. It can be initiated at localised sites where there are small surface defects such as scratches or indents. The lack of oxygen in the cavity makes it become the anode while the rest of the metal acts as a cathode forming a cell.

The crevice corrosion mechanism is similar to that of pitting corrosion, however the lack of oxygen is caused by a difference of oxygen availability within a preformed crevice between two metallic surfaces, that leads to the formation of an electrochemical cell. The metal particles and metallic ions released into the crevice fluid generate Cl^- ions which decrease the pH levels. The limited space within the crevice prevents the proper aeration of the electrolyte reducing the O_2 levels to the point of total oxygen depletion due to repassivation of the surface, hence the corrosion is heavily accelerated increasing the metal surface

dissolution. Corrosion modifies the physical and mechanical properties of the metal surface and generates metal particles. The oxide particles being trapped between the contact surfaces can accelerate the wear processes acting as third body abrasives, [34, 35], decreasing the wear resistance of the metal. In particular in body environments, the protein adsorption in the joint crevice is another cause of increased metal ion dissolution. Phosphate ions and albumin are adsorbed to the alloy surface. However, their effects on corrosion are quite different. Phospates act as an anodic inhibitor while albumin acts as a cathodic inhibitor since its adsorption impedes access of the oxidant to the metal surface [36]. At the same time it increases the dissolution rate of metal because it limits the adsorption of phosphate, thus accelerating corrosion, as discussed by Milosev et al and Igual-Munioz et al, [36, 37]. Insufficient oxygen due to crevice conditions and protein adsorption synergistically constrains stable repassivation and increases the electrochemical reactivity, accelerating the dissolution of metal ions [38, 39].

Intergranular corrosion is a selective attack of grain boundaries. Thermal treatments lead to preferred precipitation of phases and different compositions in neighbouring grains. When the potential differences between adjacent grains are high enough for one grain to act as the anode and the other as the cathode a galvanic cell is stablished across the boundary producing the intergranular corrosion.

Galvanic corrosion, also called bimetallic corrosion, results from the formation of an electrochemical cell between two metals. The corrosion of the less noble metal is thus accelerated. Galvanic corrosion has been observed between different materials in hip implants, eg. Ti and CoCrMo [40, 41] or orthodontic wires [42]. In some hip implant material combinations two different CoCrMo alloys can be used. As it was described in the previous section CoCrMo alloys can present different manufacturing process (forged, as cast, high carbon, low carbon, thermal treated) which affect their chemical composition and therefore their electrochemical behaviour when they are in contact under loading conditions.

Fretting corrosion results from the combined action of corrosion and micromotion between two surfaces. These small amplitude displacements might occur when the amplitude of the movement is smaller than the contact area width between two metal parts in contact. Fretting corrosion has been observed in the taper-trunnion interface of modular hips and also in the femoral stem-cement interfaces [33, 43].

2.2.4 Static corrosion experiments in CoCrMo alloys

Electrochemical behaviour in static conditions, without any load applied, have been evaluated previously to analyse the influence of microstructure, thermal treatments and environment (pH, temperature, protein content and applied potential). In addition the oxide layers [44] and the metal ion release rates [28, 29, 45-48] have been also characterised.

The main techniques for the characterisation of the electrochemical behaviour are Open Circuit Potential (OCP), Potentiodynamic Polarization (PD) and Electrochemical Impedance Spectroscopy (EIS) and in some cases cyclic voltammetry and electrochemical noise measurements. OCP values obtained from experiments in NaCl solutions are in the range of -166 mV vs Ag/AgCl electrode after 30 minutes immersion obtained by Sun et al for an As Cast ASTM F-75 alloy [49], carbon content not specified, to -300 mV vs Ag/AgCl electrode after 5 minutes immersion of a high carbon content Co-based alloy, 0.49 wt % , [50], or -390 mV vs SCE electrode after 1 hour immersion found by Muñoz et al using a low carbon content alloy, carbon below 0.08 wt % [36]. The main parameters obtained from PD experiments are corrosion and current potentials, E_{corr} and i_{corr} respectively. The range of values is heavily influenced by the experimental conditions, especially the initial potential value where the potentiodynamic scan starts. E_{corr} values, when cathodic cleaning is produced e.g. starting potential -2V, are close to -1000 mV vs Ag/AgCl when NaCl is used, [51], and they became more anodic, -600- -800 mV if the solution contains proteins or phosphates [44, 48]. Comparing i_{corr} values from different studies in NaCl solutions, Sun [52] after 30 minutes immersion time obtained a current of 0.11 $\mu A/cm^2$, while Valero [39] showed an increasing trend with temperature, from 0.09 to 2.10 $\mu A/cm^2$ at 24.85 and 59.85 °C respectively during 1 hour immersion times, and Ouerd et al. [44], using immersion times up to 11 hours, found corrosion currents one order of magnitude lower between 0.027 to 0.1 $\mu A/cm^2$.

XPS, Raman or Infrared Spectroscopy can be used to characterize the oxide layers and the reactivity of CoCrMo alloys in several physiological mediums. Different solutions such as NaCl, PBS, Ringer'solution, Hank solutions, Bovine Calf Serum or human synovial fluids have been used to investigate the interaction of ions, phosphates and proteins with the metallic surfaces [27, 29, 36]. Previous work has demonstrated that the presence of proteins affects the passive dissolution of CoCrMo alloys. This is due to the presence of adsorbed species at the metal-liquid interface influencing the anodic reaction by binding metal to ions and transporting them away from the solution-metal interface, enhancing the dissolution [29, 46-48]. They can also modify the cathodic reaction, affecting the

passive film formation [27] and the transpassive behaviour [46, 53, 54] of the alloy.

The influence of the manufacturing processes (forging, casting, HIP) and subsequent thermal processes (e.g. annealing) have been investigated as they dictate the final alloy microstructure [55, 56], grain size [57], carbide presence [19], carbon content [58] and phases presented [56]. In general as cast alloys present a higher corrosion resistance than forged alloys, primarily due to the grain size in the forged alloy being at least one order of magnitude below the as cast alloys, resulting in an increase number of grain boundaries. It has been shown that grain boundaries or any other interfaces such as carbide-matrix interactions decrease the corrosion resistance as they act as preferential sites for corrosion [56, 57] presenting more negative *OCP* and E_{corr} values and higher i_{corr}. Direct comparison of values between studies is difficult due to the differences between experimental conditions such as immersion time, potential range or electrolyte used.

Despite the studies mentioned above, the majority of them did not give a detailed description of the manufacturing process or the chemical composition of the alloy and none of them compare directly between forged and as cast alloys using the same experimental conditions.

2.2.5 Influence of grain orientation and grain size on the static corrosion properties of metals

Electrochemical dissolution of metals needs anodic and cathodic sites electrically connected in an electrolyte, as discussed in Section 2.2.1. At the atomic level, the metal atoms most likely to undergo corrosion are those with the highest free energy which are the ones which are less densely packed and surrounded by a lower number of neighbouring atoms. Therefore, the more dense packed crystallographic planes such as the (111) will corrode slower than (100) or (101) since the available paths for oxygen diffusion are less in number than in the others. The oxidation behaviour in single crystal metals, Ni (fcc) and Cr (bcc), was studied by Bonfrisco et al. ,[59], by comparing the relative oxidation rates for surfaces with different crystallographic orientations. The study found the oxides grown on the (111) faces contained significantly lower fractions of high-angle grain boundaries than those grown on the (001) faces. The faces oriented in the (011) formed an oxide that was polycrystalline and contained many more diffusivity paths. Thus, planes with a higher number of defects such as grain boundaries or diffusivity paths will corrode faster than the others. In addition to the studies on single crystals described above, Schuch et al. [60] used a novel technique on polycrystalline Inconel 600 alloy by measuring the oxide thickness

using atomic force microscopy (AFM) and correlating the results with the grain orientation of each grain. The corrosion rate was found to increase according to the following pattern: (111) < (011) < (001) with thicker oxide layers on the grains with crystallographic orientations which oxidized faster.

In addition, an increase in the total grain boundary length at the surface means an increase in the availability of diffusion paths for ion transport and act as initiation sites to start the corrosion process. Therefore, samples with a smaller grain size have higher number of grain boundaries, hence worst corrosion behaviour than coarser grain microstructures as it was shown in polycrystalline Mg alloys, [61, 62], with higher corrosion resistance for the alloys with coarser grain sizes microstructures.

2.3 Deformation in metals

2.3.1 Crystal Structures in metals

The common metallic biomaterials (i.e. stainless steel, Co- based alloys and Ti and its alloys) form either body centered cubic (bcc), face centered cubic (fcc) or hexagonal close –packed (hcp) unit cells at body temperature with ideal crystal lattice structures as shown in Figure 2.2. The two main crystal structures found in Co-based alloys are fcc and hcp [22, 63-66].

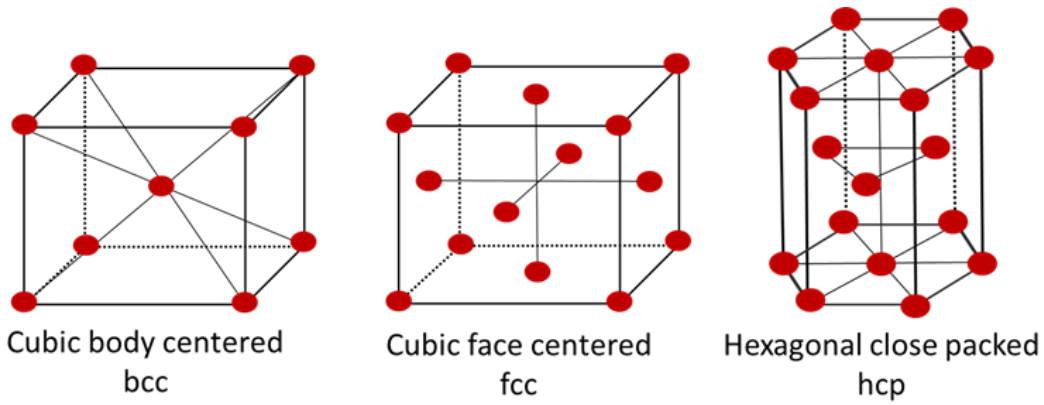

Figure 2.2 Unit cells for body-centered cubic (bcc), face centered cubic (fcc) and hexagonal close-packed (hcp) crystal structures

Atom packing arrangement can be represented as a simple solid sphere model, that results in a stacking sequence as ABCABC… for the fcc structure or ABABAB stacking sequence for the hcp structure, as represented in Figure 2.3.

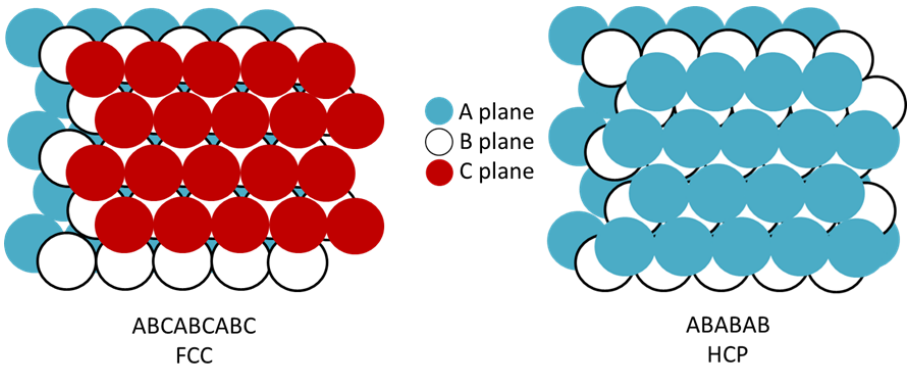

Figure 2.3 Solid spheres models showing the two stacking sequences possible in close-packed crystal structures[67]

The atomic arrangement in each crystal structure results in a different number of slip systems. A slip system is formed by the slip planes and the slip directions. The slip plane is the plane of atoms along which the dislocation motion or slip is easiest to occur. Within the slip planes the preferred crystallographic directions are the slip directions. The slip planes and directions are those of highest planar and linear packing density respectively. A higher linear or planar packing density means the distance between the atoms in the structure is shorter than in less dense packed planes or directions. For easy movement of dislocations a small repeat distance between atoms is desirable. This condition is satisfied in closed pack planes since the atomic density is the highest and therefore the planes can slip more easily relatively to each other.

For fcc systems, slip happens on (111) planes in <110>directions, with a total of 12 slip systems. For hcp crystal structures, slip usually happens on (0001), basal plane, and (1-100), prismatic plane, and the typical slip direction is <11-20>. Since there are just 3 independent slip systems on the basal planes compared to 12 in the fcc structure, plastic deformation is severely limited and during plastic deformation additional slip or twin systems need to be activated. This usually requires a much higher resolved shear stress and results in the brittle behaviour of hcp polycrystals.

Real metal crystals, in contrast to these ideal atom arrangements, contain lattice defects such as vacancies, dislocations or grain boundaries that have a strong effect on their mechanical, physical and chemical properties.

2.3.2 Plastic deformation in metals

2.3.2.1 Definition of dislocation and dislocation motion

The number of dislocations in a material is expressed as the dislocation density, which is the total dislocation length per unit volume or the number of dislocations intersecting a unit area. Most crystalline materials, especially metals, have dislocations in their as-formed state as a result of mechanical and thermal stresses related with the forming process. The presence of dislocations allow deformation at much lower stress than in a perfect crystal (no dislocations) which would require a higher energy input for deformation to occur. Therefore, dislocations are usually defined as linear defects which act as "vehicles" for plastic deformation. The mechanism of dislocation motion is through plastic shear by breaking and reforming the bonds around the defect displacing the half plane (dislocation) or the defect. The propagation of one dislocation across the plane causes the top half of the crystal to move (to slip) with respect to the bottom half.

There are two main types of dislocation: edge dislocation and screw dislocation, (Figure 2.4). Edge dislocation line moves parallel to applied stress while screw dislocation line moves perpendicular to applied stress. There are also mixed dislocations, where the direction of motion is neither parallel or perpendicular to the applied shear stress. Edge dislocations can introduce compressive, tensile and shear lattice strains, while screw dislocations can only introduce shear strain. Both of them distort the crystal lattice producing strain fields which restrict dislocation motion.

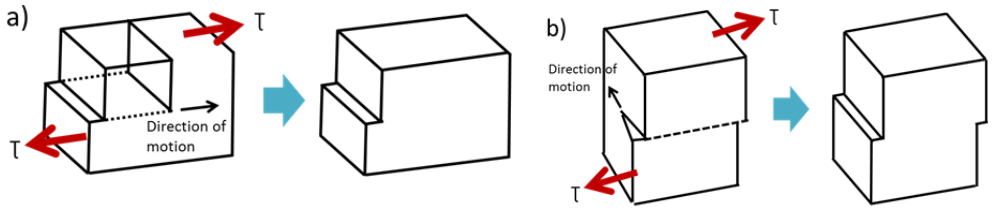

Figure 2.4 Classification of different types of dislocations: a) Edge dislocation and b) Screw dislocations

When a material's yield stress is exceeded and plastic deformation starts to occur in metals, in addition to the original dislocations new dislocation are formed. These new dislocations can be geometrically necessary boundary dislocations (GNB's), geometrically necessary dislocations (GND's) and statistically stored dislocations (SSD's) and are produced to accommodate the plastic deformation [68]. At a large scale, GNB's are formed due to the activation of different slip

systems between the neighbouring grains [69]. Dislocations stored in these boundaries are the GND's needed to accommodate lattice misorientations across the boundaries [70] while SSD's accumulate randomly by the statistical trapping of dislocations during plastic slip and do not have a geometrical consequence [71].

2.3.2.2 *Shear stress and dislocation motion*

The stress applied, σ, is defined as the ratio between the force, F, and the area, A, as defined in Equation 2.10. To move dislocations, a minimum stress must be applied to overcome the resistance to dislocation motion. Slip occurs when the shear stress, τ_R, see Equation 2.11, acting in the slip direction on the slip plane reaches a critical value, known as critical resolved shear stress (CRSS), τ_c, and is related to the stress required to move dislocations across the slip plane, see Equation 2.12 and Equation 2.14. The quantity $Cos\phi Cos\lambda$ is known as the Schmid Factor (M), where λ is the angle between the stress direction and the slip direction, ϕ is the angle between the normal direction to the slip plane and the stress direction, see Figure 2.5. From Schmid's Law, the primary slip system will be the system with the greatest M. The tensile yield stress of a material, σ_y, is the minimum applied stress needed to start slip and produce plastic deformation under a given load, see Equation 2.14.

Applied tensile stress:

$$\sigma = \frac{F}{A} \qquad \textit{Equation 2.10}$$

Resolved shear stress

$$\tau_R = \frac{F_s}{A_s}$$

$$\tau_R = \frac{F\,cos\lambda}{\frac{A}{cos\phi}} = \frac{F}{A} cos\phi cos\lambda = \sigma cos\phi cos\lambda \qquad \textit{Equation 2.11}$$

$$\tau_c = \sigma_y\, cos\phi\, cos\lambda \qquad \textit{Equation 2.12}$$

$$\tau_c = \sigma_y\, M \qquad \textit{Equation 2.13}$$

$\tau_R > \tau_c$ condition for dislocation motion to start *Equation 2.14*

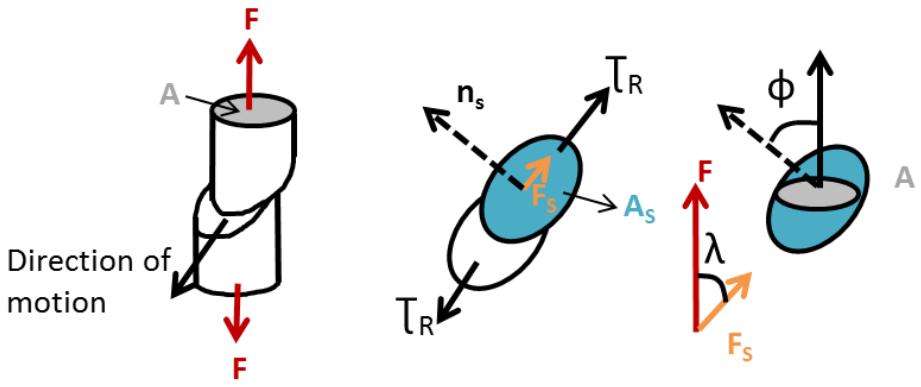

Figure 2.5 Schematics of how the applied tensile stress relates with slip direction and resolved shear stress

The yield stress changes from sample to sample depending of the position of the crystal lattice relative to the loading axes. At the nano and micro scales this is relevant due to the scratch size (100 μm length) with respect to the grain size found in the alloys under study. Results in polycrystalline materials where the deformation takes place between several planes will give an average deformation value resulting from the combination of all the interacting grains, while single grain materials or polycrystalline materials with coarser grains on the same scale as the scratches, will be dependent on their specific crystallographic orientations.

Yield will begin when the shear stress on the system reaches the critical value established by the Tresca criterion following Equation 2.15.

$$\tau_{max} = \frac{\sigma_y}{2} \qquad \textit{Equation 2.15}$$

The "soft orientation" for fcc metals is the one where the slip plane activates at a 45° angle to the tensile-compression axis. The "hard orientation", which will be the less prone to deformation, is the slip plane which activates at 90° to the tensile-compression axis.

A typical shear stress-shear strain curve for a single crystal shows three regions of work hardening, (Figure 2.6): After yielding, Region I represents the easy glide process, with low hardening rates where the shear stress for plastic deformation is constant with little or no work hardening. This happens when a single slip system is activated and the dislocation motion is unimpeded by other dislocations or lattice defects. The extension of the first region depends on the orientation of the crystal and the presence of other dislocations and defects in the

sample such as precipitates or interstitial solution elements which inhibit the dislocation motion.

When the shear stress is increased, plastic deformation increases linearly in Region II. The increase of γ produces an increase of the critical shear stress resulting in a constant hardening rate. At this stage slip is initiated on multiple slip systems and work hardening occurs due to the interactions between dislocations moving on intersecting slip planes. Finally, Region III shows a decreasing work hardening rate due to the increase in the degree of cross slip when the shear strain is increased.

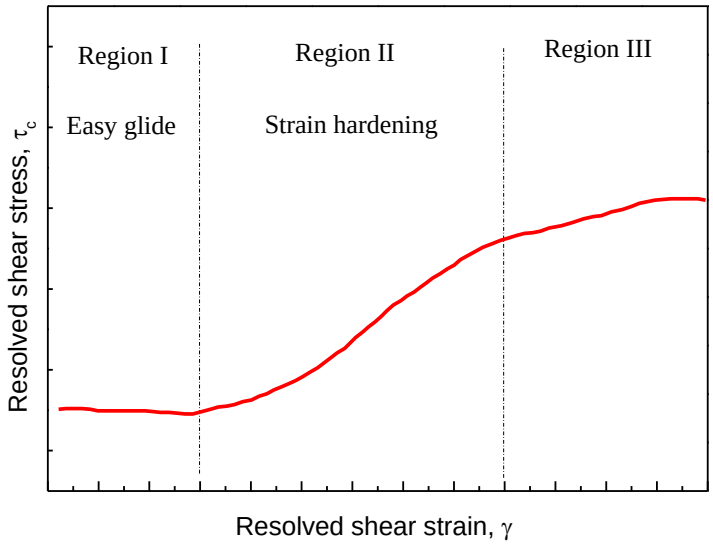

Figure 2.6 Typical resolved shear strain-stress relationship when a single crystal is deformed

For materials with low stacking fault energies (SFE) the transition between Region II and Region III occurs at high stress levels, as cross slip is minimal due to the low number of dislocations presented in the material.

Monocrystals are elastically and plastically anisotropic and they undergo deformation in one single slip system. Since polycrystals can be treated as an isotropic material (if no texturing is present), deformation cannot occur only on one slip system because various grains have to be compatible. In addition dislocation movement is harder because it is restricted to one grain. Deformation of a crystal which is surrounded by other crystals with different crystallographic

orientations will only start at the primary system if the strain taking place at the boundary is compatible with the strain present in the other crystals.

Crystals with larger shear stresses will deform first and the less favourably oriented will yield afterwards. Even those grains which can deform more easily might be limited in their deformation by adjacent grains which cannot deform so easily. In that sense, a polycrystalline material will have a stronger resistance to plastic flow than a single crystal and their plastic deformation will be more restricted resulting in higher yield stresses and greater work hardening. An example is shown in Figure 2.7. The single crystal and the central crystal in the polycrystal grain both have the same λ and θ values to calculate the minimum yield stress. However, in the polycrystal sample the crystal orientation and angle changes in the neighbouring grain, and it will require a higher strain to start the deformation. Usually the motion between grains in a polycrystalline sample results in voids or an overlap between crystals which might be corrected by the introduction of GND's or new deformation mechanisms such as twinning.

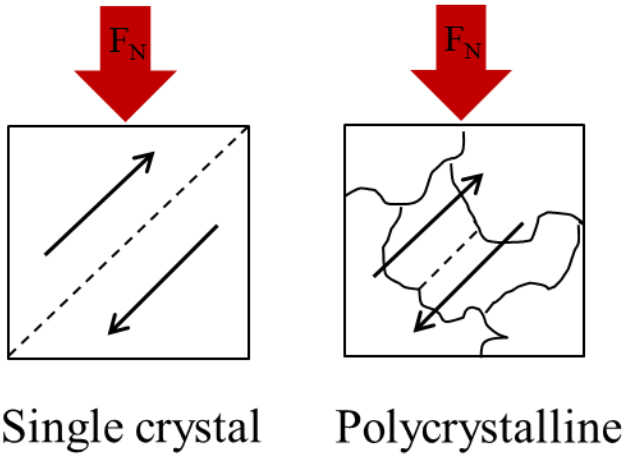

Figure 2.7 Deformation mechanisms in singles crystal and polycrystalline materials

2.3.2.3 Mechanisms to reduce dislocation motion

Dislocation motion can be inhibited by several techniques such as grain size reduction (increased grain boundaries), solid-solution alloying and strain hardening (addition of precipitates) or the presence of two different phases. All these elements and their interactions when the material is plastically deformed have an influence on the general plasticity of the material.

- Reduction of grain size:

Grain boundaries are the interfaces between crystals of the same structure. They act as barriers to slip, as the dislocation must change direction in order to move into the adjacent grain, requiring more energy than that required for standard dislocation motion. Therefore increasing the number of grain boundaries inhibits the dislocation motion. The effect will be more significant if the misorientation angle (difference of orientation angle between the two grains) is high. Impeding this dislocation movement will hinder the onset of plasticity and hence the yield strength of the material will be increased.

The relationship between the grain size and the yield strength, σ_{yield} is given by Hall-Petch Equation [72], Equation2.16, where σ_o and k_y are constants for a particular material and d is the average grain diameter. The grain size can be controlled by the rate of solidification, by plastic deformation and by heat treatments.

$$\sigma_{yield} = \sigma_0 + \frac{k_y}{\sqrt{d}} \qquad \textit{Equation2.16}$$

There is a limit to this mechanism. Grain sizes can range from about 100 μm (large grains) to submicron, below this size, the size of dislocations begins to approach the size of the grains. At a grain size of about 10 nm only one or two dislocations can fit inside a grain, favouring grain boundary diffusion. Therefore, the lattice resolves the applied stress by grain boundary sliding, resulting in a decrease in the material's yield strength.

- Solid solutions or vacancies:

Impurity atoms or vacancies distort the crystal lattice and generate internal stresses (tension-compression) which interact with the stresses associated with the dislocations. The result is repulsive forces between the dislocations and the defects which produce a barrier for dislocation motion.

- Precipitation strengthening:

The addition of impurity particles or hard precipitates such as SiC in Fe or Al can increase the material's strength. These second phase particles precipitate during the thermal process act as "pinning" sites which impede the dislocation movement and strengthen the material.

- Cold working or metal forming:

Different metal forming processes such as forging, drawing, rolling or extrusion multiply the number of dislocations making dislocation movement more difficult due to the increase of the dislocation density within the material. The average distance between dislocations decreases and dislocations start blocking the motion of each other.

- Recovery, recrystallization and grain growth:

To restore the state before cold-working it is possible to apply a 3-step thermal treatment to produce the next effect on the alloy: recovery, recrystallization and grain growth. Heating the material increases the diffusion and enhanced dislocation motion which leads to a decrease in dislocation density and the relief of internal strain energy because crystal distortion is minimised. For recrystallization to occur, a driving force is needed. The difference in the internal energy created between the strained and unstrained regions results in the nucleation of new grains. New grains will grow by diffusion of atoms into the new grains crystal lattice, helped by the heating processes.

2.3.2.4 Stacking faults and stacking fault energy (SFE)

A stacking fault is a one or two layer interruption in the stacking sequence of the crystal structure. In fcc metals the normal stacking sequence is ABCABC, but if a stacking fault is introduced it may change to ABCBC. The width of a stacking fault is a consequence of the balance between the repulsive force between two partial dislocations on one hand and the attractive force due to the surface tension of the stacking fault on the other. The equilibrium width is determined by the stacking fault energy, measured in Joules per square metre. A smaller width means the atoms are closer and therefore more energy will be needed to change their position. As a consequence materials with high SFE will deform more by full dislocation glide, as the dissociation of a perfect dislocation into two partial ones is unlikely to happen. On the other hand, low SFE materials will promote the formation of wider stacking faults, which results in cross-slip and climb being more difficult and a decrease in the mobility of dislocations. Low SFE materials usually activate other mechanisms such as twinning and the creation of partial dislocations to accommodate large strains which produce high plastic deformation levels.

As a result of the low SFE in CoCrMo alloys, plastic deformation by dislocation glide in the fcc metastable phase is highly restricted. This behaviour leads to formation of strain-induced crystal defects, such as intrinsic stacking faults, twins and regions of highly localized slip along pre-existing and strain-induced

stacking faults when these alloys are subjected to external stresses exceeding their yield strength. Thus, the ductility of these materials is small compared with other fcc metals. The interaction between dislocations of limited mobility and dissociated dislocations and/or twins lead to very rapid and highly localized hardening[73]. This leads to fracture if no other mechanisms become available to relieve the high stresses required to maintain plastic flow [74]. Twinning and strain induced phase transformations have been suggested to play an important role during large strain plastic deformation [75, 76], although their contribution to ductility improvement is still unclear. A twin is often defined as a very large stacking fault and occurs when there are not enough slip systems to accommodate deformation and/or when the material has a very low SFE. A twinned crystal consists of two individual crystals joined at the boundary in some definite mutual orientation. The lattice of one crystal is related to that of the other by symmetry.

2.3.3 Phase transformations

The equilibrium arrangement of atoms in solids is determined by factors such as atomic size, valence, and chemical affinity between the elements under specific extrinsic conditions (i.e., temperature, pressure). For a given temperature and pressure conditions, the stable state is the structure of lowest free energy. Free energy, *G*, is related to enthalpy, *H*, and entropy, *S*, through Gibbs equation as follows, where *T* is the absolute temperature:

$$\Delta G = \Delta H - T\Delta S \qquad \textit{Equation2.17}$$

Changes in state or phase transformation in solids are possible if a decrease in *G* occurs due to the transformation. While a reduction in *G* represents a necessary thermodynamic condition for the formation of a new phase, atomic rearrangement to form the new phase must occur in a reasonable time period (kinetics of the transformation). For most solid-state phase transformations, atom rearrangement occurs through thermally controlled diffusion processes (diffusive transformations) that result in a crystallographic and compositional change within the newly formed phase(s), the amount and microstructure of the new phases(s) depending on temperature and time. Atomic diffusion occurs during metal processing and determines the structure and properties of metallic components. Some processes affected by atomic diffusion are:

- Solidification during casting
- Grain growth during elevated temperature annealing
- Precipitation and growth of second phase particles
- Sintering of metal powders to form dense or porous structures

- Recrystallization (relatively strain-free crystals nucleate and grow within mechanically deformed materials)
- Formation of protective oxides over metal substrates (passive film growth)

The diffusion rate, *D*, is given by Equation 2.18 , where:

- D_0 = diffusion coefficient
- Q = activation energy for atom movement
- R= universal gas constant
- T = absolute temperature.

$$D = D_0 exp\left(\frac{-Q}{RT}\right) \qquad \textit{Equation 2.18}$$

This relationship shows that the diffusion rate falls exponentially as the temperature is reduced. Thus, at lower temperatures diffusion changes will not occur in practical time periods even though they are energetically favoured by changes in the free energy. As a result, metastable structures can exist at ambient temperatures, such as the retention at room temperature of a fcc structured phase in Co-based alloys. The fcc structure (γ-phase, austenite) is metastable at temperatures below about 970°C where free energy considerations would predict the formation of the hcp ε-phase (martensite), however, because of the slow diffusion of Co, Cr and Mo atoms at the transformation temperature they prevent the formation of the hcp phase by a diffusive transformation [77]. The fcc-hcp transformation in Co is referred to as martensitic due to its diffusionless character, its thermal hysteresis and the typical nucleation and growth process similar to martensite in steels [78]. The martensitic [79] transformation in CoCrMo has been investigated because the hcp martensite phase has been reported to improve the wear resistance of low C CoCrMo [77].

Co-based alloys exhibit the fcc to hcp transformation under three possible conditions:

- Athermal [80, 81], the athermal ε-martensite is induced by quenching from the fcc field of stability (typically above 1100°C). However, the transformation is limited and it only reaches a volume fraction of 0.4-0.5. In athermal transformations the amount of new phase forming from the original phase is going to be dependant only on the final temperature.
- Isothermal [82], the hcp preferentially nucleates at fcc twin intersections and stacking faults, including grain boundaries. In contrast to athermal transformation, aging after annealing at 1150°C can lead to a complete fcc

→ hcp transformation when aging temperatures of the order of 650-950°C are employed [75].

- Strain induced transformation (SIT) is produced by mechanical straining on the material [83-85]. SIT leads to mechanical properties such as high strain hardening rates, high strength and low ductility. The effect produced by the strain is the development of numerous parallel striation with various orientations intersecting stacking faults or annealing twin interfaces in the plastically deformed area[86]. It plays a double role during plastic deformation in this material: first, it helps to relieve the internal stresses caused by the relative inability of the fcc phase to deform plastically via dislocation glide and second: the shape change inhibits the formation on internal cracks.[87].

In solution treated cast alloys, the flow and hardening behaviours depend strongly on carbon content. It was shown that high carbon contents inhibit the occurrence of strain-induced phase transformation and the flow and hardening behaviour of these materials depend on the interactions between strain-induced crystal defects and second phase carbide particles present in the microstructure[87]. Grain size has been also reported as a factor which might inhibit the development of athermal martensite [83], although some other authors affirm that grain size doesn't have any influence [77].

2.4 Tribology of artificial hip joints

Tribology is the science of surfaces interacting under an applied load and in relative motion. The subject includes the study of friction, lubrication and wear.

2.4.1 Surface topography

The surface is defined as the boundary between the environment and the material. A surface is characterized by an extended macroscopic profile, also called a technical profile, intrinsic to the shape of the component, and by a microscopic profile consisting of surface irregularities. These irregularities are deviations from the macroscopic profile and can have a significant influence when moving components are in contact.

Roughness and waviness are the constituents of surface texture. Many surfaces exhibit both and, in addition, the surface may also be curved with form error or shape deviations such as long-period and non-cyclic deviations. The roughness of a surface plays an important role in determining the interactions with the surrounding environment, and it has a considerable influence on the life of materials, fatigue strength, resistance to corrosion or bearing lubrication.

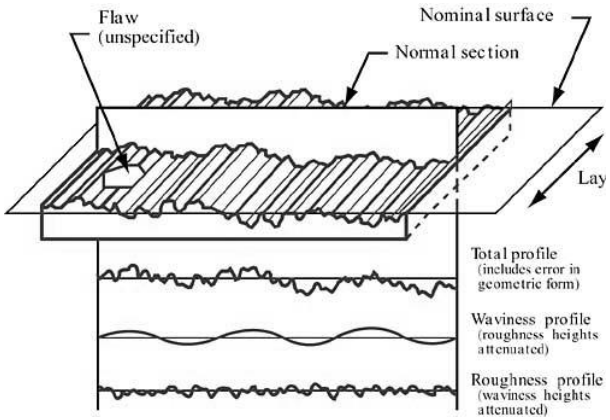

Figure 2.8 Schematic representation of the surface, waviness and roughness[88]

The basic elements to describe the surface roughness are described in Figure 2.8:

- Total profile: basis for the valuation of the nominal surface parameters.
- Roughness profile: profile derived from the primary profile by suppressing the longwave component using the profile filter λ_c
- Waviness profile: profile derived by subsequent application of the profile filter λ_f and the profile filter λ_c to the primary profile, suppressing the longwave component using the profile filter λ_f, and suppressing the shortwave component using the profile filter λ_c.

Some of the existing parameters defined by the ISO 4288:1996[89] are:

- Roughness or amplitude parameters (vertical), determined only by the height of peaks and valleys without taking into account the horizontal spacing (R_a, R_t, R_z, R_p, R_q, R_v)
- Waviness parameters (W_t)
- Parameters of the profile (P_t)
- Spatial parameters (horizontal), determined by spatial irregularities along the surface (D, P_c)
- Statistical parameters (R_{sk}, R_{ku})

It is important when measuring roughness to differentiate between terms such as sampling length (l_r) used to identify the irregularities that characterize the profile under evaluation and the evaluation length (l_n) which is the length used to assess the profile under evaluation. The specific lengths to measure the roughness is set on ISO 4288:1996 [89] and it will be chosen depending on the sample roughness.

The most important and commonly used parameter in surface texture analysis is the roughness average, also called R_a. R_a is the average arithmetic value of the

deviations of the roughness profile filtered from the mean line into the sampling length[90]. See Figure 2.9.

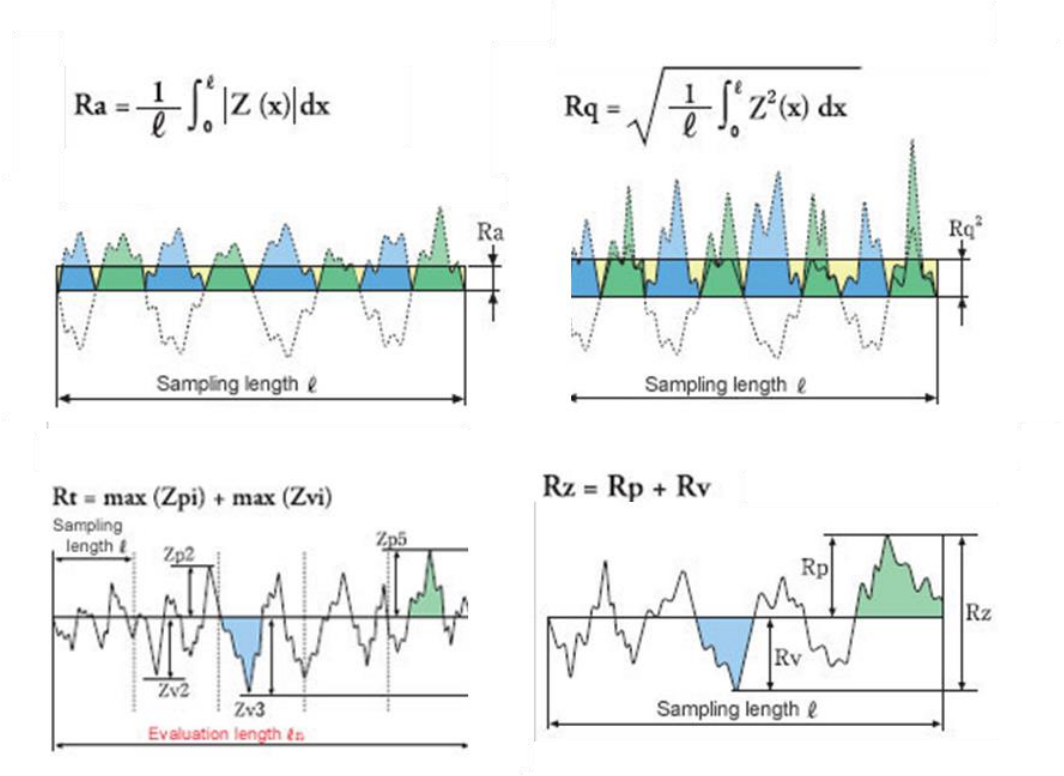

Figure 2.9 Representation of R_a, R_q, R_t *and* R_z *to analyse surface texture [88]*

It is used to detect gradual changes to the surface that can be caused by wear. The measured value of R_a on a length represents the average roughness, so the effect of isolated peaks or valleys does not influence the results and the measured length will be close to the average. However R_a won't provide information about the shape of irregularities and there is no distinction between peaks or valleys. R_q is defined as the root-mean-square deviation of the profile roughness reflecting the differences between peaks and valleys.

The maximum roughness is designated as R_t and it represents the vertical height between the highest and lowest points of the profile within the valuation length. Finally R_z is the maximum peak to valley height within the sampling length.

R_{sk}: skewness of the profile. This is the third moment of the distribution curve of the heights and indicates the symmetry of the profile. An unsymmetrical profile gives a skewed curve. The direction of the skew depends on whether the bulk of the material is above the mean line (negative skew) or below it (positive skew).

R_{sk} is sensitive to very distant points from the average surface, such as isolated valleys or peaks.

Surface texture can be characterized by many instruments, but the most commonly used is the contact profilometer. The tip is in contact with the surface and is passed across it under examination at a constant speed. It is moved vertically, following surface contours, and the height of the probe at any particular point is recorded. The resultant vertical motion of the stylus compresses a piezo-electric element, which generates a linear voltage response. The transducer of the profilometer produces an electric signal, proportional to the displacement of the stylus, which is amplified and fed to a chart recorder that provides a magnified view of the original profile.

Final roughness of implant bearing surfaces is of great importance. Following ISO 7206-2[91], the minimum roughness surface should be below 0.05 μm for metals and below 0.02 μm for ceramics. In fact, the surface of specific components, i.e. head and cup in hip joint replacement, should be as smooth as possible to avoid wear and therefore the release into the articular space of dangerous metal ions or third body particles. However, the modular interfaces require a certain degree of roughness to improve self-interlocking between components.

2.4.2 Friction

Friction is defined as the resistance to relative motion between two bodies in contact. When two objects are in contact there are forces between them. At the molecular level it can be due to electrostatic forces, Van der Waals and metallic bonds. In general the coefficient of friction (COF) between two materials is defined as the ratio between the normal force and the friction force. However, the COF is dependent on a number of factors including but not limited to the surface roughness, any lubricant between the surfaces, contact stresses, surface chemistry and sliding speed. Because of this dependence on the system variables, the friction coefficient is not considered as a material property, but a "system" property.

Specifically for scratch experiments, according to Beake et al [92] the friction force can be deconvoluted into its interfacial and ploughing components, so, the total friction coefficient can be expressed as described by Equation 2.19:

$$\mu_{total} = \mu_{interfacial} + \mu_{ploughing} \qquad \textit{Equation 2.19}$$

2.4.3 Wear and wear mechanisms

Wear is recognised as the most important limitation to long term stability of hip devices. Wear occurs when two surfaces in contact are subjected to a relative motion and material is released. The presence of a lubricant film in the contact region can mitigate surface damage. Wear depends mainly on three factors: the load applied, the relative motion between the surfaces and the lubricant regime between them [93]. The wear of hip replacement components can be split into two periods: a high wear "running-in" period that occurs during the first million cycles, up to t_1/N_{c1} in Figure 2.10, followed by a "steady state" phase when the wear rate remains constant and much lower compared to the initial phase, which would correspond to the slope at t_2/N_{c2} in Figure 2.10,[93]. Where t_n and N_{cn} correspond to the implantation time and the number of test cycles at different n durations. Wear can be measured in terms of penetration depth (P), for clinical studies, or volumetric wear (V), when the value is related with hip simulator and laboratory studies. In Figure 2.10 P_1 or V_1 represents the penetration depth and the volumetric wear after the initial running-in period and P_2/V_2 the depth and wear at a time where the steady state wear rate has been reached.

One of the reasons for that difference in the wear behaviour is due to the polishing of the bearings surfaces and the increase in the conformity between them. Although the running in period is a small percentage of the implant's life the wear loss generated can be significant [94].

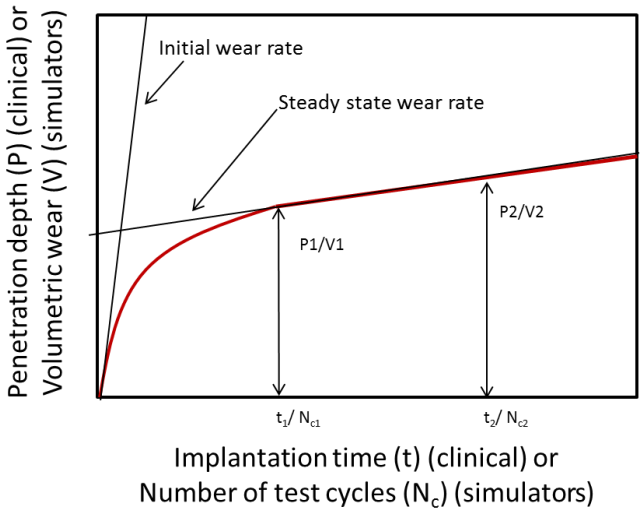

Figure 2.10 Volumetric wear (or penetration) versus time differentiating between running in period and steady state lubrication regimes of hip joints

There are four major wear mechanisms:

- Abrasive wear occurs when a hard rough surface slides across a softer surface and the softer material is abraded by the microscopic asperities on the harder surface. There are two modes of abrasive wear: two-body and three-body abrasive wear. Two-body wear occurs when the hard particles remove material from the opposite surface. Three-body wear occurs when the particles are not constrained and they are free to roll and slide between the surfaces. The three commonly identified mechanisms of abrasive wear are ploughing, cutting and fragmentation. Ploughing happens when material is displaced to the side, resulting in the formation of grooves that do not involve direct material removal. Cutting occurs when the material is removed from the surface in the form of primary debris with little or no material moved to the sides of the grooves. Fragmentation can also occur when the material removed from the surface together with the asperities produced the localized fracture of the material. The cracks can propagate in or around the wear groove, resulting in additional removal of material.
- Adhesive wear happens when two solid surfaces slide one against the other while a load is applied. Surface asperities of the softer material are plastically deformed leading to a material transfer and the increase of the friction between the pair.
- Fatigue wear affects hip implant materials when the contact between asperities produces very high local stresses when a cyclic load is applied. The repeated plastic deformation can cause the initiation of cracks under the surface, their growth towards the surface and finally the spalling of the material. Usually the particles produced roll within the contact creating additional damage.
- Corrosive wear, is a material degradation process due to the combined effect of corrosion and wear, especially when the oxide layer is removed and exposes fresh material to corrosion creating new oxide on the surface which is then rubbed off again. Corrosion products are easier to remove than the original material, therefore the wear rate is accelerated.

Wear found in hip implants is a mixture of the above mechanisms and varies depending on the materials used (microstructure, mechanical properties, final roughness, etc.), contact stresses, clearance between the surfaces, implantation time and patients activity level.

2.5 Tribocorrosion in medical implants

Tribocorrosion is a material degradation process due to the combined effect of corrosion and wear. As stated previously, tribology is concerned with the study of friction, lubrication and wear, while corrosion is concerned with the chemical and electrochemical interactions between a material and its environment. Corrosion may accelerate wear and wear may accelerate corrosion [95, 96].

Bio-tribocorrosion is a specific branch of tribocorrosion. It covers the science of surface transformations resulting from mechanical loading and electrochemical reactions that occur between the elements of a tribological system exposed to biological environments [97]. Bio-tribocorrosion in orthopaedics has been recognized as one of the major precursors to failure for total joint replacements [98]. Biological fluids are extremely corrosive for metals, the pH is around 7.4 in normal physiological conditions, but they can reach values close to 4.0 in the case of severe infections, in addition the medium is formed of an oxygenated saline solution containing a range of ions including Na^{+},Mg^{2+}, Cl^{-}, $SO_4^{2-}$and HCO_3^{2-}, and organic species such as proteins [99, 100]. The main consequences are the loss of material and the migration of dissolved metallic ions which can trigger adverse tissue reactions, pain and the need to revise the implant [101].

Another form of corrosion affecting hip implants at the macro-scale is galvanic corrosion due to the pairing of dissimilar metals such as Cobalt alloys, Ti alloys or stainless steels. Mansfeld [102] already reported in 1973 that the magnitude of galvanic corrosion depends not only on the potential differences of mixed metals but also on kinetic parameters such as corrosion rates or current densities. In addition, Papageorgiou and Mischler [103] also showed the importance of galvanic coupling happening at the micro-scale between active and passive regions under sliding conditions, i.e. potential difference inside and outside the wear track. The potential difference they observed between the two areas caused an electron flow, resulting in a corrosion rate increase in the area working as anode (depassivated area) and the protection of the areas acting as cathode (unworn area around the wear scar).

2.5.1 Deformation behaviour in CoCrMo alloy and tribolayer formation

Recent in vitro [104] and retrieval studies [105] found that there are several wear mechanisms affecting MoM implants. Tribochemical reactions (TCR) on the surface occur when the surfaces of two contacting metal bearings react with the interfacial medium (e.g. synovial fluid), resulting in the formation of a metallo-

organic composite tribolayer with a nanocrystalline microstructure between 50 to 200 nm thickness [106, 107], see matt areas on Figure 2.11. The mechanism that has been proposed to form the tribolayer is known as "mechanical mixing" [108-110] and it transforms the bearing surface from pure metallic to an organic composite material. The tribolayer formed during articulation consists of a mixture of nanometer small metallic grains and organic substances such as proteins from the environment which can act as lubricant affecting friction and wear. The mechanism suggests that areas with oxide layer and/or adsorbed proteins can act as the origin to incorporate new material. The presence of the tribofilm has been suggested to act as a solid lubricant, helping to stabilize the mild wear regime of MoM bearings in the absence of a fluid film preventing adhesion and abrasion and therefore, decreasing wear [111]. It has also been found to beneficially affect the corrosion behaviour as suggested by Wimmer et al [106]acting as a barrier for further corrosion.

The plastic deformation of CoCrMo alloys and their final microstructure depends mainly on the magnitude of the strain applied. Studies that compare retrieved implants and samples from laboratory studies,[105], have found deformation changes in a gradient from the surface towards the inner area of the sample as seen in Figure 2.12. The first layer corresponds to the TCR layer described previously, followed by a nanocrystalline layer [112, 113] mainly formed of primarily hcp ε-martensite, with grain sizes around 25-50 nm. The third layer consists of a mixed zone of ultrafine-crystalline fcc grains and orientated hcp ε-martensite needles, yellow lines, [112, 113]. The final zone corresponds to the bulk material consisting of fcc grains. This transformation from fcc to hcp crystal structures follows the mechanisms explained in the previous Section 2.3.3. Together with the SIT, grain refinement by recrystallization also occurs [114].

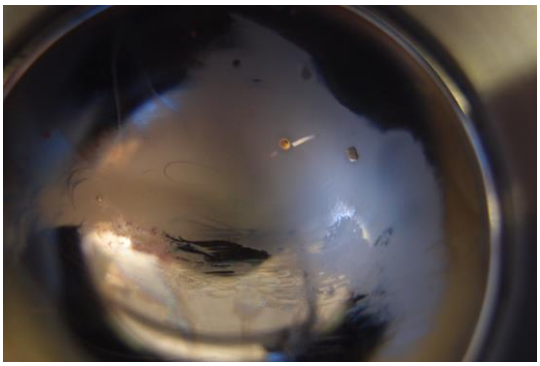

Figure 2.11 Tribolayer observed in a CoCrMo resurfacing hip after 330000cycles in a hip simulator study

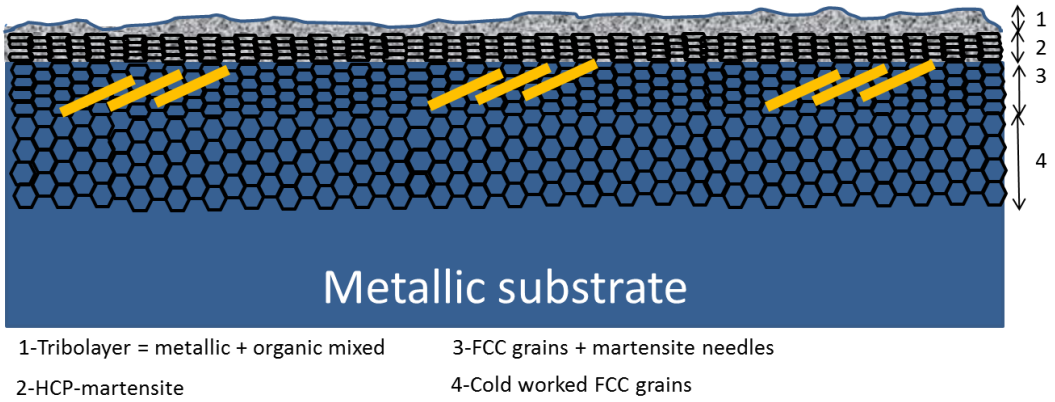

Figure 2.12 Schematic of the different layers presented in a deformed area in a metal implant under loading

The origin of the nanometer size debris found,[115], have been related with the layered microstructure described previously. When a strain is applied, cracks are originated on the subsurface within the nanocrystalline layer and propagate towards the surface generating nm debris filaments which break off and are broken up in the contact before being released as the nm particles.

The role played by the alloys microstructure, thermal treatments and the carbides-carbon content in the wear resistance has been also extensively studied in retrieval and in vitro studies. In general the As Cast-high carbon content alloys provide the better wear resistance, [18, 116, 117] when compared to low carbon as cast alloys [118] or forged alloys [119]. However, Wang et al. [120], did not find evidence of this improvement when comparing high and low carbon as cast alloys. The study by Hiromoto et al [56] where several forged alloys with different carbon contents, fcc and hcp percentages and grains sizes demonstrated a better wear resistance for the alloys with higher carbon contents.

There is a great deal of debate about the effect of carbides and their capacity to act as third body abrasive wear particles. Depending on the thermal treatment applied during the manufacturing process, the carbides within the matrix can be either bulky and well-fixed in the matrix or if partially dissolved they can be small, fragmented and poorly fixed in the matrix [64, 65, 121]. When loading conditions exceed the yield stress, fragmented-like carbides might crack causing the origin of hard particles which get trapped between the surfaces accelerating the wear of the alloys by 3rd body abrasion processes, as reported in [122-124]. Bulky carbides have a proper adhesion to the matrix but they protrude from the surface acting as hard asperities but they are less likely to come out of the matrix than the fragmented carbides.

2.5.2 Tribocorrosion damage observed in cemented femoral stems

Cemented femoral stems are fixed to the femoral bone using acrylic cements obtained from the polymerization of polymethylmethacrylate powders (PMMA).They incorporate radiopacifier agents such as barium sulphate ($BaSO_4$) or zirconium dioxide (ZrO_2) used as contrast media for radiographic assessment of the implants after the surgery. The differences between the mechanical properties of the cement and the metallic femoral stem under loading, results in micromotions between the two surfaces. $BaSO_4$ and ZrO_2 particles typically have a mean diameter between 5 and 10 μm in size, [125, 126], although bigger size agglomerates in the scale of 100 μm have been found due to mixing inhomogeneities [127].

$BaSO_4$ hardness is lower compared to ZrO_2 particles, however their influence on the wear-deformation mechanisms and bone resorption are still unclear [128-130]. Their influence on the corrosion effects was evaluated by Bryant et al [131], indicating a higher tendency to corrode than cements with ZrO_2 radiopacifier due to the disassociation of the Ba and SO_4 influencing the chemistry of the crevice solution. In contrast, ZrO_2 particles and aggregates show a hardness value around 1290 HV meaning they can act as single hard asperity particles increasing the maximum contact pressure applied at the interface creating ridges on the metal surface leading to the accelerated production of metallic particles and the depassivation of the surface as shown in Figure 2.13.

The cyclic loading of the implant produces micro-motion at the cement-stem interface, which causes the abrasive damage of the passive oxide layers. As a result, both wear and corrosion products such as metallic debris and metallic ions, black dots in Figure 2.14 are generated between the cement mantle and the metallic surface. The oxide layer stability, its adhesion to the metallic substrate and their repassivation rates will affect the evolution of the variables in the tribosystem [131, 132].

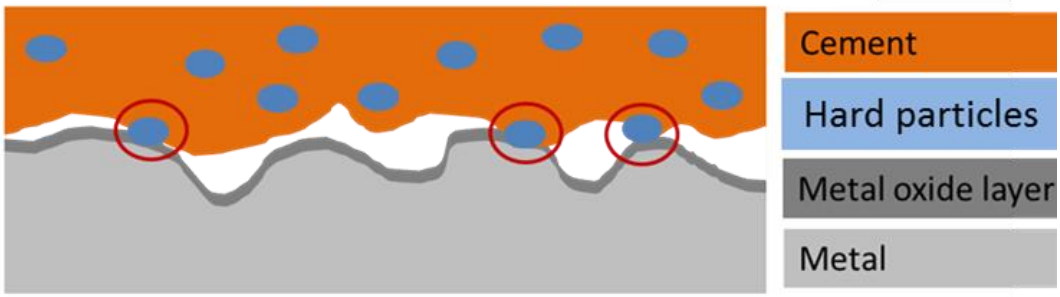

Figure 2.13 Schematics of the materials involved at the femoral stem-cement interface

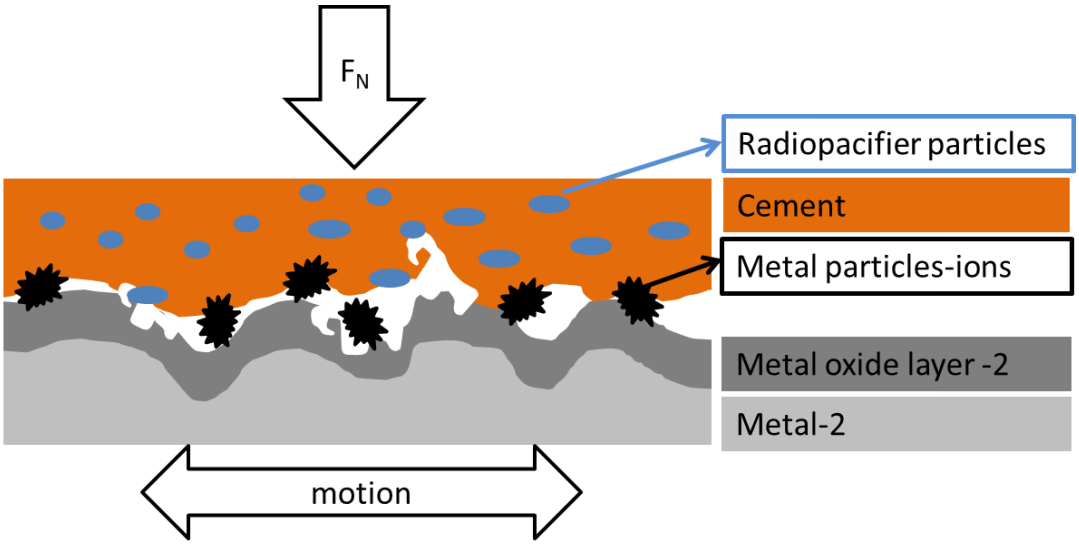

Figure 2.14 Schematics of the tribo-system when cyclic loading and motion are involved

In vivo surface tribocorrosion damage mechanisms of cemented femoral components have been reported previously by several authors [13, 133, 134] showing that the most affected zones are mainly localised in the posterior and medial regions in the femoral stem. Howel et al. [135] discussed the relationship between the stem surface finish and the wear morphology observed. Non damaged surfaces roughness between 0.016 to 0.0386 μm exhibited evidence of fretting wear processes while abrasive wear was observed when roughness values were between 0.389 and 2.59 μm. While Brown [136] and Zhang [137] discussed the incidence of the pores as initiation and propagation sites of fretting and wear into the femoral stem by in vitro experimental techniques, Blunt et al used finite element modelling (FEM) to estimate the minimum relative micromotions between the femoral stem and the cement interface to produce fretting wear [138]. The damaged observed was enough to consider this interface

as another source of metal particles and ions in addition to the debris generated from the articular surfaces which can lead to the implant loosening [26].

The main variables influencing the wear-corrosion processes in the cement-femoral stem interface are:

- Surface roughness: matte or polished [13]
- Cement porosity and shrinkage bumps after the mixing process [139]
- Mechanical properties of the counterpart materials: CoCrMo, Ti based alloys or cement (PMMA) [17]
- Type of radiopacifier particles embedded in the cement ($BaSO_4$or ZrO_2)
- Mechanical forces applied, motion conditions and lubrication regimes [140, 141]
- Solution chemistry: pH, protein-phosphate content, ion concentration

Higher roughness or higher density of pores act as initiation points where wear-corrosion mechanisms start, while hard radiopacifier particles result in two-body or third-body abrasive wear process, [43], due to the interaction of individual hard particles (single asperity contacts) with the metallic surface.

When a scratch is produced, the oxide layer depassivates and metallic ions are liberated initiating the wear-corrosion process [131]. In addition to the damage produced by cement single asperities, it was also found the generation of an oxide layer with similar characteristics to the one found in the articular surfaces [43, 133]. Bryant et al, [43], observed that abrasion damage in polished femoral stems was due to the formation and transfer of a Cr_2O_3 oxide film which act as a third body abrasive wear particulate when motion occurs between the two contacting surfaces. The mechanism proposed was that a thick oxide film forms as a result of fretting-corrosion, liberating Co^{2+}, Cr^{3+} and Mo^{2+} along with fractured oxide and metallic particulate into the interface. Cyclic loading results in the compression of any metallic oxide and debris on the counterpart cement and "blackening" of the cement was observed. A similar abrasion mechanism was also found in retrieved implants by several authors [105, 142, 143]. The formation of this oxide layer and its degradation process can influence the type and quantities of metal ions released from the interfaces to the body [144]. A detailed characterisation of the thickness, surface topography and chemistry of fretting corrosion product found on retrieved polished femoral stems was presented by Bryant [133] who demonstrates that the formation and chemistry of films are heavily influenced by the type of wear or degradation mechanism which at the same time are dependent on the levels of loading, displacement and shear stress experienced by the metallic surface. It was also found that films are

rich in Cr, O and C whilst Co is free to migrate away into the solution. This supports the findings by Hart et al. [144] who hypothesised that Co may be the clinical relevant active species responsible of the MoM failure by demonstrating that retrieved tissues were Co rich because Co migrates into the solution while Cr is favoured to undergo the oxidation reaction forming the Cr_2O_3 corrosion product.

Galvanic coupling between CoCrMo and Ti6Al4V alloys also has been found to influence the corrosion rates under static and dynamic conditions at the femoral stem-cement interface, [43] due to the large potential differences developed across the system between active and passive areas, increasing the rates of corrosion and metallic ion release.

2.5.3 Problems associated with hip replacements: metal ion release and interaction of particles within the human body

The main consequence of wear-corrosion is the production of oxide debris and the liberation of metallic ions into the biological environment. When they are released, the body reacts with an inflammatory response in the tissue around the implant [145]. The corrosion debris decreases the proliferation of osteoblasts (cells in charge of bone formation) causing the alteration of the bone formation cycle and in the long term its resorption (osteolysis) and the possible failure of the implant by aseptic loosening [146]. The size of metallic debris and its interaction within the body is a controversial point, as it could have an effect on cell growth as well as toxicity. The usual particle diameter of oxides is about 10-100μm [147], but some other studies have found nano-size particles distributed in the biological tissues [115]. Metallic particles have a high mobility and their toxicological effects are still under research. Haynes et al [148] found that Co and Cr nanoparticles are toxic to macrophages. Case et al [149] reported on small metallic wear debris particles infiltrating periprosthetic tissues causing cytotoxicity and necrosis in bone marrow or at the periprosthetic connective tissue.

In addition, the metal ions released, as Co^{2+}, Cr^{3+} and Cr^{6+} have been identified in the fluid around corroding implants [150]. The effects in the surrounding tissues depends on the specific ion, for example Cr^{3+} is not able to cross cell membranes, but Cr^{6+} can. As a consequence and together with its ability to be easily oxidized, the ion transforms into Cr^{5+} . Both ions, Cr^{3+} and Cr^{5+} have been linked to cell and DNA damage [151], metal sensitivity reactions and the generation of tumours [152, 153].

Metal ion release has been measured in multiple studies previously, in static corrosion conditions [45] and also after tribocorrosion experiments [150, 154, 155]. In general, Co ions are the most concentrated ones compared to Cr or Mo. However, the solution used for the experiments influences the results, showing that Mo ions are released in the presence of albumin in the test solution when transpassive potentials are used [156]. Also applied potentials are a key variable in the metal ion release measurements where metal ions levels increased when potential is increased.

2.5.4 In-vitro tribocorrosion

2.5.4.1 Tribocorrosion techniques

According to the literature there have been several approaches used to evaluate the tribocorrosion processes that occur in metals used for hip implants. They can be classified depending on the scale they work.

Functionalized hip simulator studies, [50, 143, 157], are focused on assessing mass losses due to the combined effect of wear and corrosion on the articular surfaces of hip implants at the macro scale. They try to analyse which proportion of the damage is produced due to the mechanical processes, due to the corrosion processes and/ or due to the synergy processes between them. The results are useful to monitor metallic ion released in more realistic conditions (edge loading, micro-separation) and to evaluate different lubrication regimes or the tribofilm formation happening during operation conditions. Yan [158] measured the evolution of open circuit potential during a simulator test observing a decrease in the potential while rubbing was occurring which is usually considered as indicative of local depassivation causing galvanic coupling between passive metal areas and .areas where the passive film was removed by friction. However, due to the complexity of the geometry involved, the loading cycles and the motion applied, it is difficult to calculate with accuracy the area subjected to depassivation and in general only potential and currents shifts can be monitored, without obtaining current densities and therefore corrosion rates.

In addition to articular surfaces, tribocorrosion techniques are also used to analysed fretting corrosion processes at the taper-trunnion interface, [159] , or at the femoral stem-cement interface. Fretting contacts have been studied from the macro-scale point of view such as in the work by Briant et al [131] who reported a decreased of 500 mV on the potential vs Ag/AgCl electrode and an increase of 6 μA on the i_{corr} values demonstrating the depassivation of the metallic surface produced an increase in the rate of oxidation taking place on the metallic surface due to the combination of loading and motion at the interface.

Tribometers have a simpler geometry, simpler motion (reciprocating sliding or unidirectional circular motions) than hip simulators and they usually run under constant loading conditions [27, 33, 160-162]. Samples are easier and cheaper to manufacture and the experiments are less time consuming. They are usually coupled with electrochemical cells to monitor the corrosion response to friction. The most widely used technique is the potentiostatic one where the sample acts as working electrode and the current passing through it is monitored constantly [157, 163]. Their simplified geometry allows a more accurate calculation of the depassivated areas, therefore it is possible to analyse current density and corrosion rate values which give a more detailed understanding of the tribocorrosion processes. They allow the study of more variables such as environment (pH, temperature, protein or phosphate interaction) or a comparison between different alloy microstructures [163].

The majority of research has focused on the analysis of the combined effects of corrosion and wear of multiple wear-corrosion events happening at the same time [96]. The disadvantage of these experiments is the difficulty in separating the contributions attributed to the corrosion and the wear respectively. On the macro-meter range the sample surface area can be in the square millimetre to centimetre range, in this case the investigated area will be an average of the total microstructure. Thus, the complex local tribocorrosion processes cannot be completely understood.

At the micro-scale, multiple works have reported the synergy between the wear and corrosion processes such as Assi et al [164] or Sun et al. [52]. They are usually single asperity contact experiments including scratch [32, 49, 165] or indentation [166, 167] to simulate single hard particles abrading the metallic surface. The simplicity of these last two approaches made them suitable experiments to investigate the basic variables which influence the wear and corrosion mechanisms.

Therefore, micro and nano-tribological studies are needed to obtain a more fundamental understanding of the processes happening. At the nano-scale, atomic force microscopy (AFM), and scanning Kelvin probe force microscopy (EKFM) techniques, [168], were used for tribological studies of engineering surfaces at a scale ranging from atomic and molecular to the micro-meter levels. This study investigated how surface roughness, adhesion, material transfer and boundary lubrication affected the tribococorrosion properties of the materials such as the characterization of the protein adsorption and corrosion behaviour of alloys in different solutions.

Usually the quantification of the material loss (when is possible) can be obtained after the rubbing time by weight loss (before and after the experiment) or by surface topography by profilometry or interferometry. These last techniques can also be used to evaluate the plastic deformation when wear is not happening and the damage produced on the sample is just displacement of the material but not removal of the material.

2.5.4.2 Repassivation kinetics evaluation and modelling

Repassivation kinetics are usually characterized by monitoring the transient currents during the wear event and fitting them to a first degree exponential decay model using Equation 2.20 to calculate the time constant, τ_1, defined as the time taken for the current to return to the initial current values before wear occurred. The rest of the parameters are described as follows:

- I_{peak}: is the peak current equal to the I_{max}-I_∞
- τ_1 is the time constant for repassivation
- t_0: time to produce the scratch
- I_∞ is the baseline current at $t = \infty$

$$I(t) = I_{peak}\, exp\left(\frac{-(t - t_0)}{\tau_1}\right) + I_\infty \qquad \textit{Equation 2.20}$$

Repassivation rates for most oxide films are on the order of milliseconds to seconds, [32, 52], depending on the loads applied and the contact conditions. Time constants can reach the order of seconds in the case when experiments are run under more aggressive conditions (abrasive particles added into the lubricant [169]) or when tests are run at the macro-scale [33]. Additionally, when corrosion occurs, parameters such as the potential and current are altered, [170, 171]. The decrease of potential and increase of currents mainly depend on the area abraded, the crevice geometries created between the contact surfaces and the area which interact during the reduction reactions. If the potential value is reduced to the active-passive transition region for the oxide, it becomes thinner and less stable, accelerating the corrosion attack [172, 173] and the generation of corrosion products.

Goldberg et al. [32] measured the current transients from depassivation and repassivation processes under fast-scratch conditions for Co and Ti based alloys. The study concluded that under abrasion conditions, CoCrMo has a stronger surface oxide with higher interfacial adhesion strength that makes it more resistant to fracture than Ti6Al4V. In addition Ti alloys take longer to repassivate resulting in more electrons released. Investigation on the repassivation kinetics of

CoCrMo alloys demonstrated that currents decrease when multiple scratches or indentations are made, [30, 32], suggesting that the reformed oxide layer can have different properties to the original oxide film. Gilbert reported extensively on the dynamics of oxide films on metallic biomaterials [174] using an electrochemical atomic force microscope. He found a direct correlation between surface dynamic changes and the electrochemical impedance behaviour, confirming the biological interaction from the proteins within the solution result in active remodelling and growth of the surface oxides.

A critical variable in the repassivation kinetics calculations is to specify accurately the depassivated area in the materials to calculate the corrosion current densities to estimate the corrosion rate. It is necessary to define the true damaged area between the contact surfaces, or the area of the surfaces which are physically in contact. At the macroscopic level, Hertz's contact mechanics model considered that both surfaces are flat without imperfections and the contact area is equal to the nominal contact area, A_n, see Figure 2.15a. At the micro-scale the real roughness of the surfaces and their asperities are considered, considering a multi-asperity contact, see Figure 2.15b, where each asperity doesn't interfere with the ones around it, [175]. Finally, Gilbert et al. proposed a new theoretical model considering the interaction of several single asperities in the same area [33], defining an overlapping abrasion area between the closest asperities, see Figure 2.15c.

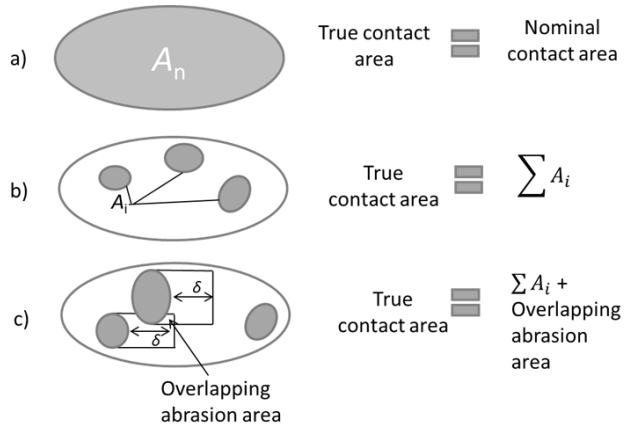

Figure 2.15 Different models used to define the true contact area in an asperity-asperity contact

In the case of single asperity testing, the characteristic deformed area is a groove similar to the one in Figure 2.16. Initially, the simplest and most used approach to calculate the deformed area under the tip was to assume it as a 2D surface,[32], see Figure 2.17a. A more accurate approach considers a 3D surface taking into account the inner lateral sides of the scratch groove and the outside lateral pile

up surfaces, see Figure 2.17b. However, is clear that the real area is still far from this method. A more accurate procedure would be the one presented in Figure 2.17c where in addition to the deformed area below the indenter, the new 3D facets created on the side of the scratch groove are also considered as areas subjected to repassivation and therefore influencing the repassivation time constant values.

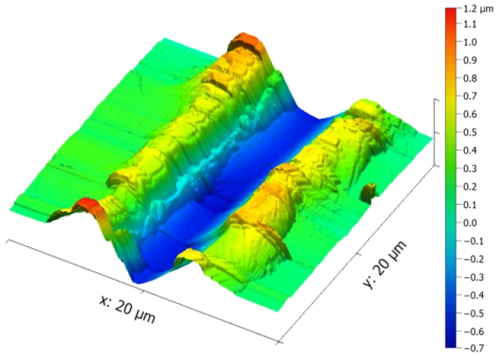

Figure 2.16 Example of the characteristic geometry in a scratch experiment

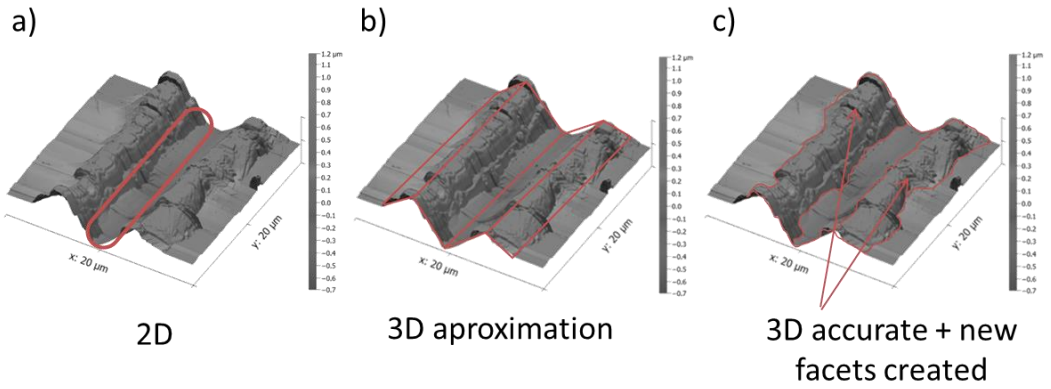

Figure 2.17 Different approaches to calculate the area subjected to depassivation: a) 2D, b) 3D approximation and c) 3D evaluation together with the new 3D feature produced due to the deformation

2.5.4.3 *Influence of testing environment*

Body fluids have access to the interface creating a crevice environment [162]. The body fluid is formed by an aqueous solution which contains proteins and some other chemical species that can corrode the metal surfaces. If the oxide layers are fractured, due to the abrasive process, the exposed surface repassivates consuming the oxygen present in the solution, making the pH decrease, which accelerates the fretting-corrosion processes as the cyclic loading continues.

Protein adsorption can also lead to the acceleration of the corrosion processes. The combination of low oxygen levels and the proteins can constrain the repassivation kinetics in the area and increase the electrochemical reactivity [38, 39]. Contu et al. and some other authors [27, 176] studied the effects of pH and proteins on the tribocorrosion behaviour of as cast CoCrMo under fretting-corrosion conditions. The results showed that both an increase in pH and the presence of proteins slow down the repassivation kinetics and the transient currents due to the protein interaction with the surface which results in thicker oxide layers which modify the charge and mass transfer.

2.5.4.4 Synergistic effect of wear and corrosion

There are three main approaches to calculate the contributions of wear into corrosion and of corrosion into wear [177]. The synergetic approach considers that the total volume loss (*T)* is equal to the volume loss due to mechanical damage (*W)* plus the volume loss due to the electrochemical corrosion (*C*) plus the synergistic effect, (*S*), which includes the increase of corrosion due to wear (*dWc)* and the increase of wear due to corrosion (*dCw*), as stated in Equation 2.21

$$T = W + C + S = W + C + (dWc + dCw) \qquad \textit{Equation 2.21}$$

The second approach is the mechanistic one proposed by Uhlig, [178], see Equation 2.20 where the total volume loss (V_{total}) is equal to the metal volume removed by mechanical wear, V_{mech}, and V_{chem} which corresponds to the equivalent metal volume removed by wear-accelerated corrosion.

$$V_{total} = V_{mech} + V_{chem} \qquad \textit{Equation 2.22}$$

This second approach is based on a very simplified phenomenological view of the processes. For example, the model does not considered that depending on the mechanical conditions the chemically active area is not just the rubbed area but also the areas surrounding the damaged region creating a galvanic cell and an increase in the corrosion processes [179, 180]. It also did not consider the build-up of third bodies which are formed by the accumulation between the contacting bodies of debris particles detached by wear from one or both contacting surfaces. The formation of third bodies can play a critical role in tribocorrosion as it was demonstrated by Mischler et al. [181]. However, this last approach although closer to reality, is still a descriptive model in need to be completed by a quantitative description of the different material flows occurring within the contact.

2.6 Summary

Micromotions at the interface between the metallic femoral stem and the cement mantle in cemented hip arthroplasties have been reported as been one of the sources of metallic particles and ions which can trigger adverse tissue reactions within the body causing the failure of the implant and its revision.

Extensive work has been done previously at the macro and micro-scale to assess the problem and understand the failure mechanisms produced by the wear-corrosion processes assuming a loss of material was involved. Models and equations have been developed to assess the individual contributions from wear and corrosion separately trying to answer the next question: does wear enhance corrosion or corrosion enhances wear?

This work will try to demonstrate for the first time that at the nanoscale corrosion is possible without wear of the surface but just with the deformation and displacement of the material. A new electrochemistry cell will be developed in combination with a commercial nanoindenter system to produce a controlled mechanical damage equivalent to the first "deformation-corrosion" event happening on the metallic surface of a femoral stem in contact with a hard particle embedded on the cement.

The obtained results will lead to a deformation-corrosion map providing a better understanding of the deformation-corrosion mechanisms happening at the femoral-cement mantle interface which will improve the Co-based alloys design process to minimise the risk to the patient.

.

3
Materials and experimental methods

3.1 Introduction

The aim of this study is to characterize the nanoscale scratch-corrosion behaviour of four CoCrMo alloys. The work investigates the relationship between the deformation and the repassivation mechanisms and their specific contributions to the general deformation-corrosion process. Figure 3.1shows a summary of the experimental work which was undertaken in this PhD.

This chapter will outline the materials and methods used in the preparation, microstructural, mechanical, chemical and crystallographic characterization of the 4 CoCrMo alloys investigated.

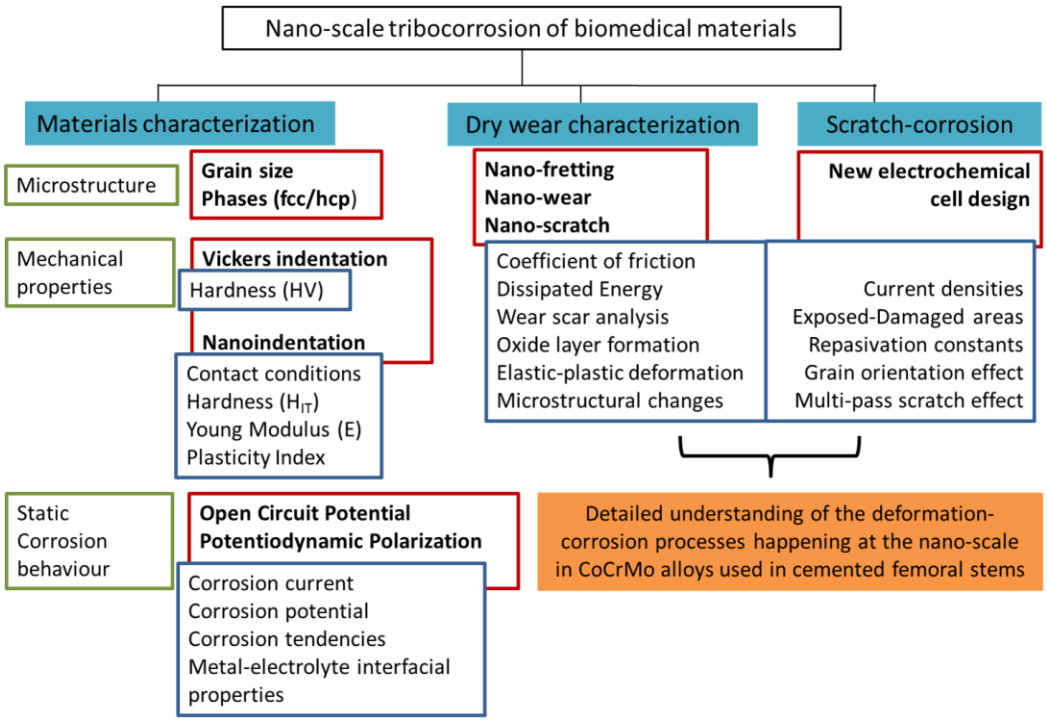

Figure 3.1 Experimental plan general overview

The second section, will present the static corrosion experimental methods, including OCP monitoring and PD polarization to calculate corrosion potential and the corrosion current to determine the different static corrosion behaviour of the alloys. This will be followed by an introduction to the Vantage system (Micro Materials Ltd., Wrexham, UK) and the nano-fretting, nano-wear and nano-scratch experiments the system can perform, outlining both the dry and liquid environments which were tested under and the experimental setup.

It is important to understand why the dry wear characterization section is formed by three different experiments: fretting, reciprocating sliding and scratching. As it is described in Figure 3.2, the initial aim of the work was to developed a new laboratory set up to understand the tribocorrosion processes on CoCrMo alloys at the nano-scale using a commercial nanoindenter system. The first approach was to use fretting experiments, but due to some limitations found, explained in detail in Section 5.6, reciprocating sliding experiments were performed, however, the presence of a piezo-electric component on the holder to provide the oscillatory motion added noise to the electrochemical sensors and the lack of space meant it was not possible to attached the electrochemistry cell to the system

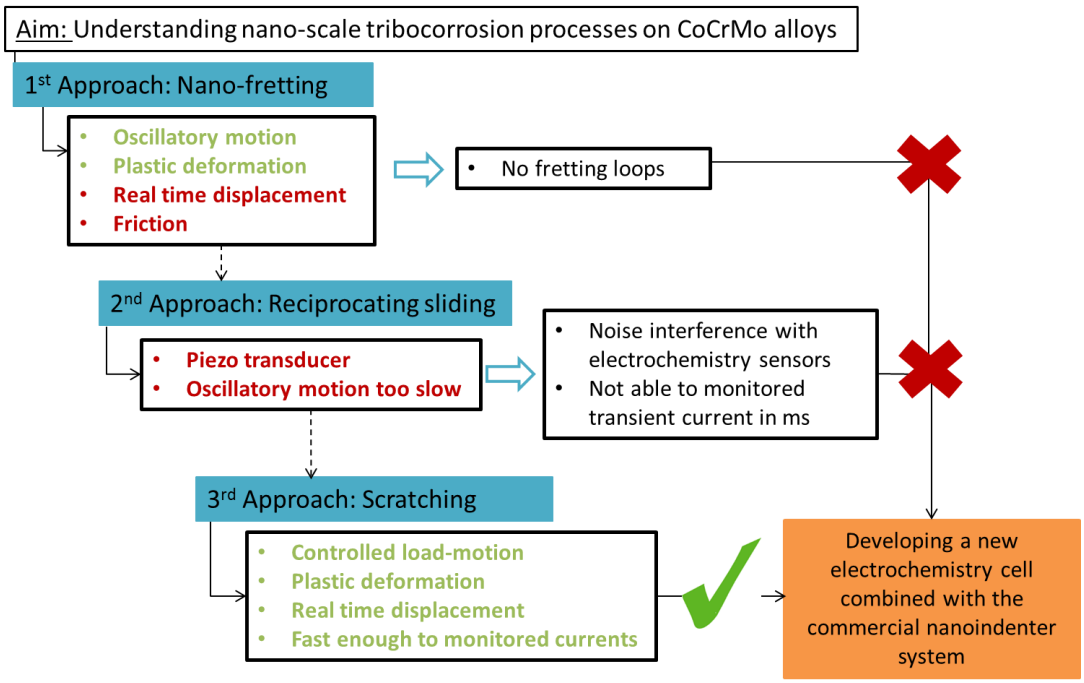

Figure 3.2 Decision tree for the different approaches taken to choose the most appropriate experiment to understand the nano-scale tribocorrosion processes

Finally scratch-corrosion experiments were chosen to be performed in combination with the electrochemical cell since it was the experiment meeting the requirements needed: monitored the electrochemical parameters and the plastic deformation at the same time the scratch was occurring on the surface fast enough to record the relevant changes.

The post-test surface analysis methods such as scanning electron microscopy (SEM), electron backscatter diffraction (EBSD), white light interferometry and atomic force microscopy (AFM) are also reviewed.

3.2 Specimen preparation

The study materials consisted of four different CoCrMo alloys characteristic of the range of alloys used in orthopaedics. The materials standard and the thermal and processing history of the alloys was unknown but was characterised though etching (3.2.2) and chemical analysis (3.2.3) to characterize their microstructure and chemical composition.

3.2.1 Sectioning and polishing

The hip implant components used for nanoindentation and dry nano-wear experiments were sectioned in samples of 3 mm thickness with a cubic boron nitride blade in a precision saw (Mecatome TZ10, Presi UK Ltd, UK). Samples used for static electrochemistry and scratch-corrosion experiments were cut into 3 mm thick and 8 mm diameter disks to fit the electrochemistry holder, by wire cutting at The Engineering Design and Manufacturing Centre (University of Southampton, UK).

A lapping machine (Kemet 15, Maidstone Kent, UK), was used to level and polish the samples to provide flat surfaces for the indentation, nano-fretting, nano-scratch, nano-scale wear experiments and nano-scratch corrosion experiments. A mirror finished surface was achieved by subsequent polishing steps using diamond liquids with particles from 25 μm to 1 μm size. Due to the limited number of samples obtained from the implants, the samples for the scratch-corrosion experiments were re-polished at least 2 times using only the 3 and 1 μm polishing steps. Therefore the final surface might result in a different finish from the first polishing process.

The roughness parameters of the samples after polishing are summarised in Table 3.1.

Table 3.1 Summary of roughness parameters for each sample

Roughness parameter	Forged	AC	AC-TT	AC-LC
Ra (nm)	12,06 ± 0,002	12,03 ± 0,001	12,07 ± 0,001	11,65 ± 0,001
Rq (nm)	14,84 ± 0,002	15,23 ± 0,001	15,13 ± 0,001	14,88 ± 0,001
Rp (nm)	27,75 ± 0,003	28,93 ± 0,001	28,84 ± 0,001	27,89 ± 0,002
Rv (nm)	27,69 ± 0,003	29,28 ± 0,002	29,82 ± 0,002	29,14 ± 0,002
Rz (nm)	55,44 ± 0,007	58,53 ± 0,004	58,65 ± 0,003	57,29 ± 0,003
Rt (nm)	106,85 ± 0,019	184,43 ± 0,089	205,58 ± 0,026	217,32 ± 0,085

The specimens were rinsed with distilled water and ultrasonically cleaned in distilled water and soap for 30 minutes, followed by ethanol rinsing and dried with compressed air.

3.2.2 Etching

To analyse the microstructural features the samples were chemically etched following the procedure outlined in the ASME Metallography and

microstructures of cobalt and chromium alloys standard [182]. The protocol dictates that as cast samples should be immersed for 5 minutes in a mixture of 15 mL of hydrochloric acid, 10 mL of nitric acid and 10 mL of acetic acid. The recommendation for the forged samples is a mixture of 20 ml of HCl combined with 4 ml of H_2O_2 3% volume concentration for 2 minutes. After the chemical etching the samples were rinsed with distilled water and dried with compressed air.

3.2.3 Chemical analysis

To determine the Co, Cr, Mo and C content of the alloys samples of each alloy were sent to the Sheffield Assay Office (Sheffield, UK). The Co, Cr and Mo content was obtained by inductively couple plasma optical emission spectroscopy (ICP-OES) while the carbon was determined using infrared absorption spectroscopy (IR) analysis after combustion in an induction furnace.

ICP-OES uses an inductively coupled plasma source to produce excited atoms and ions that emit electromagnetic radiation at wavelengths characteristic of a particular element. The intensity of the produced emission indicates the concentration of the main elements within the sample.

The IR absorption technique uses the infrared region of the electromagnetic spectrum. This technique exploits the fact that molecules absorb specific frequencies characteristic of their structure. After the sample is subjected to combustion in a furnace, the resultant gases from the sample under study and a reference sample are analysed. The reference sample is used to eliminate the instrument influence. A beam of infrared light pass through the sample and when the frequency of the IR is the same as the vibrational frequency of a bond, absorption occurs. Generally, stronger bonds and lighter atoms will vibrate at higher frequencies, known as well as wavenumber, cm^{-1}. From the transmitted light it is possible to know how much energy was absorbed at each frequency and an IR spectrum is obtained. An IR spectrum is a graph where the infrared light absorbance (or transmittance) is plotted in the Y axis vs the frequency or wavelength on the X axis. Analysing the position, shape and intensity of peaks in the spectrum gives details about the sample's molecular structure and allows identification of its chemical composition.

3.3 Materials

Forged and as cast alloys were used during this study. Details about the standard, heat treatments, nomenclature and elemental chemical composition including carbon content are summarised in Table 3.2.

The forged CoCrMo alloy used in the work was obtained from a CPT femoral component (Zimmer, Indiana, USA). A 0.044% carbon content was found in the chemical analysis and thus it is included in the low carbon CoCrMo alloys according to ASTM-F799. The alloy presents a meta-stable fcc single-phase microstructure with traces of hcp phase consisting of grains around 10 μm grain size, see Figure 3.3a.

Table 3.2 Summary of the alloys and the nomenclature used during the work

				Element composition (%)				
Alloy	**Standard**	**Heat treatment**	**Nomenclature**	**Co**	**Cr**	**Mo**	**C**	
Forged	ASTM F799	No	Forged	63.9	27.8	6.27	0.044	low
As Cast	ASTM F75-98	No	As cast	63.9	28.1	6.1	0.297	high
		Single	As cast-TT	63.7	28.2	6.14	0.595	out standard
	ISO 5832-4	No	As cast-LC	63.1	28.6	6.79	0.06	low

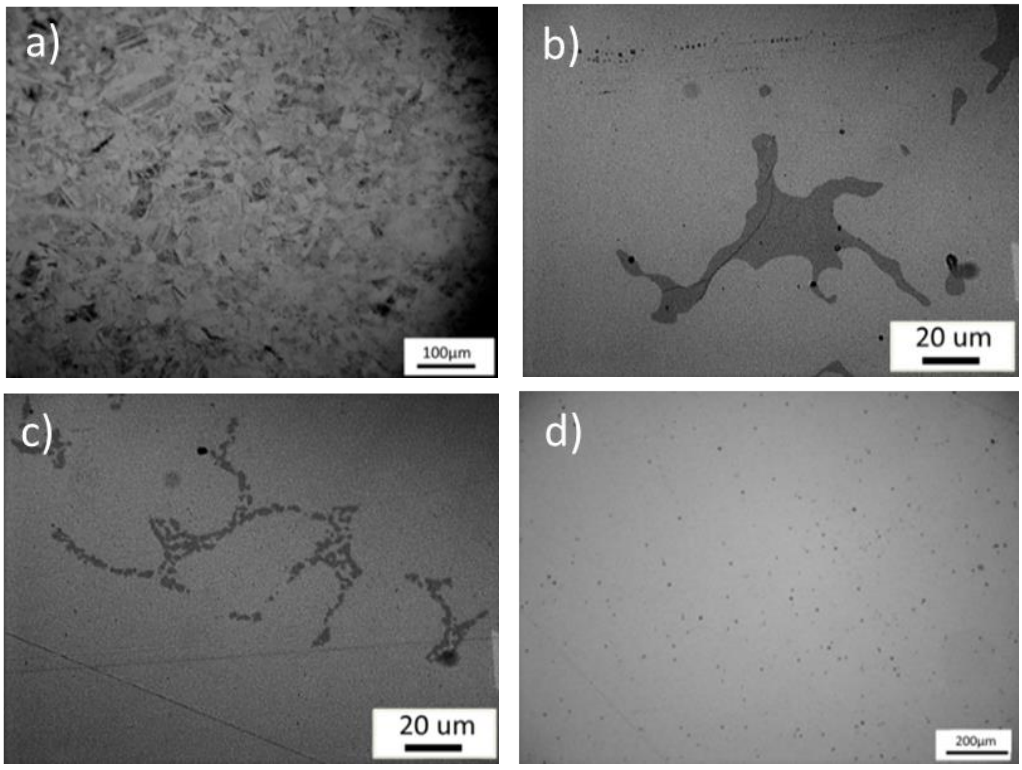

Figure 3.3 a) Forged ASTM F-799, b) As cast ASTM F-75, c) As cast ASTM F-75 single thermal treated, d) As cast ASTM F-75 low carbon content

The as cast CoCrMo alloys present a fcc CoCrMo solid solution matrix with large $M_{23}C_6$ interdendritic primary carbides. A variable content of hcp phase was also found and it will be discussed in Chapter 4.5 In the present work three different as cast alloys were used: as cast state, AC, (Figure 3.3b) from the central sprue of a casting tree, single heat treated (Figure 3.3c) obtained from a MITCH TRH acetabular cup, (Stryker, Switzerland), AC-TT and a low carbon content as cast alloy, AC-LC, (Figure 3.3d), from a Freeman stem, (Finsbury Orthopaedics, UK). In addition to the microstructural differences found, the carbon percentage also varies from 0.297 to 0.595 and 0.06 % for the as cast, as cast thermal treated and low carbon as cast samples respectively. More discussion about the differences between the microstructure of the thermal treated and non-thermal treated as cast alloys is presented in Section 4.2. The influence of carbon content in the mechanical and corrosion properties will be also discussed in Section 6.6.3.

3.4 Static electrochemical characterization

Static corrosion testing was performed to determine the corrosion behaviour of the 4 different alloys. OCP and PD polarization experiments were used. The combined results from the two techniques provide information about the role played by the microstructural features and the thermal treatments on the corrosion behaviour without the interference of external mechanical loading. The results from the static corrosion experiments were used as a baseline to compare with the nano-scale scratch-corrosion experiments. Differences between corrosion potentials and corrosion currents between the alloys gave an estimation of galvanic corrosion levels when they are coupled.

All the static electrochemical experiments were done in a 0.9% NaCl saline solution heated using a thermal bath at 37°C in a Faraday Cage to avoid the interference of external noise during the experiments. The static electrochemical experiments were done following the same two test procedures:

1) OCP monitoring for 3 hours to allow the potential to reach a steady-state
2) Potentiodynamic polarization

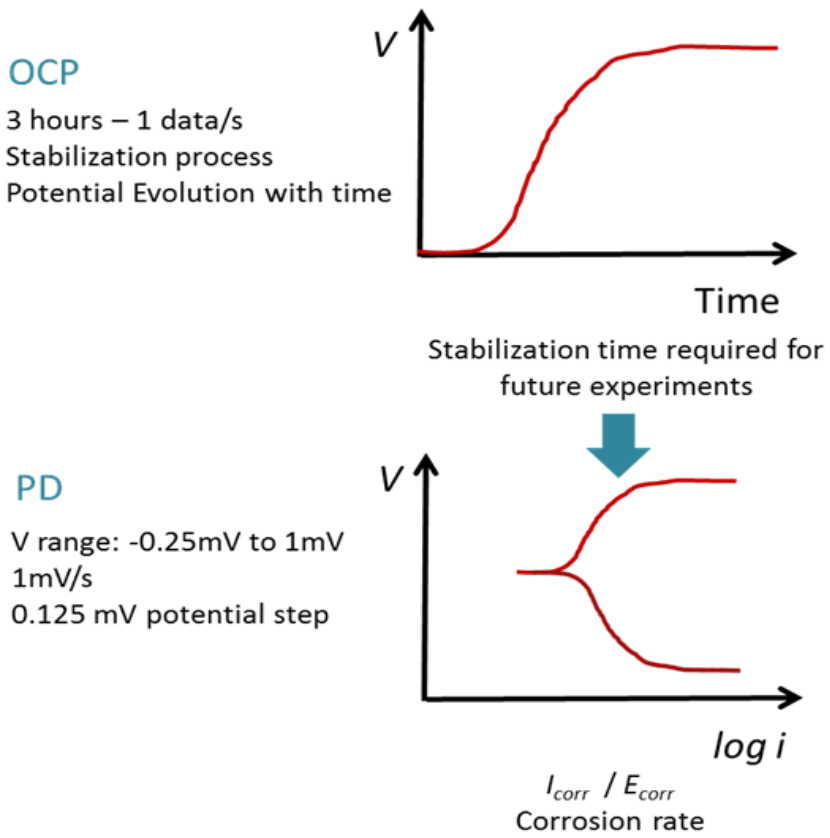

Figure 3.4 Sequential description of the static electrochemistry experiments.

A three electrode cell (Figure 3.5) was used to run the experiments sequentially, so neither the sample holder nor the electrodes changed position or were modified during the measurements. The cell consisted of a graphite counter electrode, an Ag/AgCl reference electrode and an inert PVC sample holder electrically connected between them where the CoCrMo sample is inserted. The exposed surface area was 0.2750 cm^2. All the elements were connected to the potentiostat which recorded the currents and potentials depending on the programmed experiment.

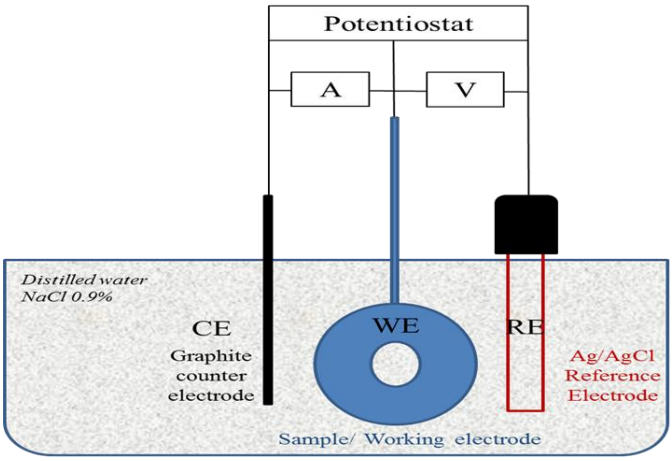

Figure 3.5 Static electrochemistry set-up

An Ivium potentiostat, CompacStast, (Ivium Technologies B.V., Eindohoven, The Netherlands), was used for all the electrochemical experiments. The CompactStat is controlled via its own software, IviumSoft, which was used to program the experimental parameters and record the potential and current results.

3.4.1 Open circuit potential measurements

To quantify the potential shift of the CoCrMo samples and to know the minimum stabilization time required to reach the steady state for the scratch-corrosion experiments, open circuit potential measurements were performed. Measurements were collected at 1 Hz for 3 hours based on previous works by Sun and Muñoz [51, 183].

3.4.2 Potentiodynamic polarization

A full potentiodynamic polarization curve, Figure 3.6, gives information about the four regions usually describe in electrochemical testing: the cathodic region, below the corrosion potential, E_{corr}, the active region, the passive region and the transpassive region. From the active region it is possible to obtain E_{corr} and the corrosion current, $i_{corr,}$ for each sample, which are related to the corrosion resistance of the material.

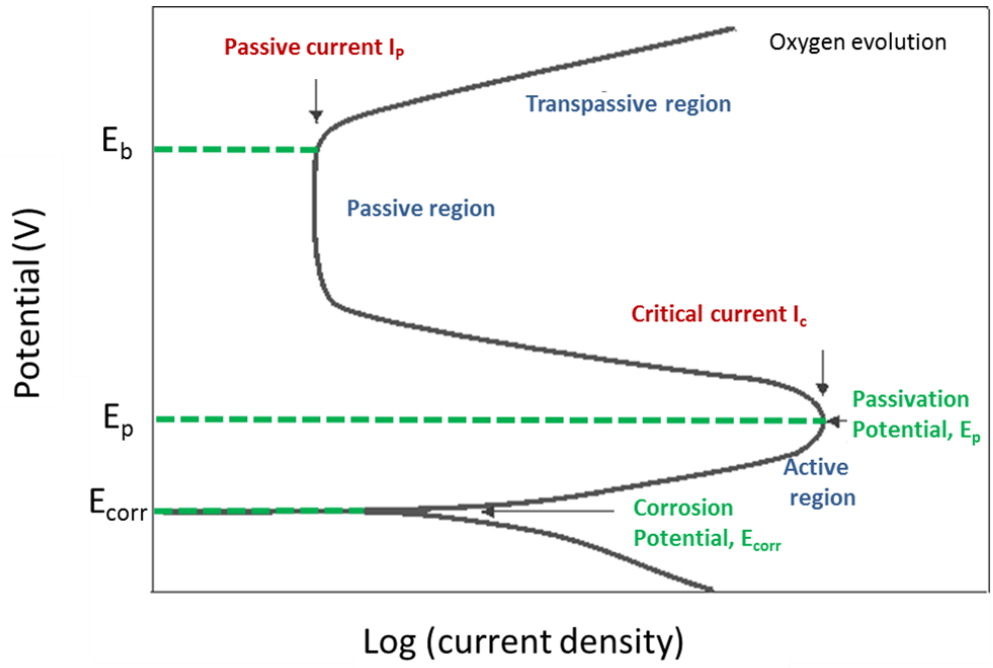

Figure 3.6 Example of a full potentiodynamic polarization curve for a generic material showing the three possible regions: active, passive and transpassive

The passive range starts after the cathodic-anodic transition and is limited by the breakdown potential, E_b, which is defined as the potential at which the current density in the passive range starts to increase abruptly.

An E_{corr} shift in the more noble, less negative, direction will mean a higher resistance to corrosion than another material with a more negative value. The different behaviour in the other areas of the curves (i_{corr}-E_{corr} shifts or breakdown current) are related with the microstructural features and the formation of a protective oxide layer due to the corrosion mechanisms happening on the surface of the samples.

Potentiodynamic polarization experiments are dependent on the applied potential [184] , thus the corrosion processes that occur on the samples could be affected, e.g. the kinetics in the oxide layer formation can be increased or decreased depending how the polarization takes place. To avoid the influences of changes in potential, the experiments were run under OCP potential conditions after the steady state was reached for all the samples.

Polarization curve starting at a more cathodic potential, -2V, from E_{corr} up to an anodic potential, +2V, were carried out to compare the corrosion kinetics behaviour between the samples. However, because this represents extreme

conditions, which wouldn't occur in-vivo, the potential range applied in the subsequent samples was set to take the linear regions from the cathodic and anodic curves (between -0.250 to 1 V with respect the OCP potential) for the CoCrMo alloys. The potential step was fixed at 0.125 mV and the scan rate was 1 mV/s to obtain scans with enough data resolution to enable analysis of the results.

Initially, the corrosion current and corrosion potential were planned to be calculated using Tafel equations, Equation 3.1 and Equation 3.2, where:

- $\eta_a - \eta_c$: anodic and cathodic overpotentials
- β_a -β_c: anodic and cathodic Tafel slopes
- i: applied current (A/cm^2)
- i_{corr}: is the exchange current density (A/cm^2)

$$\eta_a = \beta_a log \frac{i}{i_{corr}} \qquad \textit{Equation 3.1}$$

$$\eta_c = \beta_c log \frac{i}{i_{corr}} \qquad \textit{Equation 3.2}$$

Graphically, the corrosion current and potential are calculated from the intersection point between the linear parts of the anodic oxidation and the cathodic reduction branches of the Tafel plot as it is shown in Figure 3.7.

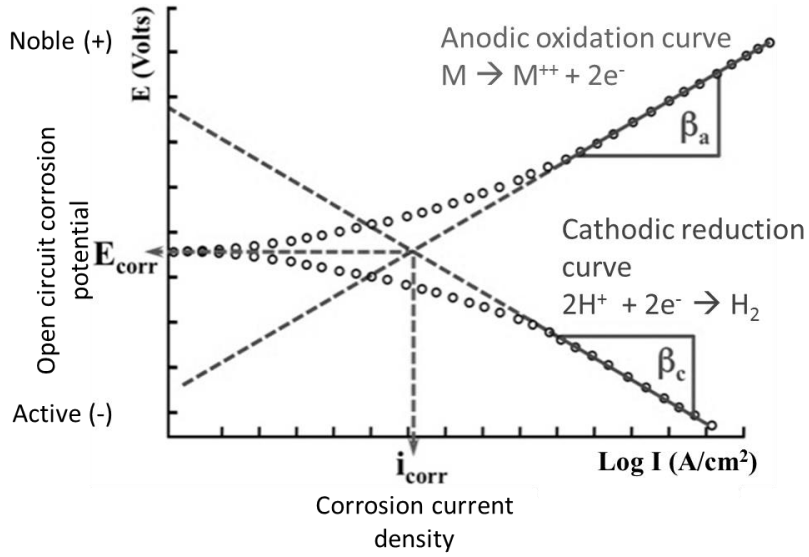

Figure 3.7 Diagram showing how to calculate graphically the i_{corr} *and* E_{corr} *from the Tafel plot*

Tafel extrapolation to determine corrosion rate is only valid for pure activation control or charge transfer control where the anodic and cathodic branches show a linear region. When the anodic and cathodic branches are not linear or symmetrical within +/- 100 mV from E_{corr}, Tafel equations are not valid. In that case the slope of the anodic region was extrapolated until it intersected with the E_{corr} value to obtain the passivation current, I_p. The passivation current is defined as the limiting value of a current that is reached as the rate of charge-transfer to an electrode is increased. It is independent of the applied potential over a specific range and it appears on the Tafel plot as a vertical line in the current axis as an indication of a mass-transfer controlled process. In mass-transfer controlled processes the polarization is controlled by the mass transport of reacting species to the electrode surface or reaction products away from the electrode surface. When the anodic branch did not show a Tafel behaviour, a good approximation to calculate i_{corr} is to use the intersection point between the cathodic Tafel slope and the E_{corr} horizontal line.

Combining the corrosion current obtained previously with Faraday's Law, Equation 3.3 , corrosion rate (mm/year) for each sample was calculated as follows:

$$CR = \frac{i}{A} \cdot \frac{EW}{F \cdot \rho} = i_{corr} \cdot \frac{M_w}{Z \cdot \rho \cdot F} \qquad \textit{Equation 3.3}$$

Where:

- i = current
- A= contact area (cm^2)
- EW= equivalent weight (g) = Molecular weight/number of mols
- F=Faraday's constant = 96487.7 C
- ρ = density (g/cm^3)
- i_{corr}= corrosion density (A/cm^2)
- M_w = molecular weight (g/mol)
- Z = number of electrons

The equivalent weight for each alloy was calculated following the ASTM G-102 Standard [185].

3.5 Indentation

Indentation is a simple technique that consists essentially of touching the material of interest whose mechanical properties such as elastic modulus and hardness are unknown with another material whose properties are known to obtain their hardness (*H*).

Historically, different macro-micro indentation hardness tests as Knoop (*HK*), Brinell (*HB*) or Vickers (*HV*) have been used. All of them are load controlled tests with the range of loads varying from mN to N. The different indenter shapes leave an impression on the surface and therefore a different value of hardness is obtained depending on the scale and the type of indenter used.

The basic principle is to observe the material's ability to resist plastic deformation from a standard source. *H* is determined dividing the load applied by the surface contact area when the indenter is in contact with the material.

Three different indentation experiments were used to characterise the alloys mechanical properties at different scales and to identify the elastic and plastic deformation transition.

3.5.1 Vickers indentation

The specific geometry for the Vickers indenter is shown in Figure 3.8. The indenter has a square base pyramidal diamond shape that makes a square impression on the surface when the load is applied. From the impression, the length of its diagonals are measured, d_1 and d_2 , and an average value, d, is calculated.

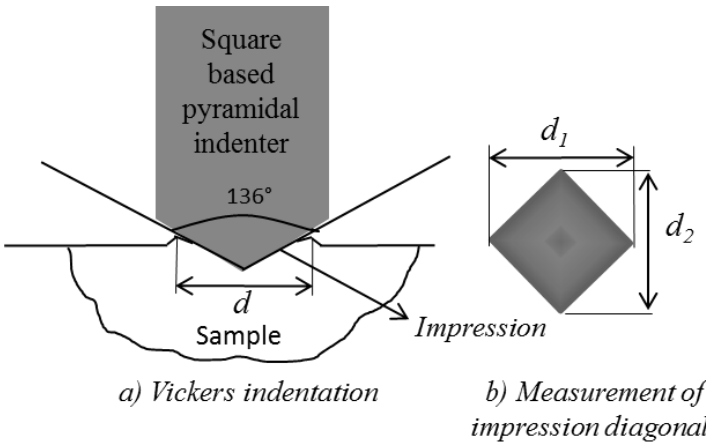

Figure 3.8 Vickers indenter geometry and measurement of impression diagonal on the sample

A Vickers hardness indenter (Matzsuzawa Seiki Co. Ltd, Japan) was used and weights of 0.1 and 1 kg, which corresponds to 1 N and 10 N loads respectively, were applied to compare the differences between hardness at the micro and the macro range. The applied load was held at its maximum value for 15 s. Ten indentations were done in each material considering a distance of 200 μm between each indentation to avoid interaction of the deformed area around each of the indentations following indications from EN-ISO 6507-1:2005 Standard [186]. The residual impressions were observed under the optical microscope, 10 x magnifications, and the diagonals were measured three times for each indentation to calculate the average Vickers hardness. The hardness for the Vickers test is obtained applying Equation 3.4 where, F is the normal load applied on the indenter and d is the average of the diagonals measured from the impression on the surface [186].

$$Hardness\ (HV) = 0.1891\frac{F}{d^2} \qquad \textit{Equation 3.4}$$

3.5.2 Nanoindentation

3.5.2.1 Elastic contact: Hertzian theory

For a contact between a rigid sphere and a non-rigid flat surface, Figure 3.9, Hertz found that the radius of the circle of contact a, is related to the indenter load L, the indenter radius R_i, and the elastic properties of the materials by Equation 3.5, where E_r is the reduced modulus of the indenter and the specimen given by Equation 3.6 where E and E' are the Young's modulus and ν and ν' are their Poisson's ratio of the indenter material and the sample respectively.

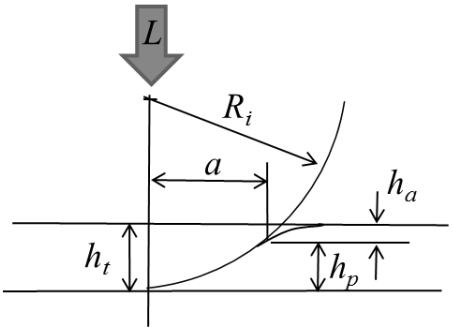

Figure 3.9 Spherical contact geometry under an applied load, L

Hertz's equation can be applied based on the following assumptions:

- The strains are small and within the elastic limit

- The size of the contact area is small compared to the size of the bodies in contact.
- Surfaces are continuous, non-conforming and frictionless

$$a^3 = \frac{3}{4}\frac{LR_i}{E_r} \qquad \text{Equation 3.5}$$

$$\frac{1}{E_r} = \frac{(1-v^2)}{E}\frac{(1-v'^2)}{E'} \qquad \text{Equation 3.6}$$

The mean contact pressure, P_m, is calculated by dividing the applied normal load, L, by the projected contact area, following Equation 3.7, where the contact pressure is related with the geometrical parameters of the contact and the materials properties. The maximum pressure, P_0, which occurs on the axis of symmetry is given by Equation 3.8. Under these loading conditions, the displacement between the two bodies, δ, follows a relation equal to the ratio between the contact radius and the radius of the sphere, see Equation 3.9.

$$P_m = \frac{L}{A} = \frac{L}{\pi a^2} = \left[\frac{4}{3}\frac{E^*}{\pi}\right]\frac{a}{R_i} \qquad \text{Equation 3.7}$$

$$P_o = \frac{3}{2}\cdot P_m \qquad \textit{Equation 3.8}$$

$$\delta = \frac{a^2}{R_i} = \frac{a\cdot\pi\cdot P_o}{2\cdot E_r} = \left[\frac{9\cdot L^2}{16\cdot R_i\cdot {E_r}^2}\right]^{1/3} \qquad \textit{Equation 3.9}$$

3.5.2.2 Nanoindentation testing

In nanoindentation experiments, the elastic modulus and hardness of the specimen are extracted from the load-displacement curve. In contrast to the micro and macro indentation, the size of the residual impression and the projected contact area are too small to be measured directly by optical techniques. Therefore, the contact area is calculated indirectly by measuring the depth of penetration, h_p, of the indenter into the specimen surface. This, together with the known geometry of the indenter, provides an indirect measurement of projected contact area at full load.

The hardness, H, is defined as the maximum load applied, P_t, divided by the projected contact area, A_c, see Equation 3.10. The projected area beneath the indenter is a function of the maximum plastic deformation during the loading of the indenter and its geometry.

$$H = \frac{P_t}{A_c}$$ *Equation 3.10*

The slope of the unloading curve at any point is known as contact stiffness, *S*. Sneddon and afterwards Oliver and Pharr, [187], presented the relationship expressed in Equation 3.11 to calculate it, where S is defined by the derivative of *P* respect to the displacement, *h*. This method uses the slope of the initial portion of the unloading curve to determine h_s and hence h_p, since $h_p = h_t - h_s$. Where h_t is the depth from the original specimen surface at maximum load, h_s is the distance from the edge of the contact to the specimen surface at full load and h_p is the plastic depth.

$$S = \frac{dP}{dh}$$ *Equation 3.11*

The most common indenters used for nanoindentation are spherical and Berkovich. The Berkovich indenter is a three-sided pyramid with the same depth-to-area relationship, see Figure 3.10.

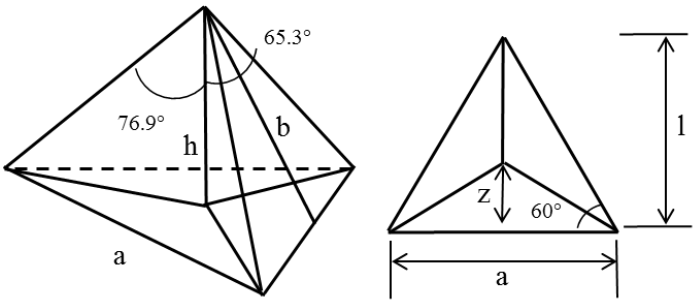

Figure 3.10 Schematics of a Berkovich indenter

For an ideal Berkovich indenter, the relationship between the projected area, A_c of the indentation and the depth h_p beneath the contact is described by Equation 3.12 according to Fischer-Cripps [188]:

$$A_c = 24.5h_p^2$$ *Equation 3.12*

However, during the experiments an approximation to the real projected area is used applying the following diamond area function (DAF) in Equation 3.13 where the generic equation is shown and an example of the numerical values used during the experiments:

$$A_c = Ah_p^2 + Bh_p = 28.05h_p^2 + 4345.71h_p$$ *Equation 3.13*

The first term, Ah_p^2, takes into account the deviation from the ideal area function of a Berkovick indenter, and the second, Bh_p, is the ideal form for a rounded indenter which captures the effect of finite rounding at the apex of every real indenter.

The reduced modulus, E_r (Equation 3.14), is calculated from the stiffness at the onset of the unloading, S, and the projected area of contact between the indenter and the material, A_c, where β is the correction factor for the shape of the indenter (1.034 for the Berkovich indenter geometry).

$$E_r = \frac{\sqrt{\pi}}{2\beta}\frac{S}{\sqrt{A_c}} \qquad \textit{Equation 3.14}$$

3.5.3 NanoTest Vantage System description

The NanoTest Vantage System (Micromaterials Ltd, UK), is a nano and a micro scale mechanical and tribological testing facility with the ability to perform indentation, fretting, reciprocating sliding wear, scratch and scratch-corrosion experiments.

The systems consists of two loading heads, a low load head (range: 0-500mN), a high load head (500mN-20N), a three axis sample positioning stage and a multiple objective microscope tower with 5x, 10x, 20x, 40x magnification lenses, which enables precision positioning (<1μm) of experiments on a sample surface. The components are all mounted on a granite frame, mounted on an anti-vibration table to minimise any external noise or vibration which may affect the experiments. This is housed within a cabinet which provides an enclosed environment, minimising the effects of temperature changes on the system.

The system is based around a pendulum, a detailed schematic sketch of the system is shown in Figure 3.11.The motion and load control of the indenter for both the low and high load heads is controlled through the interaction of the coil located at the top of the pendulum with the permanent magnet. The DC current applied in the coil is calibrated using indentation tests into a standard material so that the voltage applied to the magnet provides a known load.

The displacement of the indenter is measured by means of two parallel capacitor plates, situated directly behind the indenter holder in the middle of the pendulum. One plate is attached to the indenter holder and moves with it, while the second plate (target plate) is fixed. When the indenter is pressed into the test specimen, the spacing between the parallel plates change, hence the capacitance

changes and the indenter displacement can be measured. The maximum measurement depth is 20μm.

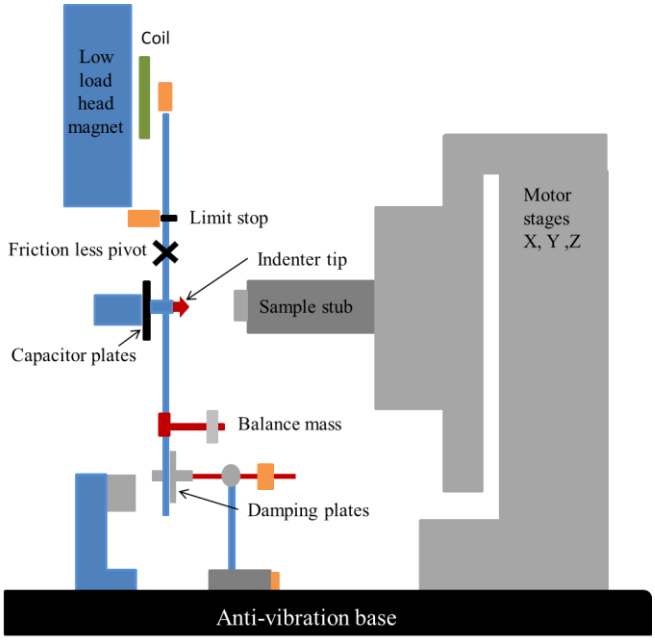

Figure 3.11 Sketch of the Nanovantage System

The limit stop, located above the pivot, is used to define the vertical position of the pendulum, and its position can be manually adjusted with a micrometre. The pendulum is in the vertical position when is touching the limit stop. At this point the coil cannot move any further towards the magnet, therefore the indenter cannot move any further towards the specimen. The pendulum is designed to be stiff enough to hold a maximum load of 500mN and can move around the pivot which is a friction free design formed by two steel plates clamped in a X pattern by four springs. This part of the system has a high compliance in rotation but is easily damaged in the other directions. The springs bend, if care is not taken when handling the pendulum or when the indenter makes the contact with the sample surface.

The pendulum should be balanced and the depth signal should be checked and adjusted before each experiment. Especially if the indenter tip has been changed or if another heavier object such as the friction probe is placed into the indenter holder. The change of the tip or weight will add an extra weight which will move the pendulum away from the limit stop modifying the results. The limit stop is defined as the value of the depth signal in Volts (V) and it should be a value between 8.5 and 9 V. It can be adjusted by a micrometre on the back of the instrument.

Cylindrical aluminium sample stubs are attached to the sample plate which will be attached to the main body which moves in the axis x, y and z. Samples are fixed to the aluminium stub with adhesive.

3.5.3.1 Indenters and tips used

Diamond spherical and Berkovich tips were used for the experiments. The spherical tips were available in two different radii: 5 and 200 μm which allow severe and mild deformation conditions on the samples. Depending on the force applied the mean and maximum theoretical contact conditions can range from 1.1 GPa to 33 GPa. Diamond tips were chosen because diamond has the closest mechanical properties to the hard ZrO_2 radiopacifier particles embedded in the cement at the interface between the bone and the metallic femoral stem.

3.5.3.2 Nanoindentation maps

Nanoindentation mapping tests were carried out in depth control applying a maximum depth of 500 nm in a matrix of 20 by 20 points using a diamond Berkovich tip. The loading and unloading rate was fixed at 2 mN/s and the dwell period at maximum load was set at 60 s. Thermal drift correction data was collected before and after the indentation test for 40 s. The hardness (H) and the Young´s modulus (E) were calculated from the depth-displacement curves. Hardness maps were obtained for each matrix and correlated with the different phases presented in the alloys.

Irregularities in the shape of the indenter, as described in Section 3.5.2.2, deflection of the loading frame, thermal drifts or initial contact loading are parameters can interfere in the accuracy of the results. To correct for these sources of errors, the depth measurement systems needs to be referenced to the specimen surface by bringing the indenter into contact with the surface with a small "initial contact force". Additional automatic corrections for thermal variations are performed by the software after the experiments.

3.5.4 Correlation of H_{IT} with other scales

The indentation hardness H_{IT} can be converted to its equivalent Vickers hardness value. The indentation hardness uses the projected area of contact, while the Vickers hardness uses the actual surface area of contact. Since for a Vickers indenter, the projected and actual surface areas of contact differ by about 7%, it is to be expected that the Vickers hardness value will be some 7% less than the equivalent indentation hardness H_{IT}. The conversion is obtained from the equations described below:

$$H_V = \frac{F}{Surface\ area\ of\ indentation}$$ *Equation 3.15*

$$H_{IT} = \frac{F}{Projected\ area\ of\ contact}$$ *Equation 3.16*

The projected contact area is calculated from knowledge of the geometry of the indenter stiffness of the contact, and from ISO 14577-1.2 [189], the ratio of surface area, A_s , to projected area, A_p, is a constant for a perfect Vickers or modified Berkovich indenter:

$$\frac{A_S}{A_P} = \frac{24.3}{24.5} = 1.08$$ *Equation 3.17*

The diagonal length measured in conventional Vickers tests is related to A_P by

$$d^2 = 2\ A_p$$ *Equation 3.18*

Taking into account changes of unit, this leads to Equation 3.19

$$HV = \frac{H_{\mathrm{IT}}\ \cdot\ A_p}{g\ \cdot\ A_s} = 0.0945 \cdot H_{IT}$$ *Equation 3.19*

Where HV is the Vickers hardness, H_{IT} is the indentation hardness, A_p is the projected area of the tip, A_S is the contact surface area and g is the acceleration due to gravity.

3.5.5 Summary of nanoindentation experimental conditions

Indentation experimental conditions are detailed and summarised in Table 3.3.

Table 3.3 Experimental conditions for indentation tests done on the CoCrMo alloys

	Vickers Indentation	**Berkovich Nano Indentation**
Load range (mN)	$1 \cdot 10^3$-$10 \cdot 10^3$	500
Tip	Square based pyramidal	Berkovich
Loading rates (mN/s)		2
Unloading rates (mN/s)		2
Dwell Period at max load (s)	15	60
Dwell Period for drift correction (s)		40
Experiment termination	Load controlled	Depth controlled to 500 nm
n/load	10	matrix 20x20
Total indents/sample	20	400

3.6 Nano-wear

Nano-scale wear and fretting corrosion is relevant to many industrial fields, such as nuclear power, food processing, marine engineering, and medicine. Focusing on the degradation of orthopaedic implants Waterhouse [190], Hoeppner and Chandrasekaran [191] already highlighted its significant impact on the lifetime of implants [192].

3.6.1 Definition of fretting

Fretting is defined as a mechanism where a low amplitude, oscillating, sliding movement appears between two surfaces under cyclic load between 1 and 10 Hz. The necessary magnitude of motion needed to create this phenomenon is generally defined between 1 and 100 μm [193]. Due to the magnitude of loading in the body, all modular junctions of prostheses are susceptible to fretting. This movement results in the formation of soluble debris that can migrate locally and

systematically and may result in bone loss by osteolysis and subsequent implant failure [33].

3.6.2 Fretting parameters and regimes

Fretting is associated with small displacement amplitudes between two contacting surfaces subjected to cyclic stresses. Depending on the contact loading (normal force, displacement amplitude, and sliding displacement), different sliding regimes have been defined [194]: partial slip (PSR), mixed slip (MSR) and gross slip (GSR), see Figure 3.12a.

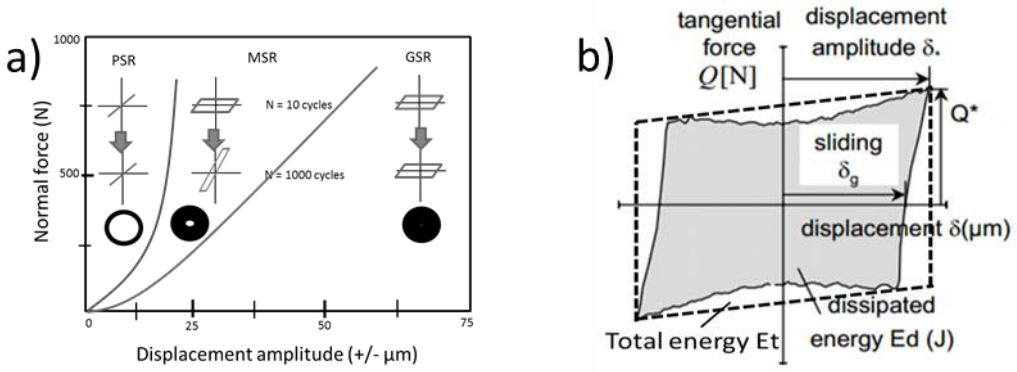

Figure 3.12 a) Diagram showing the the partial slip regime, mixed slip regime and gross slip regime [194] b) Fretting loop to calculate the total and dissipated energy from fretting experiments [195]

To analyse fretting experiments it is possible to plot a 2D graph, see Figure 3.12b. The plot, known as a fretting loop cycle, is the representation of Q (force) versus δ (distance), where δ is the displacement amplitude imposed on the system and Q is the maximal tangential force associated to this displacement amplitude. The shape of this plot gives information about the regime where the experiment is running and quantifies the dissipated energy used for the tribosystem:

A partial slip condition is associated to a closed and narrow fretting loop during the test, no hysteresis is shown, see Figure 3.12a, first region on the left. In this domain, the contact area is divided into a sticking zone in the centre of the contact and sliding zones at the edges. This regime usually is divided in two domains: a security domain without damage, and a domain where cracking appears [194].

In the gross slip regime, all the cycles of the test are quasi-rectangular (high hysteresis), see Figure 3.12a, region on the right. This regime appears for higher displacement amplitudes. The sticking zone does not exist and the whole contact is under full reciprocating sliding [194].

Finally, a mixed fretting regime is characterised by cycles that alternate between partial slip and gross slip conditions, see Figure 3.12a, central region. In that case there is a combination of linear cycles and high hysteresis cycles that leads to crack propagation and material wear.

The fretting loops also give information about the total and the dissipated energy used by the system. The dissipated energy, E_d, is the area enclosed inside the fretting loop and the total energy, E_t, is the total area given by the dash rectangle, see Figure 3.12b, where the width is defined by the maximum and minimum tangential forces and the length is given by the maximum and minimum displacements. The threshold between partial and gross slip, for a sphere-plane contact, determined by Fouvry et al [194] (Equation 3.20), determine when the tribosystem will work under fretting conditions.

$$A = \frac{E_d}{E_t} = 0.2 \qquad \textit{Equation 3.20}$$

For a sphere-plane contact, the contact area is a circle (Hertz's Theory). Contact under tangential forces has been described as a way of predicting stresses in bulk materials undergoing friction. To obtain the theoretical fretting condition, Figure 3.13a is analysed. Theoretically, to define the fretting condition, the ratio between the displacement, 2D, and the contact width, 2a, should be smaller than 1, in that situation the displacement is lower than the contact width, otherwise sliding happens. From the definition of fretting, a confined zone exists between both materials, this means that if the normal load is sufficient, the oxide layer is completely removed and is not reformed inside the contact zone, increasing the metals dissolution rate. On the contrary, in a sliding situation the contact conditions allow the metal to rebuild the layer and therefore the surface will be protected again, decreasing the rate of material loss.

a)

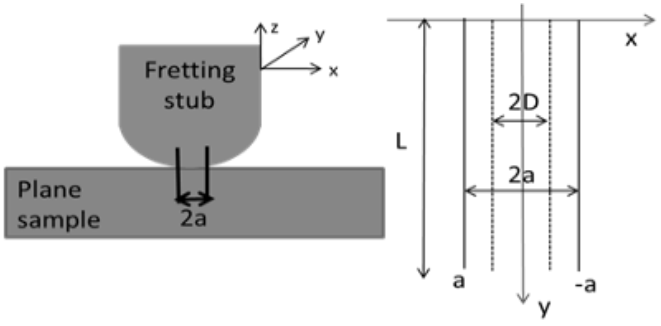

b)

$$e = \frac{D}{a} < 1$$

Figure 3.13 a) Diagram to show the contact conditions in fretting experiment. b) fretting condition equation

3.6.3 Oscillatory motion

To produce the fretting or reciprocating sliding motion, a special sample holder (Figure 3.14a) was attached to the stage. The motion of the holder is performed by a multi-layer piezo-stack which is magnified by means of a lever arrangement to achieve larger amplitudes [196]. The track length values are controlled by the piezo voltage produced by a signal generator, amplifier and transformer combination. Variation in the frequency and voltage between 0.5 to 10 Hz, and amplitudes (V), between 1.5-10 V, generates the micro-scale motion relative to the indenter Figure 3.14b. The multiple combinations allow track lengths from 2 to 25 μm.

a)

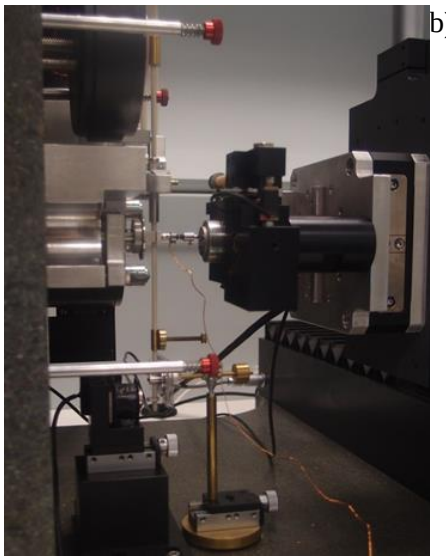

b)

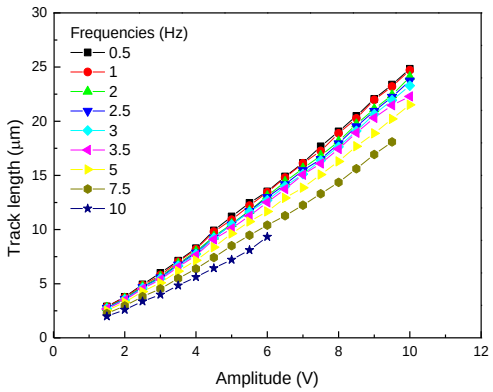

Figure 3.14 a) Oscillatory rig with sample in mounted conditions and b) Plot describing the combinations of frequencies, amplitudes to obtain the desired track length

The system is able to monitor the depth, applied load, friction force (if friction probe is connected) and time during the experiment. However, the position of the indenter relative to the sample is not monitored. As a result it is not possible to plot fretting hysteresis loops, so information about the fretting regime and the stick-slip condition cannot be obtained directly from the experiment. The applied load and sample motion can be applied constantly or intermittently. Thermal drifts are collected at the beginning and at the end of the experiment to correct for any thermal drift in the depth signal during the experiment.

3.6.4 Friction probe and friction measurements

A lateral force transducer can be incorporated between the indenter holder and the tip, enabling the friction coefficient to be determined during the experiment, see Figure 3.15a.

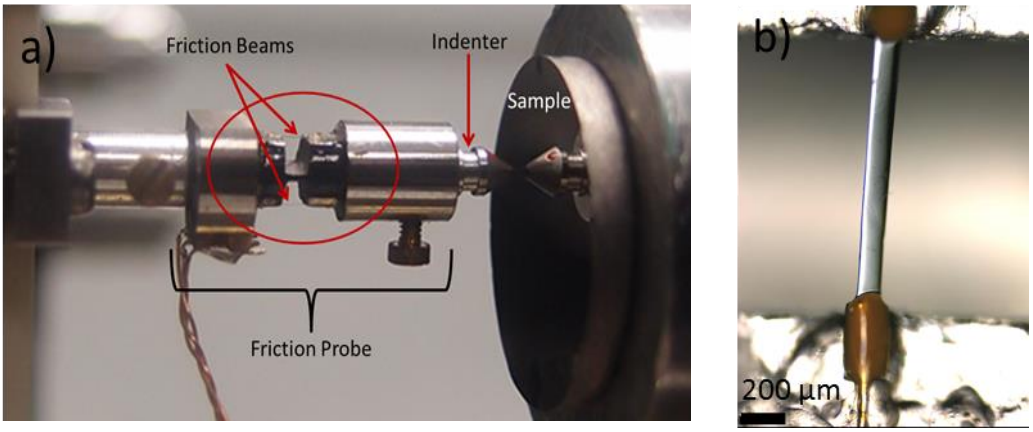

Figure 3.15 a) General friction probe description, b) Detail of one of the friction beams

The friction probe has two friction beams (strain gauges), inside the red circle Figure 3.15a-b, responsible of monitoring the lateral forces. Tangential friction force calibration was performed by a method of hanging masses before and after each of the experiments to ensure the correct functioning of the friction probe.

COF, was calculated using Equation 3.21, where μ is the COF, F_f corresponds to the lateral frictional force measured by the system and N is the normal load applied.

$$\mu = \frac{F_f}{N} \qquad \textit{Equation 3.21}$$

3.6.5 Intermittent nano-fretting experiments

Preliminary nano-fretting experiments were performed using a 200 μm radius spherical diamond tip. The fretting track length was set at 5 μm at an oscillation frequency of 5 Hz. In total, 35 nanofretting experiments were performed on each sample over a range of applied loads from 2.5 to 50 mN. Five repetitions per load were done in each sample. The applied loads correspond to a maximum theoretical contact pressure between 300 and 1400 MPa. For each nano-fretting experiment the load was linearly increased to the maximum test load over 10 s and it was kept constant for 400 s, followed by an unloading phase of 2 s. Fretting motion was applied intermittently, 200s on-60 s off, when the load reached the maximum constant value.

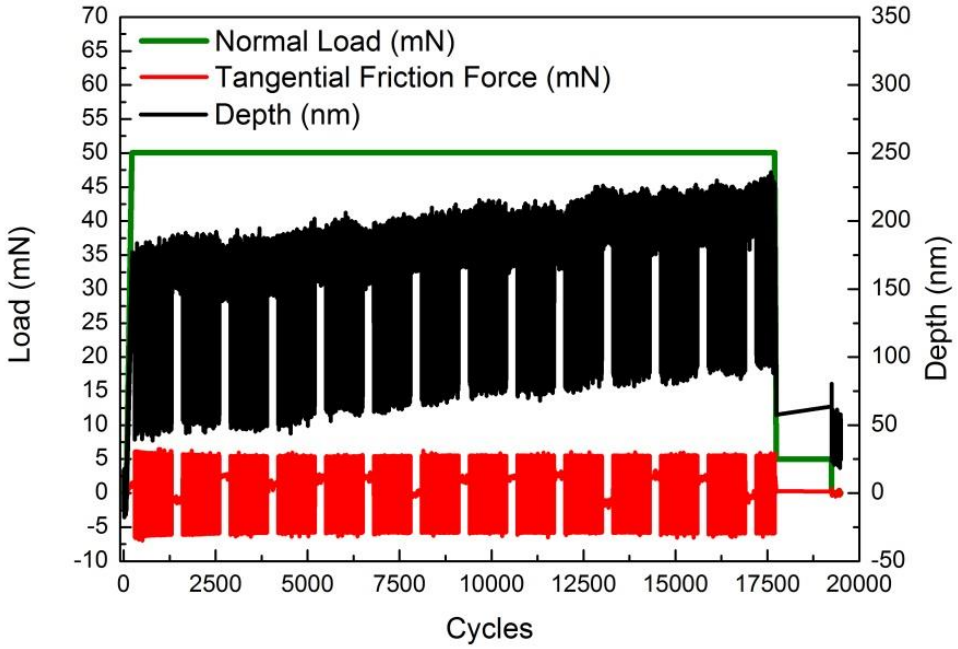

Figure 3.16 Overview of the data obtained during the intermittent nano-fretting experiments. Load profile applied (green line), tangential friction force (red line) and depth values recorded (black line)

The total number of cycles during the experiments was approximately 18000, from which 15000 cycles were "on period" and 3000 corresponds to "off periods". Figure 3.16 shows an example of the data obtained from a fretting experiment: in green is plot the applied normal load, in red the tangential friction force and in black the fretting scratch depth.

Thermal drift correction data was collected for 5 minutes before and after the experiments to enable removal of any depth changes due to drift. During the tests the tangential friction force together with the depth of the scar were recorded continuously. Unfortunately, the friction gauges which were designed for three pass scratch experiments weren't able to sustain the high number of cycles required to monitor a fretting experiment and after a series of tests the solder joints holding the friction beams failed due to fatigue.

3.6.6 Reciprocating sliding nano-wear

Two different experimental conditions were used to assess the nano wear resistance and the frictional behaviour of the CoCrMo alloys.

3.6.6.1 Nano-wear resistance

The reciprocating nano-wear resistance experiments were performed using a spherical 5 μm radius diamond tip, with a load range from 1 to 30 mN, providing contact pressures from 6.6 to 20.70 GPa respectively. This range is representative of a single asperity contact between hard inert ceramic ZrO_2 radiopacifier agglomerates present in the cement and the CoCrMo stem surface [197]. The radiopacifier agglomerates typically have a mean diameter between 5 and 10 microns in size [125, 126] although bigger size agglomerates have been found as well due to mixing inhomogeneities [127]. The diamond tips were observed under an optical microscope before and after wear experiments; no geometry changes which might affect the results were observed.

A fixed displacement amplitude of 10 μm was used on the basis of clinical studies which demonstrated that micro-motions between the femoral stem and the cement are typically below 40 μm [29, 30]. To shorten the test duration, tests were carried out using a oscillation frequency of 7.5 Hz rather than a physiologically 1 Hz frequency. Each test ran for 3000 cycles.

As is shown in Figure 3.17, an initial low contact load of 0.1 mN was applied for 15 seconds to record the initial contact depth. The load was then linearly increased over 10 seconds until the maximum test load was reached (1). This load was kept constant during the 3000 cycles (400 s), (2). Finally the samples were unloaded linearly in 10 seconds to 0.1 mN and held for the next 15 s to record the final non-loaded depth, to provide information on the permanent plastic deformation produced in the alloy (3).

All experiments were performed at room temperature and dry conditions. Five samples per material were tested for each experiment. Two-tailed paired T-test

statistical analysis was performed on the samples to establish differences and/ or similarities in the behaviour between the four CoCrMo alloys. A p-value below 0.05 was considered significant for all statistical analyses.

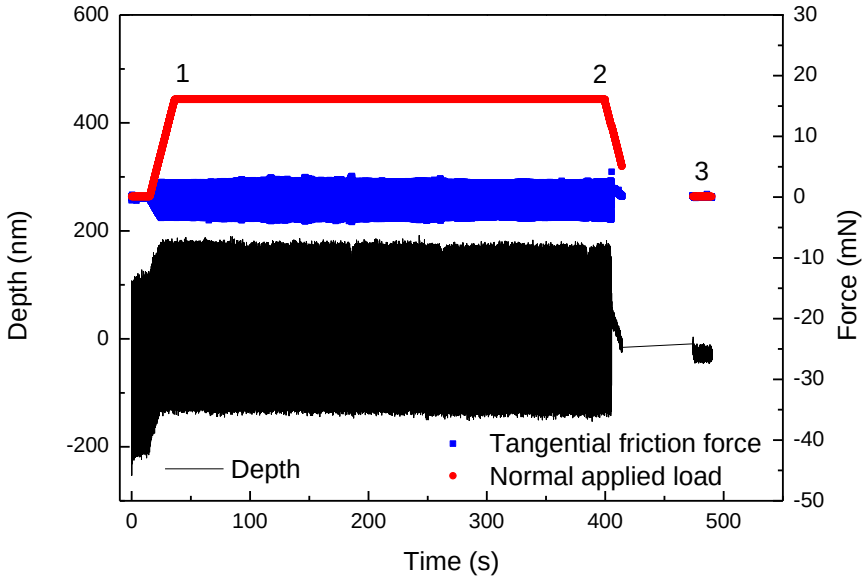

Figure 3.17 Load profile applied during the nano-wear experiments (red line), tangential friction force (blue line) and depth values recorded (black line). Note that the numbers, 1, 2 and 3 correspond to the initial depth, final depth and unloaded final depth respectively

3.6.6.2 Frictional behaviour

Same conditions as for the reciprocating sliding were applied to obtained the frictional behaviour except the radius tip was changed and the load range was limited to three loads. A spherical diamond tip of 200 μm was used while the normal loads applied were 5, 10 and 20 mN, which corresponds to maximum contact pressures of 0.97, 1.2 and 1.5 GPa, respectively. Track length was set 10 μm, frequency was 7.5 Hz and the number total of cycles was 3000.

Tangential friction forces were monitored by attaching a friction probe to the rig. Coefficients of friction were calculated from the ratio to tangential force to the normal force at the each load during running-in and steady state periods.

Dispersed energy values were calculated from the hysteresis area of the force-displacement curves as a measure of the interfacial mechanical energy dissipated during the wear experiments.

As is shown in Figure 3.18, the fretting loop graphs were obtained by plotting a three axis graph where x is the time; y is the track length and z the tangential friction force. The dispersed energy per cycle was calculated from the loops in 10 different time periods, from the "on-load periods", along the experiments using the area function in software Origin 8.5.1. As it was mentioned previously, one of the limitations of the system is that it is not able to monitored the true displacement of the indenter during the motion, therefore a full track length motion was assumed and confirmed by imaging the scars with an optical microscope after the experiments.

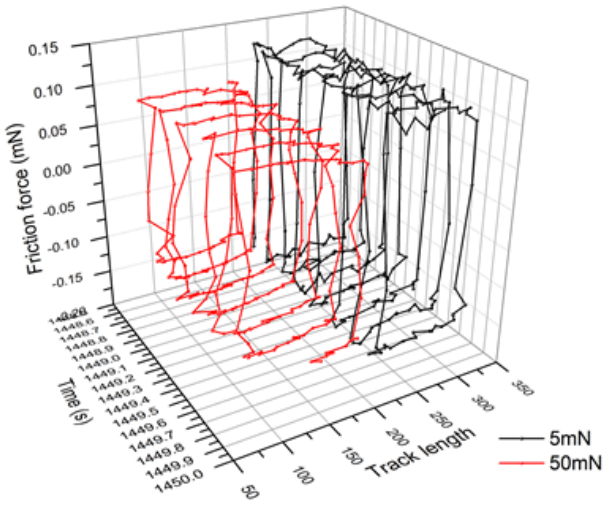

Figure 3.18 Example of the energy loops obtained from the nano wear experiments

3.6.7 Summary of nano-wear experiments

The reciprocating sliding nano-wear and coefficient of friction experiments enabled the determination of:

- Friction coefficients (μ) during the running-in and steady state periods
- Fretting loops (friction force-time-track length 3D graphs)
- Dissipated energy per cycle (nJ/cycle)
- Initial and final on load depth and final un-loaded depth

The penetration depth was monitored during the experiments and the initial on-load depth, and final depth was extracted from the depth-time graphs.

Table 3.4 summarizes the experimental conditions for the intermittent nano-fretting and the reciprocating sliding nano-wear.

Table 3.4 Summary of experimental conditions for intermittent nano-fretting and reciprocating sliding nano-wear

	Intermittent nano-fretting	**Reciprocating sliding nano-wear**
Tangential Movement	Reciprocating bidirectional	Reciprocating bidirectional
Displacement	5 μm	10 μm
Range Load	2.5-500 mN	1-30 mN: wear resistance 5-10-20 mN: friction
Tip	Spherical	Spherical
Tip radius	200 μm	5 μm
Fretting or Nano-wear reciprocating?	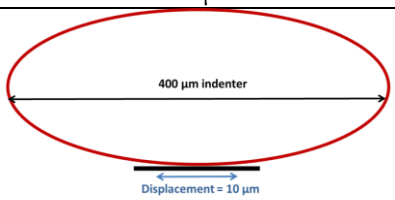	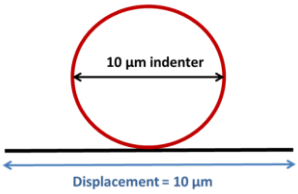
Nano-scale wear scar morphology	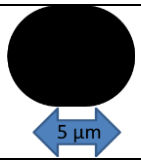	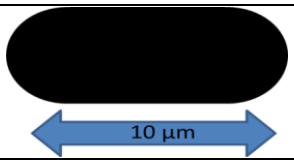
Wear mode	Gross slip regime Fretting	Reciprocating nano-wear
Max Contact Pressure	0.77-4.5 GPa	6-21 GPa
Loading rates	Ramp 0.083-16.66 mN/s	Ramp 0.1-3 mN/s
Unloading rate	Ramp 0.25-50 mN/s	Ramp 0.1-3mN/s
Environment	Dry	Dry
Frequency	5 Hz	7.5 Hz
n/load	5	5
Total -cycles	18000 (15000 on)	3000
Techniques used	SEM AFM FIB-SIMS	AFM Nanovantage Interferometry

Results obtained	Coefficients of friction Hysteresis loops Tribolayer characterization Atomic mass spectrum Element depth profiles	Coefficients of friction (5,10,20 mN) Dispersed energy Plastic deformation Measuring system validation

3.7 Scratch

3.7.1 Scanning motion

Scratch testing involves the physical scratching of a sample surface using the diamond indenter tip as described in Figure 3.19. The test can be a ramped load test where the load is continuously ramped to a predefined maximum load, or a static load test were the load is applied and held constant for the duration of the scratch. The standard scratch test uses a three pass test formed by an initial pass which gives a pre-scratch topography of the sample surface, using a low contact load to avoid deforming the surface, F_o, a second one which produces the scratch on the sample, under the normal load required, F_N, and the last one which provides the topography of the scratch, using F_o again. The number of scratches in between the topographies can be modified to do multi-pass scratch experiments to evaluate the wear behaviour after several passes. By adding the friction probe to the setup it is possible to monitor the friction forces during the scratch experiments. The friction probe is described in section 3.6.4.

The software allows programming of the topography and scratch loads, the track length, the loading and unloading speed and the indenter scratch speed.

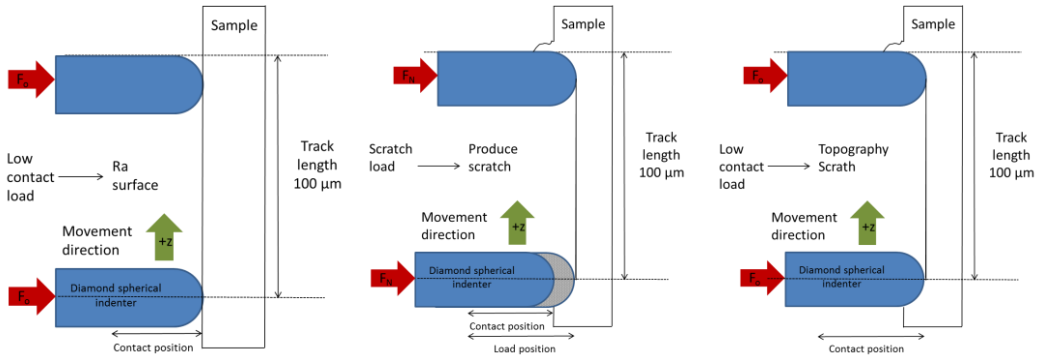

Surface sample topography *Scratch* *Scratch surface topography*

Figure 3.19 Scratch setup description and three scratch set up

3.7.2 Degree of penetration

The degree of penetration, D_p, is defined as a parameter to characterize the severity of the scratching motion and to characterize the modes in abrasive wear: cutting, wedge forming or ploughing, [198, 199]. It is defined as follows in Equation 3.22 :

$$D_p = \frac{h}{a} \qquad \textit{Equation 3.22}$$

Where a is the radius of contact and h is the on load depth of the groove as shown in Figure 3.20a.

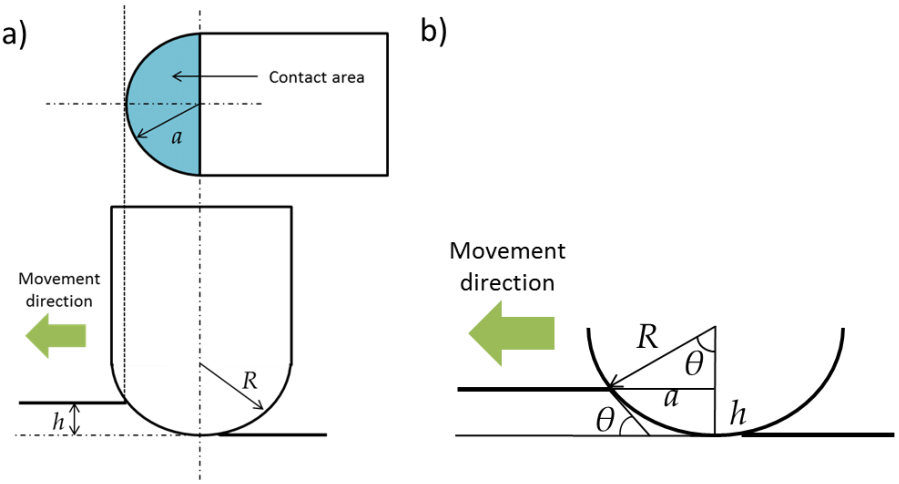

Figure 3.20 a) Model of contact between a hemisphere and a flat surface during scratching, b) Definition of θ for a hemispherical asperity

In the model described, the radius of the spherical tip, R, the on load depth of the groove, h, and the contact radius, a, should satisfy the following geometrical condition, Equation 3.23. Combining Equation 3.22 and Equation 3.23, D_p can be expressed as a function of R and a, Equation 3.24.

Finally if the contact pressure is equal to the hardness of the flat specimen, H_v, the contact area $\frac{\pi a^2}{2}$ is expressed as Equation 3.25. The theoretical degree of penetration value can be then calculated as a function of the radius of the tip, R, the load W, and the hardness of the material H_v, as described in Equation 3.26.

$$R^2 = a^2 + (R - h)^2 \qquad \textit{Equation 3.23}$$

$$D_p = \frac{R}{a} - \left(\frac{R^2}{a^2} - 1\right)^{\frac{1}{2}} \qquad \textit{Equation 3.24}$$

$$\frac{\pi a^2}{2} = \frac{W}{H_v} \qquad \textit{Equation 3.25}$$

$$D_p = R\left(\frac{\pi H_V}{2W}\right)^{\frac{1}{2}} - \left(\frac{\pi H_V}{2W}R^2 - 1\right)^{\frac{1}{2}} \qquad \textit{Equation 3.26}$$

To determine the shear strength at the contact interface it is necessary to define the hard asperity angle, θ, described in Figure 3.20b. It can be assumed that a good estimation to calculate this angle is given by the following relationship in Equation 3.27:

$$\sin\theta = \frac{a}{R} \qquad \textit{Equation 3.27}$$

3.7.3 Dry scratch

Scratches on retrieved MoM joint surfaces have been reported previously [200], the proposed wear mechanism is usually explained by the action of a third body abrasive wear that interacts in between the two surfaces when they are in motion. Scratch experiments are a useful technique to simulate this abrasive behaviour.

Tests were performed using a 200 μm radius spherical probe to enable comparison to the fretting and indentation experiments and a 5 μm radius spherical tip to compare with the scratch-corrosion experiments. The scratch test was set as a multi-pass wear test involving a pre and post topography scan either side of the scratch test. The pre and post-scratch scans were carried out using a low contact force of 0.1 mN to ensure that no deformation was done on the surface. The scratch profile is shown in Figure 3.21a.

The sample to be tested was moved perpendicular to the spherical probe whilst the applied normal load was held constant for 50 μm and then ramped to the maximum load in 1 second. The track length was set to 550 μm, where the first 50 μm were the levelling distance that was used to set the initial depth reference. The on load depth was recorded during the pre, post and scratch scans at a scanning speed of 10 μm/s, see Figure 3.21b. The data was analysed to obtain the residual depth to determine the amount of permanent plastic deformation performed on the sample and the percentage of elastic recovery. Five repetitions of each test were done for each load. Tangential friction forces were monitored throughout the duration of the experiments and their corresponding COF values

were calculated (following the same equation as in the nano-fretting experiments, Equation 3.21) and analysed for each load and sample.

Optical microscope pictures were taken on the scratch scars after the experiments at different magnifications, 10x to 100x, with an Alicona Infinite Foucs microscope (Kent, UK) to look for surface features along the wear scar, see Figure 3.21 c.

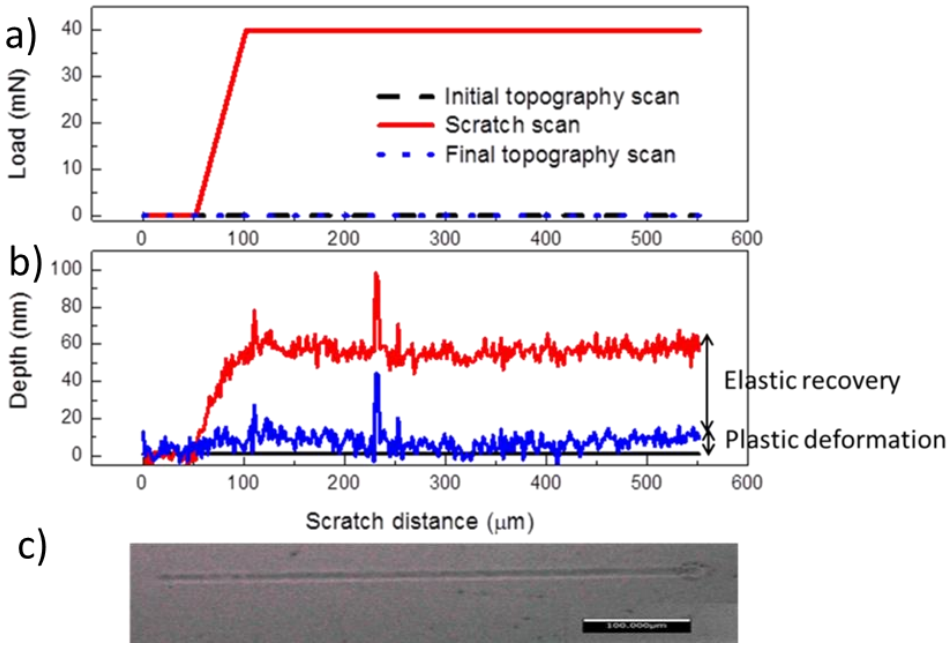

Figure 3.21 a) Example of a load profiles applied during the scratch experiments, b) Depth profiles recorded during the scratch experiments, c) Scratching scar after experiment, 10x

3.7.4 Liquid cell and electrochemistry cell design for scratch corrosion experiments

The original liquid cell, shown in Figure 3.22a, is the aluminium sample stub used for the dry experiments with two "O" rings to seal it against a glass container with an opened end to allow the tip to make contact with the sample surface. The tip also needs to be displaced from the standard position by an L-shape metallic indenter arm, shown in the left hand side of the same picture. The indenter tip is fixed into the arm by a screw and then is screwed to the loading head. The indenter is positioned in a different place than in dry experiments, therefore the load and depth calibrations change. Because the frame compliance

increases due to the "L" shaped bend of the indenter arm, a separate set of depth, load and frame compliance calibrations are needed.

The original liquid cell design is able to be used for nanoindentation, nano-fretting, reciprocating wear and nano-scratch. However, for the scratch-corrosion experiments some modifications were needed, as is possible to see in Figure 3.22 b. The metallic components included in the system were substituted by inert materials to avoid any interference with the electrochemistry results. A new L-shape zirconia holder replaced the metallic one and sapphire backed diamond spherical tip was fixed with special curing cement to the tip holder. The glass container was modified to hold the reference and counter electrodes and the front part was narrowed to allow the sample holder to fit in between the main fixing plate and the pendulum. The aluminium stub was changed for a hollow holder where the sample was inserted, see details in Figure 3.22d. The inner part of the holder, number 2, was made of stainless steel to allow electric contact between the sample, number 5, and the connectors to the potentiostat and make the sample to be the working electrode. Between the front part of the holder and the sample there is a rubber seal ring, number 6, to avoid the electrolyte leaking inside the holder. Number 3 refers to the screw which allows the electrical connections between the sample and the inner part of the holder. In addition, a metallic stub, number 4, was chosen instead of a polymeric one to maintain the stiffness of the stub and limit the compliance of the system. At the same time the outer part, number 1, was made of an inert non-absorbent polymer to isolate the sample from the electrolyte solution.

The upper part of the glass container had two holes to insert the Ag/AgCl reference electrode (left electrode in Figure 3.22c) and a Platinum coil counter electrode (right electrode in Figure 3.22c), both from BASI Analytical Instruments, Gloucestershire, UK. The working reference (sample) was connected internally to an external metallic screw which was connected to the external potentiostat (Ivium Technologies B.V., Eindhoven, The Netherlands).

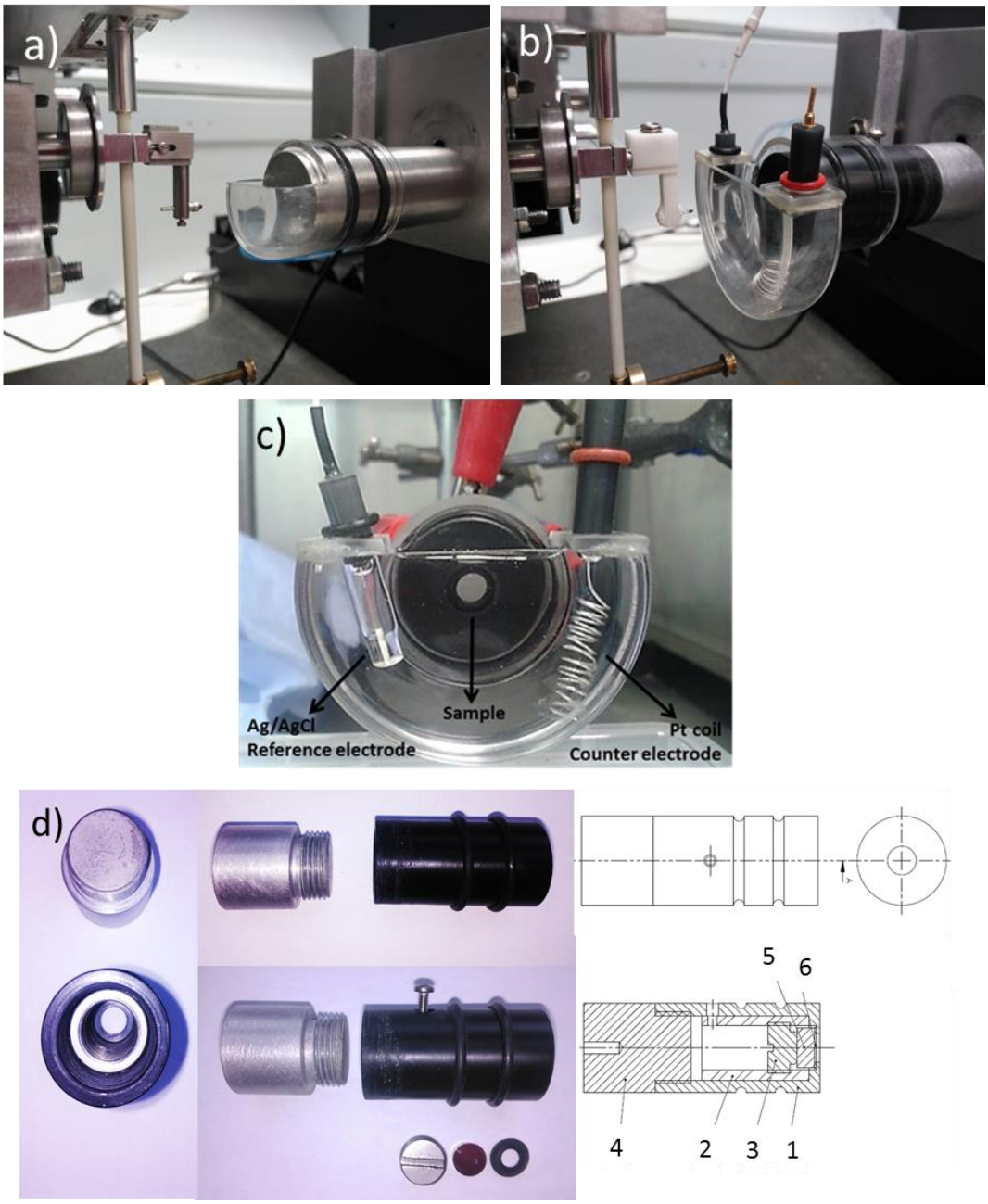

Figure 3.22 a) Original liquid cell set-up, b) New electrochemistry cell design cell, c) Front view of the electrochemistry cell mounted in the nanoindenter system, d) Schematics of the new sample holder

3.7.5 Scratch-corrosion experiments

Scratch-corrosion experiments were performed to understand the relationship between the deformation mechanisms and the repassivation processes which occur on the surface of CoCrMo alloy when a single asperity from the cement produces a scratch on the metal.

Samples were inserted in the electrochemistry cell described in section 3.7.2 and the electrolyte was added to the cell. The sample was left to stabilize within the electrolyte for at least 12 hours. 7 samples per alloy were tested in NaCl 0.9% in volume. The different immersion time respect to the static conditions was due to practical issues with the use of the equipment.

OCP was monitored during the stabilization process to confirm that it reaches a steady state to start the scratch-corrosion experiments. Due to the lack of space in the electrochemistry cell to add a set up to heat the electrolyte, the temperature inside the cabinet was set to 24 ± 0.5 °C.

Preliminary experiments with the 200 μm sphere didn't produce enough deformation on the samples to generate a measurable current signal with the potentiostat. Therefore, the tip was substituted by the 5 μm sphere. The track length was set at 100 μm, and loads, from 10 to 120 mN were applied in steps of 10 mN to find the initial load where the current was measurable. The scan speed was 75 μm/s. Experiments with different scan speeds were done on one sample to find the ideal conditions where current was measurable and the NanoVantage system was able to monitored at least 5 points along the length of the scratch, see Figure 3.23a-b. Speed values too low; see Figure 3.23 b-c, allowed for monitoring of the scratch depth accurately but the time the tip takes to do the scratch was too long to record any current since the repassivation happened before the scratch was finished. Increasing the scan speed resulted in measurable currents.

A relationship between the scan speed used and the on load depth measures provided by the system was also observed, Figure 3.23d. Lower scan speeds, 10 to 30 μm/s, result in a higher initial on load abrupt depth (black squares, Figure 3.23d) compared to the final on load depth reached at the end of the scratch (red circles, Figure 3.23d). No differences were found for the on load final depth measurements for the different scan speeds used.

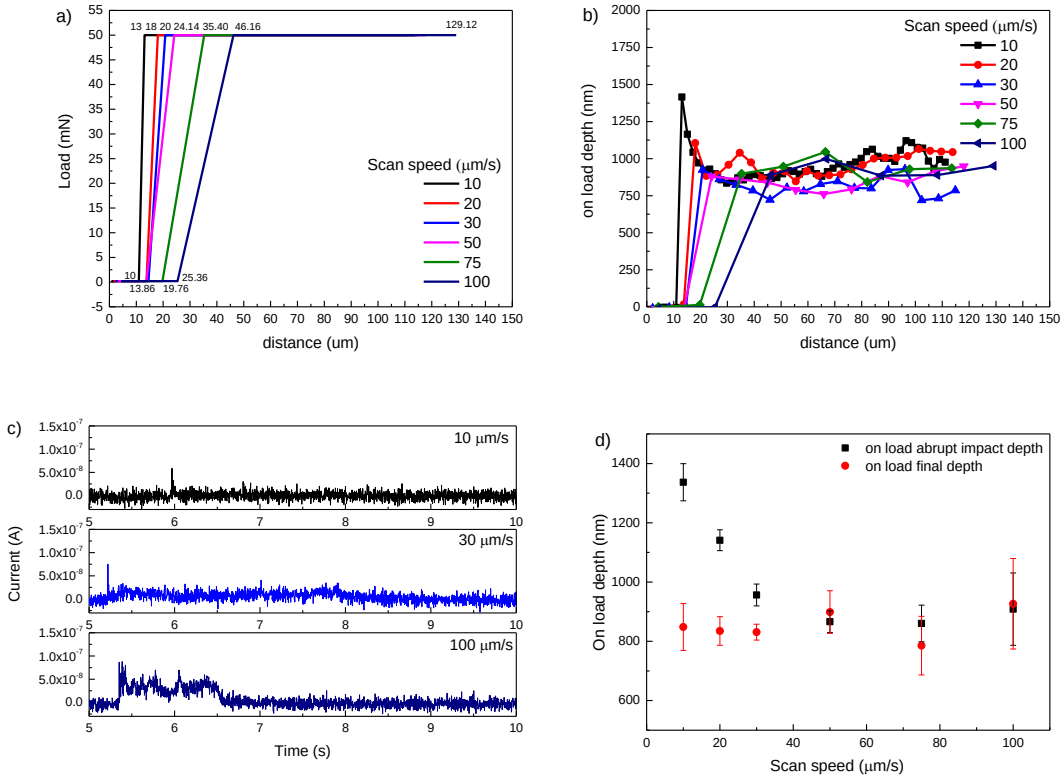

Figure 3.23 a) Track length distance-load dependence plot, b) track length distance-on load depth plot, c) Measured currents at three different scanning speeds: 10, 30 and 100 μm/s, d) Scan speed-on load depth plot: black refers to abrupt on-load depth, red to final on-load depth

The Ivium potentiostat was used in high-speed data recording mode to monitor the maximum number of data points possible so as enable visualization of the current peak when the scratch was happening. The data collection rate was set at $2.5 \cdot 10^{-3}$ Hz (400 data points each second). for 20 seconds. The short time to collect the data was due to the potentiostat restriction which only allows for the collection of 8149 data points when working at high-speed. Currents were recorded versus OCP values since artificial shifting of the applied potentials on the surface were not under the objectives of the study. An example of the data recorded during the scratch-corrosion experiments is shown in Figure 3.24a.

The current range was set to be at 100 nA, as the expected signal was not higher than 50 nA. To reduce the noise acquired for the equipment automatic filters and standard stability tests included in the potentiostat software were applied.

3.7.5.1 Current density calculations

From the current-time plots, the total current generated during the repassivation of the surface due to the scratch was calculated by integration of the area under the curve, see Figure 3.24b.

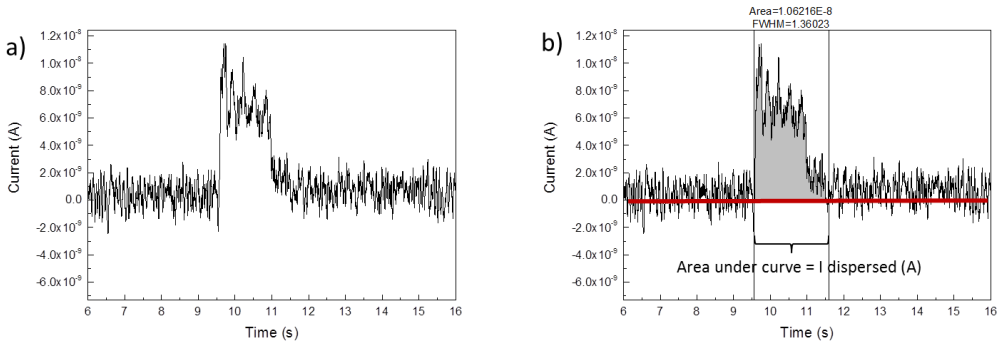

Figure 3.24 a) Example of current data recorded during scratch-corrosion experiments, b) Example of how the total current produced during the experiments was calculated from the area of the current-time plot

Current densities were calculated by dividing the total current obtained from the potentiostat by the total deformed area. The geometry of the scratches was obtained from white-light interferometer measurements as will be described in Section 3.8.6. The scratched area usually presents a V shape profile with high levels of pile up deformation on the sides (for the highest loads applied) and irregular 3D features on the sides of the scratch as shown in Figure 3.25a.

To evaluate the affected area (light blue and green areas), it was necessary to assume a regular V shape, Figure 3.25b. The area calculated was the value x times the length of the scratch. Using basic geometry, x was calculated as the hypotenuse of the red triangle by using $D_{total,}$ and half of the width of the scratch. D_{total} is defined as the sum of the height of the pile up ($D_{pile\text{-}up}$) plus the depth of the scratch ($D_{scratch}$).

However, there are some limitations applied to this measurement method, as shown in Figure 3.25c. The real affected areas extend further than the calculated ones, but since each scratch presents different deformation behaviour it was difficult to evaluate their 3D features individually. Therefore to develop a normalized process to compare between the samples, the blue and green areas were counted as the affected area for the current density calculations.

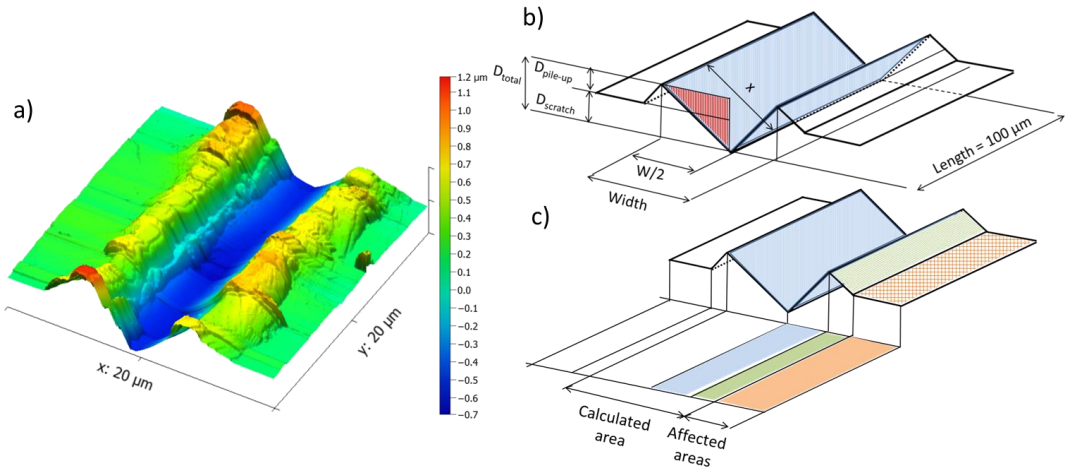

Figure 3.25 a) Partial geometry of a scratch-corrosion scar taken by AFM, b) Schematic of the model used to calculate the affected areas on the scratch-corrosion scar, c) Schematic showing the limitation of the model used: real affected areas do not match the calculated area

3.7.5.2 Repassivation time

The repassivation time for the alloys was obtained from scratches where 80, 100 and 120 mN loads were applied. As it is shown in Figure 3.26, the time constant, τ_1, was calculated by fitting the curve to a first order exponential decay equation following Equation 3.28.

$$I(t) = I_{\infty} + I_{peak} exp\left(\frac{-(t - t_0)}{\tau_1}\right) \qquad \textit{Equation 3.28}$$

Where the symbols are defined as follows:

- I(t): current level at time t
- I_{∞} : baseline current
- I_{peak}: current related constant
- t_0: test duration
- t: time t
- τ_1 : time related constant

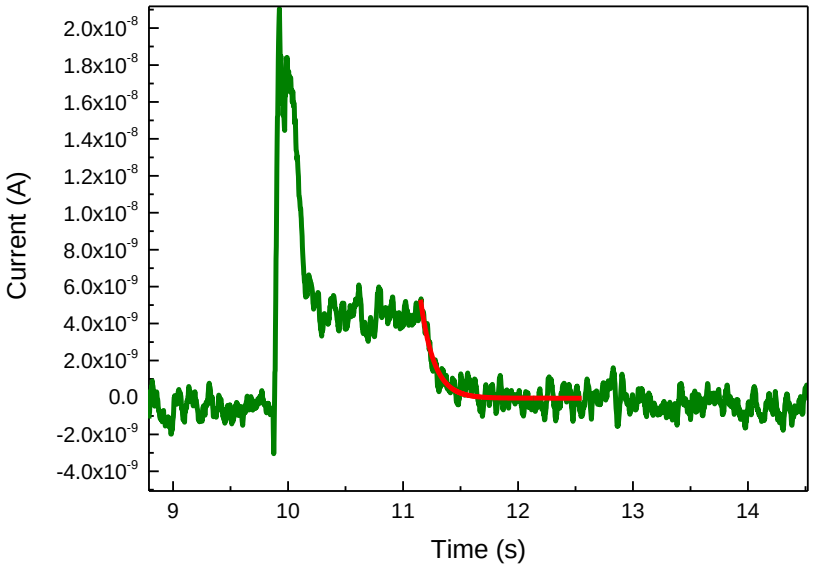

Figure 3.26 Example how repassivation times constants were calculated from the current (green line)-time plot fitting the final part to a first order exponential equation (red)

A summary with the experimental conditions for scratch and scratch-corrosion experiments is shown in Table 3.5

Table 3.5 Summary with experimental conditions for dry scratch and scratch-corrosion experiments

	Dry scratch		**Scratch-corrosion**
Tangential movement	Directional		Directional
Track length	500 μm	300 μm	100 μm
Load range	1-75 mN	20-120 mN	10-120 mN
Tip	Spherical		Spherical
Tip radius	200 μm	5 μm	5 μm
Max contact pressure	0.57-2.4 GPa	18-33 GPa	14-33 GPa
Loading rates	Ramp 1-75 mN/s	Ramp 20-120 mN/s	Abrupt loading
Scanning speed	10 μm/s		75 μm/s
Number of passes	Topo+scratch+topo		Single Scratch

Environment	Dry	NaCl
n/load	5	5
Total –samples/alloy	1	7
Results obtained	Coefficients of friction Plastic deformation values D_p	Current densities Repassivation times EBSD maps Deformation mechanisms

3.8 Surface characterization

A combination of different techniques was used to characterize the CoCrMo surfaces before and after the experiments. Surface profilometry was used to characterize final roughness of the samples after polishing. Microstructural features such as grain size, carbide morphology or wear scars and scratches morphology were evaluated using optical and SEM microscopy. fcc and hcp phase content and grain orientation was evaluated using EBSD. Finally, fretting, reciprocating sliding wear and scratch-corrosion scars were measured using 4 different systems: Nanovantage, white light interferometer, AFM and a 3D confocal interferometric microscope.

3.8.1 Surface profilometer

The final surface roughness of the specimens after polishing was measured by a surface profilometer (Taylor Hobson Talysurf 120L, Taylor Hobson Ltd. UK). The evaluation length was 5 mm, and the cut off, λ_c, was equal to 0.08, as is suggested by the ISO 4288:1998 standard to characterise surface roughness of between 0.006 and 0.02 μm [88]. The scan speed was 0.5 mm/s. Roughness profiles were taken in vertical and horizontal directions to ensure that there was not any directionality in the polishing method. Three profiles in each direction were measured to obtain their average roughness and standard deviation.

3.8.2 Optical microscopy

The Alicona Infinite Focus microscope, (Alicona, Graz, Austria) was used to take optical images at different magnifications (5x to 50x) of the microstructures, nano-scale wear scratches, corroded surfaces after static corrosion experiments and nano-scale scratch corrosion surface experiments.

3.8.3 Scanning Electron Microscopy (SEM)

Because optical microscopy doesn't have enough resolution to observe details about the microstructure (carbides and grain boundaries) or deformation mechanisms on the edges of the scratch corrosion scars, SEM (JEOL JSM 6500F, JEOL, Germany) was used to give information about the contact area morphology and the deformation mechanisms occurring in the CoCoCr alloys.

3.8.4 Electron Backscattered Diffraction (EBSD)

EBSD was used to characterize the samples microstructure (grain size and phases present) and to understand how the grain orientation in the alloys affected the deformation behaviour of the CoCrMo alloys.

EBSD is a technique that gives crystallographic information about the microstructure of a sample. An electron beam interacts with a tilted sample and the diffracted electrons form a pattern (Kikuchi bands, Figure 3.27a) that can be detected on a fluorescent screen. Each crystal structure and orientation in the sample has a characteristic diffraction pattern that can be used to determine the preferred crystal orientation (texture), differentiate between different phases (fcc, hcp), characterise grain boundaries and also gives information about the local crystalline perfection. The centre lines of the Kikuchi bands correspond to where the diffraction planes intersect with the phosphor screen. Hence, each band can be indexed by the Miller indices of the diffracting crystal plane which formed it. The intersections of the Kikuchi bands correspond to zone axes in the crystal and their positions can be used to calculate the orientation of the diffracting crystal.

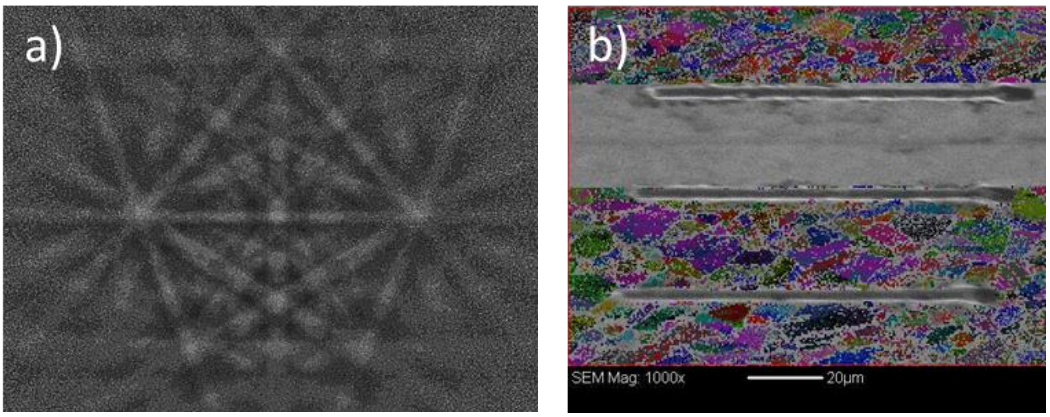

Figure 3.27 a) Example of a Kikuchi pattern for the fcc CoCrMo alloy, b) Example of a grain orientation measurement during EBSD mapping

The diffraction patterns can be used to measure the crystal orientation, crystal defects and phase transformations of metals. This enables the determination of the grain orientation where the scratches were done, Figure 3.27b, which can be linked to the deformation mechanisms and grain size differences between alloys.

Sample preparation is critical to obtain good EBSD results. The surface should be free of any deformation to obtain a high quality electron backscattered diffraction pattern. Due to this restriction, is not possible to obtain an EBSD map from the deformed surface of the scratches and they will appear as non-indexed points on the image.

Samples were electropolished following the protocol specified in American Society of Materials (ASM) Handbook Volume 9 [182]. A mixed of Percloric acid at 60% and ethanol at 96%in volume was used. Using Stainless steel as a cathode, a potential of 15 V was applied for 6 seconds for the forged alloy and 4 seconds for the as cast alloys. The solution was cooled with liquid Nitrogen to 10°C. A low temperature, provides a better surface quality keeping the power used to the minimum [201]. The samples were rinsed with ethanol and distilled water, then ultrasonically cleaned for 10 minutes, before being dried with compressed air.

EBSD maps using a 17 kV current, tilting the sample at 60°, at 1000x magnification were taken. A resolution of 259 x 194 points at 0.5 μm /point was used to obtain images similar to the one shown in Figure 3.27.EBSD data were acquired using Flamenco Software and analysed using Mambo Software, both from Oxford Instruments, UK. Noise reduction was applied in the samples where it was needed. The evaluated data were:

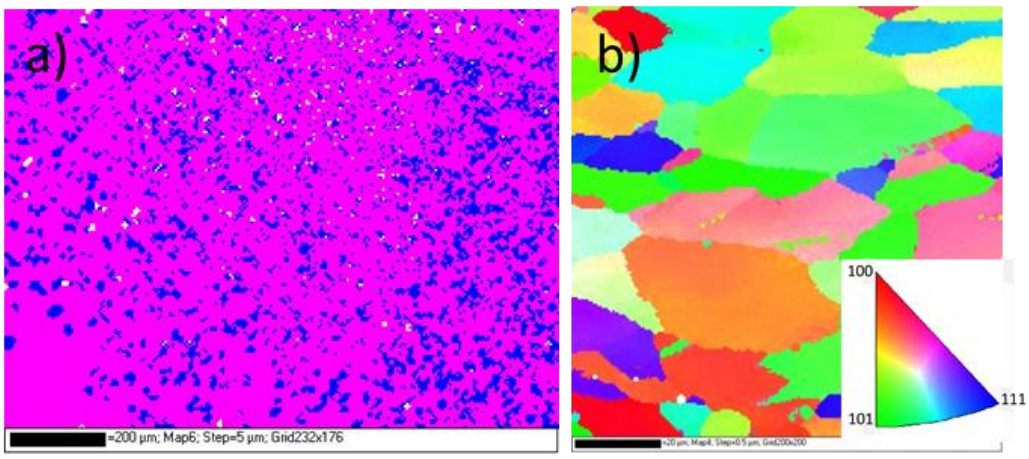

Figure 3.28 a) Phase map from EBSD in pink FCC phase, dark blue HCP phase, b) Example of a grain orientation map, insert showing grain orientation colour scale

- Phase maps: to calculate the content percentage of fcc and hcp phases (Figure 3.28a)
- Grain orientation maps: each colour in the map is assigned to a different grain orientation. (Figure 3.28b)
- Pole figures (PF) and Inverse Pole figures (IPF): Fastest way to visualise the exact orientation of a specific grain and compare between samples at the same time (Figure 3.30)

Pole figures, Figure 3.30a, are tools to plot 3D orientation information in 2D to show the orientations of specific crystallographic planes and directions within the grains that form the material. They show the projected position of a particular set of crystallographic planes, where their normal directions (poles) have been projected onto a sphere and then onto a circle (stereographic projection). On the left side of Figure 3.29 there is a single unit cell of a crystal oriented in a particular manner relative to the sample. A cubic crystal has 6 (100) planes whose normal directions would project onto a sphere as shown in the second drawing of Figure 3.29. If the plane parallel to the sample surface intersects the centre of the sphere, it will result in a circumference. Joining the points from where (100) plane normal contacts the sphere to the sphere's opposite pole will result in the third drawing. Finally, looking only into the circle, the 3D crystallographic directions have been converted into points, resulting in the pole figure for a (100) plane.

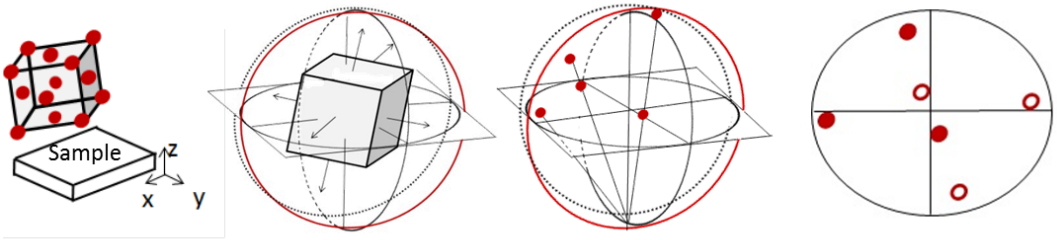

Figure 3.29 Example of how the stereographic projection for a single crystal orientated in a particular alignment is produced

The same process can be repeated for any grain to show the distribution of that particular set of planes within the sample. If the points appeared to be organized in a specific way, then the sample is said to have a texture.

Inverse pole figures (IPF), Figure 3.30b, show the distribution of crystallographic directions parallel to certain sample directions and are easier to interpret than pole figures. In Figure 3.30b it is possible to see three IPFs along the rolling direction (X0), transverse direction (Y0) and the normal to the rolling plane (Z0).

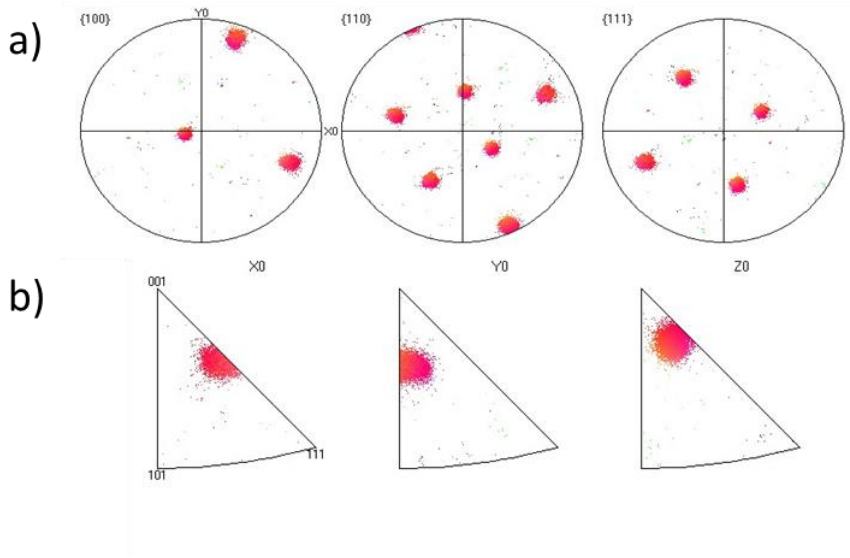

Figure 3.30 a) Example of a pole figure for a fcc crystal structure, b) Example of an inverse pole figure for a fcc crystal structure

IPFs use a basic RGB colouring scale. For cubic phases, red, green and blue are assigned to grains whose <100>, <110> or <111> axes, respectively, are parallel to the projection direction of the IPF. Intermediate orientations are coloured by a RGB mixture of the primary components, as seen in Figure 3.28b.

3.8.5 Atomic Force Microscopy (AFM)

Atomic Force Microscopy (Agilent 5500, Agilent Technologies, UK), see Figure 3.31, was used in tapping mode (non-contact with the surface) to generate 3D images of the relevant nano-fretting and scratch-corrosion wear scars.

The scanned areas were 20 x 20 μm, formed by 512 lines in the x and y direction, recorded at 0.1 lines per second. The speed was kept to the lowest value as the geometry of the scratches: narrow and with high values of pile up, made it difficult for the tip to follow the geometry when the speed was increased.

From the AFM maps geometrical parameters such as width and cross section of the wear scar were measured. Depth and pile up from at least 5 cross sections were used to calculate the damaged area involved in the repassivation processes for the scratch-corrosion experiments. The depth results obtained were correlated with depth and geometrical values obtained from alternative and faster methods such as Nanovantage System and white light interferometry (Redlux, Ltd, Chandlerds Ford, UK), which will be described in the next section. AFM was also

used to characterize material build up and fretting scar morphology produced during nano-fretting experiments, see Figure 3.31c.

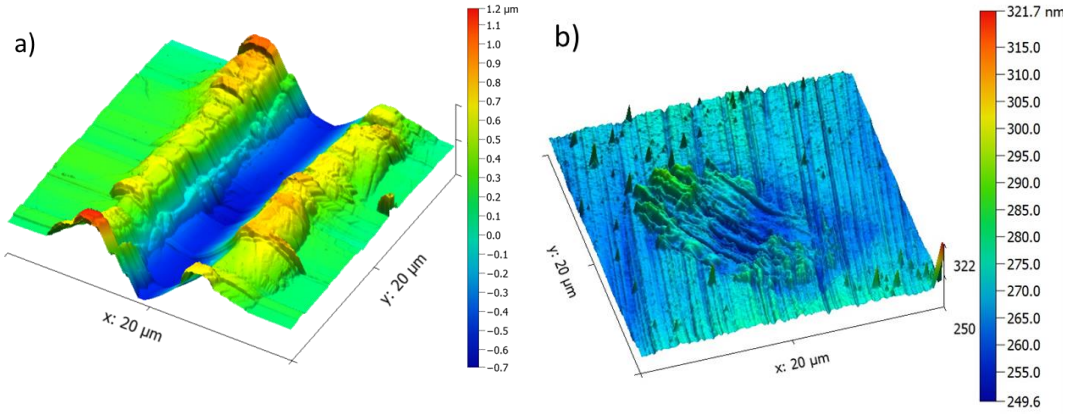

Figure 3.31 a) Example of a scratch-corrosion scar map taken with AFM, b) Example of a fretting scar morphology taken with the AFM

3.8.6 White light interferometry

A white-light-interferometer (Redlux Ltd, Chandlers Ford, UK) with a lateral resolution of 0.8 µm and vertical resolution of 0.1nm was used to perform depth measurements on the fretting and the wear scars. An example of the 3D measurements and the depth profiles obtained are shown in Figure 3.32a. Following the same process as the AFM, five cross section profiles in horizontal and transverse directions were used to evaluate the nano-wear scar depths.

3.8.7 Confocal 3D interferometry

For scratch-corrosion experiments a Contour GT-X (Bruker, Coventry, UK) 3D optical microscope was used. A 50x interferometry lens was used. As described previously, cross section profiles see Figure 3.32b were obtained. Depth and pile up were measured to calculate the deformed areas subjected to repassivation.

3.8.8 Ion Mass Spectrometry (FIB-SIMS)

Ion Mass Spectrometry was used on the surface of the fretting scars and over unaffected areas of the matrix to quantify and compare the metals (Co, Cr, Mo), oxygen, and carbon contents in different areas after the fretting experiments.

Main element depth profiles were obtained for Cobalt, Chromium and Oxygen, together with atomic mass spectra from accelerating negative or positive species to obtain mass spectra on the fretting scar and outside the fretting scar to evaluate possible chemical interactions (oxides formation) and element diffusion during the fretting experiments.

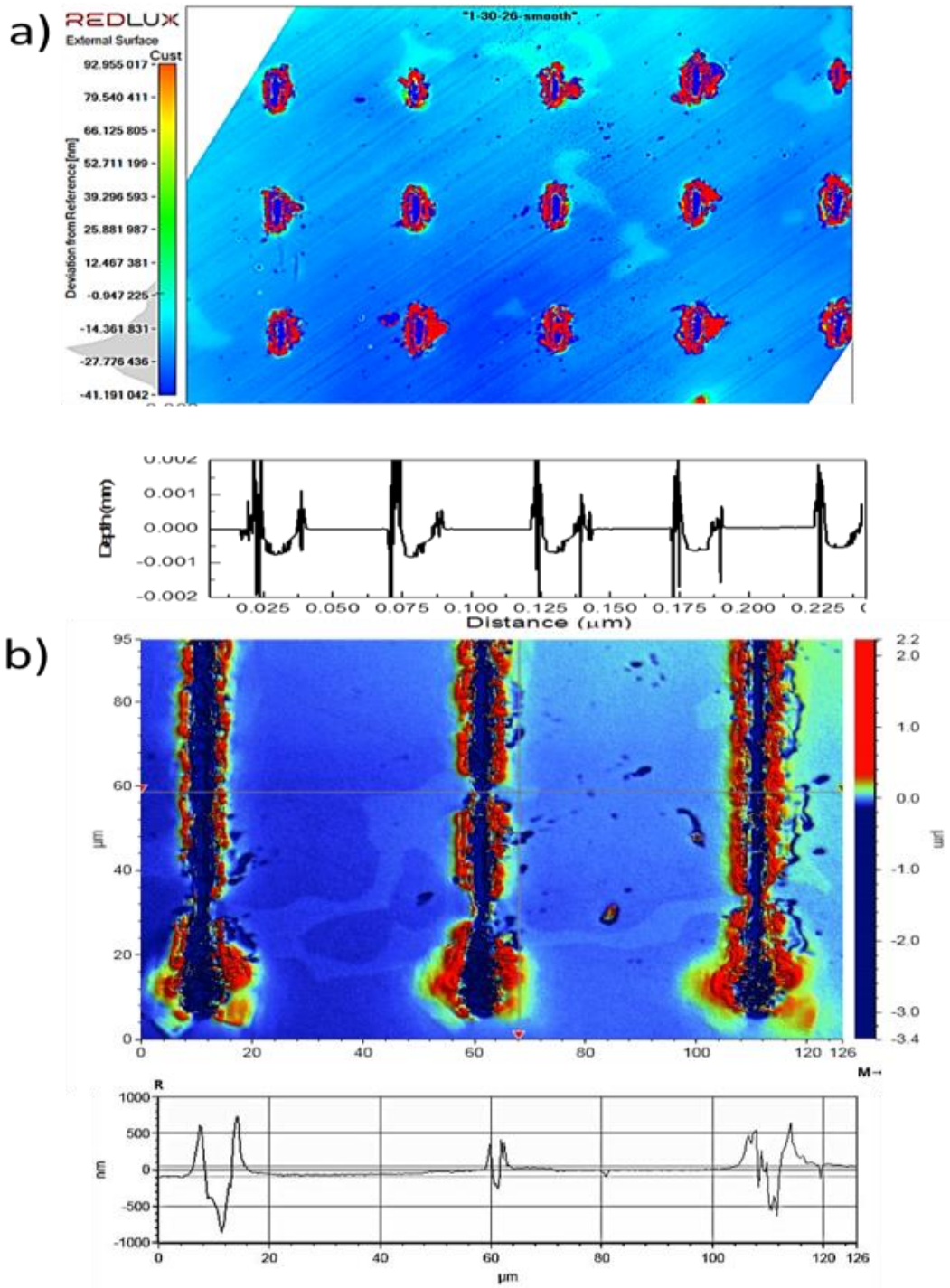

Figure 3.32 a) Example of 3D surface measurement obtained with the white-light-interferometer system and its correspondent depth profile for one of the nano-wear wear scars used to validate the depth measurements done by the NanoTest Vantage system, b) Example of a scratch-corrosion map and the profiles obtained with the Bruker Contour GT microscope

3.9 Statistical analysis

The number of repetitions for each test is shown in Table 3.6. The numbers varied depending on the experiment and the duration of the tests. The total number of experiments is the figure for the 4 different alloys tested.

The average and standard deviation were calculated using Excel 2010. Comparison between sample groups was performed via two-tailed paired T-test. This test compares the difference between two means in relation to the variation in the data. Statistical significance was considered between two sample sets when the p-value was below 0.05, demonstrating that the difference in the average value of the two groups was greater than that which be expected due to random sampling variability.

Table 3.6 Number of repetitions for statistical purposes for each of the experiments done

Experiment	**Samples / alloy**	**Number of repetitions**	**Number of loads/ conditions**	**Total number of experiments**
Roughness measurement	3	6	-	72
Micro-macro Vickers indentation	1	10	2	80
Berkovich nano-indentation	1	400	1	1600
Static corrosion	7	1	2	56
Nano-fretting	1	5	10	100
Dry Nano-scratch-200 μm	1	5	9	135
Dry Nano-scratch-5 μm	1	5	6	120
Nano-scale reciprocating wear	1	5	30	600
Scratch-corrosion	7	5	10	1400

4
Materials characterization

4.1 Introduction

Four CoCrMo alloys were used during the study. The specific details of the chemical composition, carbon content, grain size, grain orientation and phase composition were unknown, so chemical analysis, metallographic analysis and EBSD mapping were used to characterize the alloys.

The carbon content and the volume fraction, size and distribution of carbides influence the alloys final microstructures and their mechanical properties, wear and corrosion resistance [202, 203]. It is crucial to know these fundamental characteristics of the alloys in order to correlate them with the results obtained.

The hardness (H) and Young´s modulus (E), of the four CoCrMo alloys under study were calculated using Vickers indentation and nanoindentation techniques to characterize them at the macro, micro and nano-scale. Mechanical properties are needed to understand how the manufacturing process, thermal process and carbon content affect the different CoCrMo alloys under study. They were used to calculate hardness to elastic modulus ratios: H/E [204] and H^3/E^2 [205], parameters related with deformation relative to yielding and resistance to plastic deformation respectively.

The last objective of this chapter was to assess the corrosion performance of the four CoCrMo alloys in static conditions, to provide a baseline against which the new tribocorrosion setup could be compared. OCP experiments were run to investigate the minimum time needed to reach a steady state in the samples

before any scratch-corrosion experiments. Potentiodynamic curves were analysed to calculate the current and potential corrosion parameters to identify any differences between the alloys and how the formation of the oxide film occurs under static conditions. The results obtained from this chapter were used as a baseline to understand the deformation-corrosion processes investigated in Chapter 6.

4.2 Microstructural characterization

4.2.1 Chemical composition

The type of alloy, the standard which it is related to, the heat treatment the alloy was subjected to, together with the percentage of the main element composition (Co, Cr, Mo and C) are detailed in Table 3.2.

The Co, Cr and Mo contents were not significantly different between the four alloys, however the carbon content differed greatly. The as cast low carbon content alloy (AC-LC) presented a similar value to the Forged low carbon,0.06 and 0.044 respectively, while the As Cast sample (AC), 0.297 and the single thermal treated (AC-TT) sample, 0.595 %, both had high carbon contents, with the AC-TT having a carbon level outside the allowable levels set in the standard.

Table 4.1 Summary of the alloys and the nomenclature used during the work

				Element composition (%)				
Alloy	**Standard**	**Heat treatment**	**Nomenclature**	**Co**	**Cr**	**Mo**	**C**	
Forged	ASTM F799	No	Forged	63.9	27.8	6.27	0.044	low
As Cast	ASTM F75-98	No	AC (as received)	63.9	28.1	6.1	0.297	high
		Single	AC-TT (thermal treated)	63.7	28.2	6.14	0.595	out standard
	ISO 5832-4	No	AC-LC (low carbon content)	63.1	28.6	6.79	0.06	low

4.2.2 Forged alloy

After the etching process, the Forged sample presented a fine grained microstructure (Figure 4.1a-b) with grains of 30-40 µm in size with no visible carbides. The absence of carbides is due to a low carbon content, 0.044%,

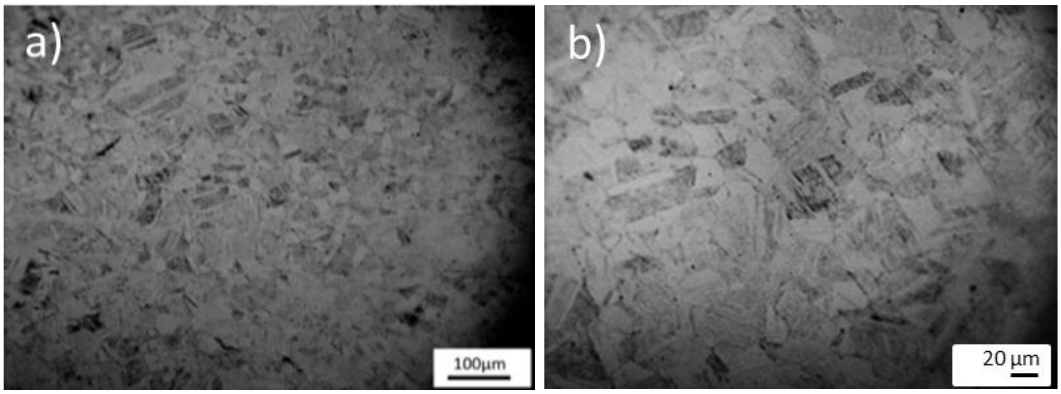

Figure 4.1 Microstructure for the forged CoCrMo alloy: a) 20x and b) 50x magnification

within the forged alloy. Annealing twins and stacking faults appeared in some of the grains, see Figure 4.1a, as a consequence of the applied thermal process.

EBSD data were used to obtain orientation colouring maps, see Figure 4.2. Each colour represents a specific grain orientation according to the colour legend on the left-upper corner in Figure 4.2. From the orientation maps, the Forged alloy presented a multiple oriented grain structure for the alloy. The green colour corresponds to grains oriented in the (101) crystallographic plane, red for the (001) plane (basal plane) and blue for the (111) plane (main slip system in fcc crystal structures). Any colour in between, such as pink or yellow corresponds to crystallographic orientation in between any of the three main systems mentioned earlier.

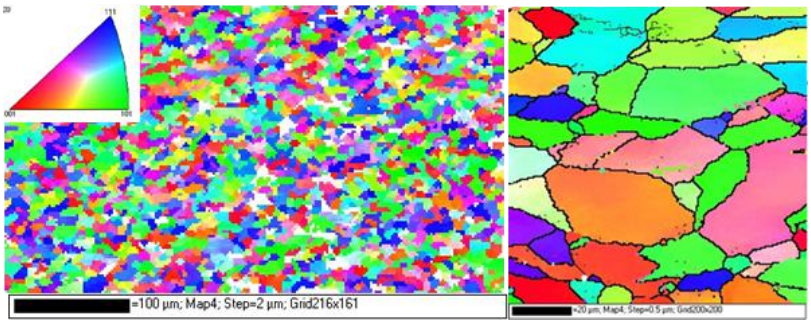

Figure 4.2 Forged alloy grain orientation from EBSD maps

4.2.3 As cast alloys

Three as cast alloys were under study: AC (as received), AC-TT (thermal treated) and AC-LC (low carbon content).

As-cast microstructures produced by investment casting without any thermal treatment usually exhibit a dispersion of second phase carbides in a uniform Cobalt matrix with very large grains, see Figure 4.3a. The interdendritic carbides present in the matrix, mainly $M_{23}C_6$, have a bulk, "solid-type" appearance, Figure 4.3c. After the etching process, Figure 4.3e, it is possible to see that there can be two different phases forming the carbides (grey and black areas). After electro-polishing, see Figure 4.4a-b, also two phases (black and grey areas) are revealed presenting a lamellar structure within the carbide.

After a solution heat treatment the cast alloy presents the microstructures shown in Figure 4.3b. At low microscope magnification, the general microstructure does not seem to be altered compared to the non-treated as cast sample. However, at higher magnification, Figure 4.3d, the AC-TT carbides have a fragmented morphology because of the partial dissolution of the bulk carbides during the thermal treatment. After chemical etching, the AC-TT alloy present a single homogenous phase ($M_{23}C_6$), Figure 4.3f. Similar observation is obtained after the electro-polishing etching, Figure 4.4c-d, where inter-granular carbides precipitated within the grain boundaries are also visible.

The AC-LC alloy exhibited a large grain size Co matrix with a dispersion of tiny carbides (black dots) within it, see Figure 4.5.

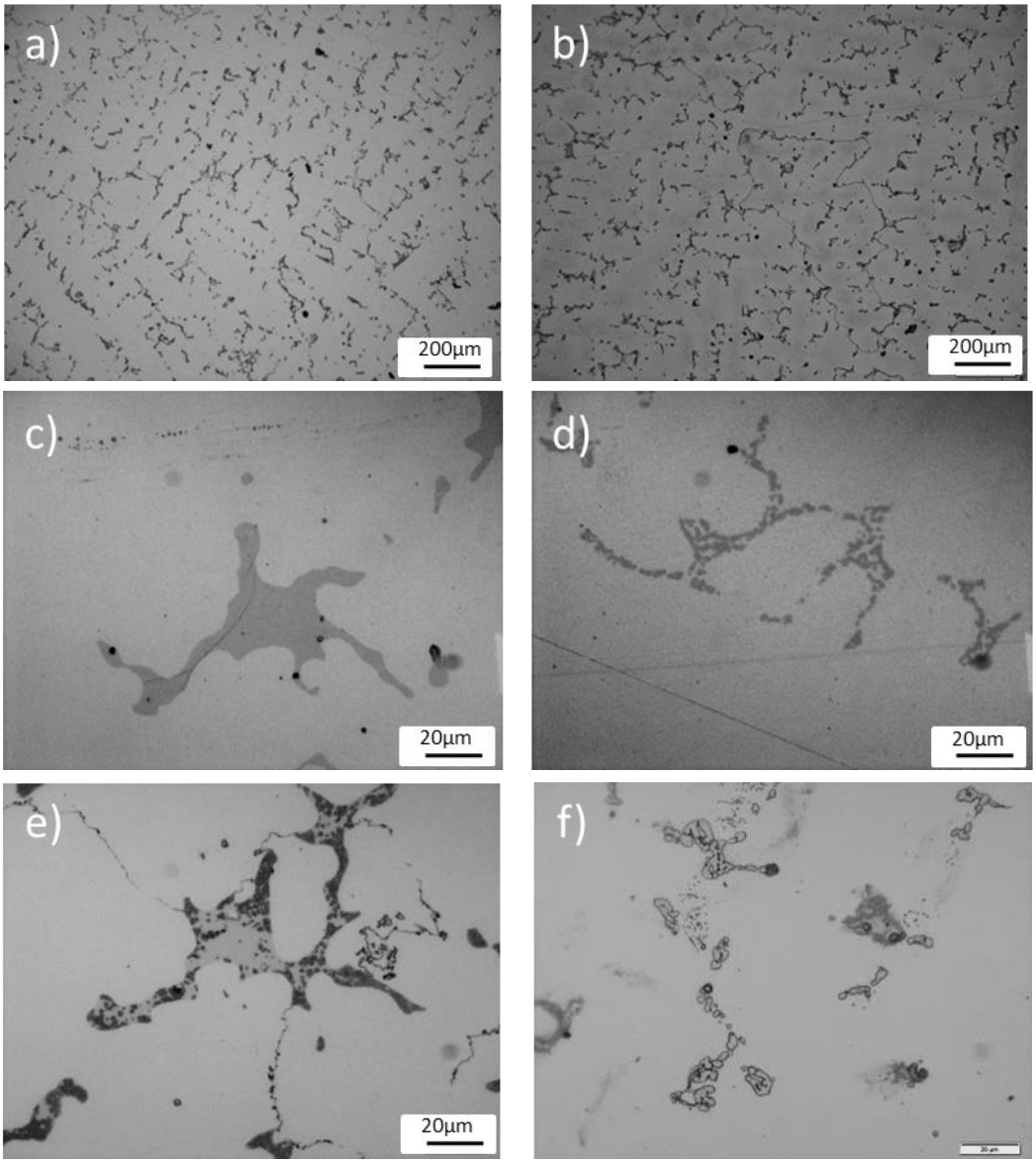

Figure 4.3 Carbides microstructure for the As Cast CoCrMo alloys: a) AC b) AC-TT, c) AC carbide, d) AC-TT carbide e) AC etched carbide and f) AC-TT etched carbide

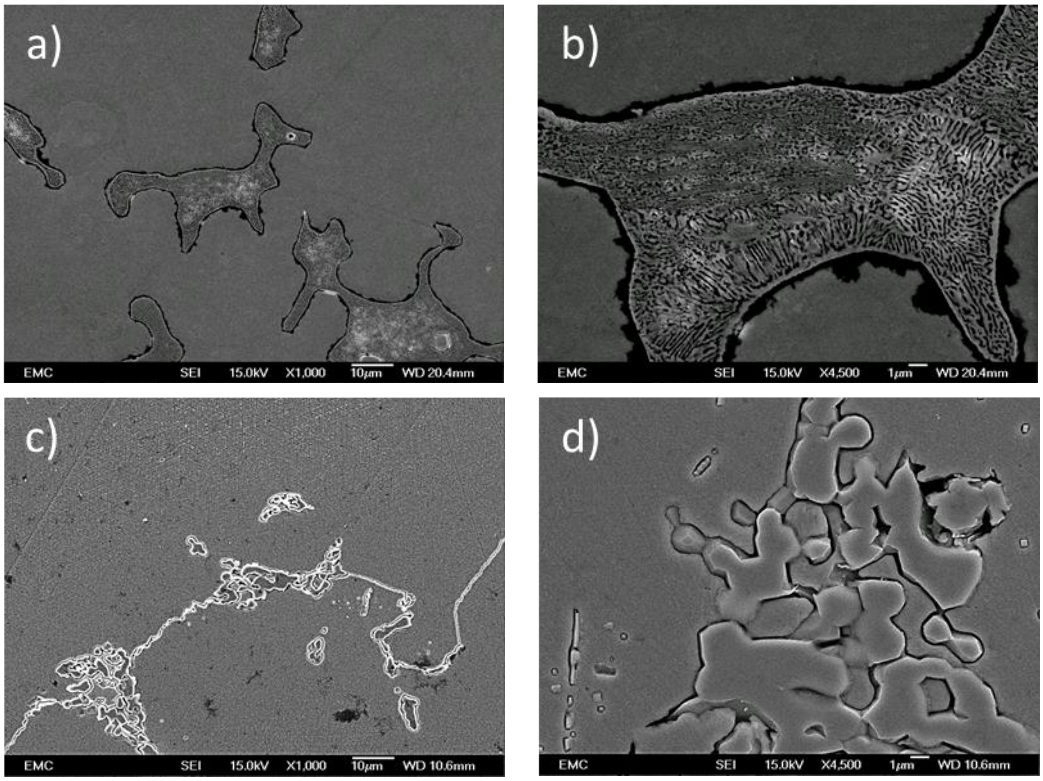

Figure 4.4 First row: AC alloy carbides at a) 1000x, b) 4500x magnification. Second row: AC-TT carbides at c) 1000x and d) 4500x magnification after electro-polishing

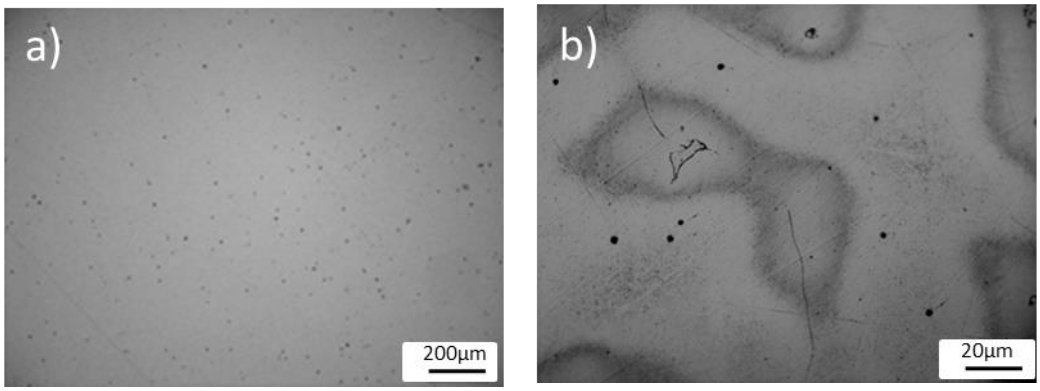

Figure 4.5 AC-LC CoCrMo alloy, a) 10x, b) 50x

Grain size in As Cast samples was obtained from microscopy images, Figure 4.6. Grains sizes between 600 μm to 1-2 mm were observed for the three of them. Figure 4.7 shows EBSD maps of two as cast samples, showing the grain boundaries and the different grain orientations represented by the different colour legend on the top-left corner. Each colour corresponds with a specific plane orientation as was described in the previous section for the forged alloys.

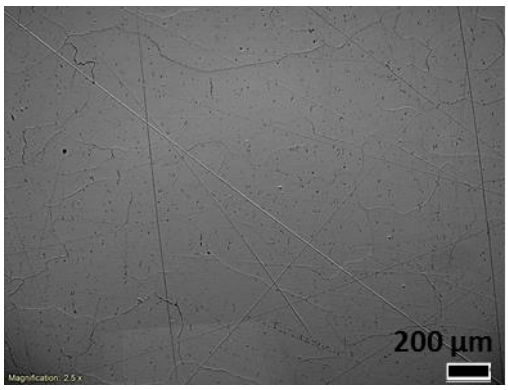

Figure 4.6 Chemically etched AC sample at low magnification used to measure grain size

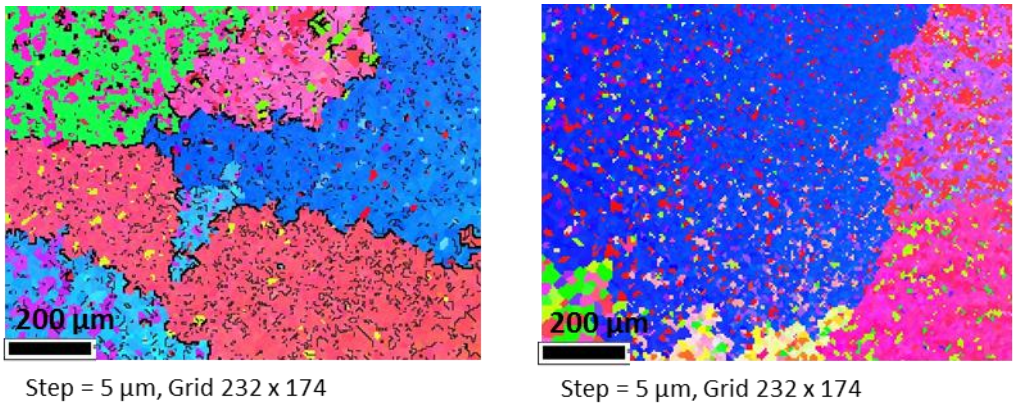

Figure 4.7 EBSD grain orientation maps for two AC samples

4.2.4 Percentage of fcc and hcp phases

From the EBSD mapping it was possible to obtained phase maps indicating the percentage of fcc and hcp phase contained in each alloy. Three phase maps from a forged and two as cast samples are shown in Figure 4.8a,b and c respectively (Note the different scale for the forged and the as cast samples).

The Forged alloy presented a combination of fcc and hcp phases, while the other examples presented two extremes, an AC sample with a high hcp content and a AC-TT sample with a really low hcp content and a majority of fcc phase. EBDS maps were run on a number of different samples, to obtain fcc and hcp percentages. Results of the fcc-hcp contents are presented in Figure 4.9. The Forged alloy, AC-TT and AC-LC carbon content alloys presented a hcp phase percentage below 10 %, while the AC sample presented a 50 ± 20%hcp content.

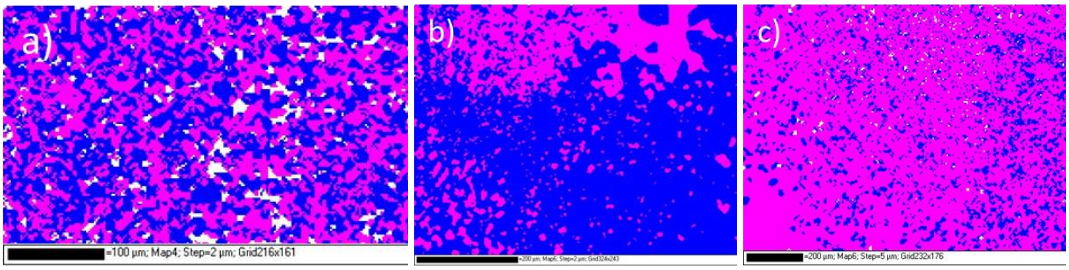

Figure 4.8 EBSD phase maps for: a) Forged, b) AC, c) AC-TT samples. Pink corresponds to fcc phase and blue to hcp phase

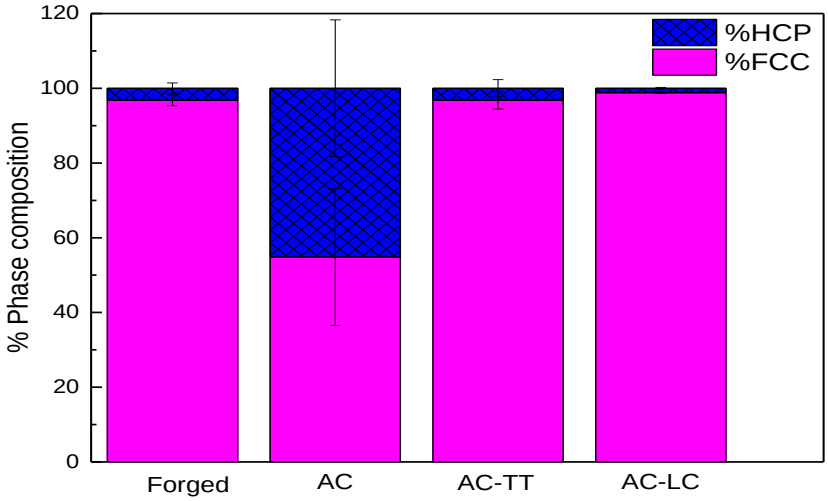

Figure 4.9 Percentage of hcp and fcc phases found in the forged, AC, AC-TT and AC-LC content alloys

4.3 Mechanical properties

4.3.1 Vickers hardness

Vickers hardness values (*HV*) were obtained at two different load levels to compare the micro and macro hardness values and how they influence the hardness measurements. The results are summarised in Table 4.2.

Table 4.2 Micro and macro Vickers Hardness average values and standard deviation for the four CoCrMo alloys

	Vickers Hardness (*HV*)			
Materials	**Micro hardness 1 N**	**Macro hardness 10 N**	**% difference macro-micro *HV***	**% difference After thermal treatments* / carbon content****
Forged	547 ± 49	451 ± 25	-18	
AC	448 ± 50	393 ± 20	-12	
AC -TT	415 ± 29	345 ± 13	-17	-7 *
AC -LC	398 ± 22	316 ± 14	-21	-11 **

The micro and macro hardness followed the same tendency when *HV* values are compared between samples. The Forged alloy showed the highest hardness value of 547 ± 49 HV compared to 448, 415 and 397 HV for the AC, AC-TT and AC-LC respectively, when 1 N load was applied. Although the same decreasing order was shown in the macro test, there was a percentage difference between the micro and the macro scale, showing a reduction in hardness from 17 %, for the forged sample, to 20 %, for the low carbon content as cast alloy. Comparing between the thermal treated and the lower carbon content as cast samples, the hardness values experience a decrease, with a reduction of 7% for the single thermal treated sample and 11% for the low carbon content alloy.

4.3.2 Nanoindentation mapping

Nanoindentation maps give more detailed information about the microstructure of the alloys and how specific elements on the surface or under the surface influence their mechanical properties; see Figure 4.10. The colour legend is individual for each of the alloys, so the same colours correspond to a different range of hardness values for each picture to avoid missing the details in maps with a broader scale. The Forged, Figure 4.10a, and the AC-LC sample, Figure 4.10d, have a more homogenous structure and show less dispersion in the hardness, from 6 GPa to 8 GPa.

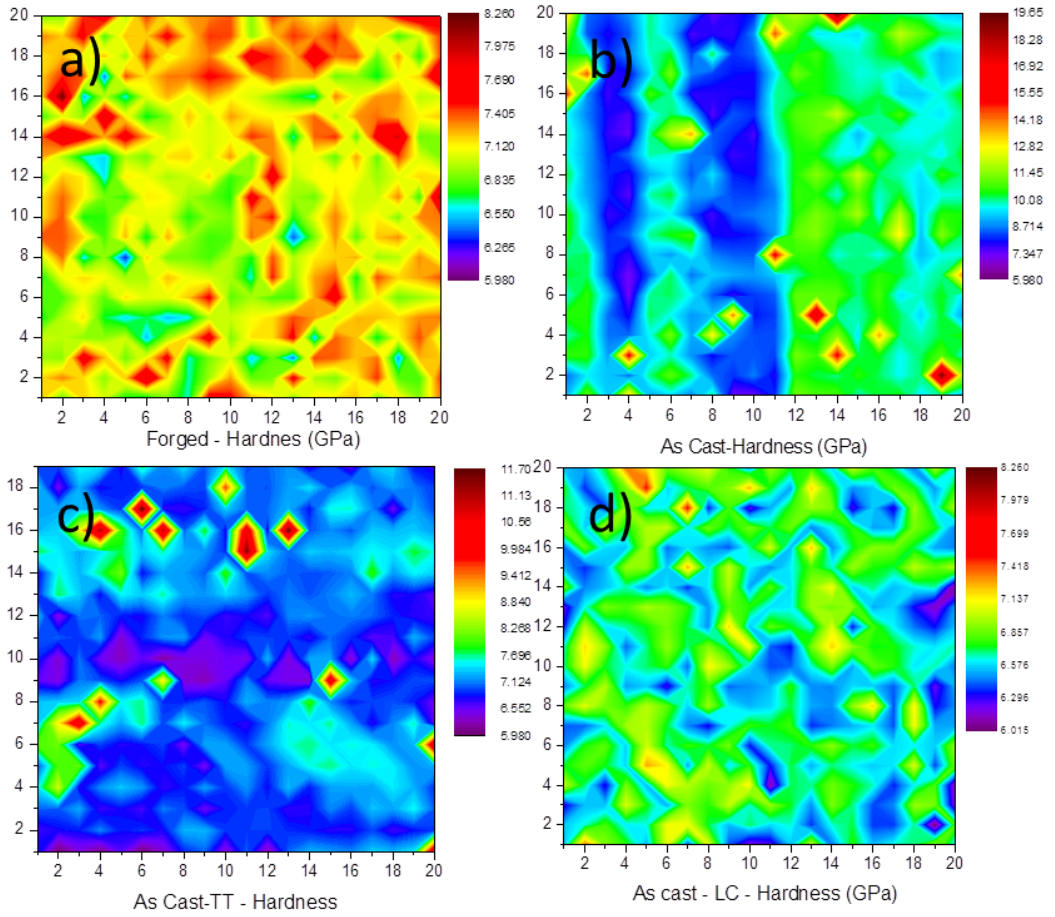

Figure 4.10 Nanoindentation-hardness mapping for the CoCrMo alloys. a) Forged, b) AC c) AC-TT and d) AC-LC

In contrast, the AC and the AC-TT samples exhibited a higher dispersion with peak values corresponding to the red regions, which are related to their carbides and their surrounding areas with, 19 GPa, and 11 GPa for the AC and the AC-TT carbides, respectively.

A summary of the nanoindentation hardness and Young´s modulus for the matrix and the carbides is shown in Table 4.3. The highest matrix hardness values were presented by the AC alloy (9.5 ± 1.1 GPa), followed by the Forged, (7.1 ± 0.3 GPa), with the AC-TT matrix and AC LC displaying no significant difference between them (6.7+/-0.5 and 6.6 +/- 0.3 respectively).Young´s modulus values are not significantly different for the Forged, AC-TT and AC-LC with values between 243 ± 7 to 241 ± 8. The AC sample presented a value 20% higher than the other alloys. Note that the $H_{IT\text{-}nano}$ values for the AC and AC-TT alloys with dispersed carbides, are reflecting a value which is a combination of the

matrix and the carbides mechanical properties. The solid carbides present in the AC alloy also showed a 50% higher hardness and Young´s modulus values when compared to the "fragmented-like" carbides from the AC-TT alloy.

Table 4.3 Summary of the nanoindentation hardness and Young´s modulus values for the alloy's matrix and their correspondent carbides for the AC and the AC-TT alloys

	Nanoindentation	
	***H*IT-nano (GPa)**	***E* (GPa)**
Forged	7.1 ± 0.3	243 ± 7
AC	9.5 ± 1.1	327 ± 22
AC carbide	14 ± 2	366 ± 20
AC-TT	6.7 ± 0.5	243 ± 12
AC-TT carbide	9.4 ± 1.5	263 ± 18
AC-LC	6.6 ± 0.3	241 ± 8

An example of the influence of the hardness of the carbides on their surrounding areas is shown in the dot-mapping below, Figure 4.11. According to the colour scale, the red dot together with the orange and the yellow ones closer to it correspond to the carbides and their influenced area with maximum values around 15 GPa. For the indentation sites further from the carbides, the hardness values decreased to ≈ 7 GPa. A more detailed explanation of the interaction volume of the tip in the material will be discussed in Section 5.3.2.

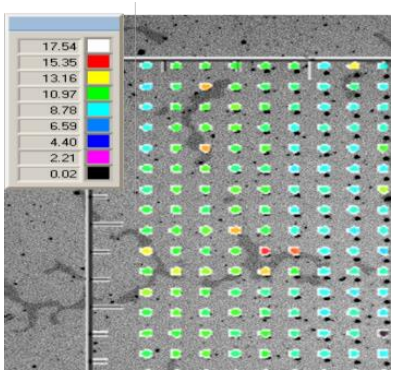

Figure 4.11 Nanoindentation-hardness dot mapping for an AC CoCrMo alloy

Figure 4.12a and Figure 4.12b show individual load-displacement curves from the matrix indents and from the carbide indents respectively for each Co alloy.

The matrix curves demonstrate that the forged and the low carbon content as cast alloy are similar, which corresponds with the similar hardness values described previously and matches with low carbon content alloys as mention in the results discussed in the chemical analysis section, (Section 3.2). The as cast alloy reached the highest load and the steepest slope during the unloading, indicating a higher hardness and modulus value, as it was shown in Table 4.3. Single thermal treated specimens exhibit the lowest load and slope.

Considering the indentation curves obtained from the carbides, it is evident that the thermal treatment has influenced both their morphology and their mechanical properties. The thermal treated carbides showed a significantly different hardness than the carbides without any thermal treatment, which can be related with the morphology and the phases observed in the microstructural study, as discussed in Chapter 3.

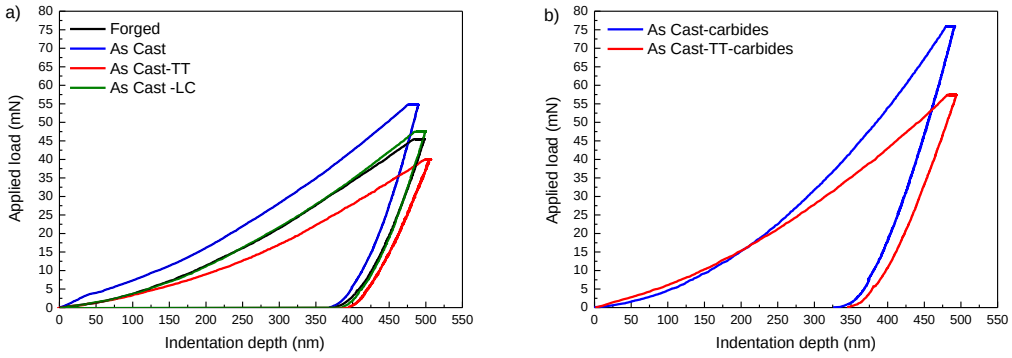

Figure 4.12 Load displacement curves from the nanoindentation tests: a) Comparison between the four CoCrMo alloys matrix values and b) Comparison between the two different carbides found in the AC and the AC-TT samples

Figure 4.13a-b shows the H/E ratio, related with a higher indentation recovery (or deformation relative to yielding) and the H^3/E^2 ratio respectively, which gives information about the resistance to plastic deformation. Both ratios are related and follow the same trends for the four alloys. The carbides with a higher hardness and Young´s modulus exhibit higher H^3/E^2 ratios than their correspondent matrix; e.g. 0.022 versus 0.008 for the as cast samples and 0.012 versus 0.0048 for the as cast thermal treated. Matrix H/E ratio values for all the alloys are ≈ 0.03, with no significant difference between them.

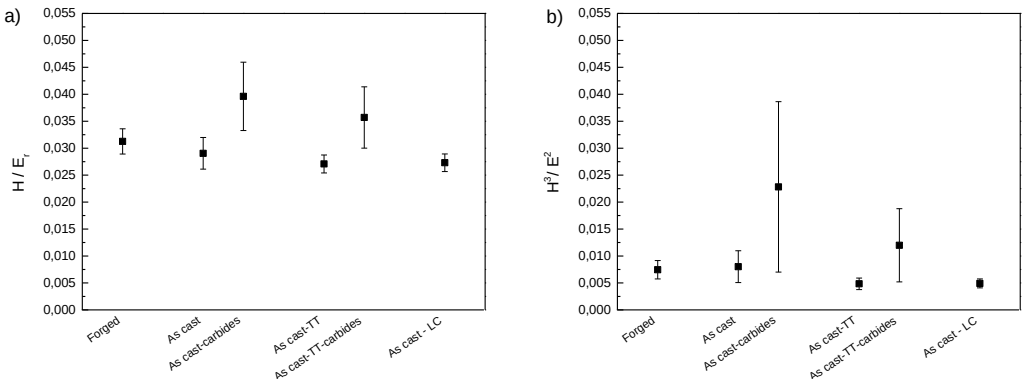

Figure 4.13 Mechanical properties comparison for the CoCrMo alloys and their carbides: a) H/E_r ratio and b) H^3/E^2_r ratio

4.3.3 Vickers and nanoindentation hardness comparison

Micro and macro hardness experiments were converted into H_{IT} measurements to compare them with the results obtained by nanoindentation. Figure 4.14 shows the comparison of the micro, macro and nanoindentation hardness (GPa) values for each of the CoCrMo alloys.

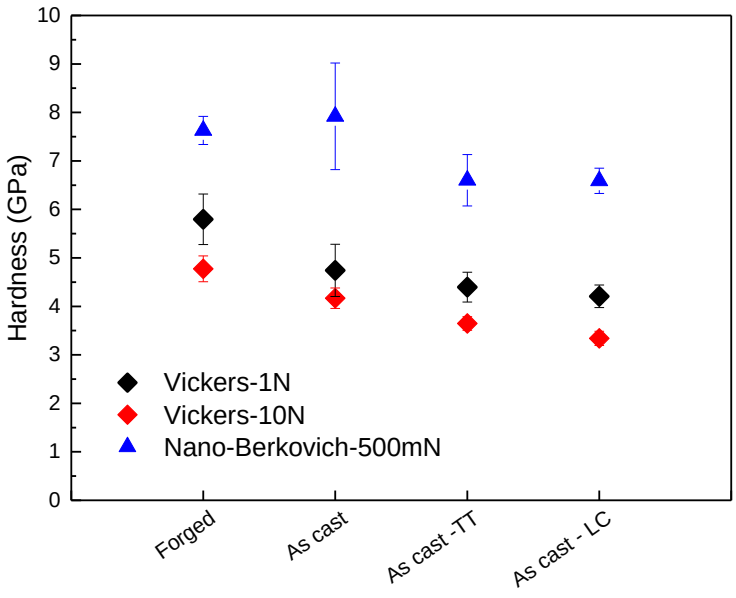

Figure 4.14 Hardness values comparison at the micro, macro and nano scale for the CoCrMo alloys

Because the conversion of the Vickers hardness (*HV*) values to H_{IT} is only related with indenter geometrical considerations, the same trends were observed for the Vickers experiments at the macro and micro scale. The highest hardness value corresponds to the Forged sample followed by the AC, AC-TT and the AC-LC sample, exhibiting values from 6 to 5 GPa and 5 GPa to 3.5 GPa for the micro Vickers tests, and the macro range load respectively. Values for the nanoindentation experiments are approximately 25% higher than the Vickers experiments for all the samples, and vary from 8 GPa for the Forged samples to 7 GPa for the AC-LC sample.

4.4 Static corrosion electrochemical characterization

4.4.1 Open circuit potential

The evolution with time of the OCP values after three hours immersion at 37°C in 0.9 % NaCl solution in 3 representative samples for each of the four CoCrMo alloys are shown in Figure 4.15. The curves shifted continuously towards more positive values with time which indicates the spontaneous formation of a passivation layer on the metal surface. Steady state was reached for all the alloys after 6000 s. More negative OCP values, -0.2V were shown by the Forged alloy, compared to the As Cast alloys for which the values were -0.12, -0.06 and -0.08 for the AC, AC-TT and AC-LC respectively. All values referenced versus an Ag/AgCl electrode.

Figure 4.16 shows the comparison between the OCP values of each of the alloys with respect to their carbon content. The AC specimens, having a less homogenous carbide dispersion within different samples, showed a higher dispersion in the data when compared to the rest of the samples with more homogenous microstructures. AC-LC and AC-TT with 0.06 and 0.591 % of carbon presented more anodic OCP values of -0.075 and -0.8 V while the AC alloy was -0.116 V with a percentage carbon content of 0.297. Finally the Forged alloy, although with similar carbon content as the AC-LC alloy, of 0.04 % in weight, registers the more cathodic potential among all the CoCrMo samples.

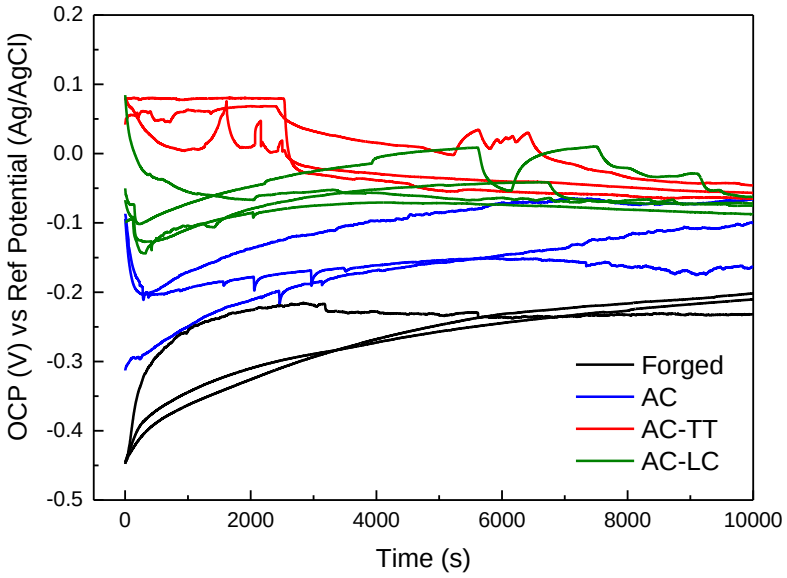

Figure 4.15 Open circuit potential curves for the four alloys

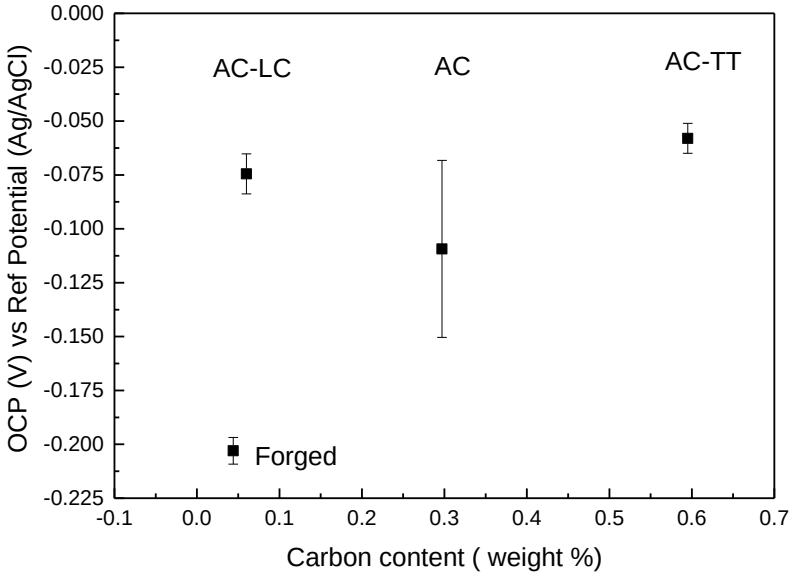

Figure 4.16 OCP values comparison after 3 hours immersion

4.4.2 Potentiodynamic polarization

Figure 4.17 represents the characteristic polarization curves shown by the Forged, AC, AC-TT and AC-LC alloys after 3 hours immersion using a potential range from -0.5 to + 1 V with respect to the E_{corr}. An E_{corr} shift was clearly shown from a more negative value for the Forged alloys (0.244), towards more positive values for the AC (0.209), AC-TT (0.110) and AC-LC (0.06) respectively, in agreement with the values obtained from the OCP experiments.

Three typical potential domains and the beginning of the transpassive domain can be observed in all the curves. The cathodic domain comprises the potential range 0.250V below E_{corr} for each of the samples, where the current is negative as a consequence of the cathodic reactions taking place on the CoCrMo surface: the reduction of water and the reduction of the oxygen molecules which should be adsorbed on the metal surface to react. The cathodic polarization branch corresponds to the oxygen reduction. The Forged sample is shifted towards more negative potentials than the AC, AC-TT and AC-LC. The second potential domain is characterised by the transition from cathodic to anodic currents at the E_{corr}. The third domain corresponds to the passive range where current is usually constant due to the oxide layer formation. Finally, the beginning of the transpassive domain shown by the shoulder between 0.6 to 0.7 V, which is usually characterised by the increase in current due to the transpassive dissolution of the chromium oxide as well as water oxidation.

The average electrochemical parameters extracted from the polarization curves, as described in Section 3.4 where possible, of at least 4 samples of each alloys, are listed in Table 4.4*:* E_{corr}, i_{corr}, R_p , corrosion rate, E_b and i_p,. The Forged alloy presented the lowest E_{corr} value, -0.244, followed by the AC sample, -0.209, with no significant difference between the AC-LC and AC-TT samples with values of -0.128 and -0.110 respectively. Although there was big difference in the carbon content between the AC-LC and AC-TT, they presented more anodic potential.

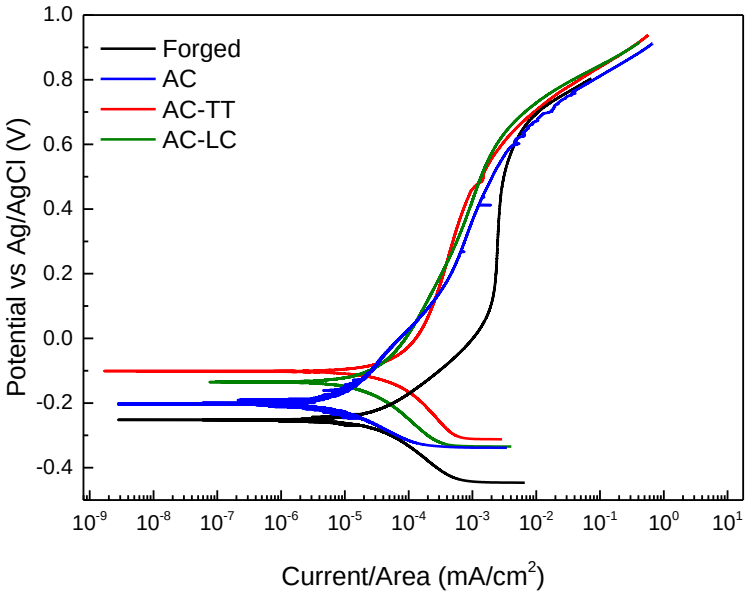

Figure 4.17 Representative polarization curves for each of the four CoCrMo alloys tested after 3 hours immersed in NaCl under a potential range from -0.5 to +1 V respect E_{corr}

Table 4.4 Potentiodynamic parameters obtained from the polarization curves for the four CoCrMo alloys, ordered by increasing carbon carbon content under a potential range from -0.5 to +1 V respect E_{corr}

	Forged	AC-LC	AC	AC-TT
Carbon content (wt %)	0.044	0.06	0.297	0.595
E_{corr} (V/AgAgCl)	-0.244±0.007	-0.128±0.01	-0.209±0.01	-0.110±0.007
i_{corr} x 10^{-2} (μA/cm²)	4.14±1.1	2.22±0.3	0.7±0.3	3.02±1.8
Rp x 10^{6} Ohm	3.55±0.8			
C. Rate x 10^{-4} (mm/y)	4.18±0.6	2.26±0.1	0.82±0.06	3.08±1.2
E_b (mV)	0.63±0.02	0.69±0.02	0.65±0.01	0.71±0.003
i_p (μA)	0.71±0.2			

values than the AC sample which is coincident with the results reported from the OCP experiments.

The more noble the E_{corr}, or the less negative the E_{corr} value, and the lower the i_{corr} value the higher the corrosion resistance of the alloy. The AC-TT and AC-LC alloys showed really similar corrosion potentials, -110 mV and -128 mV, and corrosion currents, $3.02 \cdot 10^{-2}$ and $2.22 \cdot 10^{-2}$ μA/cm² respectively. The Forged alloy

presented the worst corrosion behaviour with the more cathodic potential equal to -244 mV and the highest i_{corr} of $4.14 \cdot 10^{-2}$ μA/cm². Intermediate corrosion behaviour was displayed by the AC alloy with an E_{corr} value of -209 mV and the lowest i_{corr} of $0.7 \cdot 10^{-2}$ μA/cm².

A passivating limiting current equal to 0.71 ± 0.2 μA, i_p, was found for the Forged alloys, indicating a mass-transfer control behaviour. While As Cast alloys did not show it and a mixed-mode (charge + mass) control was observed in the cathodic passive region. The beginning of the transpassive region started between 0.65 to 0.7 V for the four alloys.

The corrosion rates, (mm/ year), were calculated for the four alloys. The forged alloy showed the highest value, $4.18 \cdot 10^{-4}$ mm/y, compared to the As cast alloys. The AC samples presented the lowest corrosion rate, $0.82 \cdot 10^{-4}$ mm/year while the AC-TT and the AC-LC alloy with $2.26 \cdot 10^{-4}$and $2.7 \cdot 10^{-4}$ mm/year presented similar values between them, higher than the AC alloy, but still better than the Forged samples.

Figure 4.18 shows the polarization curves for the four CoCrMo alloys after being immersed for 24 hours and applying a potential range of -2 to 2V from E_{corr}. The electrochemical parameters, E_{corr}, i_p and Corrosion rate are listed in Table 4.5. No differences were found in the E_{corr} values between the four samples with a value equal to -0.953 V respect the Ag/AgCl reference electrode. Tafel analysis was not appropriate in this case due to the lack of linearity of the anodic branch. Therefore a i_p value was obtained from the intersection of the horizontal line matching the E_{corr} value and the vertical line defined by the limiting current observed in the anodic region. The current values were, 6.8, 10, 35 and 14 μA/cm² for the Forged, AC, AC-TT and AC-LC samples respectively. While corrosion rates were 0.07, 0.10, 0.36 and 0.14 mm/year for the Forged, AC, AC-TT and AC-LC specimens.

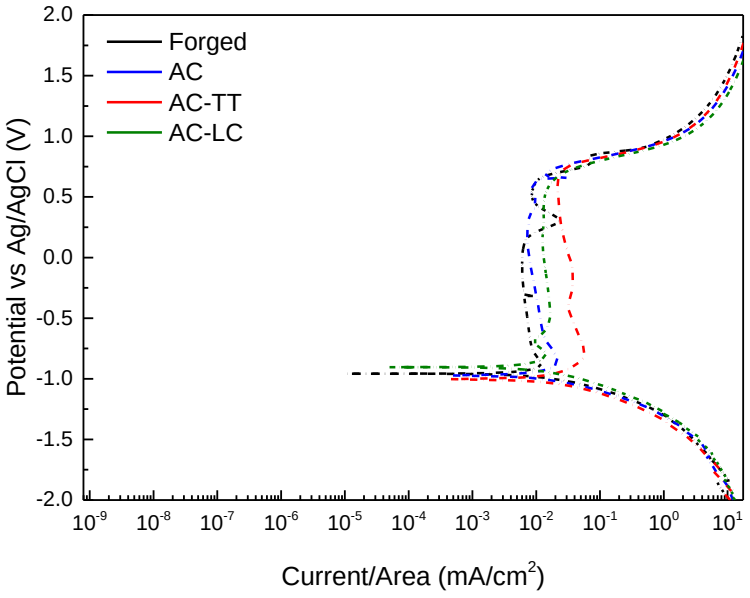

Figure 4.18 Representative polarization curves for each of the four CoCrMo alloys tested after 3 hours immersed in NaCl under a potential range from -2 to +2 V respect E_{corr}

Table 4.5 Potentiodynamic parameters obtained from the polarization curves for the four CoCrMo alloys, ordered by increasing carbon carbon content under a potential range from -2 to +2 V respect E_{corr}

	Forged	AC-LC	AC	AC-TT
Carbon content (w %)	0.044	0.06	0.297	0.595
E_{corr} (V/AgAgCl)	-0.926	-0.898	-0.954	-0.988
i_{corr}-i_p (μA/cm²)	6.8	14	10	35
C.Rate (mm/y)	0.07	0.14	0.10	0.36

After PD experiments from -2/+2V, micrographs from the surfaces revealed that dissolution starts in the matrix surrounding the carbides and from surface defects or grain boundaries. A pitted microstructure was observed for the Forged alloy, Figure 4.19a, while AC and AC-TT alloys presented preferential dissolution around the carbides and at the grain boundaries. The AC-LC sample revealed the least signs of corrosion of the three As Cast samples although some pits can still be recognized on the surface, Figure 4.19d. PD experiments from -0.5/+1V did not revealed any apparent changes in the microstructures.

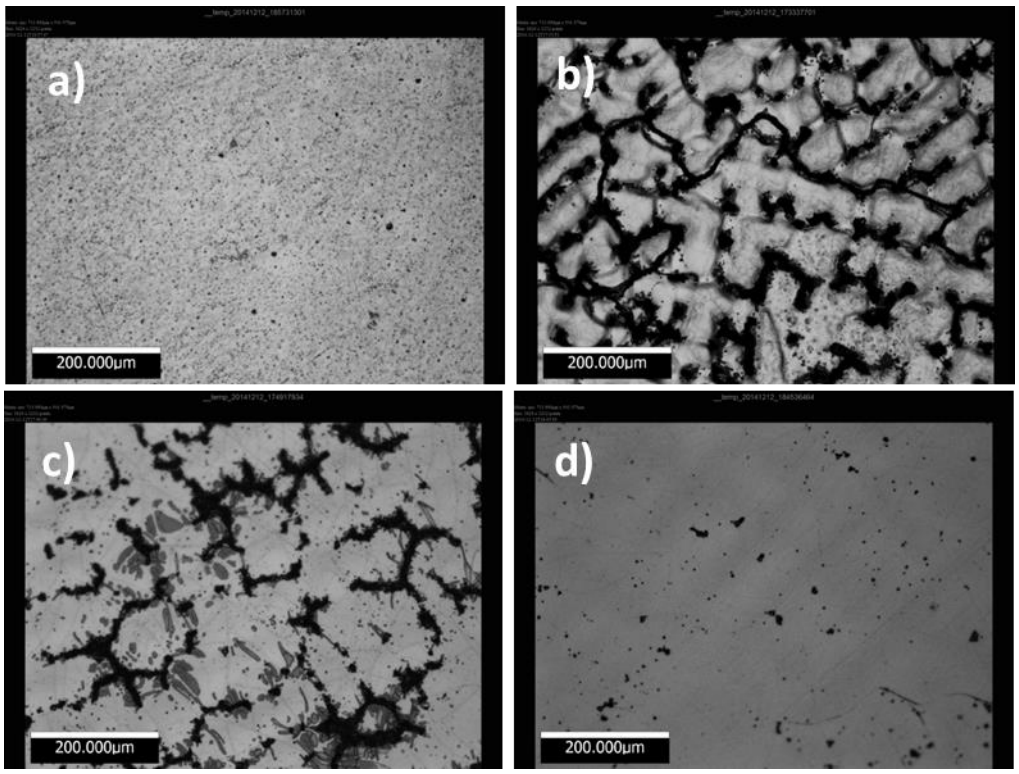

Figure 4.19 Optical pictures of the CoCrMo alloys after 24 hours immersion in 0.9 % NaCl solution and after a potentiodynamic polarization test between -2V to +2V: a) Forged, b) AC, c) AC-TT and d) AC-LC

4.4.3 Grain size influence in forged samples

Several samples from the Forged femoral stem were used for the static corrosion testing, however a bimodal distribution was noted in the results. It was found that the microstructure was not homogenous along the length of the femoral stem. The different microstructures are shown in Figure 4.20. On the left side, the microstructure of the samples obtained from the upper part of the femoral stem, on the right the microstructure from the lower part of the stem. The grain size was determined and showed the samples from the top of the stem to have a grain size between 10-15 µm while the samples from lower down had a grain size between 20-25 µm. Twinning within the grains was clearly identified in both locations.

Potentiodynamic parameters obtained from the polarization curves for the two locations within the femoral stem are summarised in Table 4.6 and two representative potentiodynamic curves for each location are plotted in Figure 4.21.

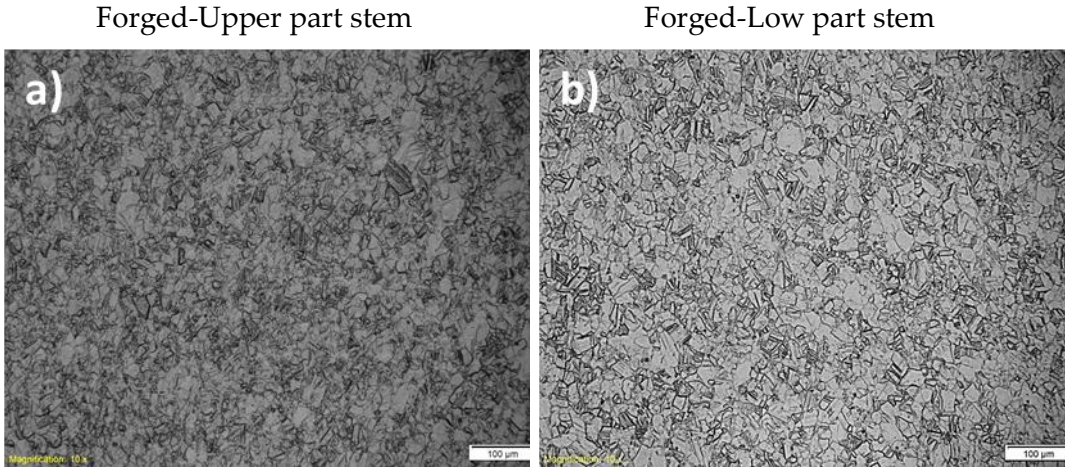

Figure 4.20 Optical pictures showing the microstructure along the Forged femoral stem: a) Upper part and b) Lower part

E_{corr} values in the lower location, coarse grain size, were 50 % more anodic than in the upper location, fine grain size. i_{corr} for the area with finer grain size was $4.14 \cdot 10^{-2}$ µA/cm^2 while for the coarser grain size it was $1.60 \cdot 10^{-2}$ µA/cm^2 . The corrosion rate values were five times higher in the upper/small grain sized location than in the lower/larger grain sized region. During the passivation domain, the small grain size resulted in a clear breakdown potential and the current remained constant just before the beginning of the transpassive region with a passivation current equal to 0.71±0.2 µA indicating a mass transfer control behaviour. In contrast, the larger grain sized samples, presented a linear increase during the passivation region, reaching the breakdown potential at 0.6 V and exhibiting a mixed control behaviour (mass-charge transfer).

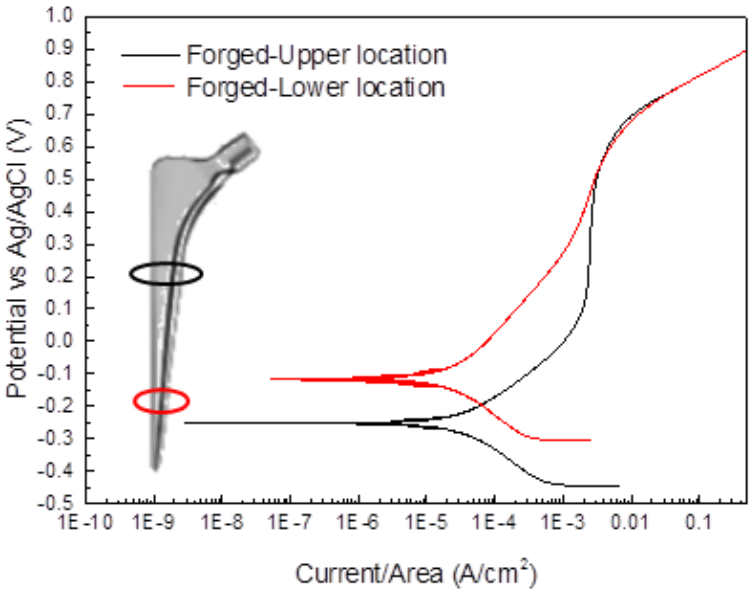

Figure 4.21 Potentiodynamic curves of the Forged samples in two different locations within the femoral stem

Table 4.6 Potentiodynamic parameters obtained from the polarization curves for the two Forged microstructures found within the same femoral stem

	Forged Small Grained	Forged Large Grained
E_{corr} (V/AgAgCl)	-0.244 ± 0.007	-0.114 ± 0.001
i_{corr} x 10^{-2} (μA/cm²)	4.14 ± 0.6	1.60 ± 0.05
R_p x 10^6 Ohm	3.55 ± 0.8	10.20 ± 3.49
C. Rate x 10^{-4} (mm/y)	4.18 ± 0.62	1.64 ± 0.545
E_b (mV)	0.63 ± 0.03	0.65 ± 0.02
i_px 10^{-2}(μA)	0.71 ± 0.2	

4.5 Discussion

4.5.1 Microstructural characterization

4.5.1.1 Chemical composition and carbon content

The four alloys being studied presented similar percentages of the main elements: Co, Mo and Cr, as mentioned in Table 4.1. The alloying elements have different purposes or impart properties to the alloy. Cr, Mo, W and Si all stabilize the hcp phase, whereas Fe, Mn, Ni and C stabilize the fcc phase. Cr also plays an important role in the formation of carbides (M_7C_3 and/or $M_{23}C_6$), and forms the main oxide in the oxide film providing the alloy with its surface oxidation and corrosion resistance. Mo contributes to solid solution strengthening and increases abrasion resistance [202]. In addition higher carbon content alloys have been proved to provide better wear resistance in as cast-as cast pairings rather than forged-forged pairings [120].

The CoCrMo matrix in the four alloys was found to be a single phase solid solution (in the Forged and AC-LC samples) with carbide precipitates for the AC and the AC-TT samples. However, although specific chemical analysis of the carbides was not an aim of this study, the lamellar components shown in Figure 4.5 for the AC alloy is consistent with what was reported by other authors to be formed of interlayered plates of $M_{23}C_6$ and a second phase which has not been properly identified yet [64, 65]. Weeton et al [206] suggested it could be σ phase, while Silverman et al [207] proposed a combination of σ and α phases. The third option described by Sims et al [208] was α or M_6C phases. Dobbs and Robertson [121], suggested that the lamellar constituent was the most detrimental feature of the microstructure and when it is removed by heat treatment, tensile strength, ductility and fatigue life can be improved.

The AC-TT sample presented single phase ($M_{23}C_6$) homogenous carbides, in agreement with [209], and the AC-LC sample did not show almost any. It is known that carbon content and cooling rate during the casting process affects the distribution of carbides and their chemical composition. Ramírez-Vidaurri et al. [210] observed that the amount of blocky carbides and eutectic constituents are considerably increased when the carbon content is also increased. It was also noted that the size of the carbides decreased as the cooling rate increased.

4.5.1.2 Grain size

The 20-30 μm sized grains, exhibiting multiple crystallographic orientations presented by the forged alloy, matches an annealed wrought low carbon

CoCrMo from previous works [211]. The carbides usually precipitate at the grain boundaries of forged alloys, however depending on the manufacturing process they might be refined and dissolved in the Co matrix as has happened in the forged alloy under study where no carbides were observed. Annealing is also confirmed by the presence of annealing twins and stacking faults in some of the grains.

The as cast grain sizes and observed microstructures matched with previous studies on different as cast Co based alloy as described in [63] , with large grain sizes between 2540 and 3394 μm and similar carbides morphologies, as discussed in Section 4.2.3.

Grain size and grain boundaries are of great importance to the mechanical properties and deformation mechanisms of the alloy. Grain boundaries act as obstacles for dislocation movement, therefore smaller grain sizes, as in the Forged alloy, increases the number of grain boundaries reducing the ease of dislocation motion and increasing the yield stress. According to the Hall-Petch equation [212, 213], there is an inverse relationship between grain size and yield strength where mechanical properties improve when the alloy presents a smaller grain size. The critical grain size below which the properties are not enhanced anymore is reached when the dislocation size approaches the grain size and the applied stresses are released by grain boundary sliding instead of dislocation movement resulting in yield strength decrease.

4.5.1.3 Phases presented: fcc and hcp

Fcc and hcp phases were found in the four CoCrMo alloys analysed in this study. As expected, the fcc crystallographic structure was the predominant one, except for the AC alloy where the hcp structure showed a significant percentage as well. The fcc crystal structure is metastable at ambient temperature and the fcc → hcp transformation is really slow to happen unless it is forced during the manufacturing process. The percentage of fcc and hcp phases can affect the mechanical properties and wear resistance of CoCrMo alloys as discussed by Saldivar-Garcia and Lopez [214]. Their results investigated the wear resistance and hardness of as cast and forged alloys with different percentages of fcc and hcp. When they were coupled during wear experiments they noted an increase in wear resistance for the pairings possessing a higher percentage of hcp matrix microstructure compared to the ones presenting a majority of fcc matrix.

Besides the manufacturing process, the fcc to hcp crystal structure transformation can be achieved by 3 ways: athermal, isothermal or strain induced transformation (SIT)[80], the last one the most predominant one in the alloys under study.

Therefore, the deformation behaviour of Co based alloys will be influenced by the fcc-hcp content of the alloys under study.

Carbon is a fcc stabilizer, so lower carbon alloys are more prone to SIT and more likely to transform to the hcp crystal structure.

4.5.2 Mechanical properties

4.5.2.1 Vickers hardness

The observed differences in indentation response are in agreement with previous reports where forged alloys are harder than as cast alloys [142] [215]. The highest *HV* value shown by the Forged sample might be due to its more homogenous structure and its smaller grain size (around 20 μm) compared to the as cast alloys (around 1000 μm), as discussed in Sections 4.2.2 and 4.2.3. The lower hardness in the As Cast samples could be attributed to the dissolution of the carbides in the matrix caused by the thermal treatment in the AC-TT sample, [121, 216], and because of the lower carbon content in the AC-LC sample [209, 217]. The difference in carbide size in comparison to the indentation size also had an influence. The indentation diagonal distance for the micro indentation experiments is around 20 μm which is bigger than the typical carbide size in the AC and AC-TT alloys. Therefore, indentations are not able to differentiate between the hardness contributions from carbide and metal matrix phases and the results are a combination of the matrix and carbides mechanical properties, as shown in Figure 4.22 where it is reflected the volume of material tested respect to the carbides size.

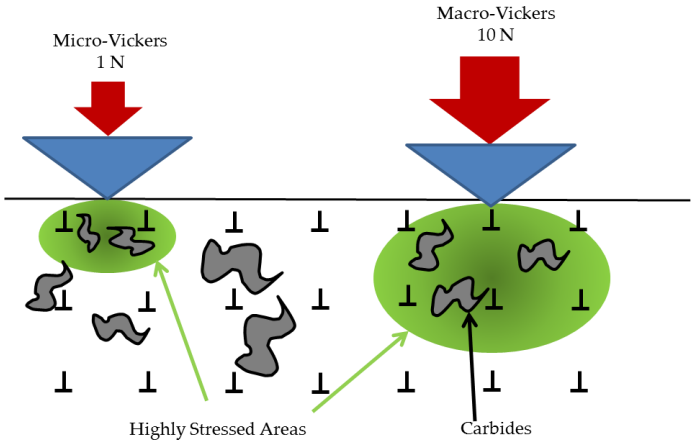

Figure 4.22 Volume interaction between micro and macro Vickers experiments respect to the carbide size in AC and AC-TT alloys

4.5.2.2 *Nanoindentation*

Values displayed in Table 4.3 are in agreement with values from previous literature, with higher hardness for the Forged alloys than As Cast alloys. Liao et al. [142] obtained values of 9.4 GPa and 6.4 GPa for wrought and as cast alloys respectively. They also reported hardness measurements on specific carbides with values of 15.7 GPa for carbides in the as cast alloy and and 30.7 GPa in the wrought alloy carbides. Similar values were also described in the work by Stemmer et al. [215] whereas cast alloys with different manufacturing processes (as cast, as cast + hot isostatic pressure and as cast + annealing) were evaluated. Carbides hardness oscillated between 14 to 19 GPa, intermediate hard phases oscillated between 8 and 11 GPa and the matrix was 7.3 GPa.

The scale at which nanoindentation experiments are done is small enough to differentiate between mechanical properties of the matrix and the carbides in the as cast alloys. The volume of material affected is in the range of the carbide size and therefore it is possible to indent over them, see Figure 4.23. Moreover, the carbide network is 3D, so some of the indents can land in a "carbide-free" area on the surface but with subsurface carbides below, as in Figure 4.23b, overestimating the hardness values of the matrix, as happens with the matrix hardness of the As Cast sample (9.5 GPa) which as a result appeared to be higher than the Forged alloy (7.1 GPa).

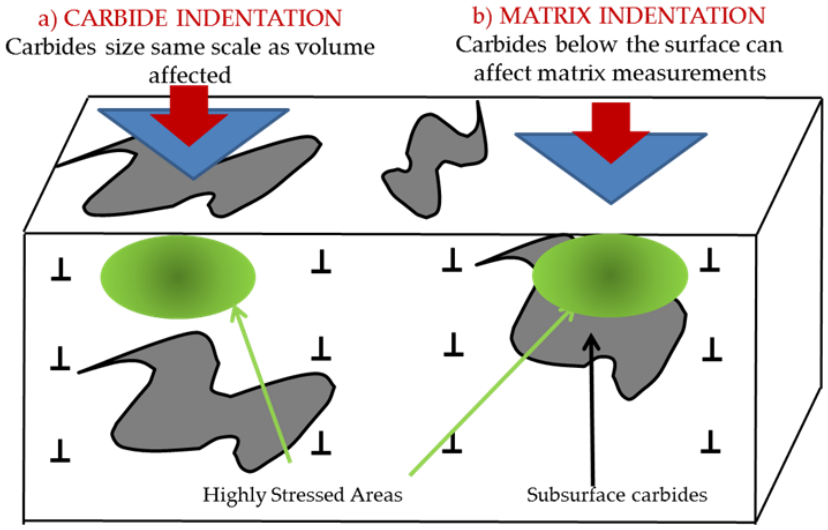

Figure 4.23 Schematics of how nanoindentation values are affected by: a) Indenter landing in surface carbide, b) Indenter landing in the matrix with subsurface carbides

The carbide morphology, bulky for the AC samples and fragmented for the AC-TT, influenced the results. The more irregular shape of the AC-TT sample led to

lower values especially if the indenter landed on the edge of the carbide or if the carbide was not well-supported by the underlying matrix. Also the different phases found in the carbides were related. AC carbides presented a lamellar structure formed by the γ phase, intermetallic σ phase and $M_{23}C_6$ carbides while the AC-TT carbides are formed by a single $M_{23}C_6$ carbide phase [22, 206, 218].

4.5.2.3 Comparison between techniques

Comparison of the values between techniques demonstrates an inverse relation between the applied load and the hardness, lower hardness values being obtained with higher loads. With a 1N load the residual impression generated on the surface is smaller compared to the impression left for the 10 N load, therefore the diagonal lengths are underestimated giving an increase in the hardness. The scatter in the nanoindentation experiments is attributed to the interaction between the indentation tip and the microstructure of the samples. In nanoindentation experiments the geometry of the Berkovich tip allows the system to spot individual features such as carbides or areas around the carbides where hardness values vary from those of the matrix. Although for the calculation of the average nanohardness these specific points have been removed there is still the presence of regions where subsurface carbides have influenced the matrix hardness results and increased the dispersion of the measurements. Thus, the as cast sample, with a higher surface area covered by the bulky carbides and a less homogeneous microstructure presented the highest dispersion in the nanoindentation values.

The increase of hardness in the nanoindentation experiments with respect to the Vickers experiments is related to the method used to calculate the hardness. In nanoindentation the projected area of the indenter is measured indirectly from the depth measurement while in Vickers experiments the area of the residual impression is used. In addition the indentation size effect (ISE) mentioned previously in different works, [219], where higher hardness values are reported when lower loads are applied during the indentation experiments can play a role in the differences found between hardness values. The ISE was confirmed by nanoindentation experiments run under a depth range from 5 to 1000 nm in a Forged and an AC-TT samples, as is shown in Figure 4.24. However, the nanoindentation experiments discussed in the chapter were measured at 500 nm depth; therefore the depth used is above any major influence of the observed ISE.

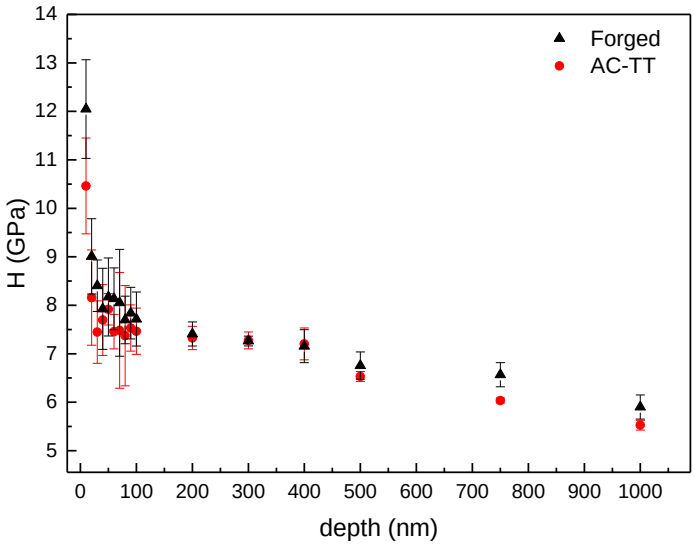

Figure 4.24 Indentation size effect in two different CoCrMo alloys

Depending on the applied loads, the stress field interactions with the defects in the material will be higher, see Figure 4.25. If indentation depth is increased because load is increased, the volume of material tested contains more dislocations and the hardness results will be affected by the ISE, showing lower hardness for higher depths. When the size of the indented volume becomes comparable with the distance between dislocations, e.g. nanoindentation, fewer dislocations are present and the average contact stress to produce plastic flow should be higher, resulting in higher hardness values.

4.5.2.4 Hardness to Young´s modulus ratios

Previous works reported the *H/E* ratio as a more suitable parameter for predicting the wear resistance than hardness alone, especially for hard metallic coatings, [220, 221].

From the results obtained, and considering the values corresponding to the matrix, without the carbides, the ratio value did not show a statistical difference between the alloys, thus considering the bulk material, there will not be differences in terms of plasticity for the alloys. However, both type of carbides showed a higher indentation recovery and greater resistance to plastic deformation when compared to the matrix.

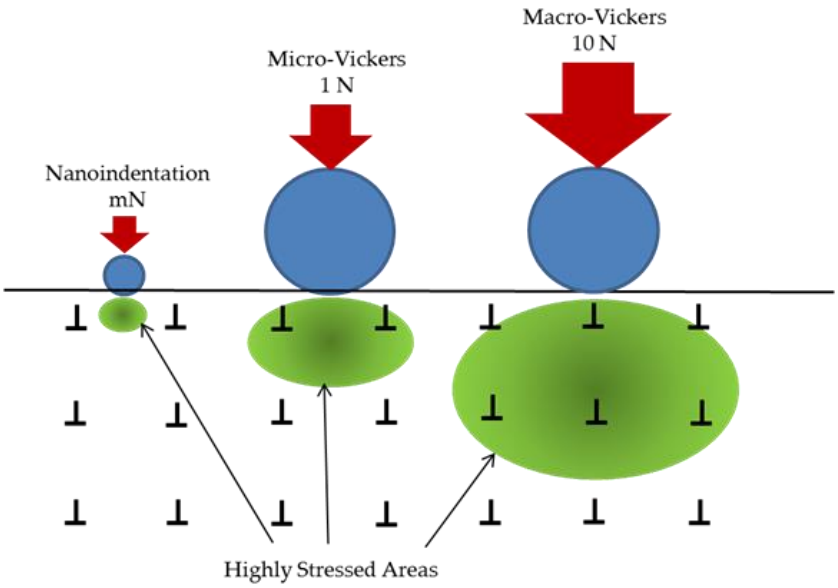

Figure 4.25 Stress field interactions with defects under different loading conditions

4.5.3 Static corrosion electrochemical characterization

The main corrosion mechanism in CoCrMo alloys is through passive dissolution, which means the dissolution of metal ions migrating through the passivating oxide layer. This mechanism is usually affected by the chemical environment [222] and the applied potential [223]. Studies from retrieved implants [16] and also in vitro studies [46], suggest that the passive film formed on CoCrMo alloys consists essentially of Cr_3O_2 that significantly slows the corrosion rate.

The double layer created in NaCl solutions is formed by the surface oxide film and the adsorption/desorption of hydrogen. After 3 hours duration immersion experiments, the newly created oxide/hydroxide film acted as a physical barrier which hindered further metal dissolution and improved the CoCrMo corrosion performance. During the formation of this passive film, chromium was oxidised and formed the main constituent of the passive layer while an oxidised cobalt dissolved and migrated into the solution [46, 224]. The reason for Co migration into the solution is mainly due the thermodynamic stability of the species with the interface where Co is more prone to dissolved than Cr. Molybdenum dissolution is very dependent on the presence of proteins [225]. Molybdenum deposits were only found in corrosion experiments where proteins were involved due to the interactions between Mo (VI) ions and the proteins resulting in protein deposition on the surfaces [156]. The passive film of the CoCrMo alloys is mainly formed of Cr_2O_3 with a minor content of other Co and Mo oxides [28, 36, 46],

therefore the corrosion resistance of the CoCrMo alloy is a result of the oxide layer stability.

OCP values for the As Cast sample a after stabilization time of 3 hours were -0.112 mV in agreement with results from Sun et al. [30, 39], -0.166 mV, using the same alloy with similar carbon content, pH and temperature conditions and slightly more anodic compared to results from Vidal et al. [39], -196 mV. The same difference was observed when comparing the AC-LC alloy OCP value, -75 mV, with the results from Yan et al. [50] reporting -280mV after 5 minutes immersion in a 0.36% NaCl solution or Muñoz et al. [36] who reported a value of -390 mV (vs SCE electrode) and 1 hour immersion test. Comparing the Forged alloy, the more cathodic OCP potential, -200 mV, compared to -300 mV and -400 mV reported by Hogdson and Petrov [56, 226]. In general the discrepancies between the values reported here and in the literature are due to the variety of experimental conditions. In most cases the alloys do not have the same carbon content, the environmental conditions differed greatly (especially when the solution contains proteins or phosphates) and the immersion times are too short to reach the stabilization time compared to the results presented here.

Although outside of the scope of this study, it has been shown that different proteins and phosphate ion concentrations can explain the different corrosion behaviour when bovine serum or PBS is used as electrolyte solution to model the body environment [36, 227] enhancing the corrosion resistance on the alloys.

E_{corr} was determined according to the mixed potential theory, where the anodic dissolution current is equal to the cathodic reduction current. The differences found between the alloys can be attributed to differences in the oxygen reduction reaction or in the anodic dissolution of the alloy. The Forged alloy presented the most cathodic E_{corr} and OCP values. This is related to the higher reactivity of the surface in contact with the electrolyte when compared to the As Cast samples, due mainly to their finer grain size, as was described by Bettini and Hiromoto [56, 57]. They found that grain boundaries and interfaces between the matrix and the carbides can play an active role in the dissolution process. They act as preferential zones to corrode the alloy due to the Cr gradient created from the carbides towards the matrix contact surface forming a galvanic cell between the carbide and the matrix. The increase of grain boundaries due to grain refinement can accelerate the anodic reaction reducing the protectiveness of the passive film on the alloy leading to the negative shift of their OCP, as was reported in Section 4.4.1 when comparing sections at different locations of the Forged femoral stem, see Figure 4.23. In addition any precipitates at the grain boundaries can form localised defects in the passive film that could also cause a decrease in E_{corr}.

Comparison between the As Cast alloys suggests that the presence of bulky carbides in the matrix altered the reactions occurring on the surface, decreasing the potential to more negative values. The samples with a lower percentage of carbides per unit area, AC-TT, or without any carbides in the surface, AC-LC, reacted less and presented more anodic potentials. In agreement with previous work, [19], the presence of precipitates and the percentage area covering the matrix can act as galvanic cells between the carbides and the matrix decreasing the E_{corr} values.

The more anodic the E_{corr} values the higher the enhancement of the passive behaviour with aging of the passive film. This increase in corrosion resistance is due to passive film growth, changes in the film composition and to changes in passive film structure. The processes occurring between the electrolyte and the metal surface can change the surface chemistry of the CoCrMo and affect the surface potential over time, as was reported by Hodgson et al. [46] where they found that E_{corr} values were shifted from -500 mV to -50 mV when the immersion time was increased from 14 minutes to 18 hours.

The potential and current differences showed in static conditions, Section 4.4.2, revealed that the potential differences (130 mV) are enough to provide the thermodynamic force to produce a galvanic cell between two different types of CoCrMo alloys: Forged and As cast. In Figure 4.26 is shown a simplified Evans diagram and how their respective E_{corr} and i_{corr} values would evolve to the mixed corrosion potential (E_{mixed}) and current (i_{mixed}). Any of the As Cast alloys would anodically polarise the Forged CoCrMo alloy, shifting the corrosion current to higher values and therefore increasing the rate of oxidation within the interface due to the large potential differences stablished between both. The relevance of galvanic corrosion does not affect only the coupling of dissimilar metals such as Co and Ti alloys as reported by Bryant [43], but also as in the case of mixing same base alloys (CoCrMo) with different microstructures and manufacturing processes. Or even as was discussed by Mischler [103] when active and passive regions are found on a material when it is subjected to tribological conditions creating a galvanic cell between the damage-depassivated area and the unworn area around the wear track, as will be discussed in Chapter 6.

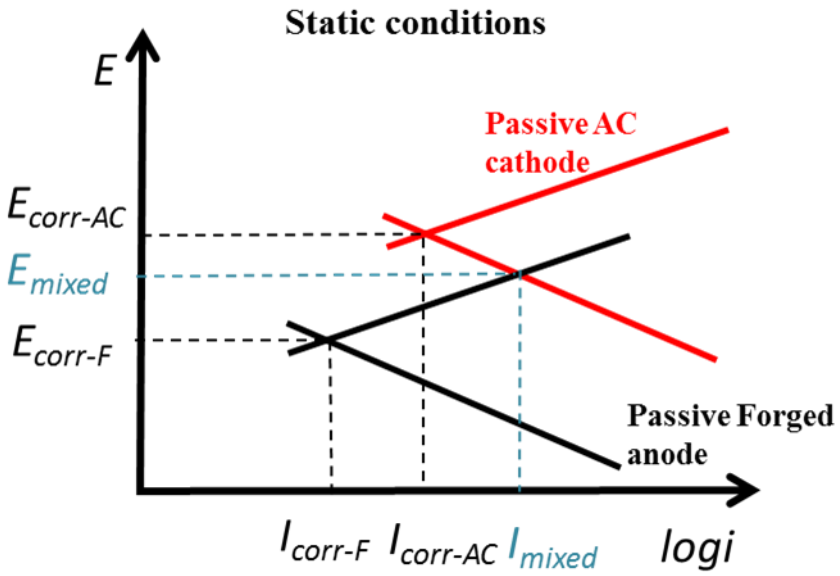

Figure 4.26 Simplified Evans diagrams demonstrating the coupling of a Forged and As Cast CoCrMo alloys

When a metallic sample is immersed in a NaCl solution, water molecules bind to the metallic/passive film interface. Cl^- and Na^+ inorganic ions can interfere with this process [28, 228]. When the charged ions interacting with the surface reach a stable state, the reactions between the surface and the electrolyte stabilize. Depending on the thickness of the passive film it might inhibit the charge transfer and the mass transport processes which is supported by the more anodic E_{corr} values and the i_p limiting current shown in the PD experiments where cathodic cleaning was produced.

During the passivation region, the Forged alloy had a limiting constant I_p value until E_b was achieved; indicating the oxide layer formed was of constant thickness and the processes were under mass transfer control. In contrast, the As Cast samples showed a linear decrease of the *Ip* current during the passivation region until E_b suggesting the oxide layer kept increasing in thickness and is governed only by a mixed transfer control process. The breakdown potential values, 0.7 V, were not significantly different between the samples, indicating that neither the microstructure nor the carbon content influenced the point at which the transpassive region started [46].

The final transpassive region was not studied because the PD experiments did not overpass potentials over 1 V as these potentials are never going to be reached by these alloys in their service environment. However, the initial value of the shoulder, around 0.6-0.7 V, is in agreement with previous works which observed

similar values [19, 28, 45] for the starting potential of the transpassive region. The increase of current at this point, which is related with the oxidation of Cr (III) to Cr (VI) [28, 46] was found to activate the surface causing transpassive dissolution of the passive surface [29]. This behaviour was also noticed in pure chromium [224, 229]. However, the comparison between corrosion behaviour of pure elements and alloys should be interpreted carefully, since the interaction between different elements within the alloy can also have an influence in the final result.

For the PD experiments from -2V to +2V, the cathodic processes occurring in the metallic surface are governed by different mechanisms than the ones starting at a less negative potential. At -2V, a cathodic cleaning is produced, removing any oxide layer growth during the 24 hours immersion and leaving an oxide free metallic surface to react with the electrolyte. For this reason the E_{corr} potentials (-1000mV) for this set of experiments are 800 mV below the experiments ran without the cathodic cleaning and in agreement with most of the literature review data, -1090 mV and -1004mV where the cathodic cleaning in NaCl electrolyte is applied as well, [45, 47, 51, 224]. Once the cathodic region is passed, all the alloys presented limiting passivation currents two orders of magnitude higher than previous experiments meaning the system works under mass transfer control while in the other case the control is based in mixed mode control.

An oxide free surface is not representative of the in vivo conditions and the objective of the chapter was to understand the evolution of the oxide layer growth while immersed in the solution in static conditions and how it changes across a less aggressive potential range. Under these conditions, the least corrosion resistant sample was the AC-TT, followed by the AC-LC, the AC and finally the Forged alloy. When the surface is cleaned cathodically, the results suggested the microstructure of the alloys does not have an influence during the cathodic region and the E_{corr} value reached (-1000 mV). Vidal et al. [48] compared three thermal treatment alloys in their study with similar observations: E_{corr} remained constant independently of the thermal treatment applied with values around -300 mV. Note the difference between the two experiments is the medium, 0.9% NaCl solution and 30% albumin Bovine Serum solution respectively.

However, i_p currents and the micrographs obtained after the experiments, Section 5.2, suggested that the carbides microstructure play a key role in the corrosion behaviour, see Figure 4.19.

The surfaces revealed that dissolution starts in the matrix surrounding the carbides and from surface defects or grain boundaries, as was noted previously

by Bettini et al. [54, 57, 230]. The nearby matrix areas close to the carbides, being less noble, act as anodic sites for the initiation of localized dissolution, with the more noble carbides acting as the cathodic sites. The result is micro-galvanic effects corroding preferentially around the carbides and grain boundaries, which act as sensitive locations for the initiation of metal dissolution. For experiments in this study not exceeding potential values of 0.5V (passive region), a thin protective oxide film was formed at the metal surface, which greatly reduced the corrosion, and no evidence of pits or damage was observed on the samples

Previous studies have investigated the influence of the microstructure on the corrosion properties of different As Cast CoCrMo alloys, [19, 48, 163] and Forged alloys [56] separately. Although there is some disagreement due to the experimental conditions, specially the potential range used and the alloys microstructure.

Some works did not find significant differences in the corrosion or dissolution mechanisms with the presence of carbide inclusions [47] or between the different thermal treatments [19] while Valero et al.,[19, 58], found that a lower percentage of carbon in the bulk alloy and thermal treatments improved the corrosion resistance in As Cast alloys which supports partially the findings presented in this work with higher carbon content alloys presenting higher corrosion rates compared to alloys with a lower carbon content. This was attributed to the homogenization of the surface due to less carbides and an increased amount of Cr to form [48, 231] a more homogenous oxide layer, reducing the release rate of corrosion products. In contrast, As Cast alloys with higher carbon contents were characterized by the presence of coarser Cr, Co or Mo carbides which depleted the metal matrix of these oxide layer forming elements, in particular Cr [34, 56] have shown worst corrosion behaviour due to preferential or localized corrosion at the grain boundaries and region around the carbides [55, 230]. In contrast, some other previous reports were in agreement with the results shown here. Jacobs et al. [232] stated that changes in the microstructure resulting from thermal treatments which reduced the amount of carbides, can cause an increase in corrosion potential and currents compared to the normal as cast alloys.

Lower currents mean the passive film is more protective: this can result from either film thickening, becoming more compact or by changing the film composition. The differences found between the alloys are due primarily to surface heterogeneities present at the oxide/solution interface, including physical phenomena such as grain boundaries, presence of carbides, impurities and surface roughness [233]. From the two PD experiments run, is clear that the potential range applied has a great influenced in the results and its interpretation.

When the potential range used is closer to the E_{corr} the reaction of H_2 is not produced and the oxide layer grows on the surface. Because the sample is cathodically protected no reaction happens until the potential reaches the passive region. In this situation, the Forged alloy samples presented a much higher i_{corr} values than the As Cast samples, suggesting that the Forged alloy favoured passive dissolution. From an in-vivo point of view, a decrease in the *Rp* implies lower resistance of the alloy to corrosive attack and higher metallic dissolution compared to the other alloys. However, because the anodic Tafel slopes were not clearly identified for the As Cast samples, the calculation of R_p was not possible and therefore no comparison between the samples was presented.

On the contrary, when the initial potential range is more cathodic, -2V, a cathodic cleaning is produced in the sample removing any possible oxide layer created on them and leaving an oxide free metallic surface that will react with the electrolyte. While the potential remains in the cathodic region no oxidation occurs because the surface is protected. However, once the sample enters into the anodic region a limiting current controls the passivation process. The passivation current value remains constant which means no further dissolution happens on the surface until the transpassive region is achieved.

This case, comparable with the previous literature [48], showed that i_{corr} and corrosion rates increased when carbon content and carbides percentage area increased (AC-TT>AC-LC> AC>Forged), except for the AC sample which in theory should be ranked in the second position according to carbon content and carbide percentage area. The disagreement might be due to the different reactivity of the carbides within the electrolyte or any other elements influencing the corrosion behaviour. Further investigation must be undertaken to clarify this aspect. However, E_{corr} values and the passivation currents are in the range of previous reported works, around -1000 mV for NaCl solutions, where they compared CoCrMo alloys with different thermal treatments. Lower passivation currents shown by the Forged alloys lead to a thicker oxide layer and a better corrosion resistance compared to the AC alloys, when the opposite was shown when the potential range applied starts closer to the E_{corr} value and there is no cathodic cleaning involved.

It is obvious that leaving the oxide film to grow to reach a steady state acts as a barrier to further dissolution decreasing the i_{corr} currents and shifting the curves (solid lines) two orders of magnitude towards the left compared to the cathodic cleaned samples (dotted lines), see Figure 4.27. When this initial barrier is dissolved, because of the cathodic cleaning on the sample's surface, the carbides microstructure and the carbon content play an important role in the corrosion behaviour. AC alloys became less corrosion resistant than Forged alloys

modifiying the kinetics. During the passive region, a mixed control (Forged) or mass control (As Cast) was observed when PD potential range was set between -0.5/1V, while charge control was shown for PD tests between -2/+2V for the four alloys.

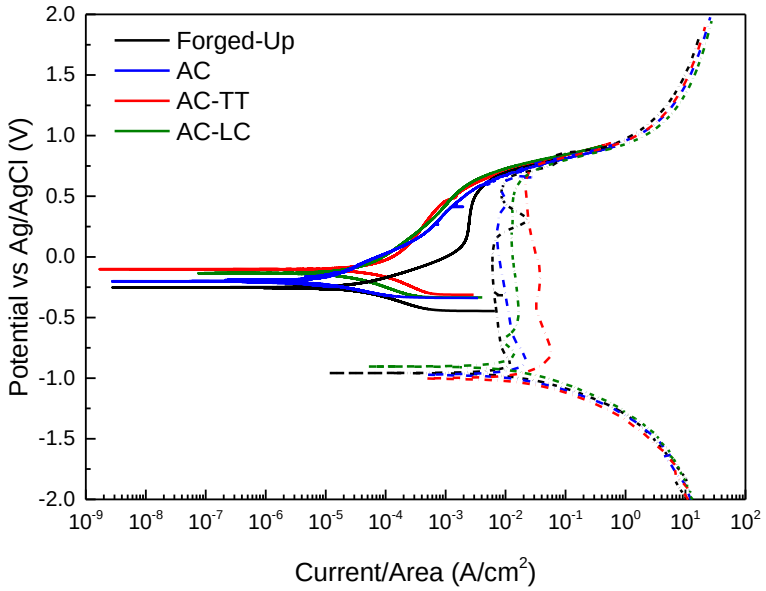

Figure 4.27 Potentiodynamic curves showing the different behaviours resulting from the different experimental conditions. Solid lines represent PD experiments run after 3 hours immersion and potential range from -0.5 V to 1V and dotted lines PD experiments after 24 hours immersion and potential range from -2V to 2V

4.6 Conclusions

4.6.1 Microstructural characterization

Four Co-based alloys with different manufacturing and thermal history were studied. The phases presented in the alloys along with the elemental chemical composition and the grain size and orientation were compared between the different alloys to confirm they met the standards requirements. All of them met the expected standards except the AC-TT alloy which presented a carbon content above the maximum allowable limit.

The conclusions obtained from the microstructural section, Section 4.2, are:

- Forged samples presented a lower carbon content, finer multi-oriented grain size and structure compared to the As Cast samples. No carbides were present and the matrix revealed a 90% fcc phase percentage.

- Grain sizes with individual crystallographic orientations in the mm range were found for the As Cast alloys. Different carbide distributions were found in the As Cast samples depending on the carbon alloy content and the applied thermal treatment. Bulk carbides in the AC sample presented a lamellar structure where σ phase, γ phase (fcc) and $M_{23}C_6$ phases were combined as described by Kilner et al. [218]. The AC-TT samples showed dissolved single phase carbides ($M_{23}C_6$) due to the thermal treatment applied with some of them remaining in the grain boundaries. Almost no carbides were found in the AC-LC samples.

- The percentage of fcc and hcp phases found in the AC samples exhibited a high dispersion, with a 50-50% ratio, due to the variation in the solidification process within the ingot. In contrast, the Forged, AC-TT and AC-LC samples displayed more homogeneous results between samples with a ratio of 95-5% fcc-hcp. The different percentage of fcc and hcp phases will affect the deformation mechanisms and mechanical properties of the alloys under study.

4.6.2 Mechanical properties

- The Forged alloy showed higher hardness and modulus values when compared to the As Cast alloys because of its finer grain microstructure. The apparent higher values presented by the AC sample in the nanoindentation experiments were due to the interaction of surrounding carbides present in the matrix.

- The AC solid carbides showed higher mechanical properties than the fragmented ones of the AC-TT alloy, due to their lamellar microstructure, more complex chemical composition and phases presented. In addition the fragmented carbides could be pushed into the matrix during indentation appearing softer than the bulk carbides which were more stable in the matrix.

- H/E and H^3/E^2 ratios only showed significant differences between the matrix and the carbides and not between the CoCrMo alloys themselves. Under specific contact conditions the different resistance to plastic

deformation between the carbides and the matrix can interfere acting as crack initiation and corrosion sites affecting the deformation-corrosion behaviour of the alloys.

4.6.3 Static corrosion electrochemical characterization

The conclusions obtained from the investigation of the static corrosion behaviour of Forged, AC, AC-TT and AC-LC CoCrMo alloys when immersed in 0.9 wt.% NaCl solution are as follow:

- OCP values evolved with time to more anodic values which means a protective oxide layer was generated spontaneously in all the alloys under static corrosion conditions.

- A minimum of 3 hours was considered necessary to allow for stabilization before any scratch-corrosion experiment.

- Different polarization behaviour was observed depending on the potential used during the PD experiments. Starting the potential range closer to E_{corr} resulted in the oxide film growing under a mixed control polarization behaviour, while more negative potentials produced a cathodic cleaning and an oxide free metallic surface and a mass controlled polarization behaviour during the passive region was observed.

- When PD experiments where held closer to E_{corr}, the carbon content in the As Cast alloys was not found to correlate with the anodic-cathodic behaviour of the alloys. However, the quantity of area covered by carbides might have an influence when cathodic cleaning is performed, with the worst corrosion behaviour seen for the alloys with a less homogenous microstructures and coarser carbides.

- E_{corr} obtained from the polarization curves and OCP values followed the same alloy ranking from more cathodic to more anodic: Forged> AC> AC-TT and AC-LC. The more anodic behaviour related to the As Cast alloys, between 50 and 130 mV, suggest that the oxide layer created was less susceptible to corrosion than the Forged alloy mainly due to the finer grain size presented in the later. The maximum range difference, about 130 mV, between the AC-TT, AC-LC and the Forged sample is enough to stablish the driving force to start a galvanic cell and accelerate the corrosion when these two types of alloys are coupled together.

- Thinner oxide films formed on the Forged samples might accelerate the dissolution of the alloy since metal ions are transported away from the solution-passive film interface. The oxide films can inhibit the pathway for metal transportation and change the overall charge transfer processes.

- The Forged alloy presented the highest i_{corr}, i_p, corrosion rates and the lowest R_p values, indicating a lower resistance to corrosion for PD experiments -0.5/+1V from E_{corr}. Smaller grain size in the Forged alloy presented the worst corrosion behaviour due to the increase in grain boundaries acting as oxidation paths which accelerate the repassivation process. The 130 mV potential difference found between the Forged samples obtained from different areas of the same femoral stem can be considered enough to stablish a galvanic cell within the femoral component accelerating the corrosion processes and the liberation of metallic ions into the solution.

5

Nano-scale wear in dry conditions

5.1 Introduction

Low amplitude motions at the micro and nano-scale between the femoral stem and the hard radiopacifier particles of the bone cement can result in fretting, nano-wear and scratches on the stem surface. These are important wear processes in cemented total hip replacements as the release of metal debris and ions can trigger adverse local tissue reactions within the body, bone resorption and subsequent aseptic loosening of the femoral component resulting in the implant failure. Damage to the cement surface has also been linked to premature fatigue failure of the cement mantle and implant loosening as reported by Shearwood-Porter et al. [234, 235].

The aim of this chapter is to investigate the wear and scratch resistance of four different CoCrMo alloys in dry conditions. The evaluation of the three different modes of wear (fretting, reciprocating sliding and scratching) available in the system was needed to know the limitations of the system and to choose the most appropriate option to investigate the tribocorrosion properties of the alloys at the nano-scale that will be further discussed in Chapter 6.

The dry measurements provided a baseline measurement of the mechanical component of the deformation and wear by the exclusion of any corrosive or fluid environment interactions with the surface. The work was used to validate the depth measurements from the NanoVantage System against AFM and a

white-light interferometer system, to ensure the accuracy of the permanent plastic deformation caused in each of the samples. It also provided an opportunity to assess the lateral force aspect of the scratch loading which was not possible in the liquid cell experiments.

5.2 Nano-fretting

5.2.1 Nano-fretting scars morphology and measurements

The nano-fretting scars were only measurable when loads exceeded 50 mN. Below 50 mN they were not visible under optical microscopy and difficult to find with any other microscopy technique. Figure 5.1a-b shows characteristic gross-slip regime nano-fretting wear scars were visible under 50 and 100 mN loads with parallel lines to the fretting movement and accumulation of material on the sides of the fretting track. At 250 and 500 mN the material deposits on the sides of the scar and the parallel grooves orientated in the fretting direction became less noticeable and not visible respectively. However, the ellipsoidal shape of the surface scars for both indicated lateral movement occurred.

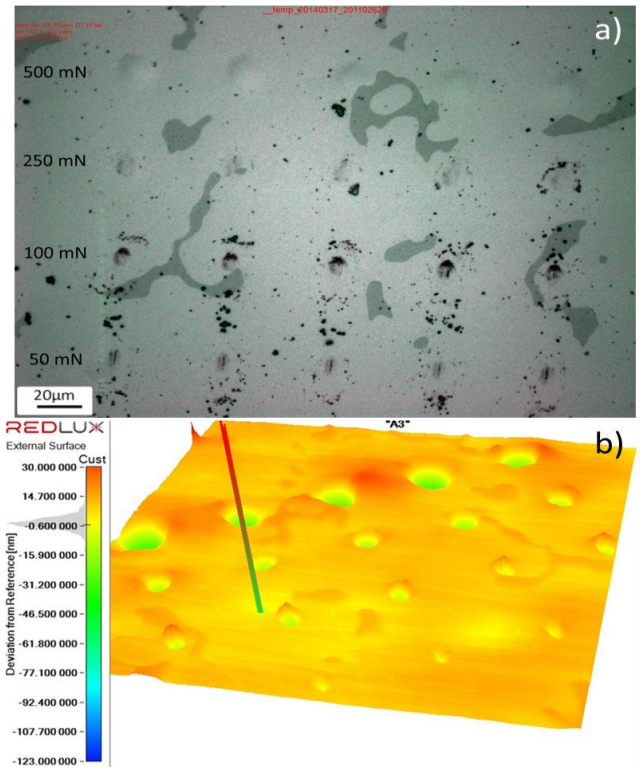

Figure 5.1 a) Optical micrograph of several nano-fretting scars under a load range between 50 to 500 mN and b) White-light interferometry 3D data topography

The AFM topographies and profiles (transversal and longitudinal), Figure 5.2a-d, showed there was an evolution in the shape and morphology of the fretting scars. Under low load conditions the accumulation of material on the sides was predominant, 40 nm, while the deformation value was minimal, 5 nm. Increasing the load to 100 mN still resulted in the accumulation of debris and increased the deformation of the inner part of the fretting scar up to 40 and 20 nm respectively. At 250 and 500 mN there was no observable accumulation of material but the fretting scar depths rose to 30 and 60 nm.

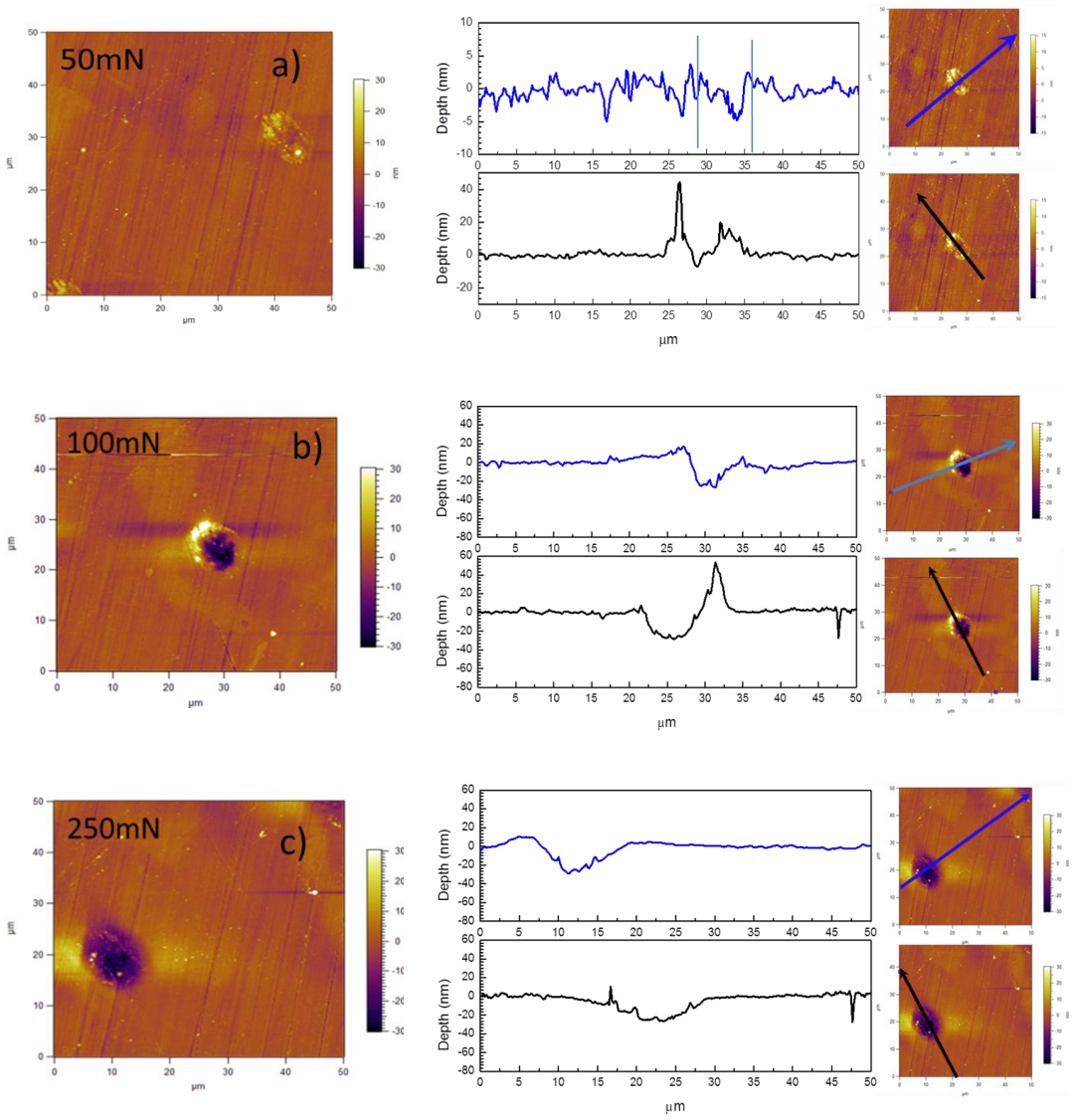

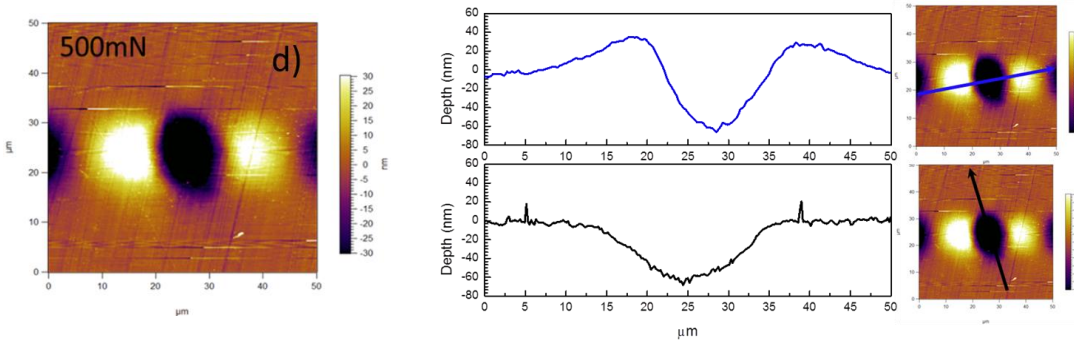

Figure 5.2 Nanofretting AFM topographies and profiles corresponding to different normal loads applied: a) 50 mN, b) 100 mN, c) 250 mN and d) 500 mN

Depth, width and length from the intermittent fretting scars measured in an AC sample are plotted in Figure 5.3. No plastic deformation was measured below 50 mN, which corresponds to a maximum contact pressure equal to 2 GPa, and the depth increased to 20, 25 and 100 nm at 100 (2.64 GPa), 250 (3.6 GPa) and 500 (4.5 GPa) mN loads respectively. The length and width values followed a rapid increase, from 5 µm to 20-25 µm when load was increased.

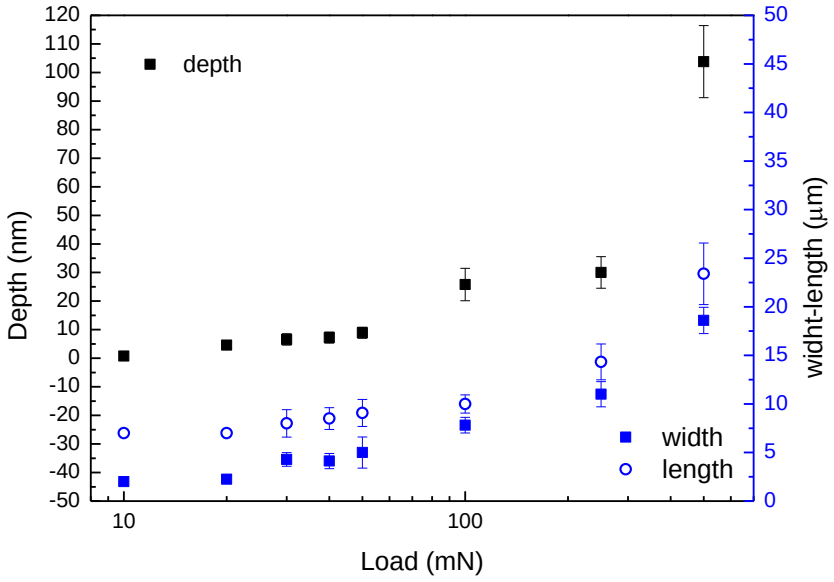

Figure 5.3 Depth, width and length of the fretting scars under load conditions from 10 to 500 mN for an As Cast sample

The fretting loops obtained for experiments under 50, 100, 250 and 500 mN loads are plotted in Figure 5.4. Note that the x axis values expressed as depth were used as an indirect measurement of the displacement of the tip, see Section 3.6.2. Full displacement of 10 μm was considered for the 50 mN loads experiments with a rectangle length equal to 72 (green dots) and a frictional force of 5 mN. When the load was increased to 100 mN the squared shape turned into a parallelogram (black dots) with the upper length equals to 44, corresponding to 6 μm displacement and the friction force remained constant compared to the previous load. Raising the load to 250 mN, (red), resulted in a decrease of the parallelogram width and displacement of 50%, with an increase of frictional force to 14 mN. At 500 mN, (blue), the length tended to 14 (2 μm displacement) and the frictional force increased 10 % up to 17 mN.

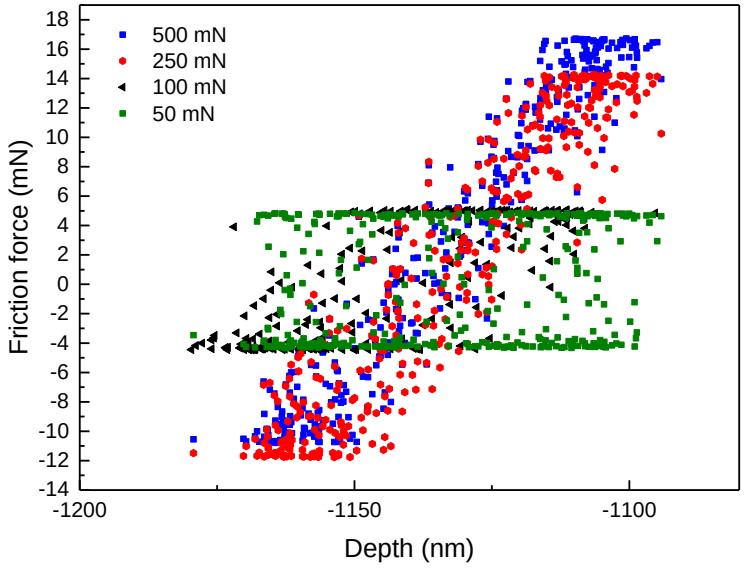

Figure 5.4 Example of fretting loops plot for loads between 50 to 500 mN

5.2.2 Oxide layer characterization

A detailed assessment of the wear scars from the 50 mN intermittent nano-fretting experiments was conducted to analyse the accumulation of material observed on the sides of the scar. The shape of the scar and the experimental set up conditions were indicative of gross slip fretting conditions. Parallel scratches aligned in the direction of motion (horizontal with respect to the picture), Figure 5.5a had modified the initial contact surface removing the original polishing marks.

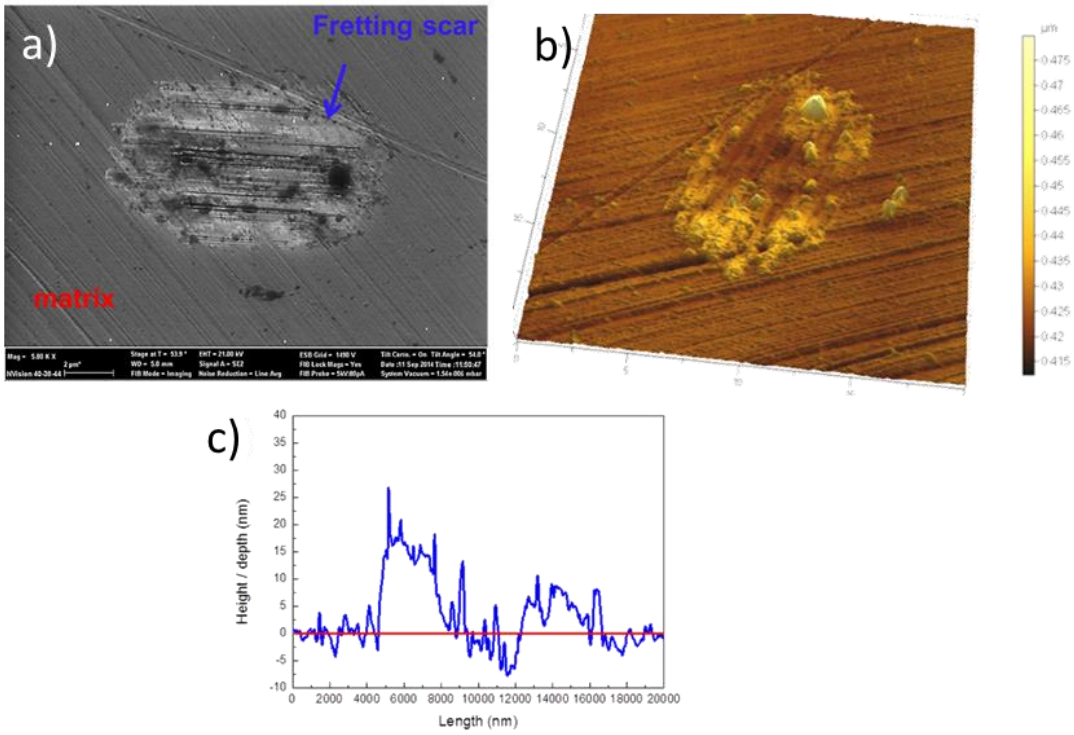

Figure 5.5 a) SEM micrograph, b) AFM scan and c) AFM profile of a fretting scar showing the built up material zones on the lateral sides

The depth data from AFM and interferometer, Figure 5.5b-c, indicated an accumulation of material between 10 to 18 nm with the maximum observable depth inside the scar below 10 nm.

To investigate this accumulated material, FIB-SIMS analysis was carried out over the fretting scar and in an unworn area of matrix to compare the Co, Cr and O_2 content before and after the fretting experiment. Figure 5.6 shows the element depth profiles in both areas with respect to the depth from the surface. The Co and O_2 levels in the fretting area increased by 33% and 50% with respect to the levels in the matrix. In contrast, the Cr levels decreased by 30%. Although the initial Cr content was lower in the fretting area than in the matrix, the content after the first nm was higher than in the unaffected area, reaching a minimum value at the same depth. The maximum peak position was shifted from 2 nm to a 5-7 nm position. An increase of Co and O_2 levels with depth was observed after the fretting experiment moving the zero detection level from 44 to 66 nm in the case of the Co and from 50 to 185 nm for the O_2.

Analysis of the new chemical elements and compounds created during fretting are represented in Figure 5.7 and Figure 5.8, which correspond to the negative

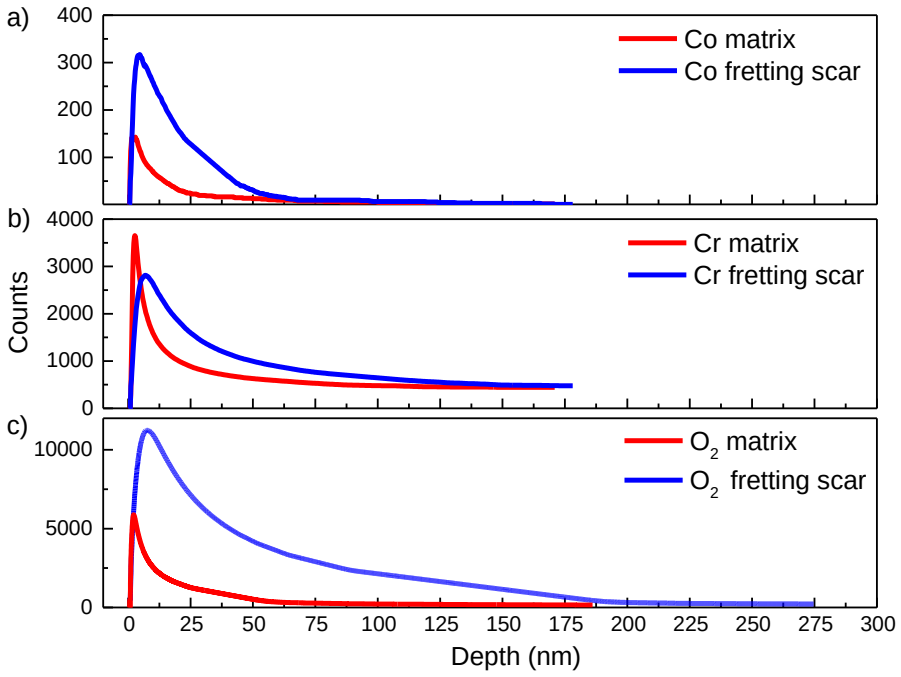

Figure 5.6 a) Co, b) Cr) and c) Oxygen element depth profiles in the matrix and in the fretting scar

and positive species found in the matrix and the fretting areas. The negative species plot indicated a higher presence of O_2 and OH^- levels, with oxides such as CoO^-, CrO_2^- or CrO_3^- not present in the matrix measurements.

In the positive species plot, the levels of Cr^+ and $CrOH^+$ were significantly higher in the fretting scar than in the matrix areas.

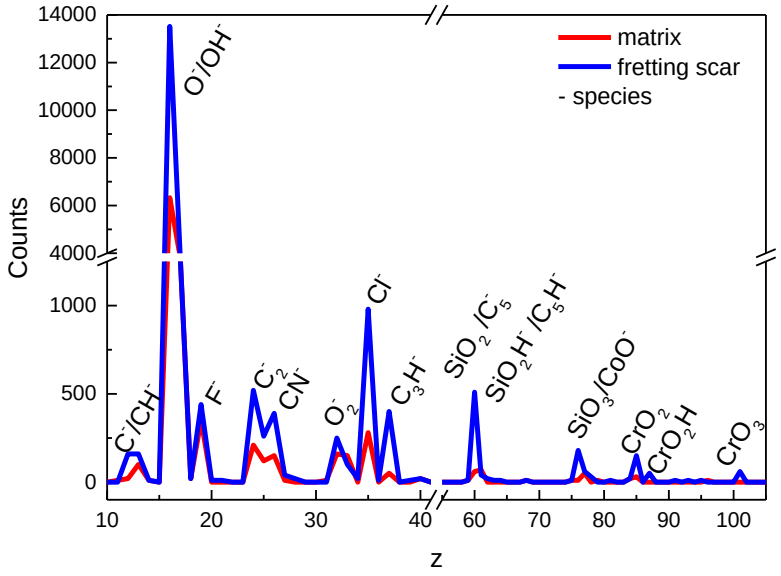

Figure 5.7 Negative species in the matrix and the fretting scar

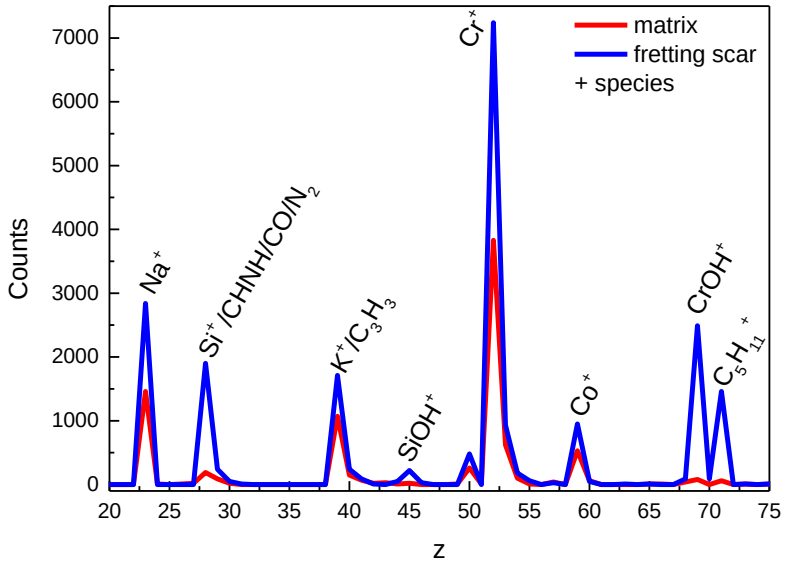

Figure 5.8 Positive species in the matrix and in the fretting scar

5.3 Nano-scale reciprocating sliding wear

5.3.1 Coefficient of friction and dispersed energy values

An example of the data captured during 0.3 s of a reciprocating sliding wear test between a diamond tip and a CoCrMo surface is shown in Figure 5.9. The tangential friction force, the calculated coefficient of friction and the depth measurement can be seen to change their values from positive to negative when the motion is reversed.

Figure 5.10 shows a full set of COF plots for 0.3 s of motion obtained during testing at three different loads. A tangential friction force plot shows a square wave with constant values as the direction of motion is reversed which suggests that no-stick-slip has occurred. Based on this, a full sliding regime was assumed for the dispersed energy calculations for the three normal loads applied, 5, 10 and 20 mN. The plateau shape with a relatively constant value found for the coefficient of friction confirms a sliding regime with no decrease in the motion amplitude. Increasing the normal contact load resulted in a lower COF, with a higher dispersion observed in the COF values at 5 mN.

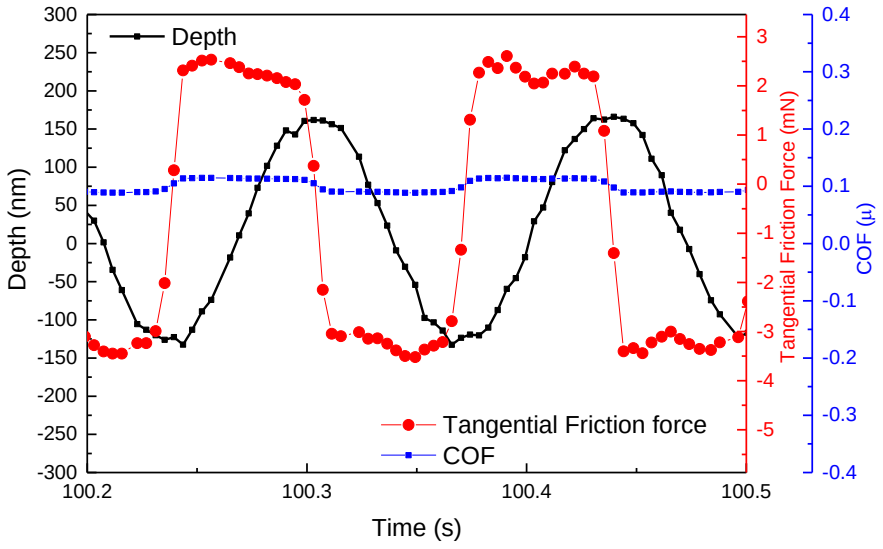

Figure 5.9 Typical data collected for 0.3 s during nano-wear testing of CoCrMo alloy. The tangential friction force (red line), the depth measurement (black line) and the calculated coefficient of friction (blue line) are shown for an applied normal load of 20 mN and a frequency of 7.5 Hz

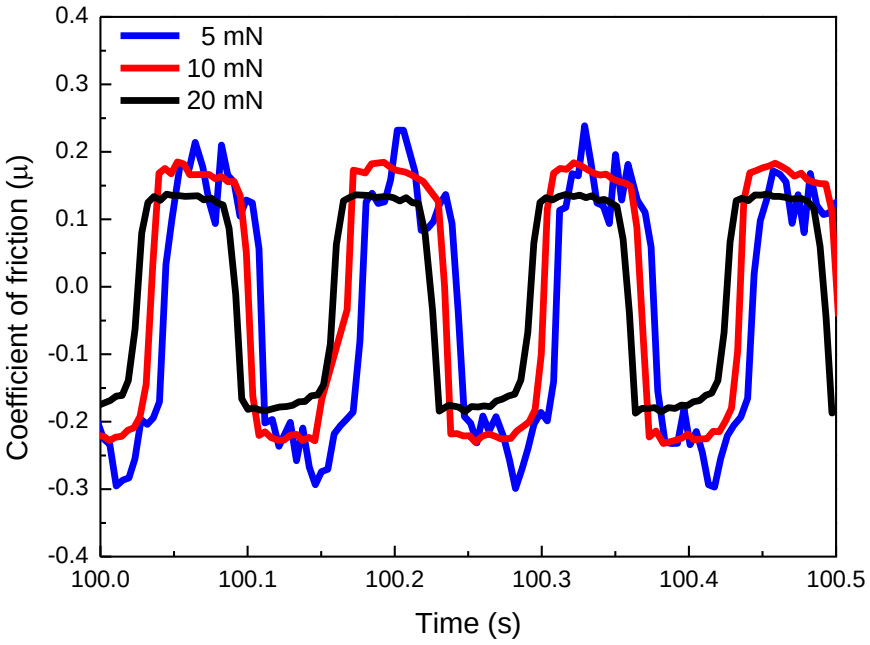

Figure 5.10 Representative COF values for aForged CoCrMo-diamond contact at 5, 10 and 20 mN normal loads.

The running in and steady state COF values for the 5, 10 and 20 mN loads on the four alloys are shown in Figure 5.11 and Figure 5.12 respectively. All the alloys tested showed a systematic variation in COF values with load, with higher loads resulting in lower COF values. For the running in period, the COF values varied between 0.175-0.2, for a 5 mN applied load, and were~0.150 for 20 mN. The range during the steady state period decreased from 0.2-0.275 to ~0.150 for the 5 and 20 mN loads, respectively. Comparison between the alloys showed there were no statistically significant differences during the running in period, however, slightly higher values were observed for the Forged alloy during steady state.

Figure 5.13 shows a representative friction force-displacement plot at three different normal loads, 5, 10 and 20 mN, for the forged sample. Due to the low theoretical contact pressures used, (0.97 to 1.5 GPa) the diamond tip was able to achieve the maximum displacement of 10 μm. Although the tangential frictional forces change when the load was increased, the load levels were not enough to decrease the effective sliding distance due to increase sticking. The dispersed energy per cycle (μJ) was calculated from the area limited by the friction force (mN) and the displacement values (μm).

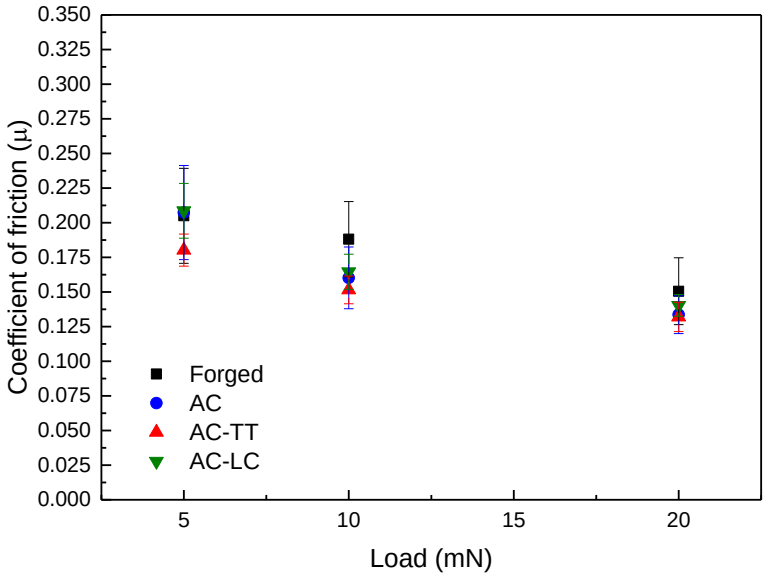

Figure 5.11 Running-in COFs at 5, 10 and 20 mN for the four CoCrMo alloys

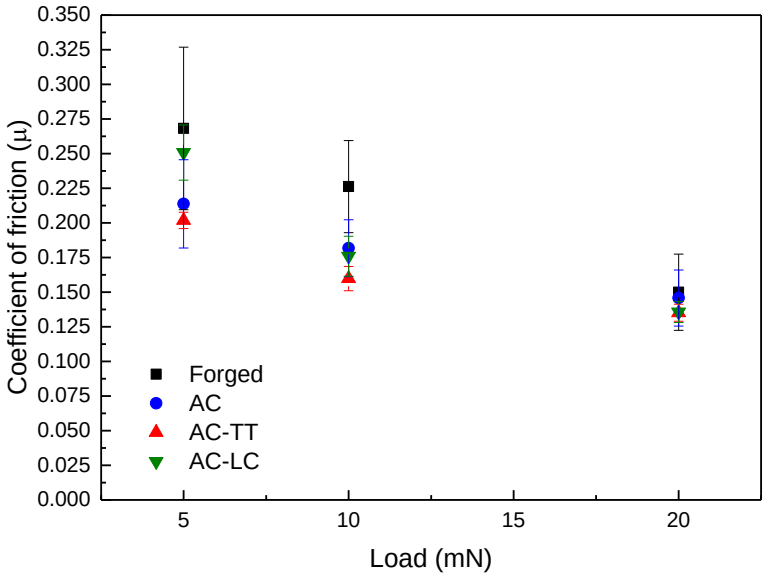

Figure 5.12 Steady state COFs at 5, 10 and 20 mN for the four CoCrMo alloys

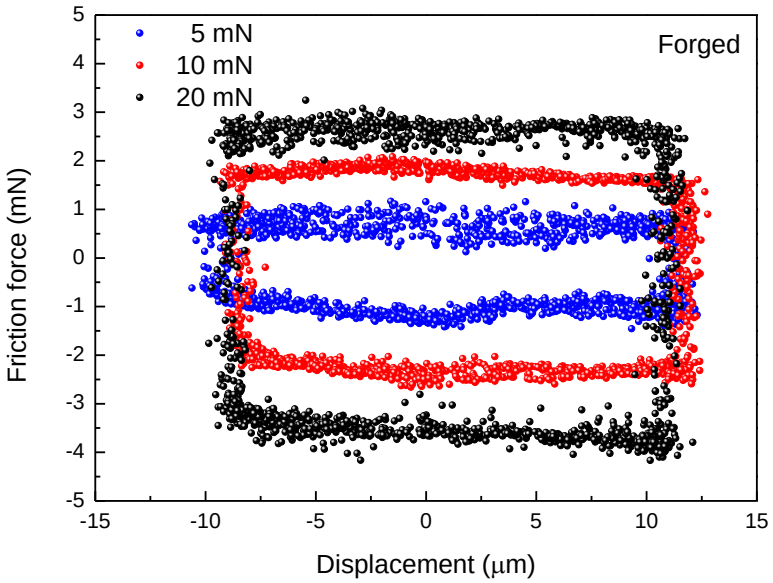

Figure 5.13 Friction force-displacement plot for the Forged alloy when normal loads of 5, 10 and 20 mN are applied

The energy values are summarised in Figure 5.14. The energy per cycle values increased linearly when the applied normal load was increased. The total dispersed energy variation was between 57 and 60 %. Although the percentage variation was similar for the four alloys, the average energy values shown by the Forged sample (21 and 31 μJ/cycle) were statistically different, p-value < 0.05, from the As Cast samples values (17 and 27 μJ/cycle) at 10 and 20 mN loads. No significant difference were found between the energy values for the 5 mN load (Forged, 9.62 μJ/cycle and As-Cast, 12.26 μJ/cycle).

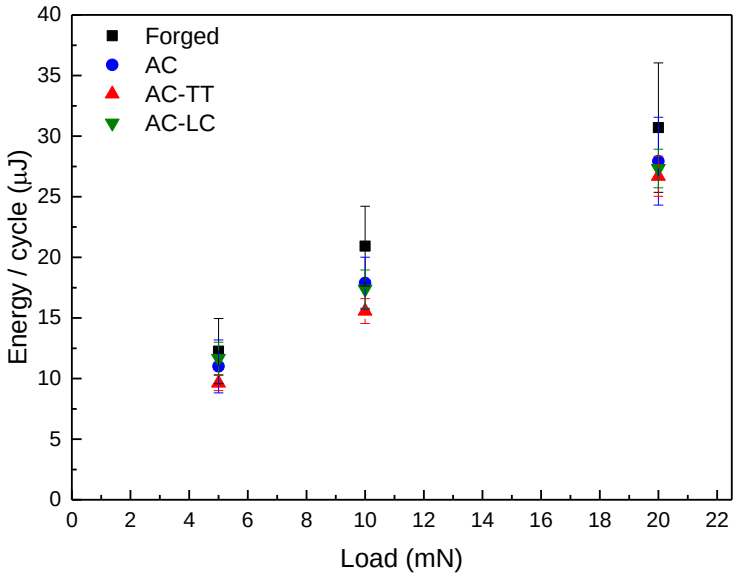

Figure 5.14 Dispersed energy values per cycle at 5, 10 and 20 mN loads for the Forged, AC, AC-TT and AC-2TT

5.3.2 Nano-wear scars depth measurement

A comparison between the initial-loaded depth, the final-loaded depth and the final-unloaded depth is shown in Figure 5.15 to Figure 5.17. The initial depth values for the AC samples were significantly higher than the other alloys for loads between 18 to 30 mN. No significant difference was seen in the initial depth between the Forged, AC-TT and AC-LC samples, with all following an increasing linear trend with load. The maximum final loaded-depths, (elastic and plastic deformation combined) for the AC and the AC-LC treated samples were significantly higher than those for the AC-TT and the Forged ones. There was no significant difference between the depth values for the four alloys for loads up to 15 mN. However, over 15 mN the depth values for the AC sample increased more rapidly than the Forged and the AC-TT and AC-LC samples reaching a maximum difference of 8 % higher at a 30mN load.

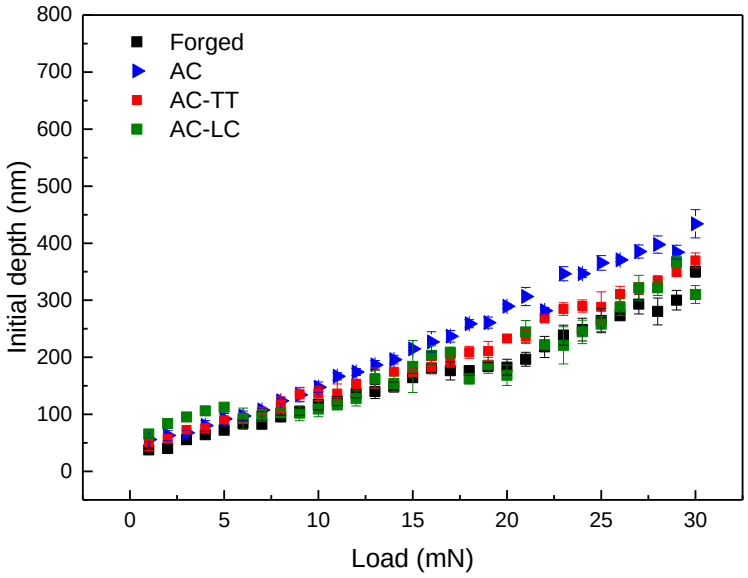

Figure 5.15 Comparison of the initial depth at 15 s of the nano-wear experiments for the Forged, AC, AC-TT and AC-LC alloys

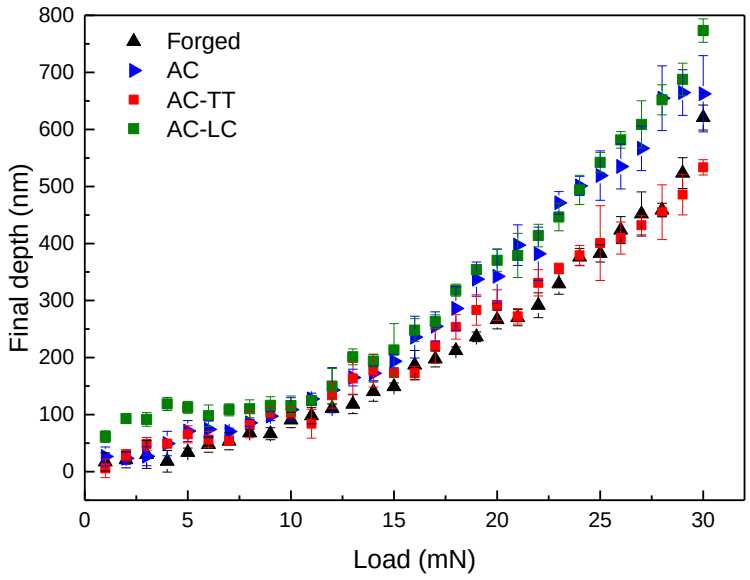

Figure 5.16 Comparison of the final depth at 400 s of the nano-wear experiments for the Forged, AC, AC-TT and AC-LC alloys

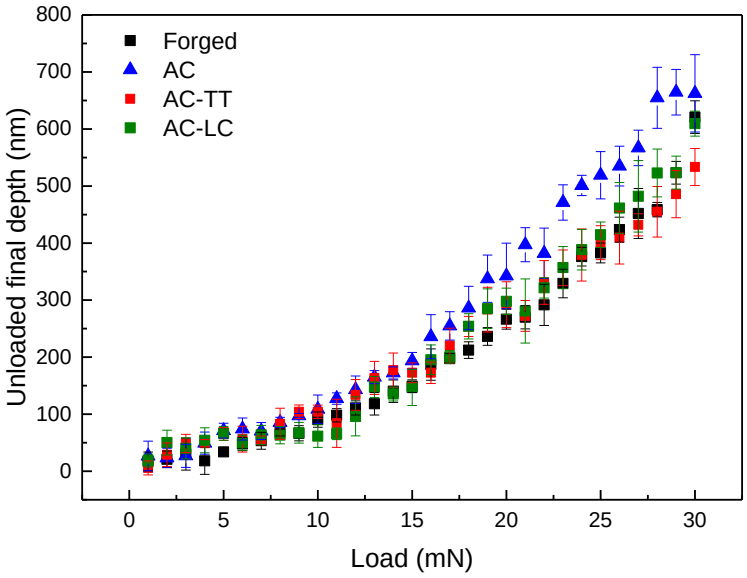

Figure 5.17 Comparison of the unloaded depth at the end of the nano-wear experiments for the Forged, AC, AC-TT and AC-LC alloys

5.3.3 Measuring systems validation: comparison between nanoindenter system, atomic force microscope and white light interferometer

Due to difficulties with applying the thermal drift correction to the NanoTest Vantage data, depth values obtained from the system were validated against AFM and white-light-interferometry measurements. Figure 5.18 compares the depth values for the load range from 1 to 30 mN for the As Cast CoCrMo sample. From 1 to 27 mN almost all the values obtained by the three techniques were coincident, however, for the highest loads, the AFM values are triple that measured by the NanoTest Vantage and the interferometer system. The distribution in the interferometer values is higher compared to the AFM or the NanoTest Vantage system.

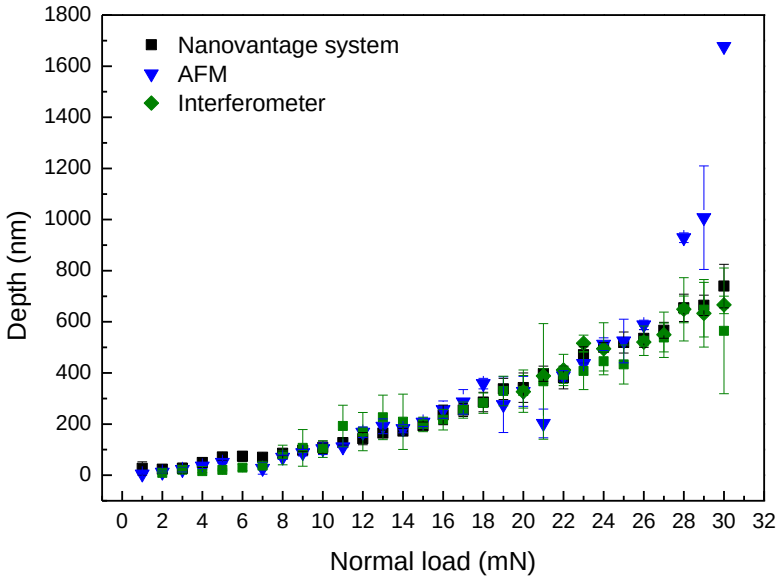

Figure 5.18 Comparison of the final depth values by the three different techniques used: NanoTest Vantage system, AFM and white light white-light-interferometer for the as cast sample

Linear correlations between the depths values of the different techniques are plotted in Figure 5.19 to Figure 5.21. The AFM and NanoTest Vantage system measurements exhibited a strong positive correlation, with a R^2 value of 0.89 if the depth values up to 1000 nm are considered. However, R^2 can reach 0.94 if the depth values are just compared up to 500 nm, as is shown in the inset of Figure 5.19. The white-light-interferometer and NanoTest Vantage system and the white-light-interferometer-AFM R^2 values were also high: 0.88 and 0.90 respectively. Note that values obtained using the AFM microscope at higher loads have been excluded from the analysis because the AFM tip was not able to obtain representative results when the combined pile up and wear scars depth exceeded 950 nm.

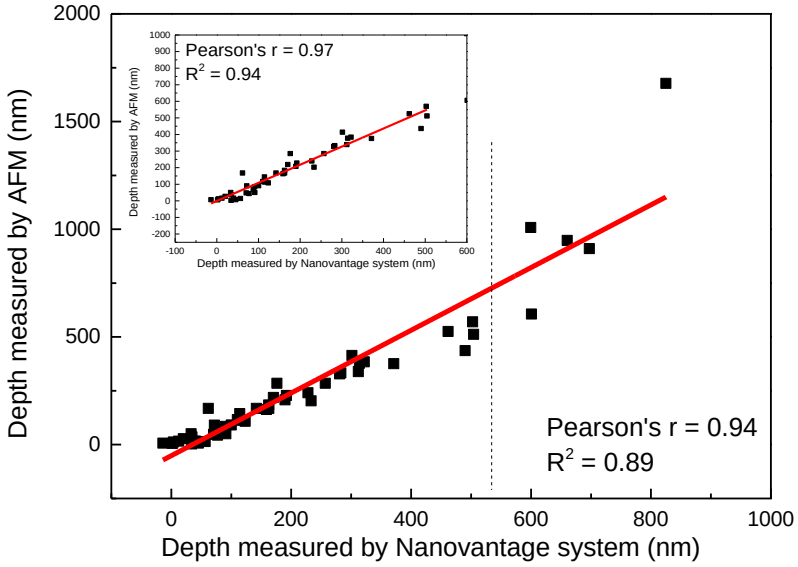

Figure 5.19 Correlation between the residual depths measured by the NanoTest Vantage system and the AFM

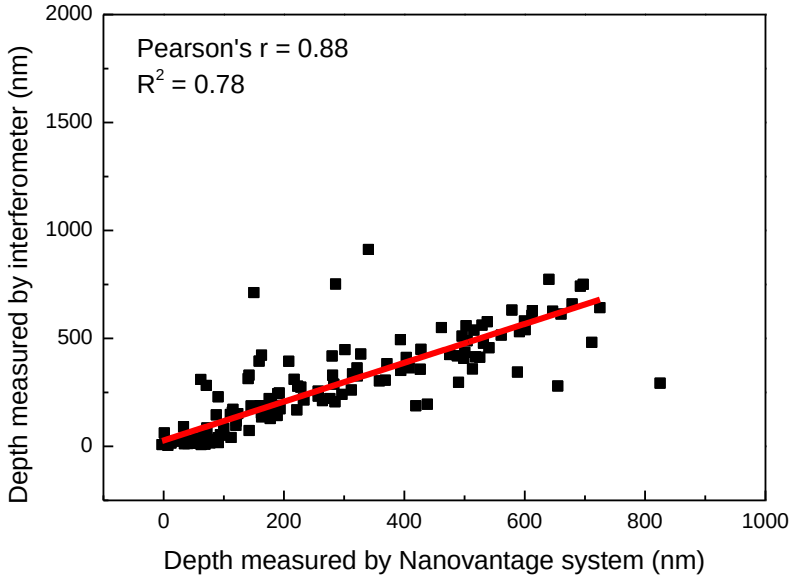

Figure 5.20 Correlation between the residual depths measured by the NanoTest Vantage system and the white-light-interferometer

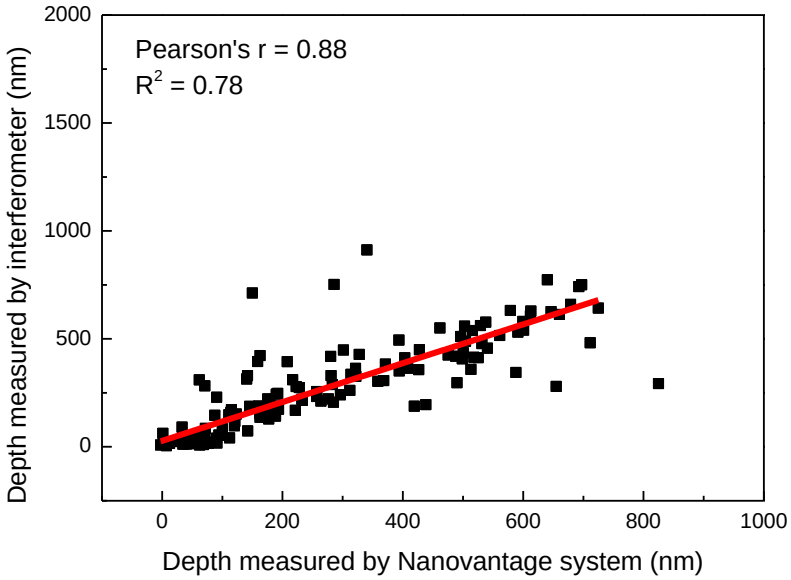

Figure 5.21 Correlation between the residual depths measured by the AFM and the white-light-interferometer. Note the final measurements, over 900 nm, measured by AFM are excluded from the correlation

5.3.4 Reciprocating wear scar morphology

Post-test surface imaging of the wear scars was performed using an optical microscope (Alicona Infinite Focus, Graz, Austria) and a SEM microscope to investigate the possible wear mechanisms and the sliding wear scar morphologies.

Table 5.1 shows the characteristic wear scar morphologies for the Forged, AC, AC-TT and AC-LC for different group loads. At the lowest loads, 1-2 mN, which correspond to maximum contact pressures between 6.6 to 8.4 GPa, sliding wear damage was only visible for the AC sample. Significant plastic deformation, defined as ploughing in the surface and production of platelet-like debris, was observed at the highest loads on all the alloys. Particle debris and pile up on the scar edges started to be visible when the applied stresses passed 20 mN. All the samples showed a predominantly ductile response to sliding wear with ploughing resulting in pile-up and wear debris at the sides of the wear-track.

Table 5.1 Optical images of the nano-wear scars under 1, 10, and 30 mN load for the Forged, AC, AC-TT and the AC-LC CoCrMo alloys

Load (mN) / σ_{max} (GPa)	**1-2 mN 6.6-8.4GPa**	**9-10 mN 13.8-14.3GPa**	**29-30 mN 20.4-20.7GPa**
Forged	Not Visible	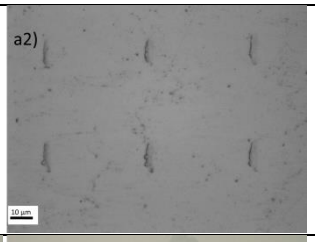	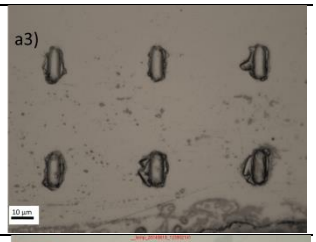
AC	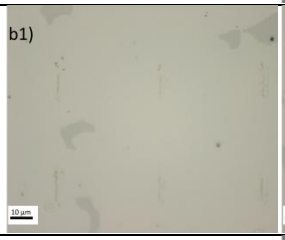	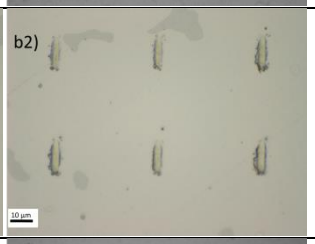	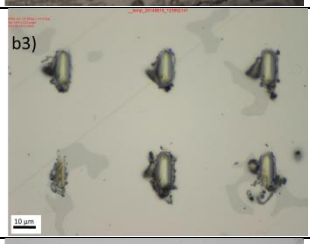
AC-TT	Not Visible		
AC-LC	Not Visible	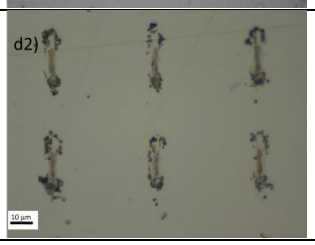	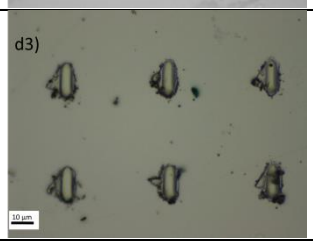

However, the quantity and shape of the debris around the nano-wear scars in the AC-LC sample was larger than in the rest of materials.

SEM images in Figure 5.22 show the evolution of the wear scar as the load increased. At low loads, (Figure 5.22a and b), a reduced material displacement was seen together with some particulate debris, with typical particle sizes around a micron size at the top and bottom part of the scar. Once the load was increased, the wear particles generated around the wear track increased in size forming aggregates and also some plate-like delamination debris, (Figure 5.22c). At the highest loads severe pile up was predominant over particle debris formation, see Figure 5.22d.

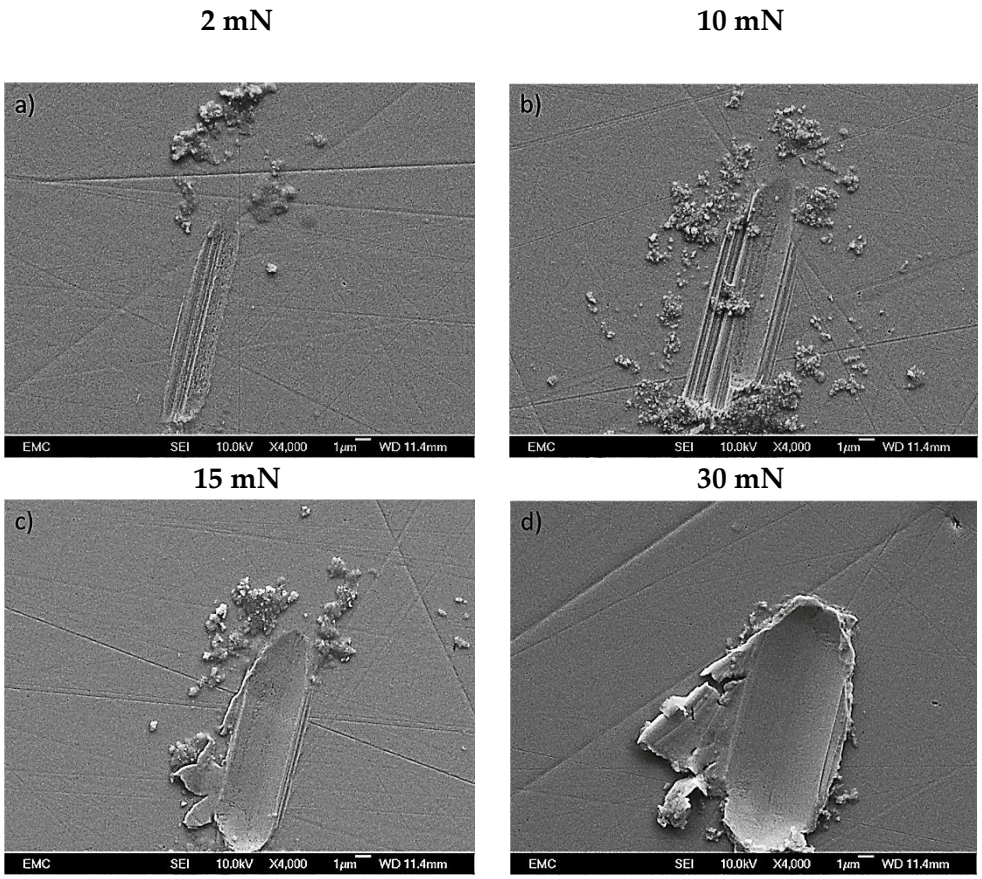

Figure 5.22 SEM images of nano-wear scars morphologies for the As Cast-LC sample at four representative load levels

5.4 Dry scratch experiments

5.4.1 Friction force

Friction forces monitored during nano-scratch experiments for the four alloys are plotted in Figure 5.23 for the two sets of experiments using the 200 and 5 μm diamond tips. A linear trend relationship between the applied load and the friction force was found up to a maximum level of 500 mN for the 200 μm sphere while the trend is a rapid increase when the tip used was the 5 μm one. The friction forces measured for the 200 μm sphere experiments were below 10% of the normal loads applied. However, when the small radius sphere was used the percentage was below 10% for the 20 and 40 mN loads, while the percentage raised between 15 to 25 % for loads between 60 to 120 mN respectively. No significant differences in the friction forces levels were found between the four alloys for any of the two set of experiments.

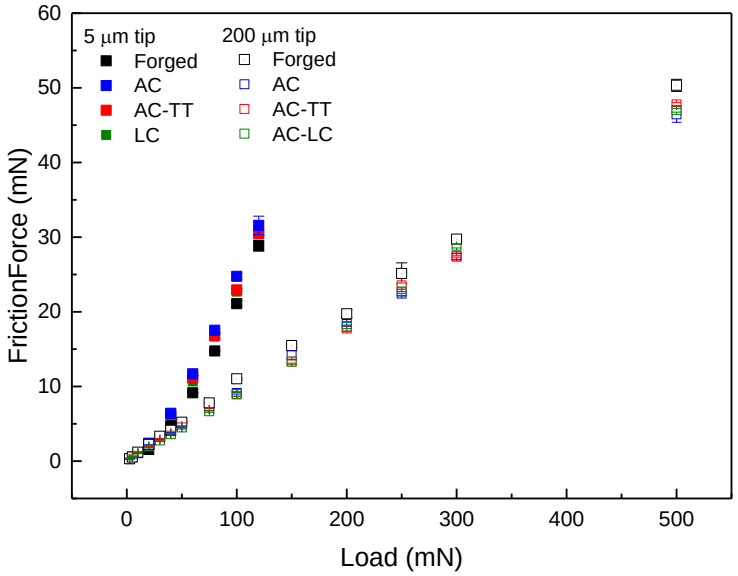

Figure 5.23 Friction forces from dry nano-scratch experiments for the Forged, AC, AC-TT and AC-LC alloys using a 5 and a 200 μm sphere

5.4.2 Coefficient of friction

COF values obtained from the ratio between the frictional and the normal force are shown in Figure 5.24 for the two experiments run using the 200 μm spherical tip (hollow symbols) and the 5 μm tip (solid symbols). For experiments run using the 200 μm spherical tip, a rapid decay was presented in the alloys starting at a maximum COF values of 0.13 reaching a minimum of 0.09. The highest dispersion in the results was observed for load levels between 2.5 to 20 mN. Dispersion levels were reduced when loads were increased. The Forged alloy started with a maximum level of 0.13, decreasing to 0.1. Similar initial values were monitored for the AC-TT and AC-LC alloys although from 20 mN and onwards the values were 10 % lower than the Forged values under the same loading conditions. AC alloys also showed a 0.09 COF value at the highest loads, however at initial loads, COF was 70 % lower than the rest of the alloys.

In contrast, the COF values obtained from experiments using the 5 μm tip showed a rapid linear increase while the load was increased starting at 0.1 for under 20 mN loads to 0.260 for the 120 mN load. Statistical significant differences were found between the As Cast and the Forged alloys under all the loads, with the Forged alloy presenting the lowest COF between all of them.

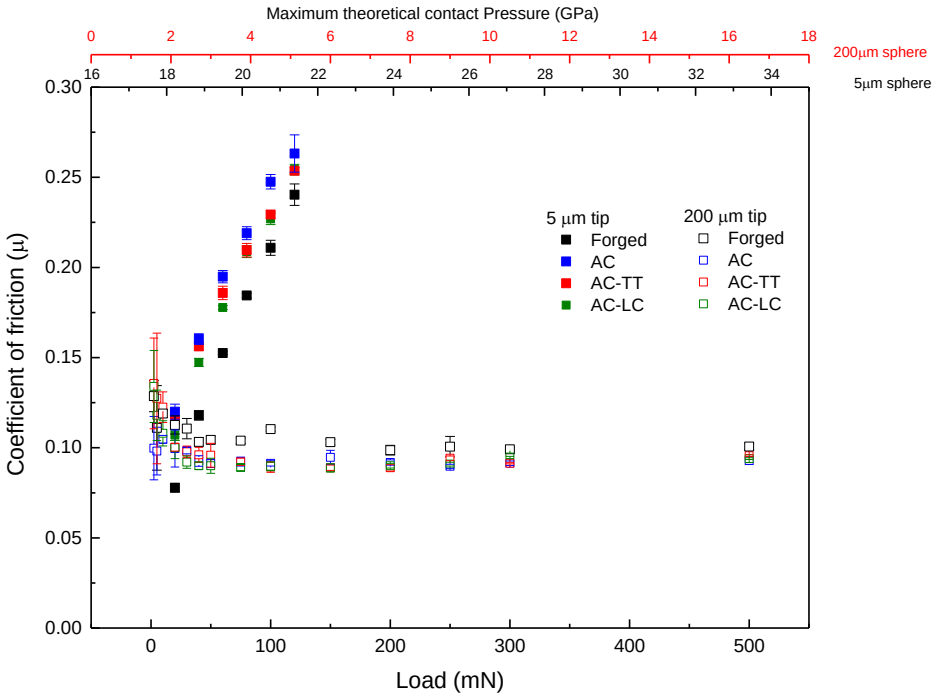

Figure 5.24 Coefficient of friction for a load range from 2.5 to 500 mN (lower x axis), for the Forged, AC, AC-TT and AC-LC alloys. Note the upper x axis represent the equivalent maximum theoretical contact pressures calculated with Hertz equations for the 200 μm sphere contact (red) and 5 μm sphere (blue) for each of the loads applied

5.4.3 Deformation

5.4.3.1 Groove scratch morphology

Scratch morphology measurements in 2D and 3D, (Figure 5.25), were used to measure depth and pile up, Figure 5.26a, and width, Figure 5.26b, for loads between 150 and 500 mN in a Forged sample using a 200 μm sphere. Depth measurements were the permanent plastic deformation produced on the alloy starting at 5 nm when the low loads were used and increasing up to 50 nm for the highest loads. The same increasing trend was observed in the width evolution when the load was increased. No pile up was produced under 100 and 200 mN loads. Minimum measurable pile up was 10 nm at 250 mN, reaching 20 nm for the maximum load.

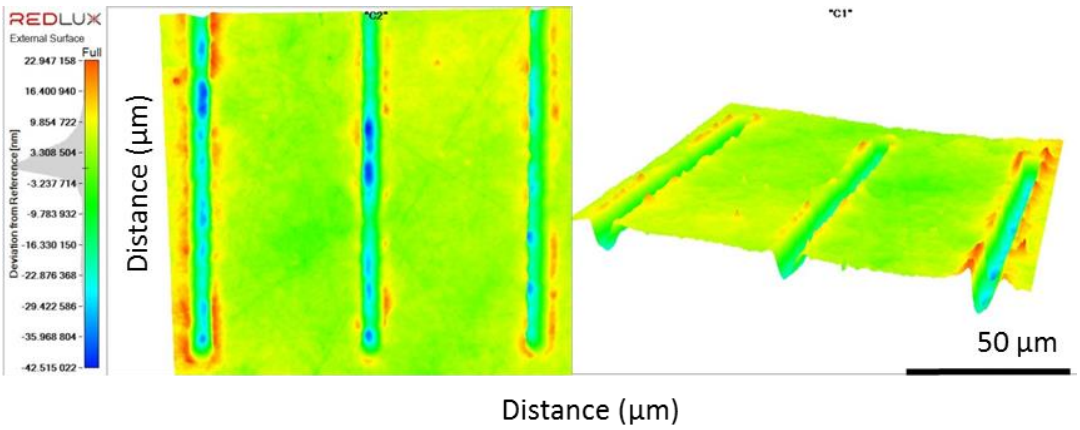

Figure 5.25 Example of interferometric scratch measurements in a Forged sample under a 300 mN load

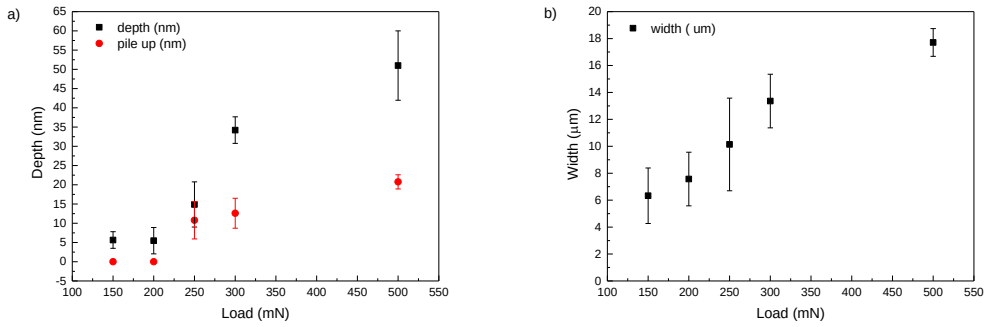

Figure 5.26 Evolution of a) Depth and pile up and b) Width produced during scratch experiments in a Forged alloy

5.4.3.2 Plastic and elastic percentages

The comparative results for the loading depth (plastic + elastic deformation components), the elastic depth, and the plastic depth (permanent plastic deformation over the samples) are plotted in Figure 5.27, Figure 5.28 and Figure 5.29 respectively from the two sets of dry scratch experiments run with the 5 and 200 µm spherical tips. Statistical differences were found in the elastic depth data between the CoCrMo alloys for the 200 µm sphere experiments for scratches produced under 500 mN loads with the AC-TT and AC-LC alloys showing values 25% higher than the Forged and the AC alloys. When using the 5 µm tip the loading depth was increased linearly from 100 nm to a maximum between 450 to 700 nm for the Forged and the AC alloys respectively. For all the loads, the

loading depths were statistically higher, p-values below 0.05, for the AC and AC-TT samples than the Forged and AC-LC alloys.

No significant differences in the elastic depth values were shown after the scratch experiments using the 200 μm and 5 μm tips by the AC-TT and the Forged alloys up to 120 mN. However, the AC and AC-TT alloys exhibited an elastic component 4 and 5 times higher than the other Co alloys for the 5 μm tip tests and double for the AC-LC alloy under 120 mN compared to the Forged alloy. No significant differences were found between the elastic depths for the four alloys using the 200 μm spherical tip.

Analysing the plastic depth values (permanent plastic deformation), Figure 5.29, 200 μm tests only produced a deformation of 100 nm for all the alloys, while the experiments run with the small tip reached values between 200 to 350 nm under 120 mN load.

Percentages of elastic and plastic deformation for the 200 μm dry scratch experiments are plotted in Figure 5.30. Hollow symbols correspond to the elastic deformation component and solid symbols to the plastic permanent deformation percentage. For the whole range of loads the elastic component remained mostly constant starting at 90 % for the lower loads and decreasing slightly to 85 % of the total deformation produced over the samples under a 500 mN load. The plastic component followed the opposite trend starting at 10 % up to 20%.

Figure 5.31 a-c shows the plastic and elastic percentage for the Forged, AC, AC-TT and AC-LC samples respectively where scratch experiments were run with the 5 μm spherical indenter. For the four alloys, at low loads, the elastic component was 60% of the total deformation. When the load is increased, the elastic component decreased and the plastic component increased. For the Forged and the AC-LC samples the load at which elastic and plastic components are equal is at 40 mN while AC and AC-TT is at 80 and 70 mN respectively. Under maximum loads, 120 mN, the Forged alloy exhibited the highest plastic deformation component, 70 %, followed by the AC-LC and the AC with a 60 % and finally the AC-TT with 40 % of the total deformation.

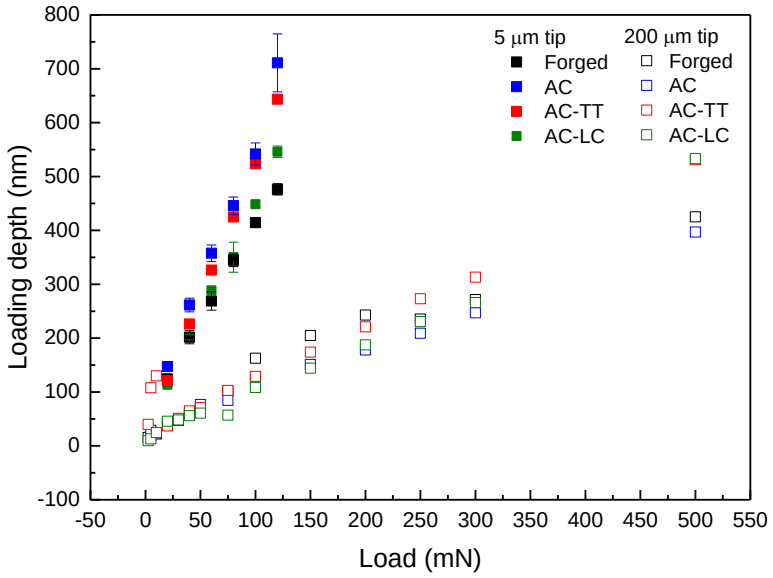

Figure 5.27 Loading depth for the four CoCrMo alloys under dry scratch experiments using a 5 μm and 200 μm spherical tips

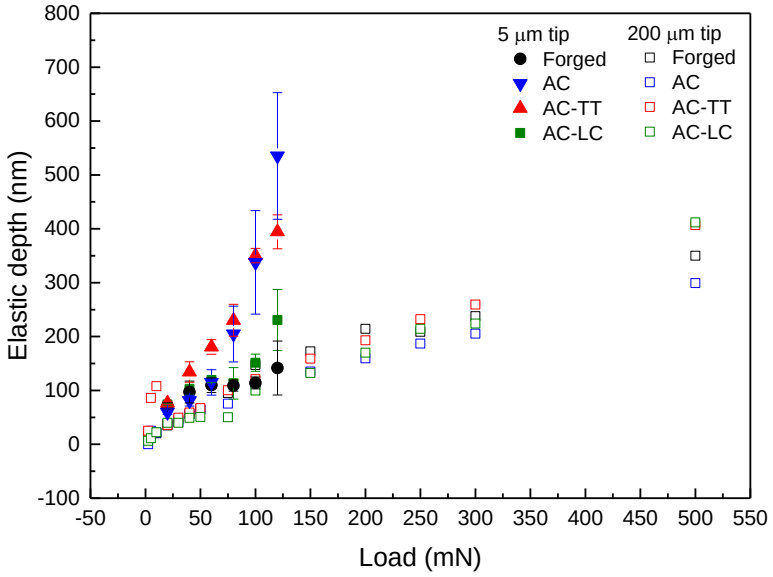

Figure 5.28 Elastic depth for the four CoCrMo alloys under dry scratch experiments using a 5 μm and 200 μm spherical tip

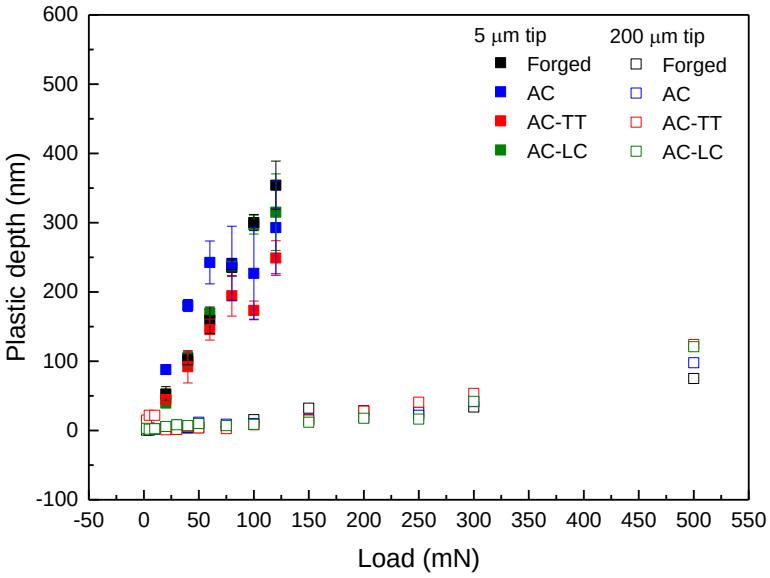

Figure 5.29 Plastic depth for the four CoCrMo alloys under dry scratch experiments using a 5 μm and 200 μm spherical tip

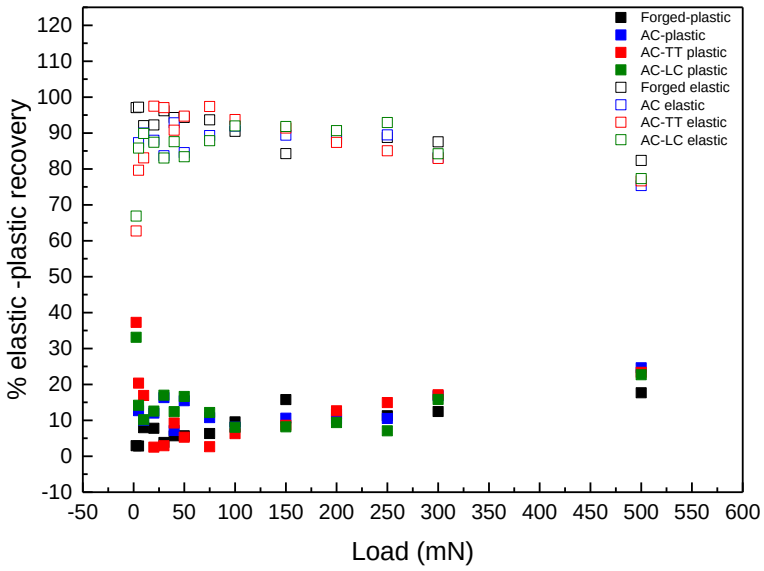

Figure 5.30 Percentages of plastic and elastic deformation for: a) Forged, b) AC, c) AC-TT and d) AC-LC alloys after dry scratch experiments with the 200 μm spherical tip

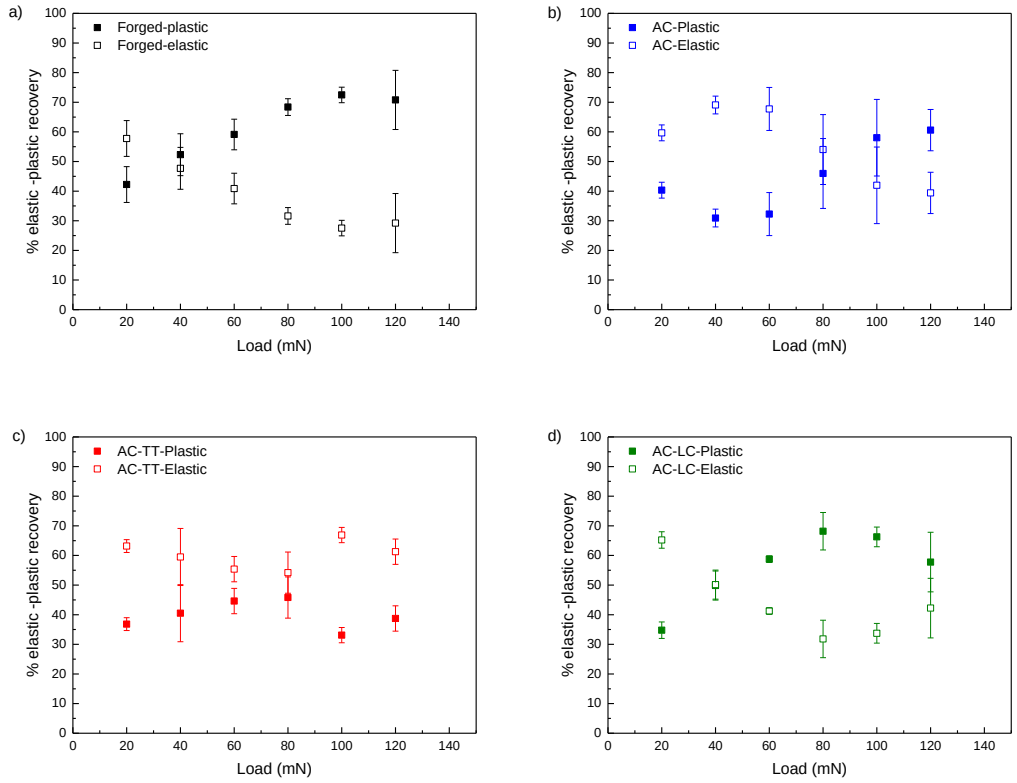

Figure 5.31 Percentages of plastic and elastic deformation for: a) Forged, b) AC, c) AC-TT and d) AC-LC alloys after dry scratch experiments with the 5 μm sphere

5.4.3.3 Degree of penetration (D_P)

Theoretical and experimental D_p values, calculated according to Equation 3.24, are plotted for the 200 μm sphere experiments in Figure 5.32 and for the 5 μm sphere in Figure 5.33. Hollow symbols correspond to the experimental D_p value calculated using the plastic and the elastic depth combined while for solid symbols only the plastic deformation depths were used. In the case of the 200 μm sphere experiments, the theoretical values fit closer to the experimental plastic depth values than the ones considering the elastic + the plastic depth, with maximum values below 0.02. In contrast, the experiments using the 5 μm sphere showed better agreement between the elastic + plastic depth with the theoretical, with the exception of the Forged alloy which had values 50% below the theoretical ones.

Correlating the COF with the D_p, Figure 5.34 and Figure 5.35, a constant value of 0.1 was found for all the D_p values when the 200 μm sphere was used with no differences between the alloys.

For experiments using the 5 μm sphere the main observation was the Forged alloy presented a positive trend increasing the COF from 0.05 to 0.22 for a D_p range between 0.16 to 0.27. The As Cast alloys however followed a rapid increase trend with similar COF values as the Forged alloy but the D_p increased significantly from 0.15 to 0.4 for the AC and AC-LC and to 0.5 for the AC-TT samples.

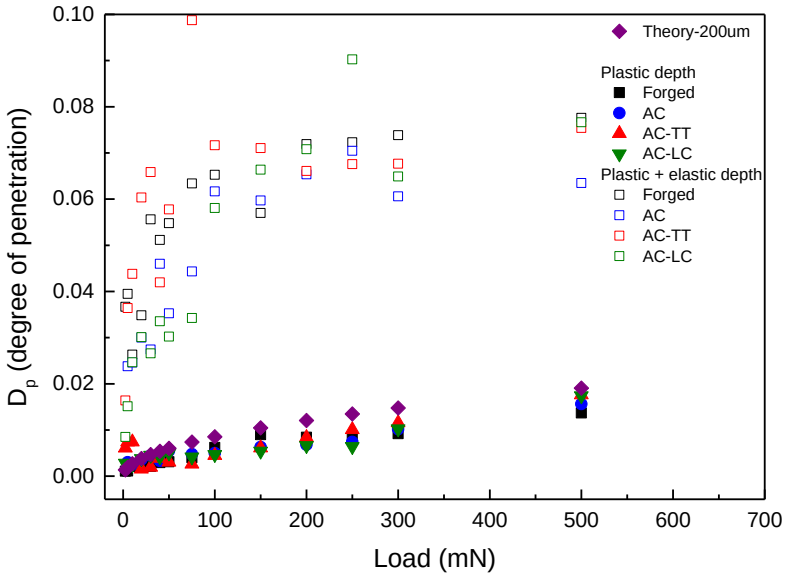

Figure 5.32 Theoretical and experimental degree of penetration calculated for the dry scratch experiments done with the 200 μm sphere. Solid symbols correspond to plastic depth values. Hollow symbols correspond to plastic+elastic depth values. Solid symbols in purple are the theoretical D_p values

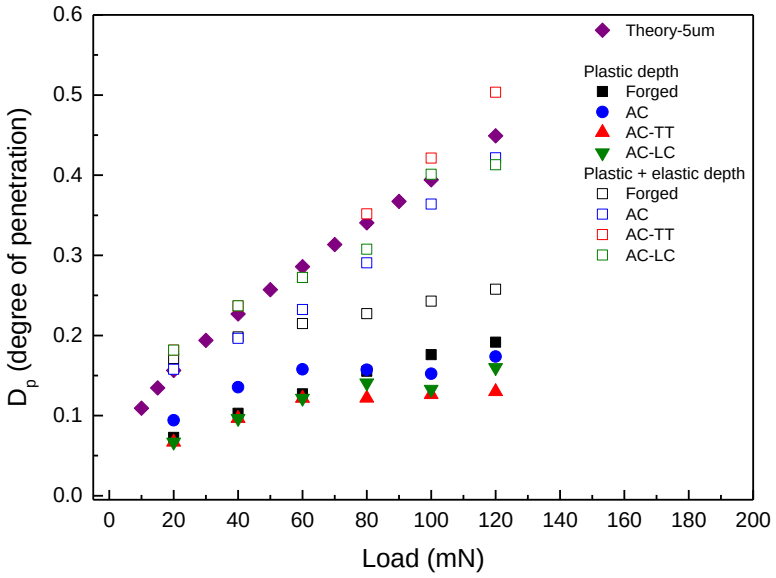

Figure 5.33 Theoretical and experimental D_p values calculated for the dry scratch experiments done with the 5 μm sphere. Solid symbols correspond to plastic depth values. Hollow symbols correspond to plastic+elastic depth values. Solid symbols in purple are the theoretical D_p values

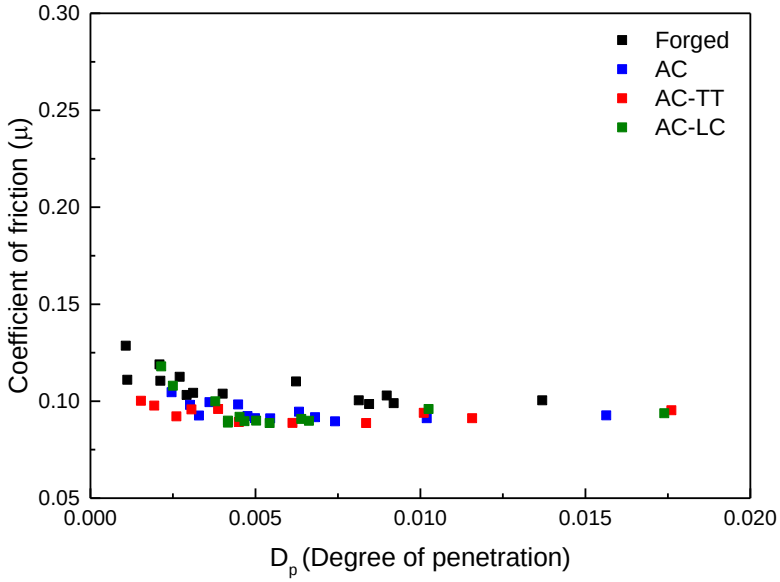

Figure 5.34 Correlation between the degree of penetration and the coefficient of friction μ for the dry scratch experiments performed with the 200 μm spherical tip

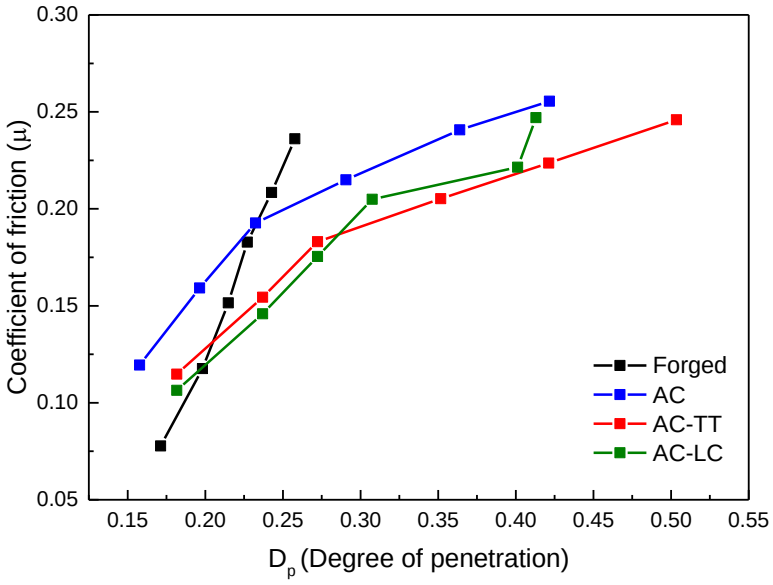

Figure 5.35 Correlation between the degree of penetration and the coefficient of friction μ for the dry scratch experiments performed with the 5 μm spherical tip

5.5 Discussion

Initially, the ideal requirement to evaluate the wear resistance at the nano-scale was to carry out nano-fretting experiments on the metallic surface. For that purpose the aim was to develop an experiment combining intermittent fretting motion together with the real time monitoring of the tangential friction forces, the plastic deformation and the displacement of the indenter. However, the system limitations found during the study (and discussed in detail in Section 5.6) resulted in a change in the testing plan to reciprocating sliding and scratch experiments.

5.5.1 Oxide layer characterization

The intermittent fretting experiments provided the opportunity for the oxide layer to reform on the surface during the course of experiment as well as upon completion. The depth profile characterization of the reformed oxide revealed a mix of metal oxides and a different chemical composition to the oxide in the unworn areas. Although contact conditions and environment are not the same as the one described in this work, tribolayers formed between metal on metal lubricated contact conditions have been observed in retrieved implants and in

experimental works [222, 236]. The chemical composition of the tribolayer formed on the fretting scar was found to be a mixture of oxides more rich in Cr than Co, although Co was still present. This is in agreement with Milosev et al [28] where the layer was composed mainly of Cr_2O_3 but also CoO and MoO_3 in the vicinity of the metal-oxide interface and the outer layer respectively. The thickness of the tribolayer was found to be about 1.8 nm over the alloy surface [28]. Bryant et al reported the formation of a similar oxide in a cement-metal contact on a CoCrMo femoral stem [133]. The study characterised the surface topography and surface chemistry on retrieved polished femoral stems were characterised by XPS suggesting an oxide layer formation mechanism based on the thermodynamic stability of the species.

In a corrosive environment, Cr will oxidize as it has a lower activation energy than Co, resulting in the formation of Cr_2O_3. The Co, with a higher solubility, will migrate and leave the interface towards the body and dissolve into the solution. This theory is in agreement with the clinical studies by Hart et al [144] where higher levels of Co were found in retrieved tissues around the implants.

In dry conditions during fretting experiments, Co ions do not dissolve in the solution and they remain in a higher concentration in the oxide layer on the surface as shown in Figure 5.6. The release of ions from the metal surface has been demonstrated to be the source of dissolved ions, the cause of thickening of the metal oxide during repassivation and/or surface corrosion in some reactive metals, [16, 45].

5.5.2 Frictional behaviour

In dry conditions under reciprocating sliding and scratch conditions, the COF showed a significant load and material dependency. The higher COF values during the steady state period for the lower loads during the reciprocating sliding experiments (Figures 5.11 and Figure 5.12), are in agreement with the findings of Maruymama et al. [237] and directly related with the low contact pressures applied and the stresses produced in the contact area. The same observations were detected during single scratch experiments when the 200 μm sphere was used, Figure 5.24.

Under low contact pressure conditions, minimal plastic deformation is induced and a high dispersion in the COF was found. These values are related to an elevated friction force signal due to the poor interaction between the tip and the surface which falsely increases the value resulting in higher COF values which do not correspond with the real conditions occurring in the surface.

When the load passes a critical limit, the tip indents into the surface increasing the contact area. At these higher loads the surface asperities are deformed during the first cycles, forming a wear scar and the measured COF values remain constant during the test duration. Previous studies have focused on the evolution of friction and wear of metallic materials such as Ti, Cu or Ni during micro-scale sliding, [238, 239]. The study demonstrated that yield stress plays the dominant role in the evolution of friction, independently of the grain size and decreasing with increasing hardness. That was confirmed from dry scratch experiments using a 5 μm sphere, where the Forged alloy, with a higher hardness presented lower friction values than the As Cast ones. A material with a higher yield stress will deformed less than a softer material when the tip indents. Therefore, if the contact area in the scratch groove was lower, the friction force and the COF when interacting ahead from the tip decreased too. This results were in disagreement with the work by Huang et al [240], where wrought alloys presented higher steady state COF values, 0.25, respect to the As Cast CoCrMo alloys, 0.21. Their differences in friction were attributed to the interaction between the carbides and the stacking faults hcp layers with the counterface (polymer) for the as cast and the wrought version of the alloys. In Huang's work a pin-on-disk configuration was used, and although the steady state COF value for the wrought alloy was higher than the AC, the initial run-in period followed the opposite trend, supporting the results obtained from the single scratch experiments reported here.

For low contact pressures a constant interfacial COF of 0.1 was found. However when the 5 μm sphere was used the increasing linear trend found when increasing the load is related with the degree of penetration which is one order of magnitude higher for experiments ran with the smaller tip than the ones using the 200 μm sphere, see Figure 5.36. The D_p has been used previously as a measurement of the deformation produced on materials due to abrasive processes [198, 199] using tips of different sizes as in the work reported by Woldman et al [241]. Depending on the D_p value and the coefficient of friction the abrasive processes will result in cutting mode, D_p over 0.3, wedge forming mode, D_p around 0.2, or ploughing mode when D_p is below 0.2. Due to the conditions used in the dry scratch experiments namely a 200 μm sphere, the degree of penetration did not reach the minimum value to produce a permanent plastic deformation level to analyse the abrasive resistance of the CoCrMo alloys under study and the interfacial COF was monitored. On the contrary, the levels observed for the scratch experiments using the 5 μm tip were enough to produce significant deformation levels to evaluate the deformation behaviour required, and ploughing mode was observed in most of the samples.

According to Bowden and Tabor [242], the behaviour observed in Figure 5.24, corresponds with the interpretation of the two components which defined the friction coefficient in Equation 2.19. When using the 200 μm sphere, the damage produced on the surface is minimal, and the ploughing component is really small, so the interfacial friction is the dominant element. In contrast, if the 5 μm sphere is used, the friction ploughing component increases dramatically and it is the one which dominated the friction measurement.

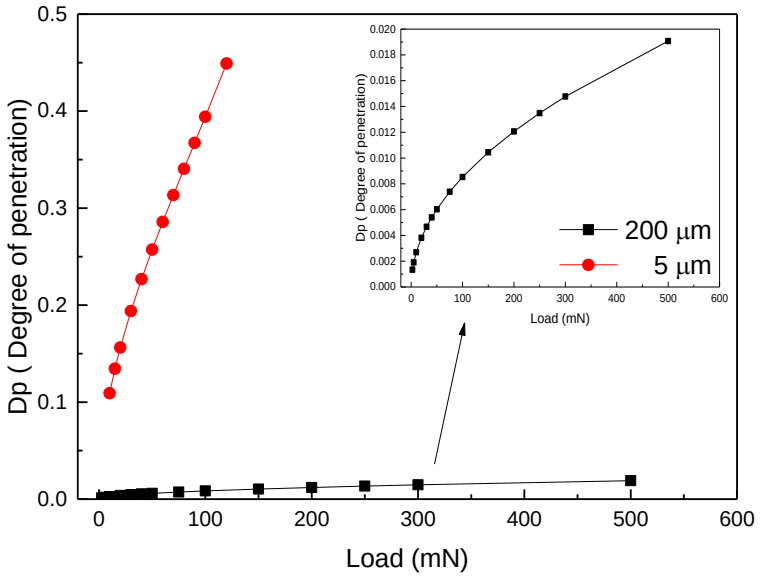

Figure 5.36 Comparison between the theoretical degree of penetration values, calculated using Equation 3.44 ,[199], between the scratch experiments using the 200 and 5 μm diamond tips

5.5.3 Dispersed energy per cycle

The dispersed energy per cycle obtained from the reciprocating sliding experiments, (Figure 5.14), showed that the Forged alloy, with highest hardness value, presented the highest dispersed energy, which means the work needed to deform the material is higher than for the As Cast alloys. At this contact pressure level the thermal treatment applied or the carbon content of the as cast sample did not play a significant role in the dispersed energy. Full sliding was assumed for all the samples. This assumption was made as no slope changes were observed in the tangential frictional forces recorded for any of the applied loads, which according to [243], indicates no partial or full sticking occurring.

The preliminary fretting hysteresis loops under various loading conditions showed that at low loads the indenter is able to achieve the full displacement with no significant changes in the friction force or the loop shape. When the load was increased the energy values reduced due to the width of the loop decreasing because the effective displacement being restricted resulting in the different fretting modes, changing from partial sliding, to slipping and finally sticking regime as was shown in Figure 5.4.

5.5.4 Deformation behaviour and depth measurement validation

The deformation behaviour of the four alloys was dominated by the matrix properties. The increase of carbon content is known to increase the stacking fault energy, [244], which produces narrower stacking faults, increasing the mobility of dislocations and making the deformation process easier. Therefore, the AC sample matrix deformed more initially when the sample was loaded, Figure 5.15. The levels of final on load depth, Figure 5.16, were similar for the AC and the AC-LC samples and were 57 % higher than the Forged and the AC-TT. The unloaded depth at the end of the experiment showed the AC sample to have a significantly higher level of plastic deformation. However, the scratches which landed on carbides showed a decrease in contact depth when compared to the matrix. The smaller size carbides present in the AC-TT alloy do not exhibit the same effect as the carbides in the AC alloy.

Ploughing and pile-up have been observed in previous studies at the nano and micro-scales [196, 245] under sliding conditions. At low loads, and low degrees of penetration, the sample material tends to deform plastically, pushing the deformed material downwards rather than to the side [241]. As the degree of penetration increases, the material is forced upwards and sideways causing pile up to form along the edges of the reciprocating scars and single scratch experiments. The significant increase of wear debris in the AC-LC alloy, but also observed in the AC-TT sample, suggested that besides the level of plastic deformation at intermediate stress, the thermal treatments plays a role in the production of wear debris. The size and quantity of metallic particles disseminated in the human body can cause osteolysis, loosening of the implant and its revision [118, 246, 247].

AFM was used extensively as a measuring system and although it provided high levels of detail about the wear scars in this study, it was time consuming due to low area covered. In addition it was unable to measure highly deformed scars, as the height range exceeded the range of motion of the tip. The combination of in-situ depth measurements using the NanoTest Vantage system and the white-

light-interferometer validation confirmed the interferometry measurements were faster and reliable even for the high deformation levels.

5.6 System limitations

The aim of the project was to develop an experimental setup which allows investigation of the tribocorrosion processes happening between a single hard asperity and a metal surface. Several experimental conditions were tested and a number of limitations found, related to the fretting set up and the influence of the friction probes on the final results.

To analyse fretting results it is necessary to obtain fretting hysteresis loops. For a complete hysteresis loop the variables needed are: real displacement of the tip, friction force and time. The NanoVantage System can monitor the time, the depth and the friction force but not the real tip displacement. As a result it was not possible to plot fretting loops to see changes of fretting regime, associated with differences in the displacement of the tip or calculate accurate dispersed energy values. Preliminary fretting experiments allowed the measurement of COF values up to 50 mN and by assuming the tip motion was achieving the full displacement fretting loops could be generated. Fretting scars were only visible for loads between 50 to 500 mN. This meant it was not possible to investigate the relationship between the fretting scar morphology and the COF since friction forces were not monitored for loads over 50 mN (except some preliminary cases).

In addition, the friction probes were not designed for high frequency, long-lasting experiments and they failed by fatigue. For the experiments where the friction force was monitored there were problems related with the tip size, as shown in Figure 5.37. When the 200 μm tip (red square) was replaced for the 5 μm sphere (black dots), the friction sensors were not able to monitor the friction and depth properly resulting in invalid data.

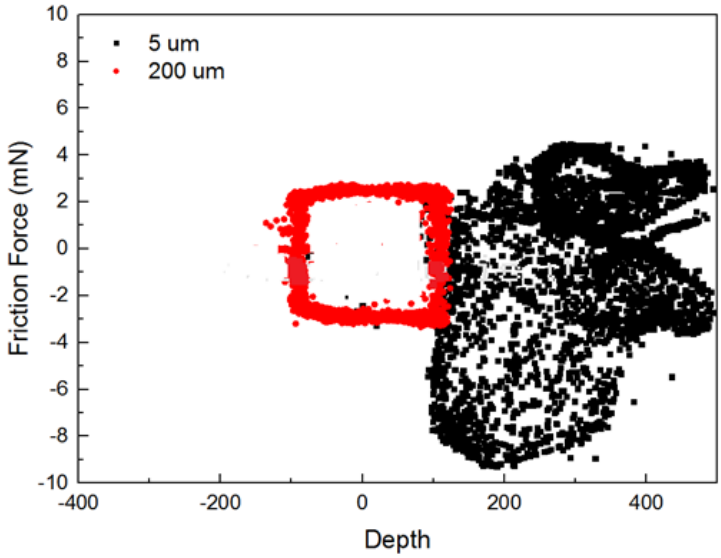

Figure 5.37 Friction force-depth graph comparing the output using a 5 (black) and 200 (red) μm spherical tips

Under reciprocating sliding conditions, the wear scar morphology and geometry (width and length) varied depending whether the friction probe was inserted or not, see Table 5.2.

Experiments at 7.5 Hz, setting a 10 μm length and using 3 different loads: 5, 10 and 20 mN were done to demonstrate that having the friction transducer inserted makes the displacement of the tip behave differently.

Intermittent-fretting and low frequency motion resulted in long duration experiments. Although the temperature in the laboratory was controlled, there was significant and variable thermal drift during the experiments. The level of drift correction with regards to the low resultant depths meant the output were hugely dependent and affected by the drift.

In light of these issues and restrictions, single scratch experiments were chosen as the best option to understand the combined effect of the plastic deformation and the corrosion processes occurring in the CoCrMo alloys.

Table 5.2 Comparative between wear scars morphologies under three different loading conditions with and without the friction probe in the system

Experiment conditions	Friction probe IN	Friction probe OUT
7.5 Hz/5.7 V/10 μm 5 mN	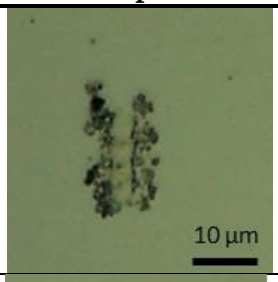	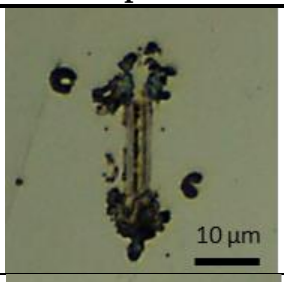
7.5 Hz/5.7 V/10 μm 10 mN	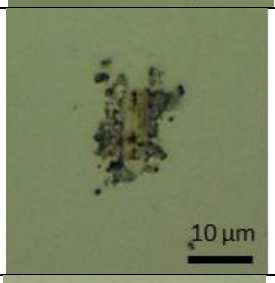	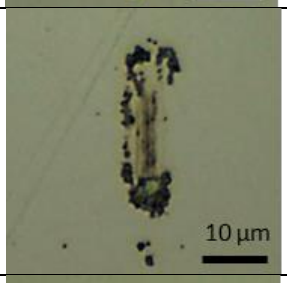
7.5 Hz/5.7 V/10 μm 20 mN	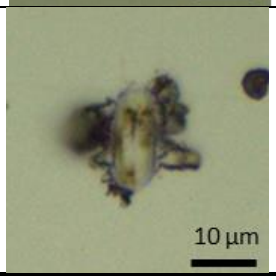	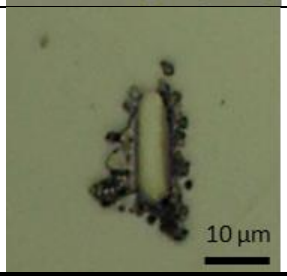

5.7 Conclusions

In the present chapter, four CoCrMo alloys were subjected to nano-scale intermittent fretting, reciprocating wear and single scratch experiments to compare their wear resistance and their frictional behaviour. The aim was to investigate the role played by the plastic deformation component in the wear-corrosion processes. The following conclusions could be drawn from this chapter:

- After investigating the intermittent fretting and the reciprocating sliding wear experiments and their set up limitations, scratch experiments were considered as the most appropriate test to evaluate the tribocorrosion properties.

- The oxide layer formed on the fretting scar area in dry conditions was a mix of Co and Cr oxides that form due to mechanical or thermal

activation. The thickness of the oxides was estimated to be between 10 to 15 nm.

- COF values for the reciprocating sliding and scratch experiments were load dependent with lower values shown by the Forged alloy compared to the AC alloys. Reciprocating sliding showed a decreasing trend in friction when the load was increased due to the smoothening of the wear track and the reduction of the asperities between the contact surfaces. A linear increasing trend was found for the scratch experiments under high contact pressure conditions due to the ploughing process between the tip and the deformed area in contact. A constant COF value equal to 0.1 was observed when the yield stress of the material was not exceeded.

- The Forged alloy exhibited dispersed energy values significantly higher than the As Cast alloys under 10 and 20 mN loads during the reciprocating-sliding experiments.

- Permanent plastic deformation of the samples was dependant on the specific microstructure, manufacturing process and thermal history to which the alloy were subjected and the experimental conditions used (reciprocating sliding or single scratch experiments). The AC sample underwent higher deformation levels with visible sliding wear scars under reciprocating sliding experiments at lower loads than the rest of the samples. However, observing the SEM micrographs, the AC-TT and AC-LC samples generated a higher number of particles around the fretting scars compared to the Forged and the non-thermal treated As Cast samples. Single scratch experiments result in a lower degree of penetration for the Forged alloy compared to the As Cast samples.

- Under maximum loads, during scratch experiments, the Forged alloy exhibited the highest plastic deformation component, 70%, compared to the AC-LC and the AC alloys with a 60 % and the AC-TT- with 40% of plastic deformation percentage.

- The degree of penetration calculated from the scratch experiments showed different deformation behaviour between the Forged and the As Cast alloys. For the same D_P values, the Forged alloy had statistically higher COF values.

- The white-light-interferometer system was validated by linear correlation against the plastic deformation depths obtained from the NanoTest

Vantage system and the AFM measurements. The white-light-interferometer was proved to be able to measure the wear scars at the nano scale.

- The Forged alloy for the scratch, nano-fretting and sliding experiments consistently showed a lower level of deformation when compared to the AC alloys.

6
Nano-scratch-corrosion

6.1 Introduction

In previous chapters the alloys microstructure, their corrosion properties under static conditions and the plastic deformation resistance of the four alloys was analysed and compared. In this chapter deformation and corrosion mechanisms were evaluated at the same time by scratch-corrosion experiments. The aim was to determine the onset load required for the oxide film disruption and repassivation kinetics when plastic deformation occurs as these are central to the characterization of the tribocorrosion processes.

Plastic deformation and rupture of the passive oxide film on a metal while it is immersed in an electrolyte produces transient current peaks without the need for the removal of material from the surface. In the Literature Review, Section 2.5.2, the importance of calculating accurately the depassivated area was discussed. The affected area subjected to repassivation was only considered as the scratched area under the indenter,[32]. However previous work on abrasion-corrosion of CoCrMo ,[49], pointed out the affected area includes the zones around the scratch where the film is also disrupted, hence it should be taken into account if a more accurate analysis of the repassivation kinetics is to be obtained. In an aqueous environment, oxide fracture can produce oxide particles and expose the reactive base alloy to the surrounding fluid. Subsequent electrochemical events (oxidation) result in dissolution of the base alloy (producing metal ions) and reformation of the oxide film (repassivation).

Scratch experiments in dry conditions have been used before by Ahmed et al, [248], to understand metal deformation mechanisms without relating them with the corrosion processes. Gilbert et al., [32], used a high speed scratching technique to relate the levels of plastic deformation and corrosion properties of a single cast CoCrMo and Ti alloys at the nano-scale and also studied the dynamics of oxide films repassivation on metallic biomaterials [174].

A new enhanced nano-scratch-corrosion test was developed in this study to investigate the depassivation-repassivation behaviour of four different CoCrMo alloys at the nano-scale. The chapter aimed to investigate the effects of mechanical load and microstructure (grain size, grain orientation, type of carbide) on current densities, repassivation times and magnitude of plastic deformation, resulting from the fast scratching of the surface and fracture of the oxide film.

6.2 Plastic deformation analysis

To better understand the mechanical behaviour of the oxide film, it is important to determine the stress state of the oxide and substrate at the contact point between the diamond indenter and the alloy surface. The nature of the single-scratch experiments meant it was not possible to analyse the magnitude of any material loss and therefore the wear of the material. However, plastic deformation and material "displacement" on the scratch edges were observed.

The sphere on plane geometry of the contact surface induced a deformation by shear. Using Hertzian equations and modelling the scratch test as a sphere on a plane, average, maximum contact stresses and contact radius were determined. Penetration depth and contact area (or scratched area) were also calculated. Data are summarised in Table 6.1. If the Tresca criterion is applied, [249], the following Equation 2.15, maximum shear stresses and the location below the surface were determined.

However, using the experimental width obtained from the interferometry measurements, the experimental contact radius was determined as half the width at the zero level of the scratch, with respect to the flat surface (Table 6.2). Since the contact radius increased from 15 to 65% for the 10 to 120 mN load range, the contact area did as well, while the contact pressures and shear stress were reduced to around 1/5 of the theoretical values. Figure 6.1 shows the theoretical (black line) and experimental (red line) values from the depth and contact radii.

Table 6.1 Theoretical contact values calculated from Hertzian theory

	Load (mN)				
	10	**50**	**80**	**100**	**120**
radius sphere (μm)			5		
E* (GPa)			195		
a-contact radius(μm)	0.57	0.98	1.15	1.24	1.32
Average contact pressure (GPa)	9.56	16.36	19.13	20.61	21.90
Maximum contact pressure(GPa)	14.35	24.54	28.70	30.92	32.86
Shear stress (GPa)	4.44	7.60	8.89	9.58	10.18
Depth sub-surface shear stress (μm)	0.27	0.47	0.55	0.59	0.63

Table 6.2 Experimental contact values calculated using geometrical values from interferometric and AFM measurements of the wear scratches

	Load (mN)				
	10	**50**	**80**	**100**	**120**
radius sphere (μm)			5		
E* (GPa)			195		
a-contact radius (μm)	1.11	2.55	2.97	3.47	3.69
a-contact radius (μm)-corrected	0.65	1.5	1.74	2.04	2.17
Average contact pressure (GPa)	7.53	7.07	8.41	7.65	8.11
Maximum contact pressure(GPa)	11.3	10.61	12.62	11.47	12.17
Shear stress (GPa)	5.65	5.30	6.03	5.73	4.05
Depth sub-surface shear stress (μm)	0.31	0.72	0.83	0.97	1.04

Although the theoretical and experimental contact conditions did not match, for both sets of maximum contact pressures and shear stress levels were beyond the CoCrMo tensile yield strength (~450 MPa) and caused yielding and permanent

plastic deformation in the material. Note the average contact pressure values obtained from the experiments oscillated instead of following a linear trend, because they are calculated using the geometrical parameters (depth and width) from the experiments.

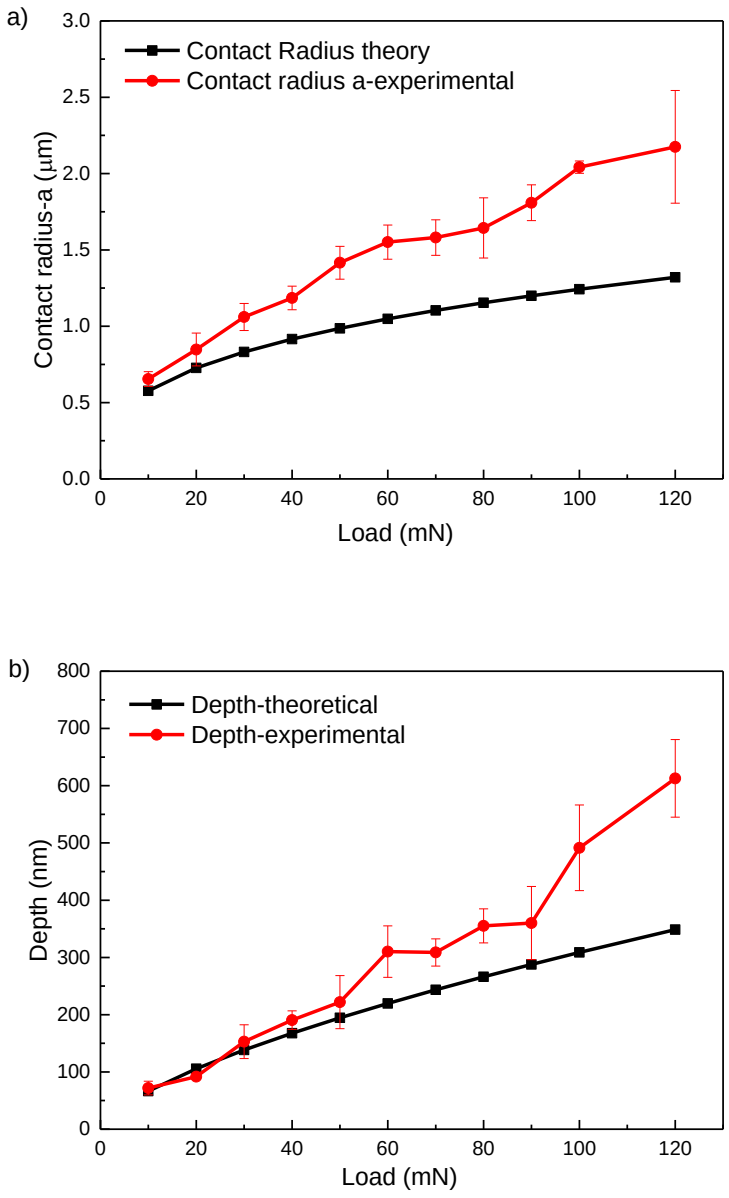

Figure 6.1 a) Theoretical and experimental contact radius values comparison, b) Theoretical and experimental depth values comparison

Figure 6.1a-b shows the theoretical and experimental contact radius and depth values respectively. Hertzian contact stress equations predicted the same contact radius for the 10 and 20 mN loads, but the values then diverged with the experimental values increasing by 25% to 50% for the 30 mN and 120 mN respectively. Comparison of the depth values showed the theoretical values supported the experimental ones up to a load of 50 mN, after which the discrepancy between values increases, with the highest loads (100 and 120 mN), also showing a difference of ~50%.

Plastic deformation depth data for the four CoCrMo alloys are shown in Figure 6.2. The plots summarise the average of 5 scratches per load per sample repeated in 5 different samples per alloy. Similar trends were found for the Forged, AC, AC-TT and AC-LC alloys. At 10, 20 and 30 mN loads there was no discernable depth increase, followed by a linear increase in depth with load up to 90 mN and then a reduction in the rate of the depth increase reaching maximums between 500 to 700 nm for the AC-TT and the AC-LC respectively. Statistical differences between the repetitions of the samples for the same alloy were only found in the samples marked with an asterisk (Figure 6.2).

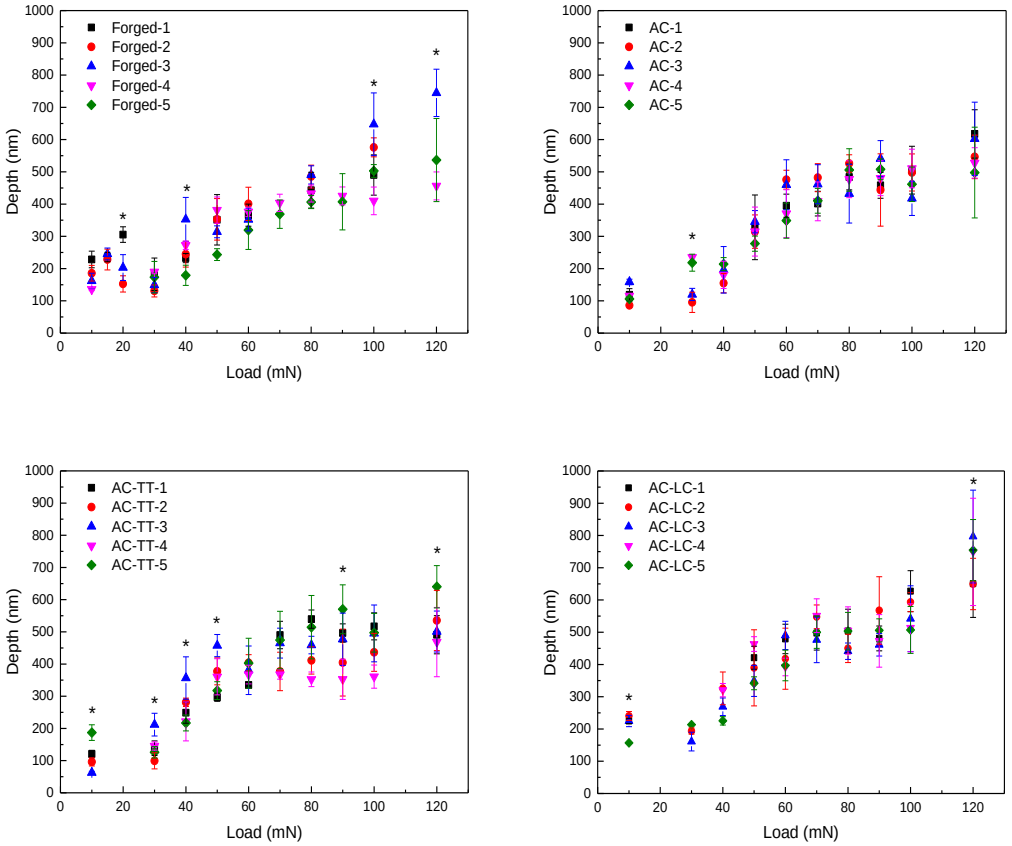

Figure 6.2 Depth measurements for each of the alloys for a load range from 10 to 120 mN

Measurable plastic deformation, as expected from yield stress criteria, was produced in all the alloys at each test load. The evolution of the scratch morphology with increasing load was shown by the AFM scans for scratch experiment at 10 mN, 60 and 120 mN loads (Figure 6.3a,b,c). For loads higher than 60 mN, the pile up on the scratch sides presented intricate 3D features. The shape of this features affected the depassivated area calculations, as explained in Figure 3.25, and therefore the corrosion current densities in Section 6.3.

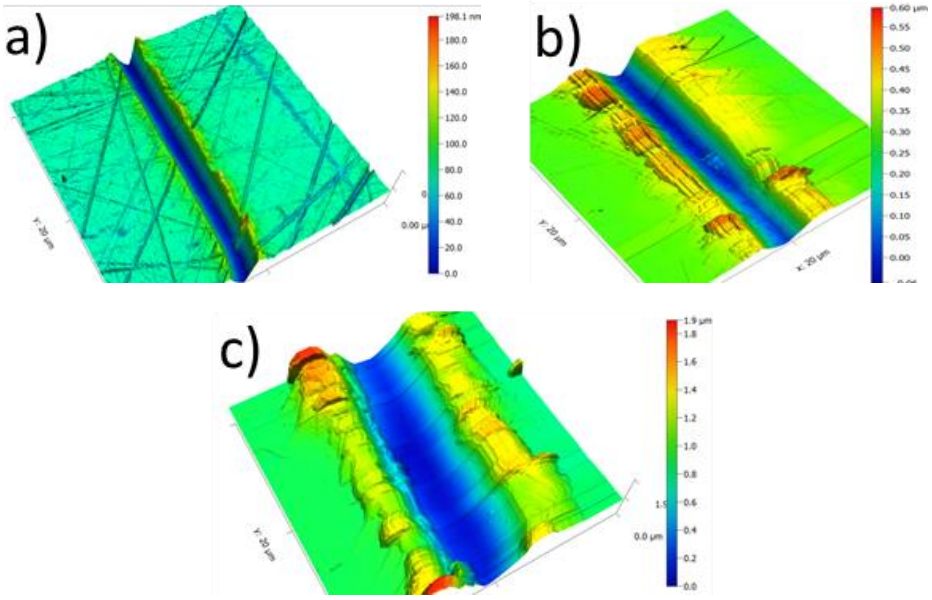

Figure 6.3 Example of the plastic deformation produced under: a) 10 mN, b) 60 mN and c) 120 mN loads

Comparison of the applied load and depth for the 4 different alloys, (Figure 6.4), demonstrated that the alloys displayed the same trend with increasing applied load. Statistical significant differences were found between the AC-LC samples and the rest of the alloys for the loads marked in orange in Figure 6.5. In addition significant difference were found between the AC and the AC-TT samples at 40 mN and the Forged and AC at 10, 40 and 90 mN loads. The high depth distribution found for each sample of each alloy, meant that averaging the results masked the three region trend described before.

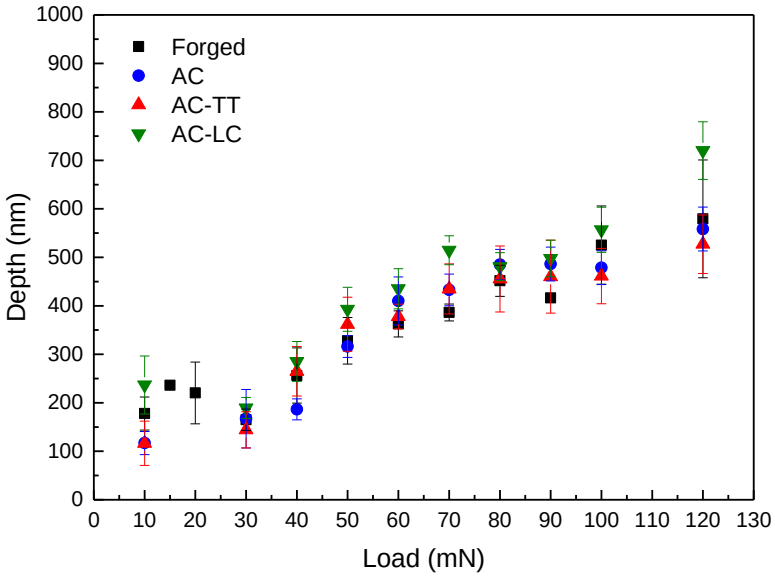

Figure 6.4 Depth measurements for each of the alloys for a load range from 10 to 120 mN

Forged	AC 10	30	40	50	60	70	80	90	100	120
10	0.04									
30		0.96								
40			0.07							
50				0.67						
60					0.14					
70						0.15				
80							0.17			
90								0.02		
100									0.33	
120										0.83

Forged	TT 10	30	40	50	60	70	80	90	100	120
10	0.12									
30		0.37								
40			0.82							
50				0.38						
60					0.44					
70						0.19				
80							0.92			
90								0.31		
100									0.24	
120										0.61

Forged	LC 10	30	40	50	60	70	80	90	100	120
10	0.2									
30		0.27								
40			0.46							
50				0.08						
60					0.02					
70						0.02				
80							0.21			
90								0.01		
100									0.52	
120										0.24

AC	TT 10	30	40	50	60	70	80	90	100	120
10	0.99									
30		0.59								
40			0.03							
50				0.19						
60					0.29					
70						0.95				
80							0.46			
90								0.55		
100									0.62	
120										0.43

AC	LC 10	30	40	50	60	70	80	90	100	120
10	0.03									
30		0.59								
40			0.02							
50				0.02						
60					0.46					
70						0.01				
80							0.84			
90								0.67		
100									0.96	
120										0

TT	LC 10	30	40	50	60	70	80	90	100	120
10	0.03									
30		0.11								
40			0.58							
50				0.41						
60					0.05					
70						0.04				
80							0.52			
90								0.41		
100									0.46	
120										0

Figure 6.5 Statistics done over the depth measurements for the average values for the four alloys: Forged, AC, AC-TT and AC-LC

6.3 Current density calculation: variable load tests

Transient currents were created when the oxide film was ruptured due to mechanical loading and/or relative motion between the tip and the surface. When the motion stopped and the load was removed, the oxide layer reformed. The time required for the layer to be reformed is known as the repassivation time and is an indicator of the kinetic reactions happening on the surface.

The current density (nA/μm²) for the four different alloys was plotted against the scratch load (mN) (Figure 6.6a-d).

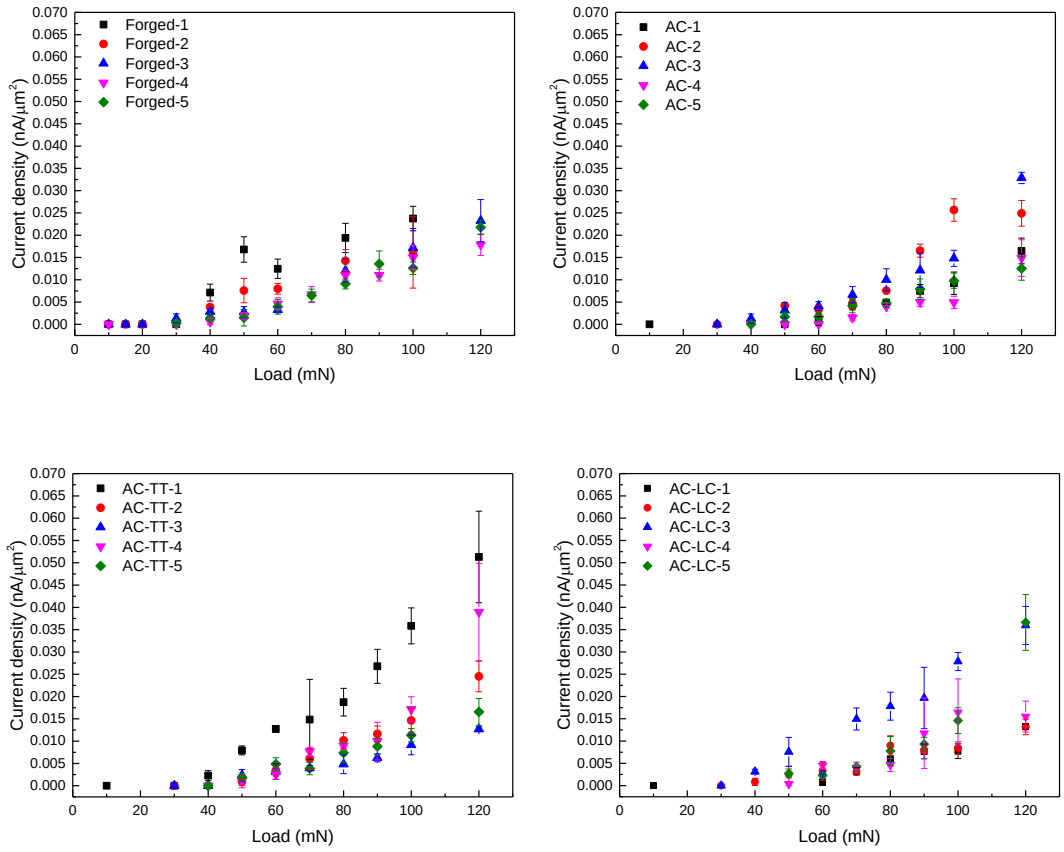

Figure 6.6 Average current density (nA/μm²) for the four alloys

The first significant peak above the noise level for the Forged sample occurred at 30 mN. As the load increased, mean peak current densities continued to increase linearly, reaching a maximum of 0.020 nA/μm² at a load of 120 mN.

The effect of load on mean peak current densities for the AC samples showed that the first detectable peak occurred at a load between 40 and 50 mN. The current densities increased rapidly with load, reaching a maximum value between 0.020 to 0.025 nA/μm^2 for the AC and AC-TT samples respectively.

Significantly different values were obtained between the Forged-1 samples and the rest of the Forged specimens for the 40 to 100 mN range. Comparison of the current densities for the 3 non-forged alloys, showed a higher distribution between the samples of the same alloy, especially for the AC-TT and the AC-LC samples. The maximum current density values were 0.030, 0.055 and 0.035 for the AC, AC-TT and AC-LC respectively. Higher current density values for the whole load range were observed in the AC-TT-1 and the AC-LC-3 samples. A different behaviour between all the samples in the alloys was found for the 120 mN loads in all the samples.

Figure 6.7 summarizes the median current density values for the 4 alloys. The median values instead of the average values were considered due to the high dispersion found due to the nature of the alloys. The "interquartile range", abbreviated "IQR", is the length of the box in the box-and-whisker plot and it measures how spread-out are the values around the central point. According to Tukey 1.5 times IQR is the limit for a value to be included inside the box. All the points outside the box are called “outliers”. The asterisks mark the extreme values. There was a rapid increase in the current density with load. The Forged samples generated higher current transients at lower loads, starting at 30 mN, while the As Cast samples all started between 40 and 50 mN. No statistically significant differences were found between the current values of the As Cast samples. The current density difference between the As Cast and Forged alloys decreased as the load increased, with no statistically significant difference at 100 and 120 mN loads.

At open circuit potential conditions, for all the load levels from 40 to 100 mN, the current densities observed in the Forged alloy were at least 50 % higher than the other alloys. At 120 mN the trend was not clear as the dispersion in the AC-TT alloy values was too high to obtain conclusions.

6.4 Repassivation kinetics

Decay current variation with time was measured from the current-time data graphs generated during the scratch-corrosion experiments, as described in Section 3.7.5.2. The rate at which the repassivation process takes places is directly related to the amount of corrosion product released into the body.

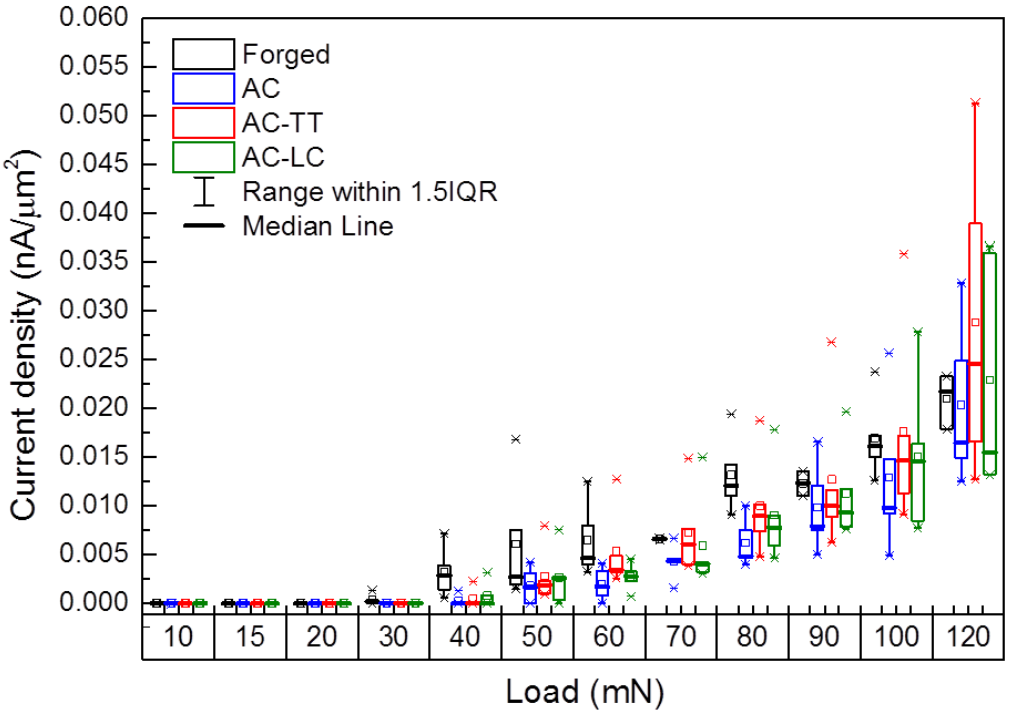

Figure 6.7 Current density-load dependence relation for the Forged, AC, AC-TT and as AC-LC

Similar current curves to the ones described in Section 3.7.5.2 describe the repassivation kinetics after scratch-corrosion experiments as a first order exponential decay.

Experiments were carried out under different loading regimes. For low loads (from 10 to 60 even 70 in some cases) it was not possible to calculate valid repassivation times because the noise signal was too high. Repassivation times constant τ_1 calculated according to Section 3.7.5.2, and defined as the time to restore i_{corr} prior to scratching, for the 80, 100 and 120 mN loads are compared for the Forged, AC, AC-TT and AC-LC specimens in Figure 6.8. Statistical significant differences between the alloys were marked with an asterisk. The Forged alloy had a longer repassivation time for all the loads when compared to the other alloys. The average values for the forged alloys were 131, 138 and 153 ms for the 80, 100 and 120 mN loads, compared to values between 30 to 33 ms for the AC and AC-TT loads and 66 to 106 ms for the AC-LC at 80 and 120 mN respectively. Although there was a great deal of scatter within the data, the repassivation kinetics were load and deformation dependant, increasing in line with load and deformation. The statistical differences diminished when the load was increased. At 80 mN, all the repassivation time constants were different, while at 120 mN only the Forged alloy was significantly different to the AC and AC-TT.

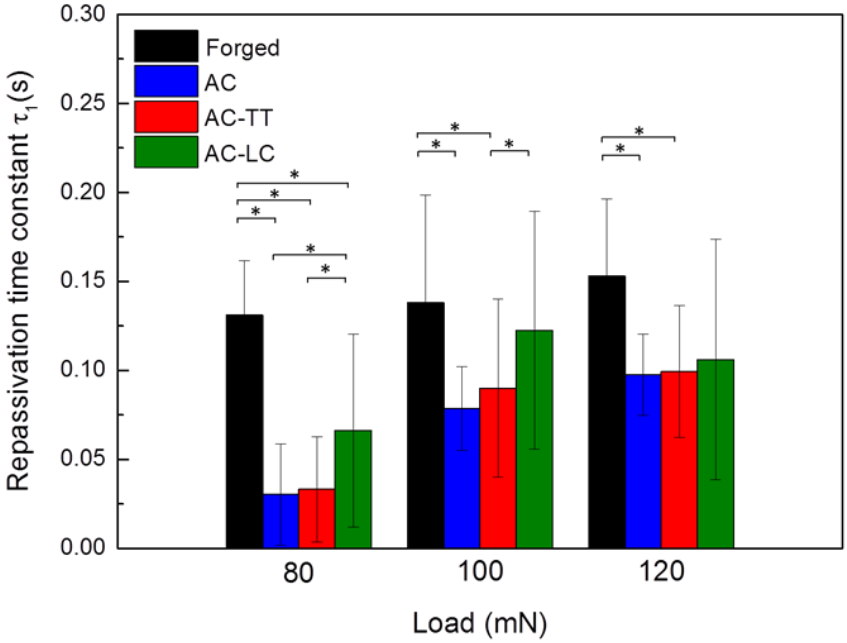

Figure 6.8 Repassivation time under different load conditions: 80,100 and 120 mN for the Forged, AC, AC-TT and AC-LC

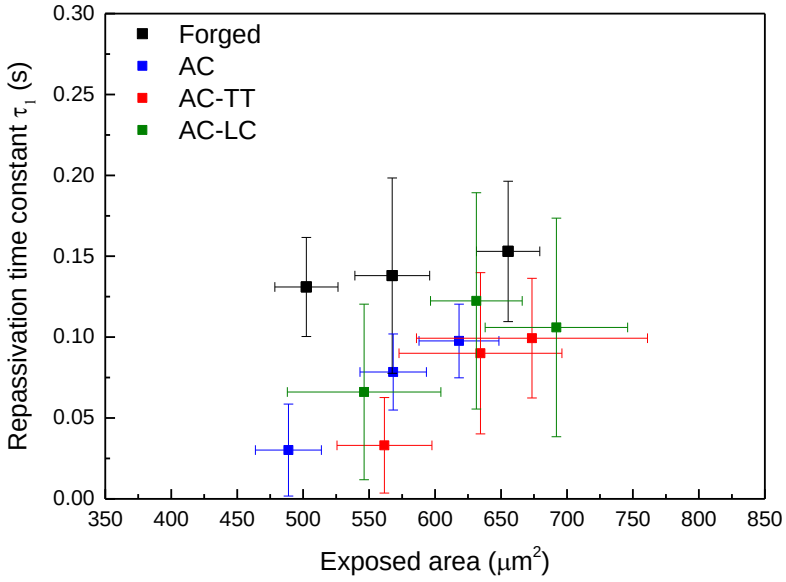

Figure 6.9 Repassivation time- exposed area correlation for the Forged, AC, AC-TT and AC-LC alloys

Correlating the repassivation times and the exposed area subjected to repassivation, calculated according to Section 3.7.5.2, showed that for a similar exposed area value for the As Cast samples, the Forged samples presented repassivation times 40 % higher, Figure 6.9. The AC-TT and AC-LC samples had slightly lower repassivation times, 10-20 ms, with higher exposed areas, 50 μm^2, than the AC, which had lowest affected area values but took longer to repassivate compared to the thermal treated and the low carbon alloys.

6.5 Scratch scars morphology evaluation

Micrometre wide scratches are visible on retrieved MoM implants. They have been found on the articular surfaces [250]and also at the surface of the femoral stem within the cement-stem interface [251]. These scratches are thought to be caused by third body particles generated in vivo for the articular surface and because of the radiopacifier particles present in the cement.

The deformation to the surfaces of the CoCrMo alloys was observed using high resolution SEM and AFM examination. The deformation modes were correlated to the current density and repassivation kinetic results discussed in previous sections. All the pictures were taken in relevant regions of the scratches with the sliding direction of the indenter moving from the upper part of the picture moving downwards. Pronounced activation of different crystallographic systems was observed around the scratch areas with specific modes of deformation depending on the grain orientation of the sample.

The following nomenclature was used in this section for the different samples and loading conditions:

Nomenclature	**Letter**	**1st number**	**2nd number**
Stands for	Type of alloy	Number of sample	Load applied
Example	F-3-80		
Possible options	F: Forged AC: As cast AC-TT: thermal treated AC-LC: low carbon	1-5	10-120

6.5.1 Forged alloy

Figure 6.10 shows high resolution micrographs of scratches on the forged CoCrMo sample at 50, 80 and 100 mN loads.

The images showed the scratches resulted in four different plastic deformation mechanisms:

- Slip band traces forming triangular features on the edges of the scratch areas seen in F-4-50, F-4-80 and F-4-100 mN, F-5-80 and F-5-100 mN.
- 45° degrees slip lines adjacent to the scratch edge, see F-4-80 mN.
- Micro cutting producing extruded material at the edges, as seen in F-1-100 mN.
- Formation of semi-circular cracks inside the scratch area in the same direction as the indenter movement, see F-4-80 mN and F-5-50 mN.

The images of scratches on F-1-50 and F-1-100 samples showed grooves within the scratch, orientated in the scratch direction, suggesting asperities on the tip or small particles trapped between the tip and the surface which were dragged through the contact. This type of two body grooving abrasive deformation mechanism was only seen in this sample and it was included to explain the high scatter in the current densities values presented in the sample. The width of the groove was estimated from SEM images to be between 230 to 615 nm for the F-1 sample. Before imaging the samples under SEM, they were ultrasonically cleaned, therefore no particles or loose debris were found on the surface.

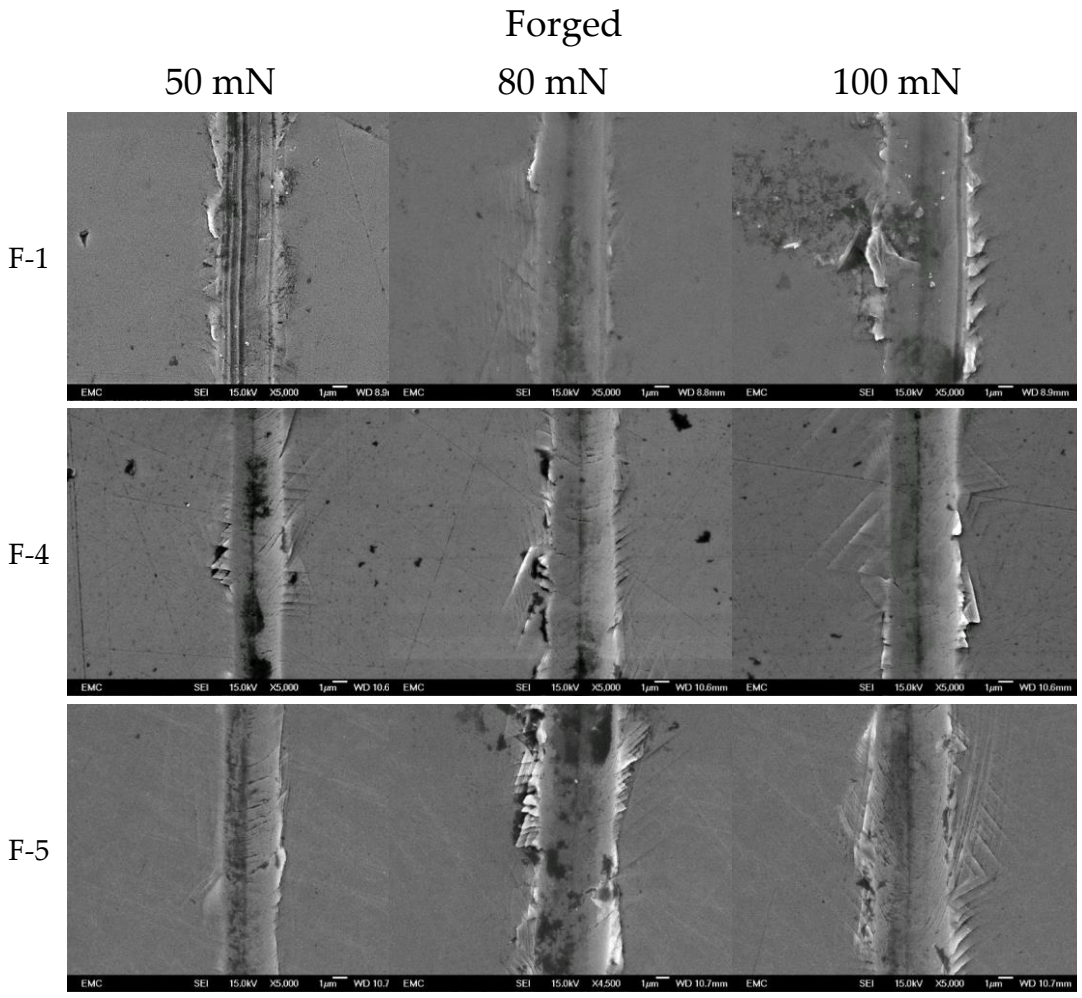

Figure 6.10 SEM pictures for forged-1, forged-4 and forged-5 samples under 50, 80 and 100 mN. Scratch direction from the top to the bottom of the pictures

The generation of directional grooves inside the scratch led to a higher exposed area subjected to depassivation and therefore higher currents densities were obtained.

6.5.2 As cast alloys

6.5.2.1 As Cast

Figure 6.11 shows the micrographs for the as cast samples. AC-1 and AC-5 show slip lines at 45 °degrees to the scratch direction which becomes more pronounced as the applied load is increased.

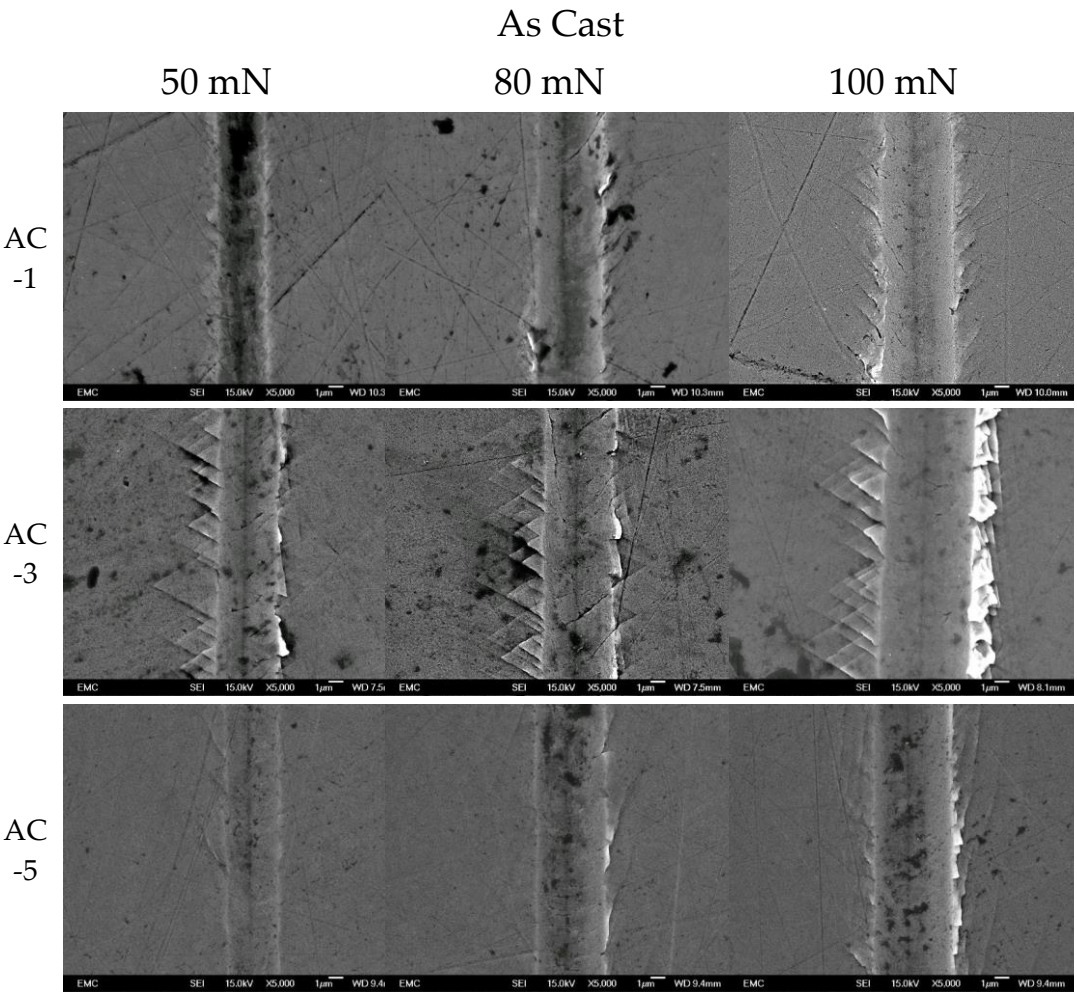

Figure 6.11 SEM pictures for AC-1, AC-3 and AC-5 samples under 50, 80 and 100 mN

The deformation around the scratch in AC-3 presented as symmetrical triangular slip lines for the 50 and 80 mN loads samples with a triangle side size between 1 to 4 μm.

When the load level was increased to 100 mN, AC-3-100, the image indicated the load was enough to deform the triangular slip bands around itself creating a folded structure on the right side of the scratch area. Cracks in line with the triangular structures were observed inside the scratch scar of the AC-3-50 and AC-3-80 mN.

6.5.2.2 As Cast-Thermal Treated

Micrographs of the AC-TT samples are shown in Figure 6.12. The AC-TT-1 alloy showed increasing levels of micro-cutting as the load was increased.

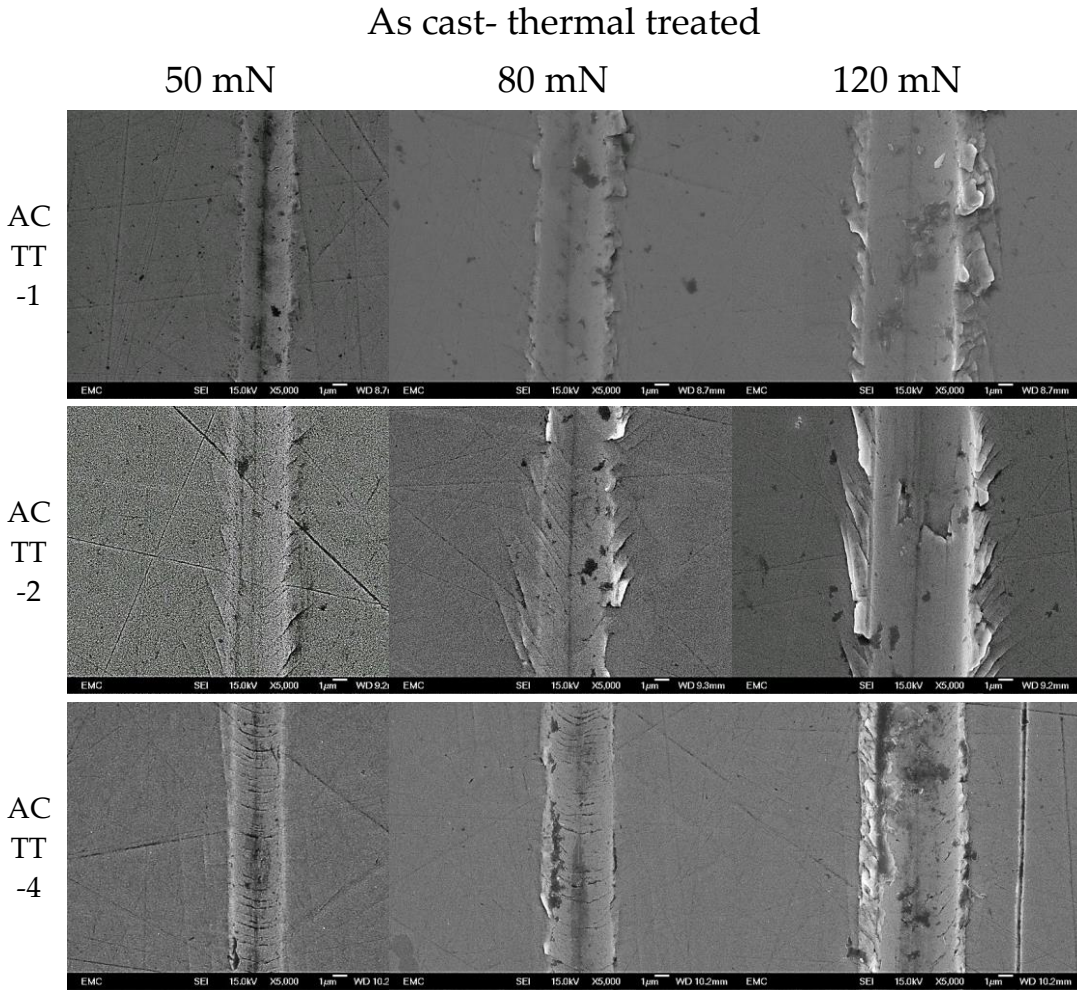

Figure 6.12 SEM pictures for AC-TT-1, AC-TT-2 and AC-TT-4 samples under 50, 80 and 120 mN

45° diagonal slip traces were visible to the sides of the scratch of the AC-TT-2 sample for all the loading conditions. For the AC-TT-2-50 and AC-TT-2-80 tests the diagonal slip traces continue inside the scratch groove. There were lower amounts of pile up on the sides of the AC-TT-4-50 and AC-TT-4-80 sample scratches, compared to the other two thermal treated samples and semi-circular cracks were visible within the scratch track in the same direction as the indenter movement.

6.5.2.3 As Cast-low carbon

SEM images for the AC-LC samples are shown in Figure 6.13. Non-symmetrical slip line traces at 45 degrees to the scratch direction were visible on one side of the scratch scar for the AC-LC-2, AC-LC-3-50 and AC-LC-5-80 mN loads.

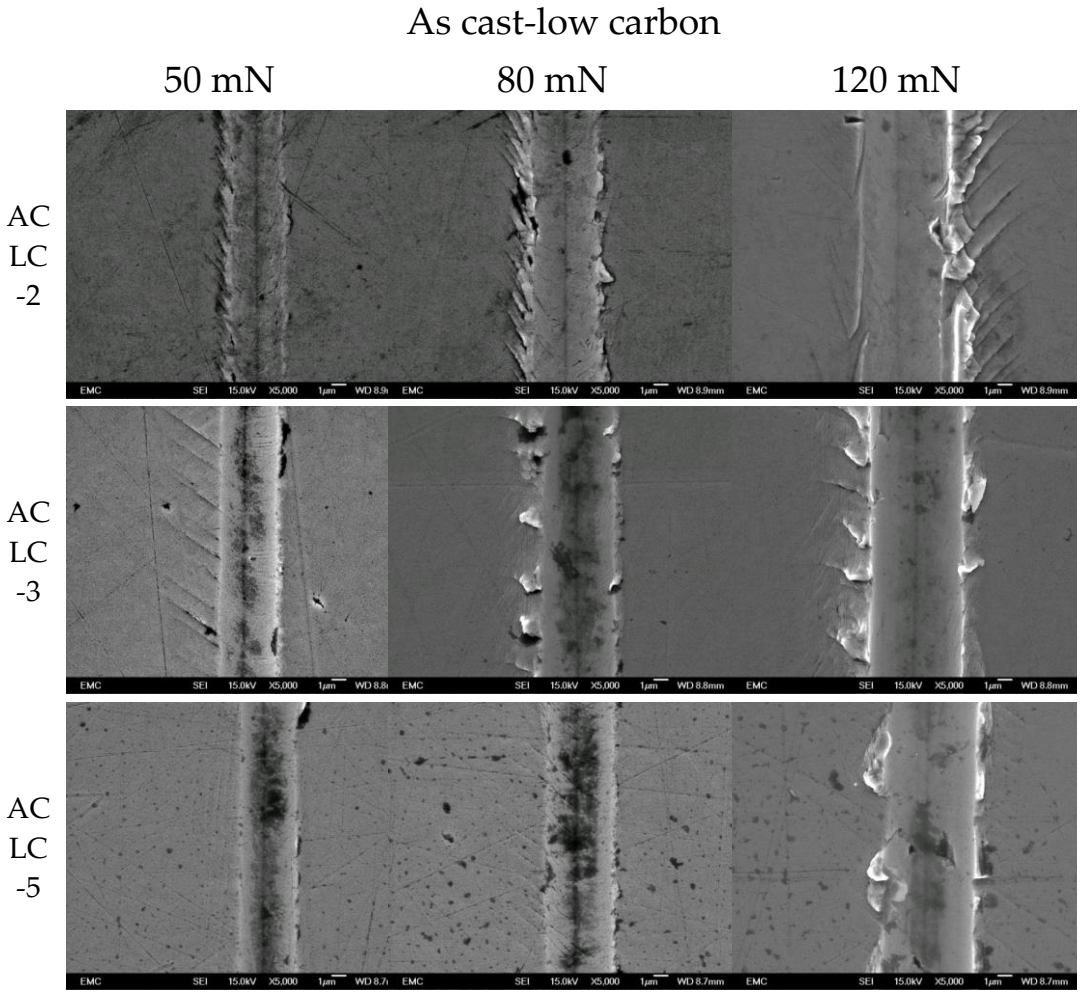

Figure 6.13 SEM pictures for AC-LC-2, AC-LC-3 and AC-LC-5 samples under 50, 80 and 120 mN

The rest of the samples, AC-LC-3-80 and 120 mN and AC-LC-5-120 mN revealed micro-cutting and material displacement at the edges of the scratch scar which increased in magnitude with load.

Pile up material at the end of the scratches was found in some samples (AC-LC-5), indicating material was not only displaced on the sides of the scratch but also removed by micro-cutting, see. Figure 6.14. The material was pushed forward in front of the indenter, resulting in material pile up at the end of the scratch.

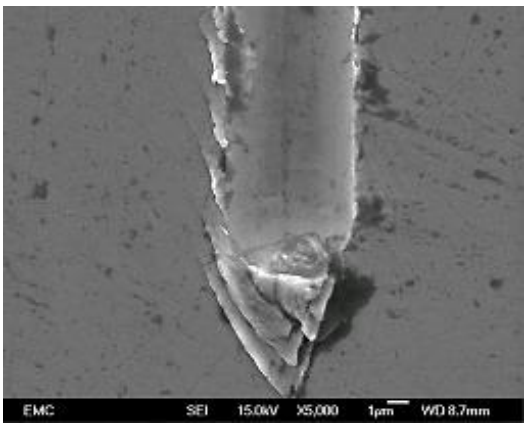

Figure 6.14 SEM micrograph for the AC-LC-5-100 mN showing microcutted material at the end of the scratch scar

6.5.3 Carbide influence on scratch morphologies

As described in the microstructural characterization, Section 3.4, the AC and the AC-TT samples presented carbides with two different morphologies: bulk solid and fragmented respectively. The deformation caused by the tip changed when the scratch passed over the carbides. Figure 6.15 shows how the amount of pile up and the scratch width were reduced when the scratch passed over a carbide, with no observable slip lines or micro-cutting signs.

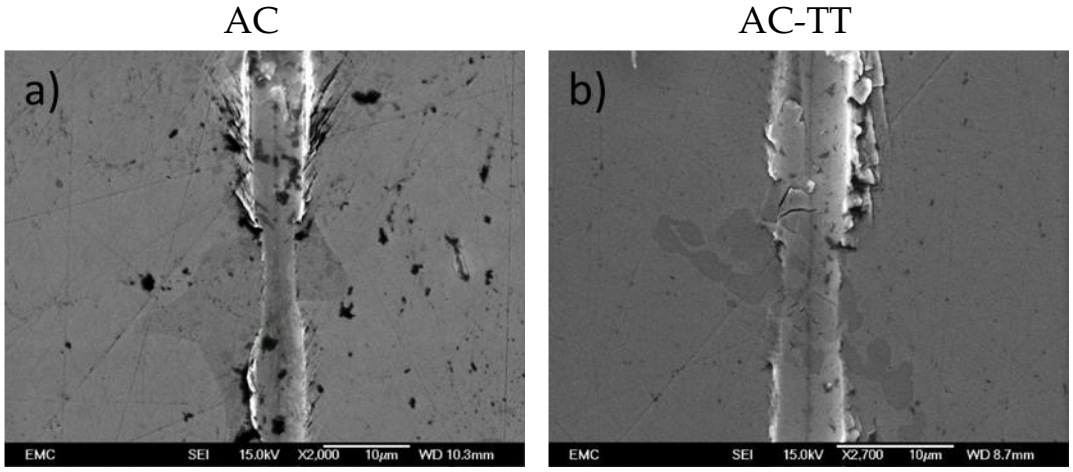

Figure 6.15 a) As cast 120 mN scratch over a bulky carbide, b) As Cast-TT 120 mN scratch over a " island-like" carbide

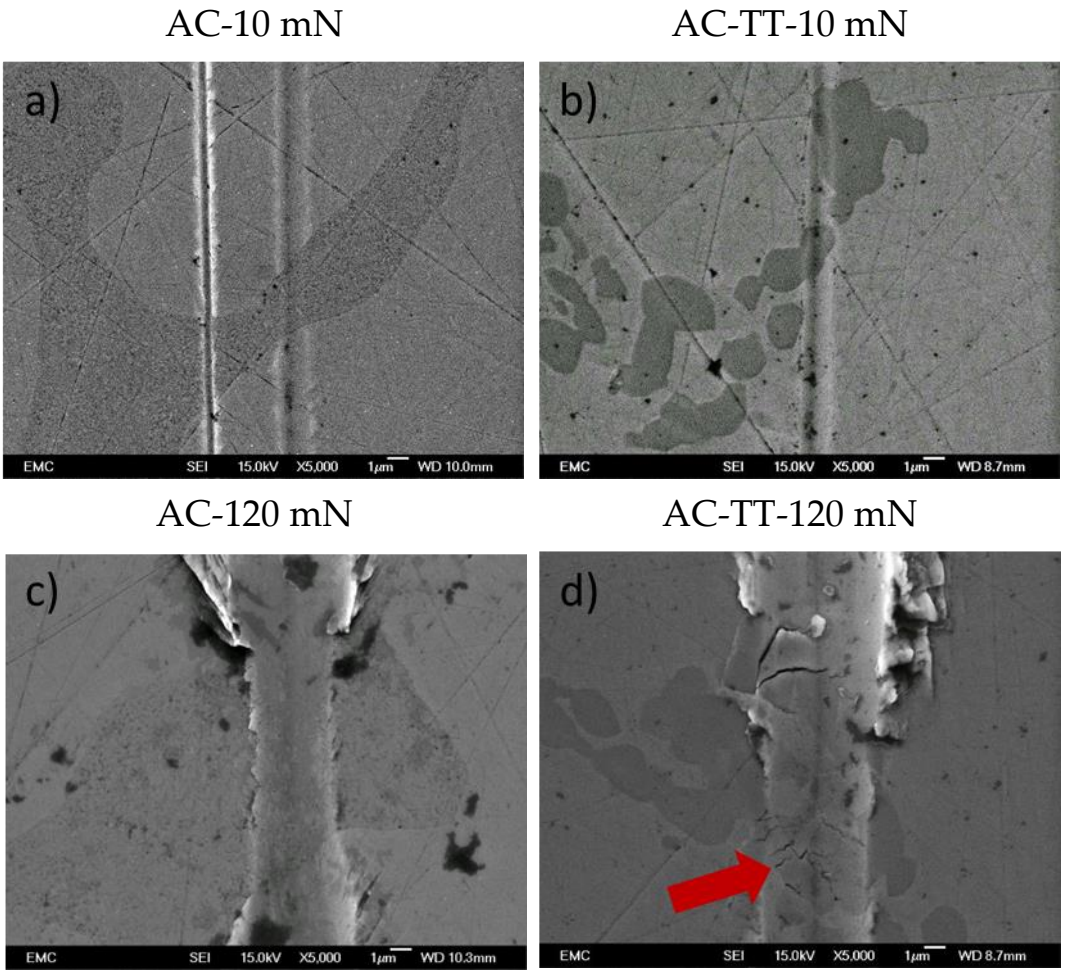

Figure 6.16 a) AC-10 mN load scratch over a carbide, b) AC-TT-10 mN load scratch over a carbide, c) AC-120 mN load scratch over a bulky carbide and d) AC-TT-120 mN load scratch over a "island-like" carbide

The influence of load is visible in Figure 6.16. Under a 10 mN load scratch the carbide in the AC and the AC-TT samples absorbed the deformation and they deformed with the matrix. However, when the load was increased, the bulky carbides were deformed without apparent sign of fracture while the fragmented carbides fractured creating cracks inside them, as shown by the red arrow in Figure 6.16d.

Transverse and cross-sectional depth profiles obtained from the interferometry measurements, (Figure 6.17 and Figure 6.18) demonstrated that the carbides reduce the deformation and scratch depth, when compared to the matrix deformation.

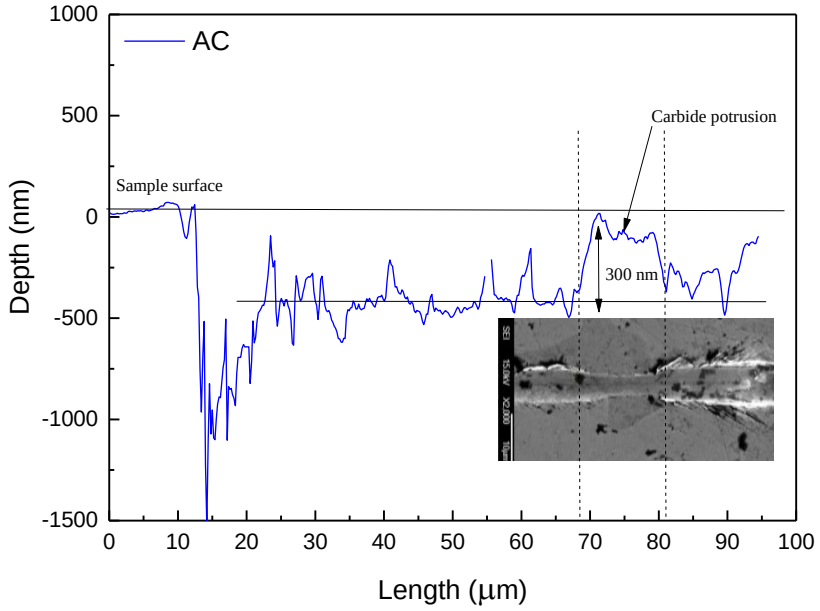

Figure 6.17 Transverse profile inside the scratch track of an AC sample showing the different plastic deformation between carbide and matrix areas

The cross-sectional profiles through the scratch (Figure 6.18) demonstrated the difference in the scratch depth and pile up between the carbide (black) and matrix areas (red) 600 nm and 250 nm vs 175 and 150 nm for the matrix and carbide respectively. In addition, the red profile demonstrated that the pile up on the edge of the scratches can reach heights around 200 nm, increasing the surface area subjected to depassivation.

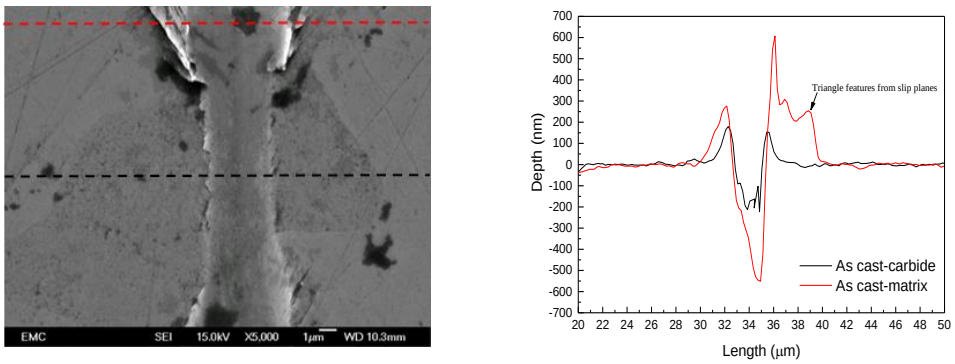

Figure 6.18 Cross section profiles in a carbide (black line) and a matrix area (red line)

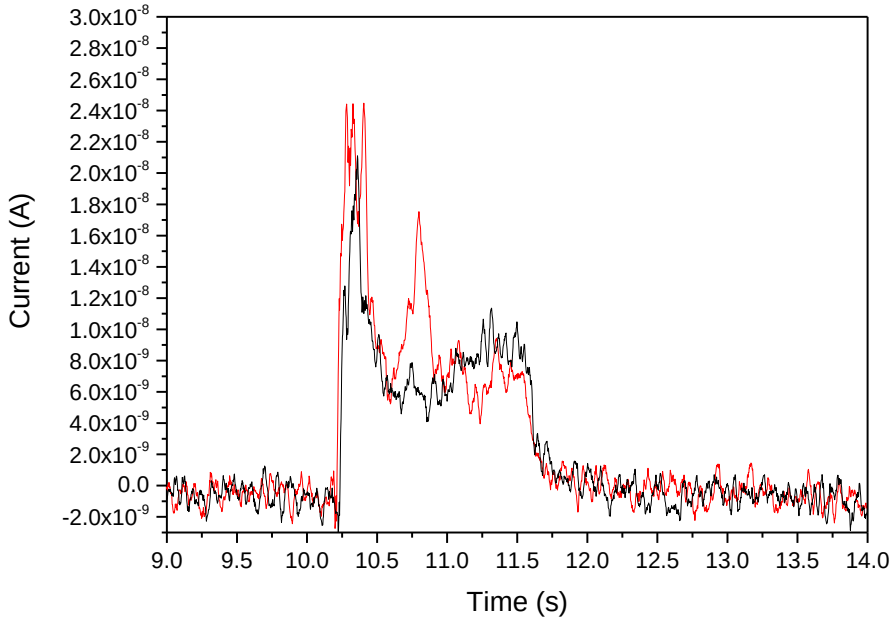

Figure 6.19 Example of a current-time graph for a scratch over a matrix area (black) and over a scratch passing over carbide (red)

In terms of electrochemical response, the system was able to register differences in the current transients generated when the tip passed over a carbide. Figure 6.19 compares between the current recorded when the scratch was done fully over the matrix (in black) and when the scratch passed over a carbide (in red). A current peak appeared when the indenter passed through the carbides with a 50% current increase with respect to the average current for that specific scratch.

6.6 Crystallographic grain orientation analysis

The results of the scratch testing in Sections 6.2 and 6.3 showed that there were differences between the alloys but also a large amount of scatter within the current density results for particular alloys. In addition there were differences in the deformation morphology between the alloys and the different samples of the same alloys, clearly identified in current transient values from Figure 6.6.

To determine the underlying origins of these differences, the crystallographic grain orientation was analysed. To analyse the grain orientation around the scratches, crystallographic orientation maps were acquired by EBSD on a selection of the characteristic samples. The resulting data was compiled into

inverse pole figures for each phase, fcc and hcp, to confirm the specific orientation of the grain.

6.6.1 Grain maps and phase maps

Left column in Figure 6.21 shows EBSD grain orientation maps on the scratched regions for the four CoCrMo alloys. Each colour represents a specific crystallographic orientation according to the inverse pole figure (IPF) colouring legend shown in Figure 6.20.

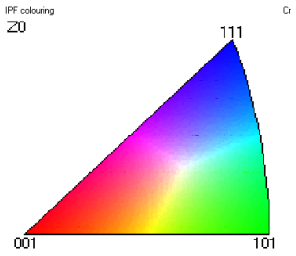

Figure 6.20 Inverse Pole Figure crystallographic orientation colouring legend

Heavily deformed areas (scratches), non-etched areas (carbides) or regions not properly prepared, produced poor Kikuchi patterns where diffraction was suppressed and they are shown as white non-indexed areas. However, the EBSD maps enabled the determination of the crystal orientation in the grains where the scratches occurred.

The Forged-1 and Forged-4 grain orientation maps showed the 5-10 μm grain size of the microstructure shown previously, (Section 4.2.2), with a mixture of crystallographic orientations across the scratch surface. In contrast, the AC, AC-TT and AC-LC samples showed only one preferred crystal orientation under the examined area. The single colour representation of the crystallographic orientation varied depending on the crystal orientation of the specific grain and is marked with a black dot in the individual colour legend on the left side of each map in Figure 6.21.

	Grain Orientation map	Phase map
Forged -1	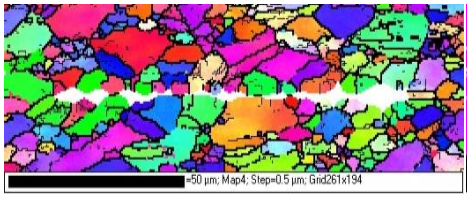	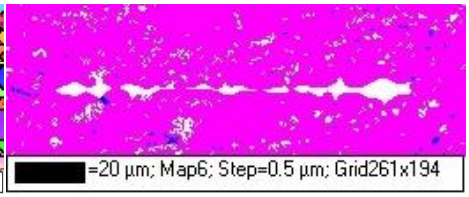
Forged -4	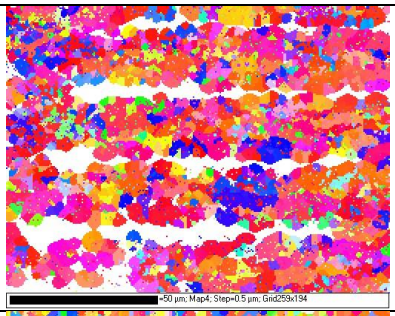	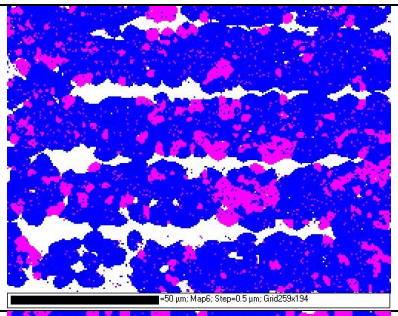
AC-1	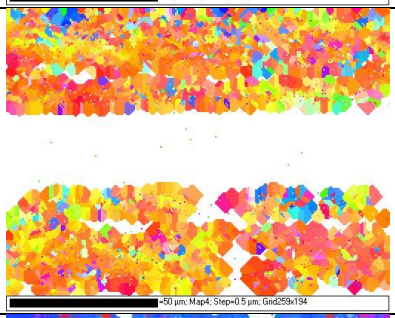	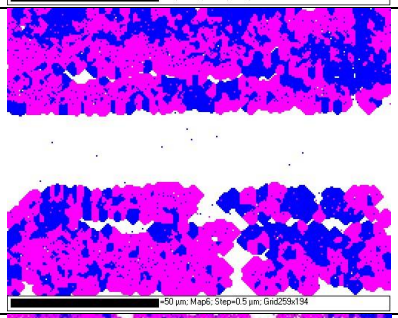
AC-3	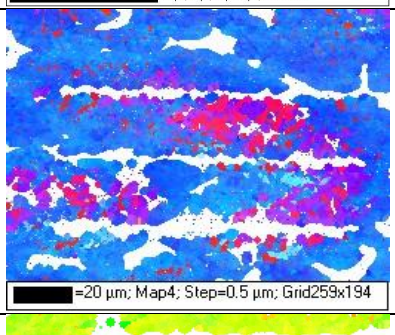	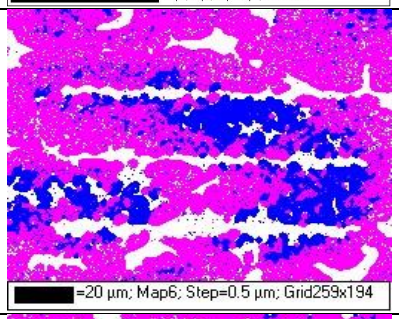
AC-TT-1	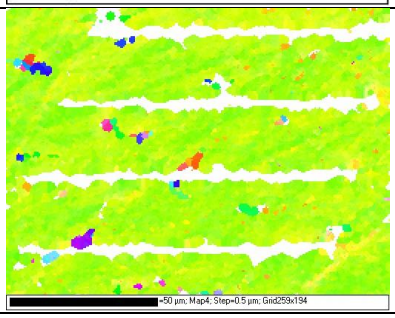	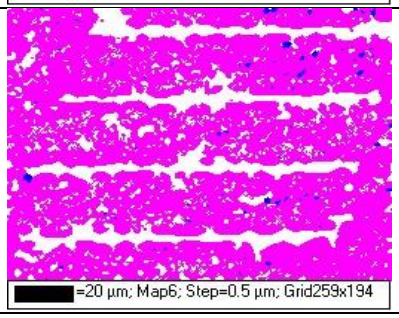

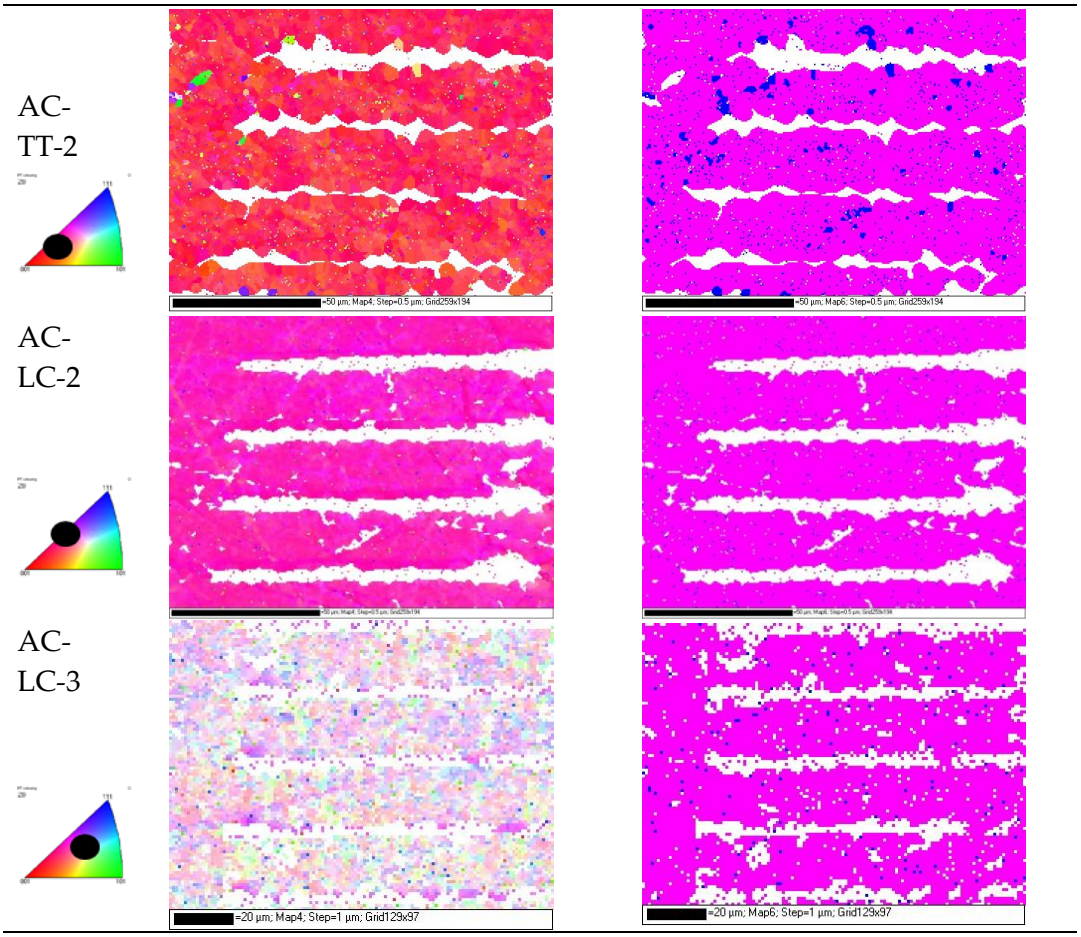

Figure 6.21 Left column: Grain orientation maps for the relevant samples under study. Right column: Phase maps for the relevant samples under study

The right column of Figure 6.21 summarises the phase maps for the samples. The pink colour represents the fcc phase while blue is for the hcp phase. Differences were found between the two forged analysed samples. Forged-1 showed an average of 96 ± 1.42 % fcc phase and a 3.24 ± 1.42 % of hcp phase, while Forged-4 presented an opposite trend with a 18.42 % fcc phase and 81.57 % of hcp phase. The as cast samples, AC-1 and AC-3, contained almost equal amounts of fcc and hcp with a balance of 54.83 ± 18.30 % fcc and 45.16 ± 18.30 % hcp phase. The AC-TT and AC-LC samples had similar percentage phase distributions with 96.76 ± 2.30 and 98.82 ± 0.22 for the fcc phase and 3.23±2.30 and 1.17 ± 0.22 for the hcp phase respectively. In general, the alloys exhibited an fcc structure with the exception of a few samples (Forged-4 and AC-3) where the hcp fraction was higher.

6.6.2 Inverse Pole Figures

The inverse pole figures (IPF) of the scratch microstructures are shown in Figure 6.22. Due to the colour contrast in the orientation maps, the orientation dependence of the scratch morphologies can be readily compared between the different alloys. The left column shows the specific crystal orientation for the crystals with fcc phase and the right column the ones with hcp phase. All the results presented in this section are focused in the Z axis (third triangle from IPF figures) since this is the axis of loading during the experiments.

The forged alloy IPF figures showed that there was no tendency for a preferred orientation and that there was a wide range of different colours and indexed points spread around the triangle. This trend was clearer in the F-1 sample than in the F-4 one since the percentage of fcc oriented crystals was higher. Hcp oriented crystals in the Forged-1 sample did not show a specific orientation, while the Forged-4 specimen hcp grains were mainly positioned around the basal plane (0001) (Figure 6.22).

In contrast to this, the AC samples exhibited a really high crystal orientation trend. Each alloy under study presented a specific grain orientation as indicated in the left column of Figure 6.22. AC-1 was orientated close to the basal plane (001) and slightly tilted towards the (101) with an orange-yellow colour, while AC-3 was close to the (111), dark blue, which is the main slip system for cubic structures.

The AC-TT samples also exhibited specific crystal orientations, (001-101) for the AC-TT-1 and (001) for the AC-TT-2. Finally the AC-LC samples presented a pink colour related with a crystal orientation between the (001 -111) planes for the AC-LC-2 and a pale pink colour for the AC-LC-3 which revealed a misorientation angle for the plane not oriented in any of the main characteristic directions. Therefore, the indexed points appeared in the centre of the triangle.

The low % of hexagonal phase grains in the as cast samples was not high enough to relate them with a specific crystallographic orientation, and the IPF triangles are therefore white. However, the AC-3 sample presented a cluster of points in different areas of the triangle, red, blue and violet, with a higher number positioned in the violet area than for the hcp phase, related with an orientation between the basal plane (0001) and the prismatic plane (2-1-10).

Forged-1	
fcc	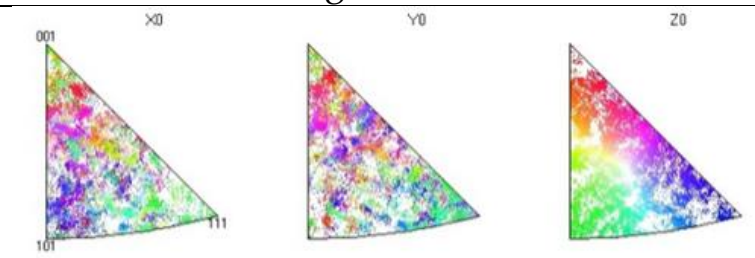
hcp	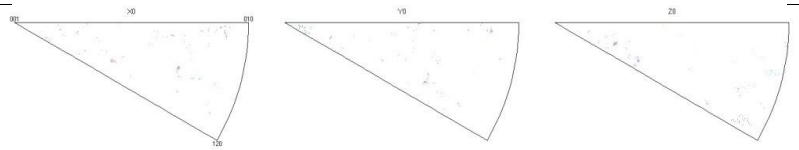
Forged-4	
fcc	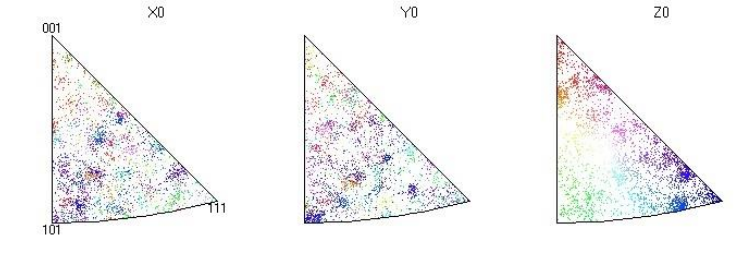
hcp	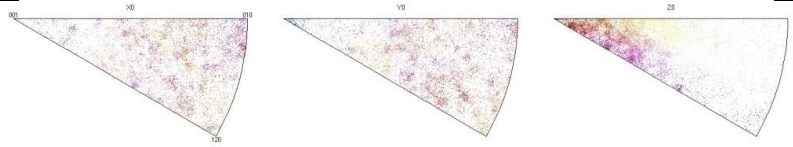
AC-1	
fcc	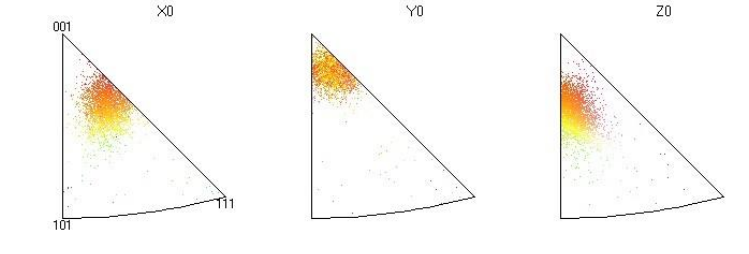
hcp	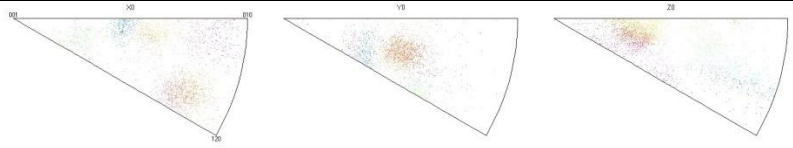

AC-3	
fcc	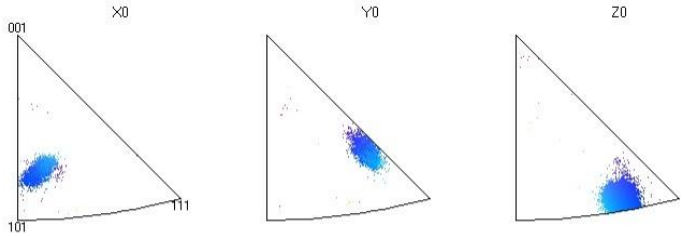
hcp	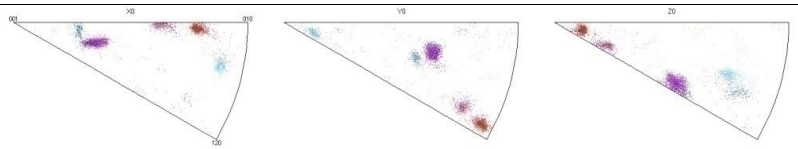
AC-TT-1	
fcc	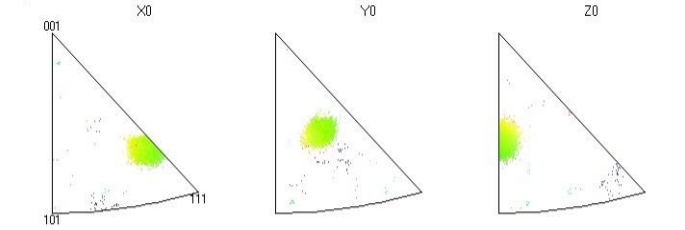
hcp	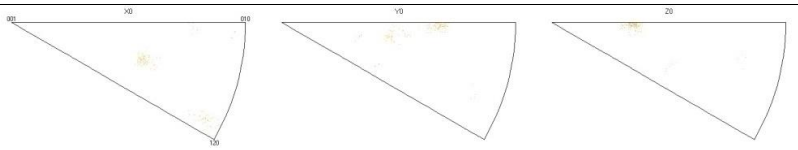
AC-TT-2	
fcc	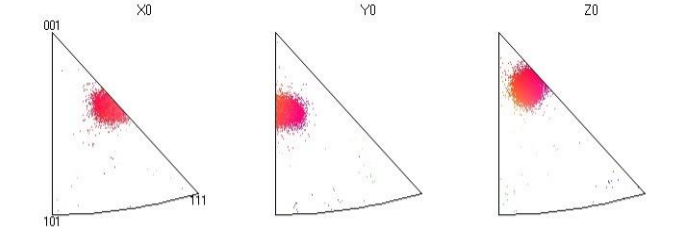
hcp	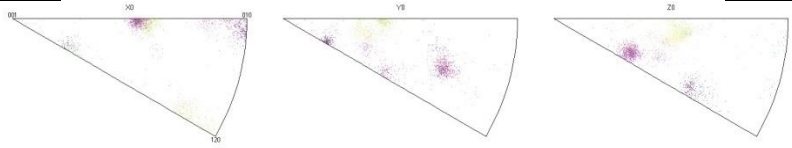

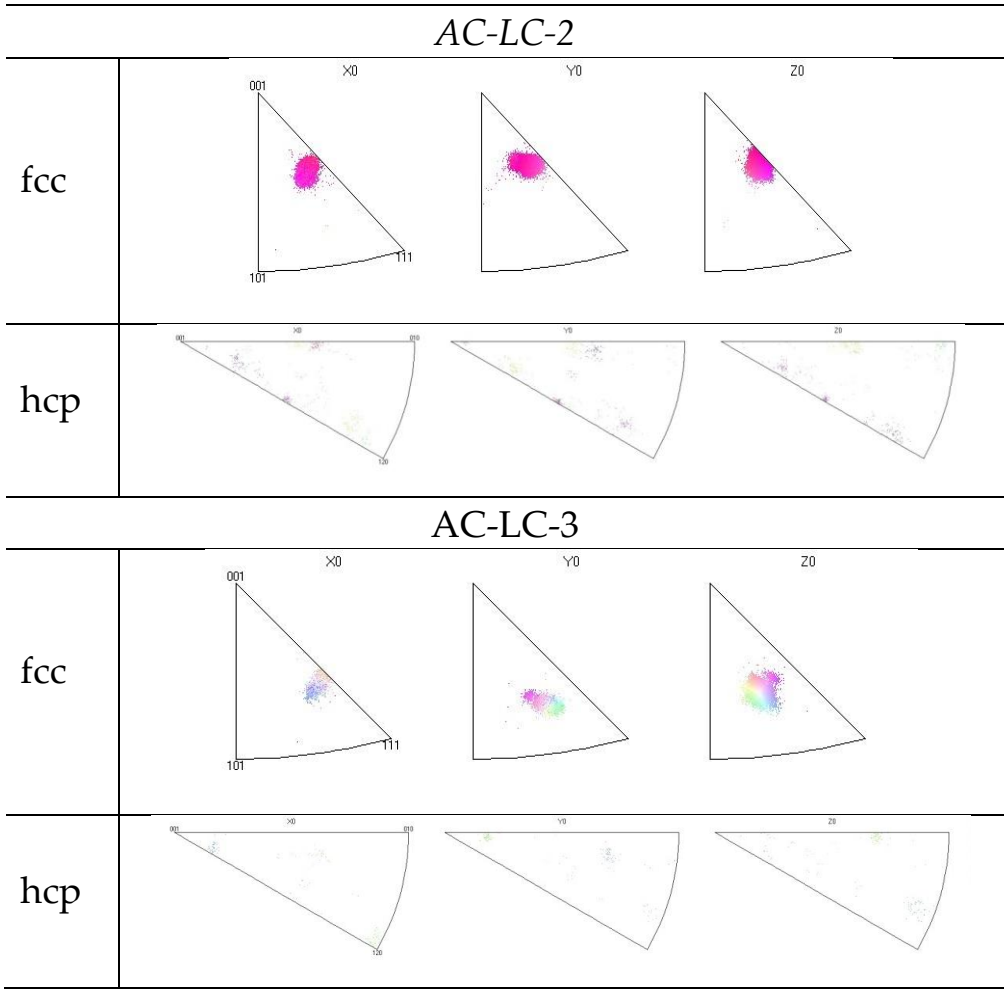

Figure 6.22 Inverse pole figures for the fcc phase and hcp phase for the relevant samples analysed by EBSD

6.7 Influence of grain orientation analysis

After finding a great dispersion within samples obtained from the same implant, it was noticed that the grain orientation in the metal was the key factor which governed the repassivation process under different contact conditions. Several deformation mechanisms were found within the same alloy depending on the grain orientation where the scratches were produced, as is shown in Figure 6.23 where examples of specific deformation modes have been related with their specific grain orientation on top of the inverse pole figure colouring legend, independently of the thermal treatment or the carbon content.

Re-analysis of the previous data (exposed area, current transients and repassivation time constants) in terms of crystal orientation instead of alloy type,

demonstrated that As Cast grains with random orientation or orientation between two specific crystal orientations presented the highest current density values, see Figure 6.24 (samples over the green and center areas respectively in Figure 6.23). They were followed by the poly-crystalline Forged alloy (also with multiple orientations, on the right top side of Figure 6.23) and finally the grains oriented in the basal (samples on the red, orange and pink areas of Figure 6.23) and main slip planes with the lowest values (blue area). Regarding the general orientation dependence of the scratch topographies, see Figure 6.23, similar orientation showed comparable patterns. In some cases the analysis became complicated by the activation of different kinds of deformation systems and the potential interaction between them (fcc and hcp mixed crystal structures).

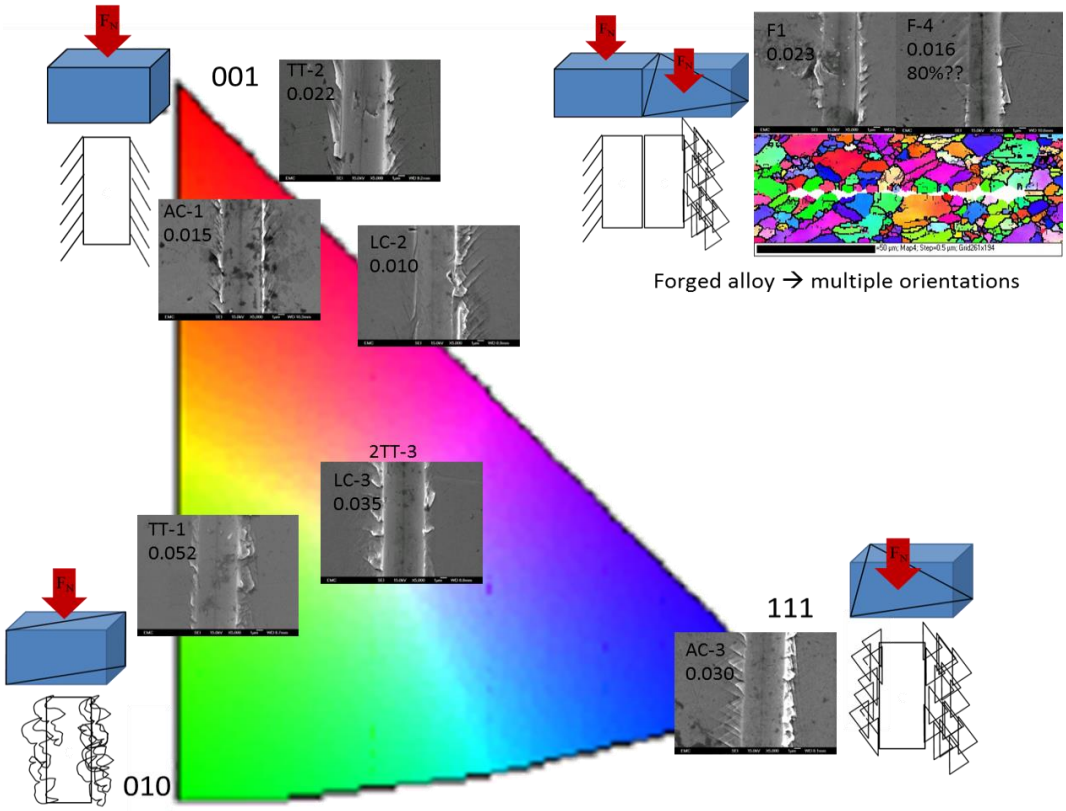

Figure 6.23 EBSD inverse pole figure summary with the main relevant deformation mechanisms found in the CoCrMo alloys respect to their specific crystallographic grain orientation. (001) (red upper corner) correspond to the alloys oriented on the basal plane, (010) (green lower corner) correspond to the samples oriented on the "edge" plane and (111) (blue right corner) makes reference to the main slip plane in an fcc structure

Statistically significant differences were found in the repassivation processes indicating different kinematics related with the affected areas and the deformation levels, (Figure 6.25). Samples with higher current density values,

(Forged and multiple oriented As Cast grains) had the highest repassivation times which increased with load. Those samples were the ones which presented higher levels of micro-cutting on the sides of the scratch-groove (for As Cast samples, Figure 6.12, AC-TT-1 and Figure 6.13 AC-LC-3) and multiple combination of damage mechanisms (triangular and angular slip lines and micro-cutting) presented in the Forged sample were due to its multiple grain structure orientation, see Figure 6.10. Repassivation times for the basal (Figure 6.11, AC-1) and main slip plane orientations (Figure 6.11, AC-3, Figure 6.12, AC-TT-2 and Figure 6.13 AC-LC-3) showed values 50% lower than the previous ones with triangular slip lines for the samples with (111) orientation and angular slip lines deformation mechanisms for the basal plane oriented samples as the more relevant ones.

Figure 6.26, shows the correlation between the repassivation kinetics constant τ_1 and the exposed affected area. For exposed areas between 500 and 600 μm^2 the Forged alloy showed τ_1 values of 130 ms while the As Cast samples oriented in the (111) plane and the basal plane (001) were reflecting values between 80-100 ms and 40-50 ms respectively. As Cast samples with multiple oriented grain time constant was 110 ms. When the exposed area values increased the multiple orientation As Cast samples presented the maximum τ_1 values around 200 ms followed by the Forged and (111) oriented As Cast samples with 150 ms. The minimum value was shown by the basal plane oriented As Cast samples, 110 ms, although the exposed area was the maximum of 700 μm^2.

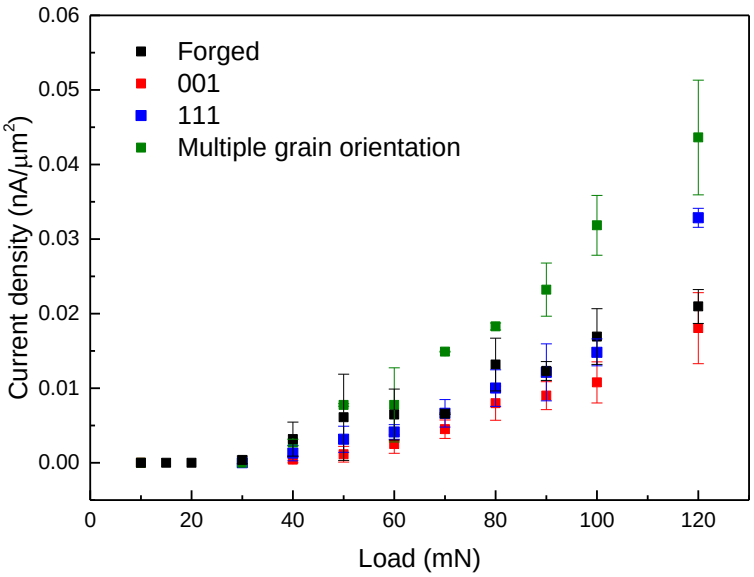

Figure 6.24 Average current density values for specific orientation in CoCrMo alloys

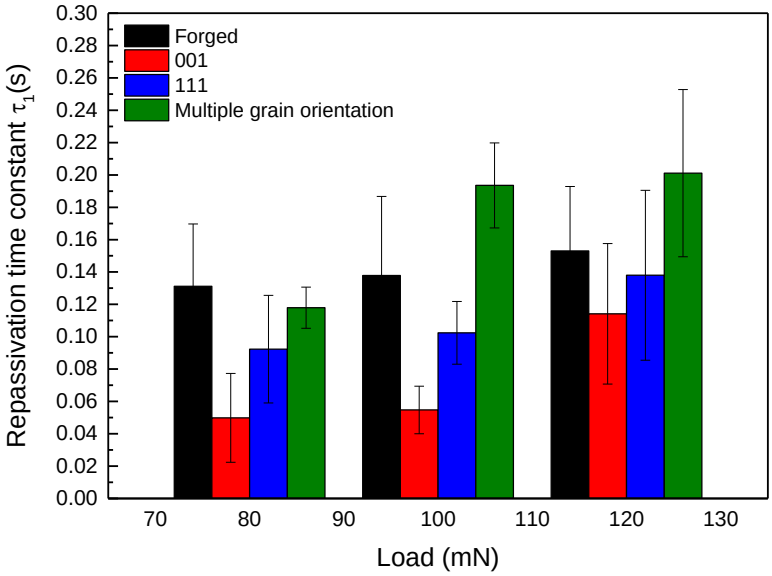

Figure 6.25 Repassivation time constant (τ_1) comparison for specific orientation in CoCrMo alloys

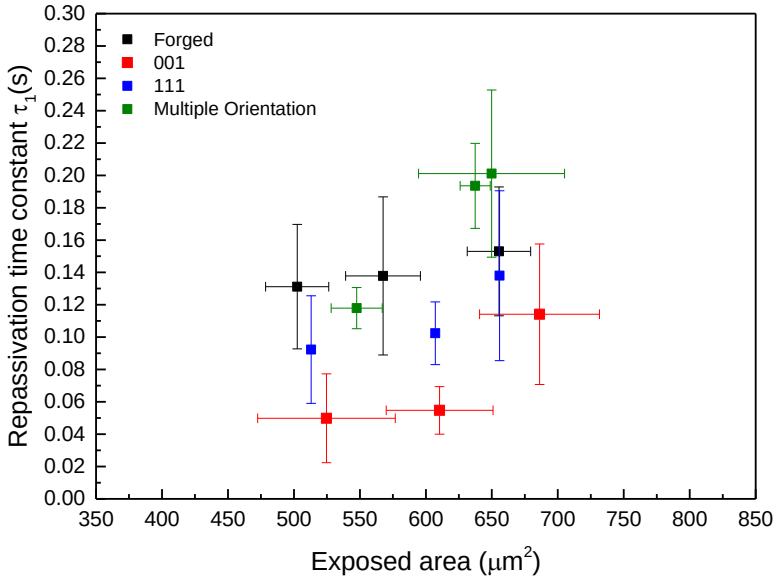

Figure 6.26 Repassivation time constant (τ_1)- exposed area correlation for specific grain orientation in CoCrMo alloys

6.8 Multi pass scratch-corrosion experiments

Preliminary multi-pass wear experiments were performed on the samples in NaCl to understand the effect of multiple passes over the sample and how the repassivation processes might be affected when the surface was already deformed.

Multi-pass (n =5) scratch corrosion experiments were performed on the CoCrMo samples at a 120 mN load. Similar deformation morphologies to the single scratch-corrosion experiments were found after SEM observation. Multi-pass scratch experiments resulted in scratches 1 μm wider than the single scratch experiments, with more material pile up to the side of the scratch and slip lines moving and crossing forward to the external side of the scratch edge. In some experiments the number of lines to the side of the scratches matched the number of passes, see Figure 6.27b, This indicated that each time the indenter deformed the surface it moved the favourable slip planes in that direction.

Figure 6.27a, b and c present examples of multi-pass scratches on two forged samples; a and b belong to sample F-6 and c to sample F-7. The deformation mechanisms were similar to the ones described in Section 6.5.1 with triangular slip lines, Figure 6.27a, parallel sliding lines to the scratch groove, Figure 6.27b and micro-cutting and ploughing, Figure 6.27c. No cracks were observed in the inner part of the scratch. Extruded material, already observed on the single scratch experiments (Figure 6.27d) became more prominent on the edge of the scratch after multiple passes (Figure 6.27c) which potentially can be the origin of submicron platelets and metallic particles.

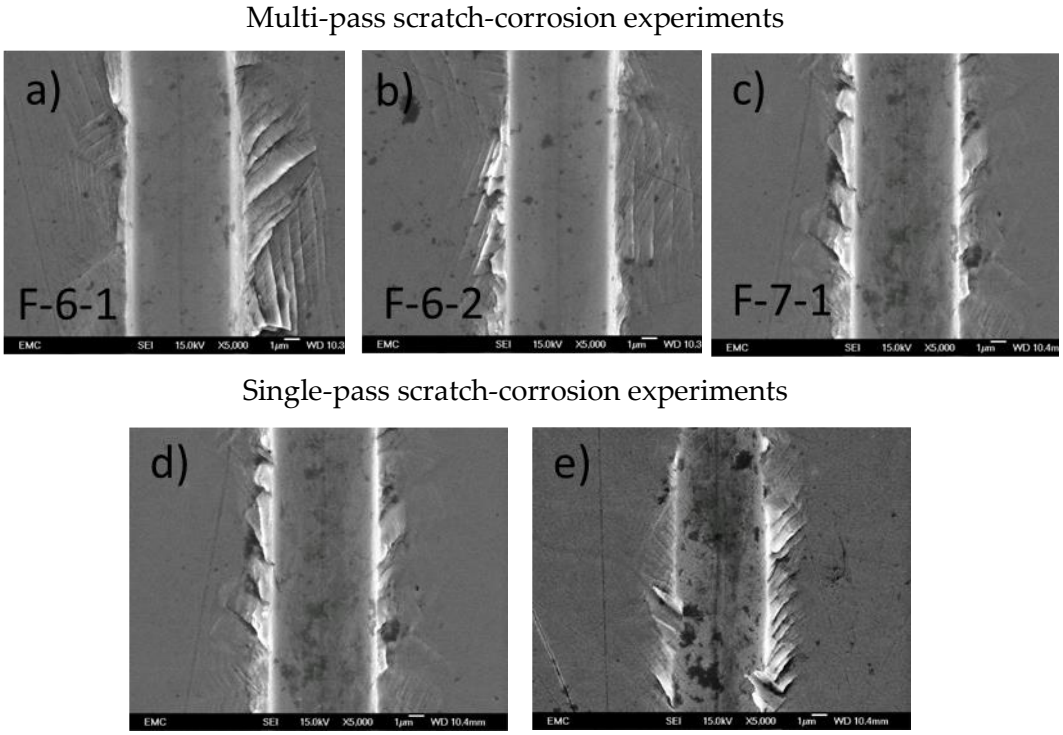

Figure 6.27 Morphology comparison between multi pass scratch experiments: a, b and c and single pass scratch experiments: d and e for the forged alloy

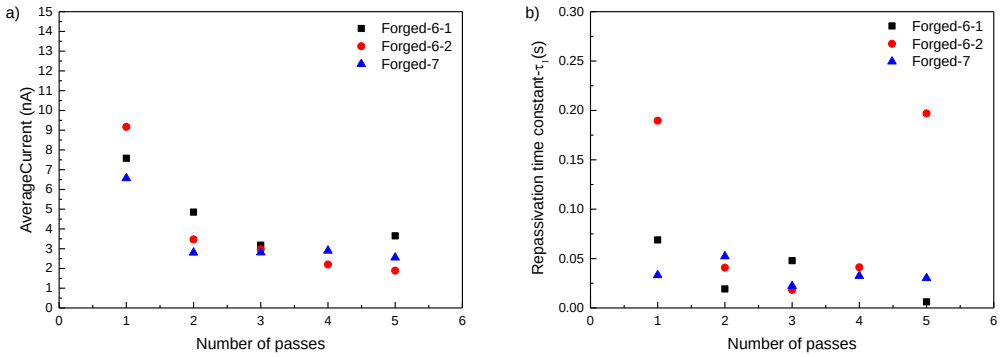

Figure 6.28 a) Average current and b) Repassivation time for the multi-scratch experiments in the Forged sample

Analysing the average currents and repassivation time constant as a function of the pass number, Figure 6.28a-b, the average current decayed rapidly for the three samples. A decay of 50 % of the current occurred from the first to the second pass, while after the second pass the decay kept decreasing to a third from the previous value. Average currents reached a steady state current value equal to 2 nA after the fourth and fifth passes.

Repassivation time constants, τ_1, followed a decreasing trend related to the average current results observed before. A high dispersion for the first pass scratch with times between 200 to 50 ms was observed. The second pass decreased the values to around 40 ms, reaching a constant value after the third pass of 35 ms.

The multi-pass scratch experiments in the AC samples presented two different deformation mechanisms. Figure 6.29 a and b, exhibits 45 degree angle slip lines and triangular features, although the first sample appeared to have a heavier level of deformation than the second one.

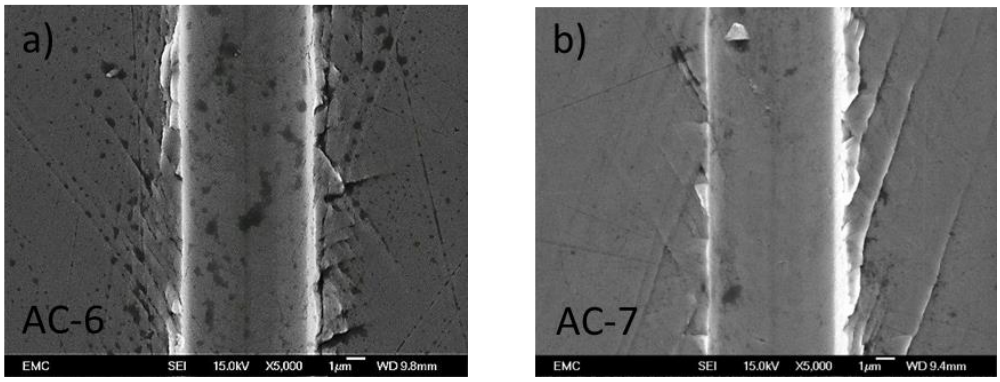

Figure 6.29 Multi pass scratched experiments for the as cast alloy

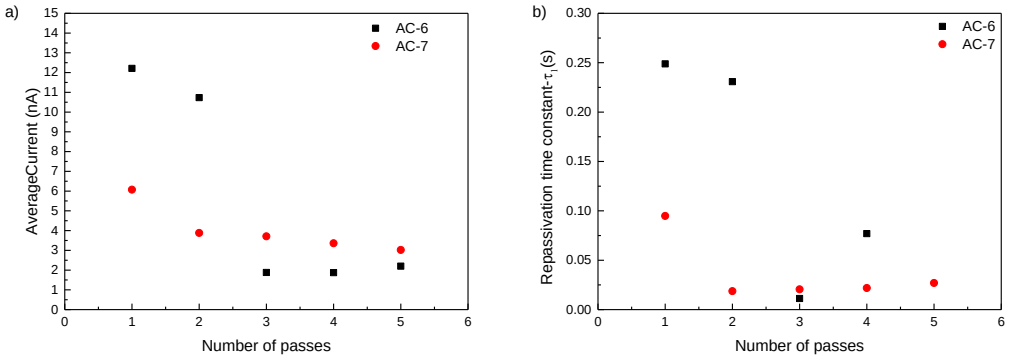

Figure 6.30 Average current and b) Repassivation time for the multi-scratch experiments in the As Cast sample

The average current values for the first pass scratch presented values of 12 and 6 nA for the as cast-6 and AC-7 samples respectively. The same percentage difference of 50 % was shown for the second pass. However for the third pass while AC-6 dropped from 11 to 2 nA, AC-7 current only decreased 1 nA. After the third pass, the current values remained constant between 1 and 3 nA for both

samples. Higher repassivation times, 250 and 240 ms respectively, were found for the first two passes in the AC-6 sample, (Figure 6.30b), linked with the higher current values recorded. AC-7 presented an initial repassivation time value of 100 ms, followed by a drop to 10 ms during the second pass which remained constant for the following passes.

The AC-TT samples, (Figure 6.31), showed 2 different deformation mechanisms. AC-TT-6 showed parallel slip lines to the edge to the sample with some pile up on the right side of the scratch, while AC-TT-7 presented triangular slip line features and 45 degree slip lines on the left side, forming triangular features on the closest area of the left edge.

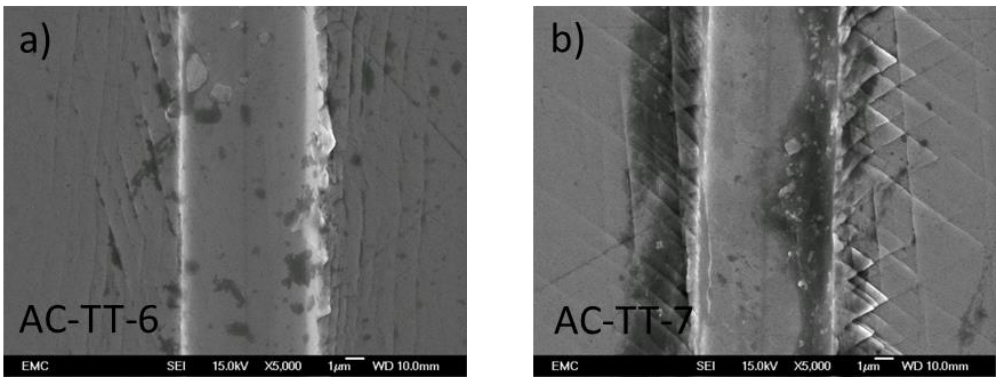

Figure 6.31 Multi pass scratched experiments for the AC-TT treated alloy

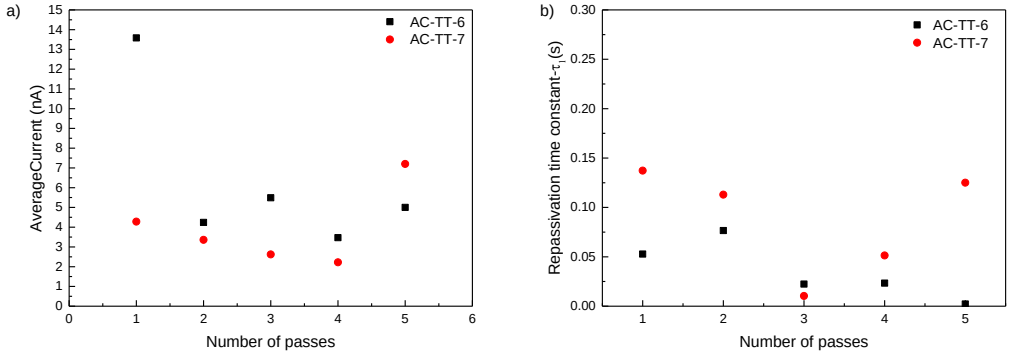

Figure 6.32 Average current and b) Repassivation time for the multi-scratch experiments in the AC-TT sample

There was a visible difference in the average current of the two samples. Initial average current for the AC-TT-6 reached 14 nA while for the AC-TT-7 was only 4 nA. As in the previous alloys, there was a fast decrease in the average current while the repassivation time varied between 0.6 and 0.4 s. The repassivation

constants for the AC-TT samples were constant for the AC-TT-6, 50 ms, while AC-TT-7 decreased from 140 ms to 110, 20 for the 2nd and 3rd pass respectively and increased again to 50 and 120 ms during the 4th and the 5th pass.

AC-LC samples, Figure 6.33, presented slip lines and some deformation lines for the AC-LC- 6. A non-symmetrical behaviour was found in AC-LC-7 with almost no deformation in the left side of the scratch while the right side was heavily deformed with almost vertical slip lines emerging from the edge of the scratch.

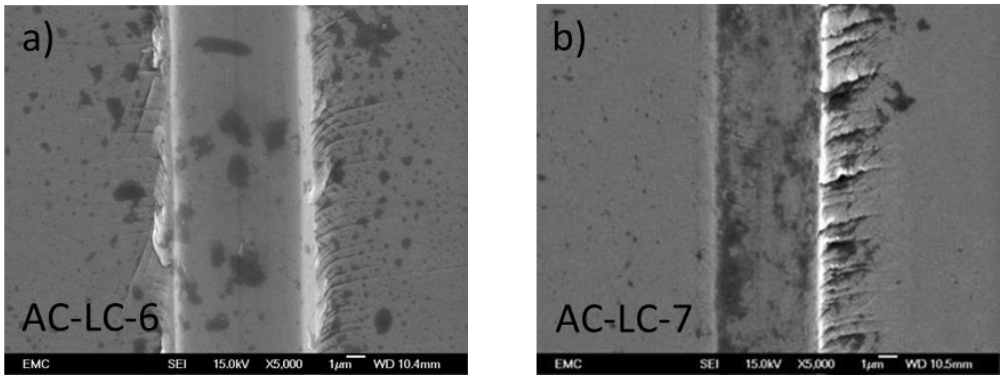

Figure 6.33 Multi pass scratched experiments for the AC-LC content alloy

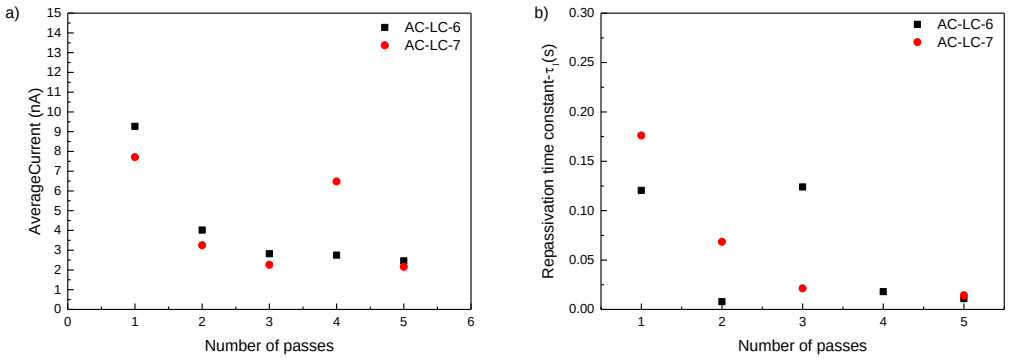

Figure 6.34 Average current and b) Repassivation time for the multi-scratch experiments in the AC-LC samples

Average current values for the AC-LC samples presented decay behaviour after the first scratch, starting at 9 nA and reaching a constant value of 1.75 nA. Repassivation times did show a decay from 170 ms to 20 ms for the AC-LC-7, while AC-LC-6 started at 120 ms during the first pass decreasing to 10 ms at the end of the 5th pass.

Comparing the average current and repassivation results for the four alloys, (Figure 6.35 and Figure 6.36), no significant differences were found between the alloys. However, in some of the cases only two samples were tested so the results obtained are only preliminary values to analyse current and repassivation time trends when scratches were repeated in the same location.

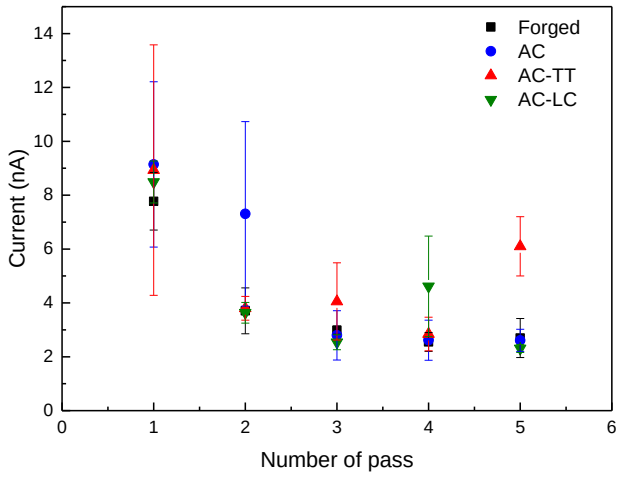

Figure 6.35 Current transients for the four CoCrMo alloys for the multi pass scratch experiments after 1 to 5 passes

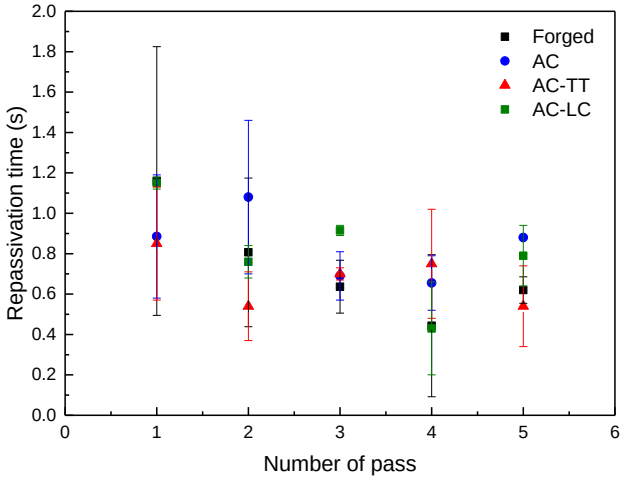

Figure 6.36 Repassviation times for the four CoCrMo alloys for the multi pass scratch experiments after 1 to 5 passes

6.9 Discussion

The aim of the scratch-corrosion experiments was to investigate the differences between four different CoCrMo alloys with respect to their scratch resistance and corrosion behaviour. The testing was designed to identify the conditions needed to depassivate the alloys, the differences in current generated and their repassivation rates, and to identify the origins of the differences between the alloys. To the author's knowledge, a direct comparison of this kind has not been previously performed.

6.9.1 Deformation mechanisms

A single scratch experiment would be expected to produce different levels of plastic deformation depending on the normal load applied and the materials properties. In this study the load range applied was enough to produce plastic deformation even at the lowest applied load (10 mN), with increasing plastic deformation in line with the load, as seen in similar works using scratch testing [252, 253] and as was predicted by the theoretical calculations shown in Table 6.1 and Table 6.2. The deformation during the scratch test occurred initially via the applied load creating an indentation. When the indenter started moving, the friction forces and shear stresses displaced the material both down and to the sides of the tip. If micro-cutting occurred it also accumulated material at the end of the scratch, see Figure 6.14.

For the four CoCrMo alloys the increase in load caused a fast increase in the width and depth of the scratch as well as the pile up at the scratch edges, as described in Section 6.2. This is in agreement with work by Gilbert et al where they observed the same exponential trend when the load was increased [32]. The load-depth relationship within these results presented three regions which are linked to the elastic-plastic transformation of the alloy. According to the calculations from the contact mechanics equations, Table 6.1 and Table 6.2, all the loads applied resulted in permanent plastic deformation which was also confirmed by the AFM and interferometry measurements, see Figure 6.3. The practical and theoretical data shown in Figure 6.4 did not match that calculated from Hertzian equations, because the conditions (maximum contact pressures between 14 to 33 GPa) used during the experiments were above the elastic limit. Therefore, the yield stress was overcome for all the loads and the shear stresses produced while the indenter is moving were not considered in the theoretical model. Beake et al [92] discussed that an approach based on indentation to estimate the contact pressure required for the failure of a film can be used just

when the contact conditions are close to Hertzian equations, being not valid when the geometry moves away and friction and plasticity increased.

One limitation of this study was that friction forces were not monitored during the scratch-corrosion experiments due to space restrictions in the electrochemistry cell and the design of the ceramic arm. Therefore the calculation of the real shear stresses in front of the tip was not possible. Even so, the friction values obtained from the dry scratch experiments discussed in Section 5.4 were extrapolated to the results observed in this Section.

Plasticity in metals results from dislocation motion [254] as described in the Literature Review Section 2.5.2. The presence of dislocations allow deformation at much lower stresses than in a perfect crystal, because plastic deformation occurs by shear when one plane of atoms slides over an adjacent plane by defect motion. If depth-load curves obtained from the scratch-corrosion experiments, Figure 6.4, are superimposed onto shear stress-strain plots, Figure 2.10, a similar trend is seen Figure 6.37. Region I corresponds to easy glide where pre-existing dislocations slip on the slip planes. Easy glide occurred in test with low applied loads where plastic deformation was produced, but no evidence of slipping features or cracks was visible on the microscopic images.

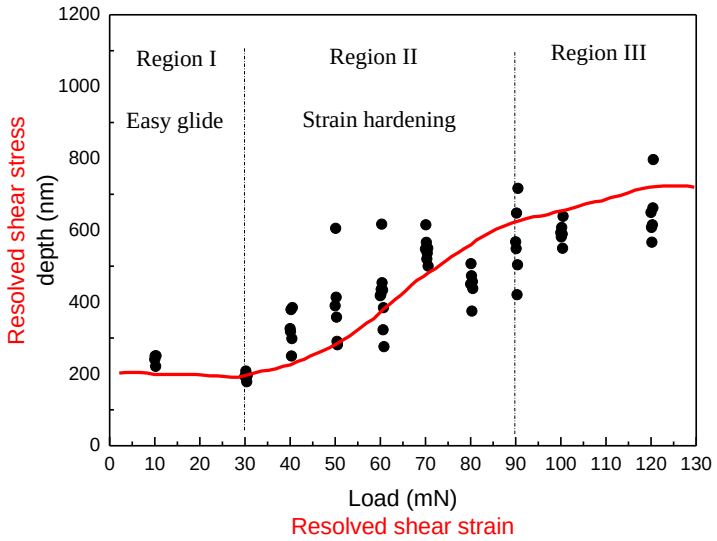

Figure 6.37 General depth –load relationship regions obtained from the analysis of the experimental depth values

When load is increased, a higher dislocation density is generated by the deformation process as extra planes of atoms in the original atomic lattice. Co

based alloys have very low stacking fault energies and as a consequence plastic deformation by gliding in the fcc phase is highly restricted. Therefore when the material is subjected to plastic deformation over the yield stress, several mechanisms including formation of strain-induced defects such as geometrically necessary dislocations (GNDs), intrinsic stacking faults and/or twins are produced to release the mechanical stresses and avoid fracture of the material. As the number of GNDs [255, 256] and statistically stored dislocations (SSDs) [257, 258] increases, the interaction between them and other features within the metal increases and dislocation glide is inhibited, making the crystal more difficult to deform (work hardening process). In order to accommodate the plastic deformation produced, the crystal structure starts to deform drastically. Features such as transverse semicircular cracks inside the scratch (Figure 6.12 AC-TT-4-50), or angular and triangular slip bands (Figure 6.11 AC-3-100) on the edges of the scratches are produced.

For loads between 90 and 120 mN, Region III, the plastic deformation continues to increase but in a less abrupt way. The high applied loads are enough to overcome the increased dislocation interactions and other obstacles to slip increasing the plastic deformation (depth) and the shear stress.

Superimposing the resolved shear strain-stress plots (black) over the theoretical shear stress calculated from Tresca criterion, defined in Section 2.5.2.2, [249] (red), where the shear stress is equal to 0.5 times the maximum contact pressure, Figure 6.38 is obtained.

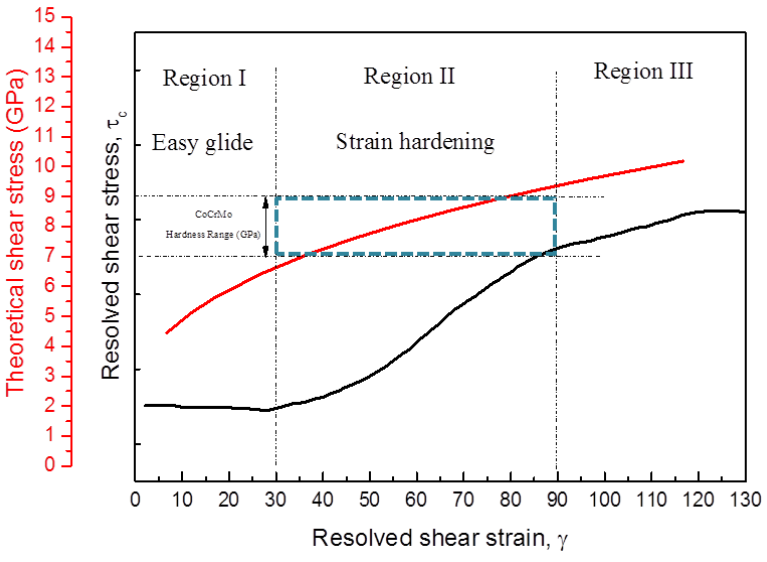

Figure 6.38 Resolved shear stress-strain plot superimposed over the theoretical shear stress calculated using the Tresca criterion

The strain hardening region matches with the theoretical shear stress values in the range of the CoCrMo alloys hardness tested (area marked in blue stripped lines). Under low loads the indenter ploughed the surface deforming it plastically, forming a groove around the indenter and displacing material to the sides of the scratch. For loads where the theoretical shear stresses were below the hardness of the alloy, material was displaced without any evidence of cracks, micro-cutting or slip damage. When the load was increased and the shear stresses exceeded the yield stress, in addition to material displacement, the GNDs dislocations present in the material became confined below the indenter tip increasing the plasticity of the material producing deformation features to accommodate it and release the internal stresses. The stresses produced by the compression are the origin of crack generation and crack propagation below the surface. When cracks grow due to increased stresses and are unified with other cracks, debris is formed and they may detach from the surface. This is the first step of the wear process and the generation of metallic ions [259].

No significant difference was found between the levels of plastic deformation for the four different alloys. However a high dispersion in plastic deformation levels was found within samples from the same alloy. The crystallographic orientation of the test surface had a significant impact on the deformation behaviour shown by the different samples as seen in previous work where the hardness of single fcc crystals with different orientation was evaluated [260-262]. The scratch length during the experiments transversed multiple grains in the case of the Forged alloys while for the AC alloys, with coarser grain sizes (500-1000 μm), the scratches were done within single grains, with a specific grain orientation and no grain boundaries crossing them. Different crystallographic orientations resulted in the activation of different slip systems producing characteristic deformation features [263]. In the Forged alloys grain boundaries affected the dislocation motion acting as obstacles for dislocation mobility [264], therefore, their deformation mechanisms were influenced by the number of boundaries crossed by the scratch.

The main deformation mechanisms found were a combination of several processes including ploughing and pile up formation, triangular and angular slip line formation along the scratch side, micro-cutting and formation of parabolic cracks inside the scratch groove together with carbide fracture, Figure 6.16c. These deformation mechanisms are linked with slip motion and the formation of planar dislocation arrays which have different morphologies depending on the specific grain orientation. They were described previously in the study of the abrasive wear mechanisms using scratching tests at the macro-scale [265-267].

Some other studies also related the deformation processes with the strain induced phase transformation from fcc to hcp,[81, 84, 268] and/ or the formation of twins [269]. EBSD maps revealed specific crystal orientations for each of the samples tested, however due to the high level of plastic deformation which occurred in the scratches it was not able to provide any changes in phase around the scratches due to the limited indexed points collected. Although no FIB or any other technique was used to study the subsurface deformation mechanism, previous work by Sun et al, [30], during single and multiple scratching experiments on an as cast CoCrMo alloy found a phase transformation from fcc to hcp in the regions closest to the wear scratches compared to the non-damaged areas. In addition grain refined areas were confirmed by FIB-SEM on the subsurface areas below the scratch.

A similar fine grain structured layer has been found in the subsurface of retrieved joints. Its formation has been attributed to the cell formation/rotation under a high strain field as suggested as well by some other authors which described extensively the SIT processes in Co based alloys [73, 74, 86]. Buscher et al [270], observed a reduction in grain size on an as cast Co-based alloy by a factor of up to 20000 which was achieved by recrystallization within a zone thinner than 100 μm from the contact surface. Recrystallization occurs via cross slip and climb of dislocation generating sub-grains, which immediately start to rotate or slide against each other.

A fine grain polycrystalline or sub-grain structure has been reported for low SFE fcc metals when the applied stresses are high enough to produce plastic deformation [271]. The grain refinement process involved the formation of planar dislocation arrays, twins or martensite by SIT within deformed grains [86]. Salinas et al [272], suggested that due to the low SFE of Co based alloys the deformation by dislocation slip in the fcc phase would be difficult and plastic deformation would be accommodated by alternative mechanisms such as the formation of intrinsic stacking faults or twinning. These interactions between the original dislocations and the new ones were considered as the major source of localized strain hardening, which eventually can lead to material fracture if no other mechanisms release the applied stresses, as described by Wu et al. [273].

The crystallographic orientation of the grain with which the tip is interacting will determine which slip planes the dislocations will move along. CoCrMo alloys with a fcc structure have three main slip systems, the main slip system (111), the basal plane (001) and the "edge" plane (110). Slipping in fcc crystal is more energetically favourable in the close packed-planes of the (111) type and the observed slip direction is [110] type. When slip along the basal planes, (001), happens, the cube's face in the crystal structure is perpendicular to the applied

load. Therefore compression stresses are produced and the plane motion is restricted. At the same time the indenter moves forward and pushes down into the sample. As a consequence, basal planes cannot accommodate the deformation levels and 45° slip lines are created along the scratch groove, Figure 6.39a.

For scratches applied perpendicular to the main slip plane system (111), the deformation is favoured because dislocations motion is easier. In closed packed planes, atomic density is higher compared to less dense planes because the distance between atoms is smaller, therefore dislocations can move more easily in them. The typical triangular features are shown, see Figure 6.39b, in agreement with work done on abrasion-corrosion by Sun et al. [30] where an as cast CoCrMo sample was subjected to nanoindentation and nano-scratch experiments and slip band and triangular features were also found. Shetty et al. [266] and Ahmed et al [248], found the coarse slip bands are evidence of the planar slip expected from a fcc Co alloy of low stacking fault energy where dislocation cells do not form as would be expected in higher stacking fault energy materials [73, 274]. They are also a sign of work hardening and evidence of the strain induced phase transformation. As a consequence intersecting slip lines appear on the sides of the scratches as triangular features. In this specific case the deformation mechanism was related with the movement of the main slip system for a fcc metal, where deformation takes place in the close packed planes (111) and in the <110> close packed direction (which are three in each (111) plane) forming a triangle. When the load was applied normal to the main slip direction, the planes move forward forming the stepped-triangular structure because of the activation of several intersecting slip systems. The cracks aligned with the triangular structures are related to the amount of plastic deformation that the planes can absorb. If the stress produced exceed the strength of the material, the matrix fractures creating cracks parallel to the sides of the planes to reduce the stress conditions under the indenter tip.

Finally, when the load was applied on an edge type plane (010) or a mixed combination or the previous ones, the deformation mechanisms were restricted ones and the deformation resulted in micro-cutting on the surface generating irregular flakes and the start of delamination debris, see Figure 6.39c [267]. Micro-cutting and debris formation on the edges of the scratch were the origin of the detachment of material and particle debris production. This type of deformation mechanism was observed in the alloys with a random orientation of their crystals or closer to the (101) planes, see Figure 6.13.

Transverse semi-circular cracks inside the scratch groove appeared because of the action of two main components: the normal force which opens the crack perpendicular to the sliding direction resulting in tensile stress fields behind the

tip and the bending effect produce by the movement of the tip in the scratch direction which tries to open the crack in the parallel direction. The combination of both produces the angular cracks [275].

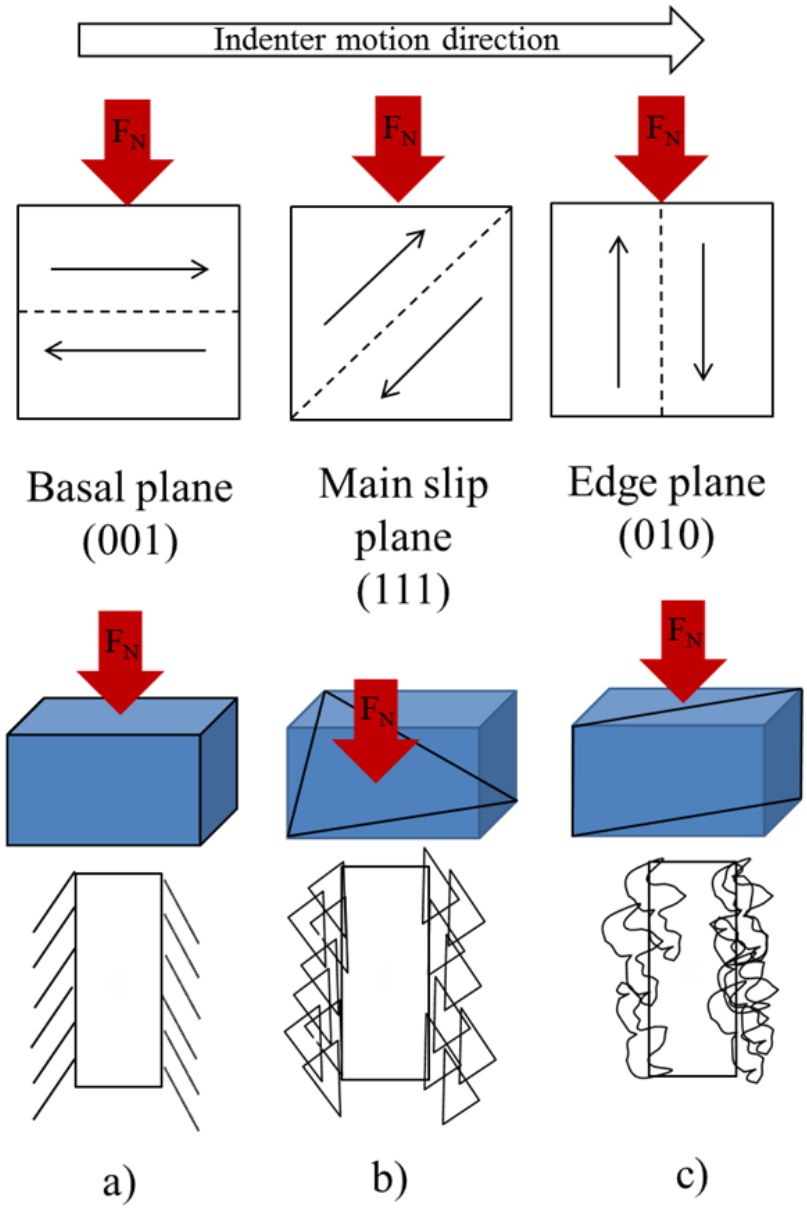

Figure 6.39 Main slip systems activated when the normal load is applied over grains with different crystal orientations, a) Basal plane, b) Main slip plane, c) Edge plane. The dotted line represents the slip plane and the arrows the slip direction

6.9.2 The influence of carbides

Carbides inhibit the deformation of the alloy due to the interaction between the carbide phase and the matrix. They deform less than the Co matrix since its hardness is 40% higher than the matrix, see Table 4.2 in the materials characterization chapter. In addition, they restrict the deformation produced on the surface and the dislocation movement, acting as a barrier for the planes to move forward. When the carbides cannot accommodate the deformation anymore they fracture. Previous studies [18, 276] have found that carbon content improves the wear resistance in the high carbon alloys as carbon stabilizes the fcc crystal structure, limiting the amount of strain-induced transformation to a hcp structure. This results in better wear properties as the hcp phase is more brittle and prone to fracture and particle generation than the fcc crystal structure. Sun et al [277] also observed that slip lines along the scratch groove did not appear when a carbide was present in agreement with the observations presented here in Figure 6.16. In the same work, smearing of the matrix over the carbide was reported for multiple scratch experiments; however similar behaviour was not detected in the experiments reported in this study because they were single scratch tests.

The smaller size and fragmented nature of the carbides in the AC-TT samples mean they are less mechanically stable in the matrix. When the same load is applied, the smaller carbides cannot accommodate the same level of deformation as the bulky carbides and more readily fracture. Kamali et al [117] noted the same observation with better wear and abrasion resistance for the large AC solid carbides than the fragmented carbides. No detachment of carbide fragments were observed since the indenter only moved once in the scratch direction. However, the initiation of cracks in the carbides might be the origin of third body abrasive particles [18, 117], which could accelerate the wear process if the experiment ran for multiple cycles [30, 267]. Carbide pull out could also generate pits or fractured carbides could act as a pit in the surface affecting the corrosion behaviour of the alloy. Unfortunately the multiple-scratch corrosion experiments done during the work didn't land in carbides, so no further observations could be made about the effects of multiple scratches on them.

6.9.3 Transient currents

The passive film on a CoCrMo surface has a thickness which can vary between 1 to 4 nm [28, 32, 174]. Since the measured scratch depths were in a range of 100 to 700 nm the layer would be expected to be disrupted for all the applied loads. In agreement with Gilbert et al, [32], it was found that plastic deformation of the substrate was needed to observe transient currents. However, in this work

deformation of the surface was produced but no transient currents were observed for the lower loads, as in [278]. The results indicated that the oxide layer was strong enough to be deformed together with the substrate and currents were only detected when the oxide/substrate interface fails or the deformation needs to overpass a point, where by ploughing, resulted in the oxide removal.

The minimum load required to produce a detectable current transient peak measures the oxide/substrate deformation strength. There was no significant difference between the residual scratch depth for the different alloys, so the differences in the magnitudes of the transient currents derive from the oxide film properties and the deformation modes exhibited. All the alloys presented measurable scratches at 10 mN, but no current was detected. This implies either that the oxide layer was not breached despite the deformation, or that the current was not high enough to be detected.

The lowest loads resulting in the first detectable current transient peak above the background noise provides an indication of the minimum load required to fracture the oxide or cause failure of the oxide/substrate interface. These loads are a measure of the mechanical strength of the oxide or the oxide/substrate interface. During the variable load tests, a significantly higher load was required to depassivate the surface of the As Cast samples (between 50 and 60 mN) than the oxide on the surface of the Forged samples (onset load between 30-40 mN) which means the oxide layer from the Forged samples will be more susceptible to fracture and to repassivation producing a higher liberation of metallic ions.

In the Forged samples, the refined gain structure meant that multiple grains of different orientations were affected by the scratch. As a result, the variability in the corrosion response resulting from the different deformation mechanisms were less evident and the Forged samples provided a low deviation in the currents between samples and scratches. The anomalous values observed for the F-1 sample were due to a third body particle trapped in the contact area, which resulted in parallel grooves in the scratch path, depassivating a bigger area.

In the case of the As Cast alloys the difference between the samples came from the specific grain orientation of the samples as was shown by results obtained from the EBSD maps. Grain orientation closer to the basal plane, (100), produced lower current densities (0.010-0.022 $nA/\mu m^2$) than the ones between two different main orientation slip systems such as the basal and the (010) plane with values around 0.052 $nA/\mu m^2$. Finally, samples whose grain orientation is closer to the (111) plane, the main slip plane system in fcc crystals, presented an intermediate current density value and a higher degree of deformation with their typical triangular slip features on the sides of the scratch groove. For the specific cases

where the deformation producing the folding of the triangular features, the current values found were 50 % higher than their similar AC alloys under the same loading conditions due to the increased depassivated area. Previous work has found the effect of crystal orientation on the static corrosion properties in different metals such as stainless steels [279] or high strength Magnesium alloys [280]. Stainless steels showed higher pitting resistance for a crystallographic orientation closer to the (111) and (100) planes than planes with lower atomic density. The comparison with Mg is more complicated to interpret since it presents a hcp crystal structure with a lower symmetry than the fcc crystals.

Scratches under 50 mN load produced measurable current densities without any indication of slip plane activation, but with measurable plastic deformation, which means that plastic deformation of the surface without visible features of activated deformation mechanisms such as slip lines or semi-circular cracks, was enough to produce the depassivation of the surface.

6.9.4 Repassivation kinetics

The repassivation time is the time required for the depassivated surfaces to reform the oxide layer (primarily Cr_2O_3) after a scratch event. It can be used as a measurement of the kinetics of repassivation occurring on the sample surface [31]. The repassivation time is defined as the time between the moment the scratch finished and the moment the transient current returns to the baseline current. Higher repassivation times imply higher levels of metallic ion release, which contributes to acceleration of the wear-corrosion processes [154]. As in previous works, the repassivation times observed followed an exponential decay shape. There has been a number of models developed for the depassivation/repassivation and peak current of metals and alloys in different tribocorrosion systems [30, 32]. However, the differences between the models reflect the complexity to model satisfactory the corrosion mechanisms happening in the damaged area.

Baseline currents only showed a statistical difference between the AC (-0.94 nA) and the AC-TT samples (-0.48 nA) while the other samples presented current baselines around -1±0.75 nA. The higher baseline currents (less negative values) observed for the AC-TT indicate the oxide present on the surface was less of a barrier to ionic diffusion. This was due to the presence of a higher density of defects on the sample surface or the presence of partially dissolved carbides which act as defects in terms of electrochemical response [19, 230].

The repassivation times of the Forged and As Cast samples were not significantly different when comparing the exposed areas with respect to specific type of

alloys. However, if the specific crystal orientation of the alloys was considered, the results showed that the Forged samples crossing multiple grains and the As Cast samples with single mixed crystallographic grain orientations showed the highest repassivation times. Several studies have attempted to correlate the specific grain orientation of several metals with their corrosion properties in static conditions, measuring the growth of the oxide films in more or less aggressive environments. Schuh et al,[60], studied the anisotropic surface processes experienced by an Inconel alloy. They concluded that specific crystal orientation oxidize differently, producing differences in the formation of their passivation films. Surfaces with (100) directions grow thicker oxide layers compared with (111) planes because oxides grown in (100) faces of Ni contain many high angle grain boundaries, while (111) surface oxide layer are more tenuous and contain diffusion resistant twin boundaries (which might slow corrosion). Some other authors have pointed out that specific crystal orientations in Ni [281, 282] or Cu [283] produced different oxidation rates, where less dense planes exhibited the fastest growing oxide films while the more dense ones were slower to repassivate, which is in agreement with the observations in this study. Co alloys with (111), which have the highest plane density, had the highest repassivation time, which means it forms the oxide layer slower than the alloys with a (001) orientation. The Forged and the As cast alloys with multiple grain orientation showed the highest repassivation times, although the interpretation of the results became more difficult due to the multiple grains occurring at the same time.

6.9.5 Multi-pass scratch corrosion experiments

Multi-pass scratch groove morphologies exhibited a higher amount of protruded material on the sides of the scratch compared to the single scratch experiments which potentially can lead in the production of submicron metallic particles, debris and the generation of metallic ions.

When repeated scratches were made in the same location, the successive current transient peaks and the repassivation times decreased in magnitude rapidly. According to previous discussion in Section 6.9.3 and Section 6.9.4 it would be expected that the higher affected area on the sides of the scratch would produce an increase of the current transients. However, and in agreement with the results from the static corrosion experiments in Section 4.4.2, the corrosion current and corrosion potential values were dependent on for the period of time over which the oxide film formed. During the multi-pass scratch corrosion experiments, the first scratch was performed on a surface where the oxide layer was grown over 12 hours, while the second and subsequent scratches were made at intervals of 10 minutes between the scratches, growing a thinner oxide layer which produced

lower transient currents when it is disrupted This suggests two possible options: the re-formed oxide has different mechanical and chemical properties and behaves differently from the initial oxide that was fractured, which is supported by the repassivation studies of Bryant et al [131] where a decrease in i_{corr} values was observed when increasing the number of loading cycles. The second hypothesis is that the surface is tribologically modified, e.g. the first scratch produces the greatest deformation on the surface with a possible grain refinement and SIT phase transformation, according to [30], which can affect the current transient peak levels. Therefore, only the motion of the slip planes produces transient currents since the scratch groove is already deformed. As a consequence the amount of metallic ions produced will be decreased since the oxide layer takes a shorter time to be reformed. In practical terms the scratch-corrosion response will be higher when a new scratch is done than when a particle gets trapped between two contacting surfaces and motion occurs between them. However, it would be interesting to know the exact chemical composition produced for different immersion times and which type of metallic ions is liberated into the solution to understand the effect within the body.

6.10 Conclusions

The scratch test and post-test imaging procedures provide a sensitive and useful method to assess the electrochemical response of oxide films and the mechanical behaviour of 4 different CoCrMo alloys. This method can be used to determine the relative corrosion and plastic deformation resistance of surface oxides and alloys, and be used to predict the effect of different microstructures and single grain orientations on scratch-corrosion environments.

The main conclusions obtained from this chapter are:

- The single scratch experiment simulates the first incident of damage to a metal implant surface in-vivo. One hard particle interacting with the metal surface produces several plastic deformation mechanisms with different morphologies depending on the specific grain orientation. Irrespective of the mechanical properties, carbon content or thermal history of the CoCrMo alloy, the deformation morphology of the surface and the corrosion behaviour was related to the grain orientation where the scratch was placed.

- The presence of carbides influences the plastic deformation mechanism. Fracture of the carbides was observed, which in the long term can result in pull out of carbide particles, accelerating the wear-corrosion process.

- Increasing the number of passes produced an expansion of the deformation patterns and the depassivated surface area. The current transients monitored decreased rapidly with respect to the first scratch due to the chemical and mechanical changes in the oxide layer reformation and the tribological changes (grain refinement and SIT) of the surface affecting the deformation-corrosion processes and therefore the liberation of ions.

- The electrochemical response, transient currents and repassivation times were linked to the specific crystal orientation of the grain. Forged and As Cast samples with multiple oriented crystallographic systems have a more limited motion of their active slip systems and presented higher transient currents and repassivation times compared to As Cast alloys oriented in the basal or the main slip system planes.

- Transient currents in Forged alloys start under lower load levels, which indicated a higher response of the oxide layer during the scratch compared to the As Cast samples. In addition they presented higher repassivation times. The combination of both lead to an increase in the liberation of metallic ions into the electrolyte resulting into worst scratch-corrosion resistance.

7
General discussion

Previous chapters have discussed individually how the mechanical properties, corrosion resistance, plastic deformation behaviour, and the deformation-corrosion processes are influenced by the CoCrMo manufacturing processes and thermal treatments.

This chapter targets to combine the individual discussions from previous chapters to understand how all are interconnected and especially how the specific crystal orientation of the grains in each alloy is related to the deformation-corrosion mechanisms observed at the nano-scale.

The aim of the thesis was achieved by developing a novel technique able to reproduce the tribocorrosion damage occurring at the nano-scale where hard single asperities scratch and damage the metallic femoral stem in cemented hip implants without removing material but producing plastic deformation on it.

The relevance of simulating this specific interface in hip implants is because clinical studies have revealed that is one of the sources, together with the articular surface and the taper-trunnion interface, which generates metallic particles and ions which can trigger an adverse reaction within the body causing implant failure. Therefore, understanding the deformation-corrosion processes at the nano-scale is a key point to improve the design of new materials in future commercial implants.

Macro and micro scale wear-corrosion processes have often evaluated the surfaces of materials on a scale which incorporates multiple grains and microstructural features due to the macro scale of the experimental set up as in the case of hip simulators or pin on disk devices or the nature of the alloys used if the grain size is

small compared to the damage produced. As such the results represent the average performance of many fine grains and grain boundaries, rather than the electrochemistry or deformation-corrosion behaviour of a single grain with a defined crystal orientation. When working at the nano-scale, as in this study, the specific grain orientation was found to play a significant role in the deformation-corrosion processes in CoCrMo alloys.

Previous work has investigated the influence of crystallographic orientation on the mechanical and corrosion properties in single crystal materials, [59, 283, 284]. However, to the authors' knowledge this work represents the first study to provide a correlation between the deformation processes and the corrosion mechanisms at the nano-scale in CoCrMo.

7.1 Deformation mechanisms

Biomedical CoCrMo alloys can be classified depending on the manufacturing process from which the component was formed. This can be either through forging to provide a polycrystalline fine grain sized alloy or casting, which produces coarse grain sized alloys with different percentage of carbides within the matrix. At the nano-scale, the As Cast samples can be used for the analysis of single grain materials, as the size of the scratches produced are one order of magnitude lower than the grain size. In contrast, the Forged alloy is a polycrystalline material where the scratches affect multiple grains.

Analysing the penetration-load relationship shown in Figure 5.27, there was no evidence of any differences in the deformation behaviour when comparing the alloys by their manufacturing processes or thermal treatments. However, the degree of penetration-COF relationship, Figure 5.35, suggested a different deformation mechanism between Forged and As Cast alloys. The As Cast alloy had a degree of penetration 2.5 times higher than that for the Forged alloys for the same friction forces. The deformation mechanisms are dependent on the material mechanical properties: hardness and yield stress. The Forged alloy's hardness is approximately 0.8 GPa higher than that for the As Cast alloys mainly due to the alloy grain size being two orders of magnitude lower, see Chapter 4, [142, 215]. When the indenter was pressed into the surface and moved forward, under the same loads and contact stresses, the material with a higher hardness and yield stress will deform less and require a higher frictional force to displace the material to the sides of the scratch, producing a higher COF. Similar observations were made by Hokkirigawa [199] who compared the abrasive wear behaviour of brass (HV = 3-4) and stainless steel (HV=5-8.5). Under similar degree of penetration values, 0.1-0.2, the stainless steel showed a friction force 4 times higher than the brass, confirming that higher

hardness values makes deformation more difficult and therefore increased the friction forces and COF when the indenter moved forward in the sample.

According to Beake et al [92], the behaviour observed in Figure 5.24, is consistent with the interpretation of the two components which define the friction coefficient in Equation 2.19. When using the 200 μm sphere, the damage produced on the surface was minimal, and the ploughing component was really small, so the interfacial friction was the dominant element. In contrast, when the 5 μm sphere was used, the ploughing component increased proportionally with the load, dominating the monitored COF values. The interfacial component found was constant for all the alloys, Figure 5.34, while the ploughing component varied between the Forged and the AC alloys, Figure 5.35, which confirms the theory of a different deformation mechanism occurring between them.

The crystal orientation of the CoCrMo alloys, affected the surface deformation during the scratch-corrosion experiments. Grains oriented in the (001) direction exhibited a higher deformed area, than the one with a (111) orientation, followed by the multiple oriented grain and the Forged alloy, as described in Figure 6.26. These results are in agreement with the rolling friction experiments on single Cu crystals reported by Dyer, [285], who found that rolling resistance was increased by 32 % and the track width was reduced by 31 % when changing from (100) to (110) directions. These observations are also in agreement with Swadener, [286], who reported that the depth of scratches generated in four individual grain of a TiNb alloy were dependent on the specific grain orientation. As a consequence, the plastic deformation of the material and the COF were higher when the test direction was aligned with the more dense packed slip directions, (111). However, the interpretation of the results in this last work was limited in some of the grains due to the limited knowledge of its active slip systems, where it was not possible to apply the basic dislocation theory as in the (111) direction.

The COF values were not obtained during the scratch-corrosion experiments due to space restrictions inside the electrochemical cell and the design of the ceramic arm. However, the dry scratch experiments, Chapter 5, demonstrated that higher penetration depth values resulted in higher COF values. The exposed area values varied between alloys with AC-TT > AC-LC > AC > Forged, which matches with the trend followed by the degree of penetration in Figure 5.35. Comparison between the exposed area and the grain orientation, Figure 6.26, showed that (001) grains presented a higher exposed area, followed by (111) planes, multiple orientation planes and finally the multiple grain oriented Forged alloy. This demonstrates that (001) grains exhibit a higher level of deformation which indirectly implies a lower yield stress and hardness values when compared to the (111) and (110) oriented grains. This is in agreement with previous work where mechanical properties have

been also related with specific grain orientations of metals by nanoindentation techniques. As an example, Salehinia et al, [262], showed that the compressive stresses modelled in a metastable stainless steel were 5 times higher in the (111) and (101) orientations than in the (001) plane, with intermediate values for the rest of orientations or austenite grains. Roa et al.[287], found the same trend with grains on the (001) planes being softer than grains in the (111) orientation, meaning that the (111) grain required more stress to activate slip and glide the dislocations. The friction force increase shown in Figure 5.23 was related to the total shear strength of the contact area (between the deformed material and the indenter), thus when the friction forces are high, shearing occurs producing maximum values of COF with higher friction for the directions which produce a greater deformed area between the tip and the material. Steijn, [288] demonstrated this using single crystals of fcc (Cu,Al, Ni and α-brass) and bcc (β-brass and α-iron) metals. An increasing linear relationship was gathered between the friction forces registered during the scratching and the deformed area produced. Metals with lower yield stress exhibited a higher deformed area and thus higher frictional forces.

Specific deformation features such as triangular slip lines, micro-cutting and debris formation or transverse semi-circular cracks were observed to be dependent on the grain orientation of the alloys. The wear-deformation patterns observed were the result of the arrangement of the specific slip planes activated in the stress fields produced. While triangular slip lines were related to the (111) oriented planes, micro-cutting was with the basal plane (001). When the plane was closer to the (101) orientation or in between different orientations, the features observed were mainly produced by micro-cutting and the start of delamination debris, see Figure 6.23. Sun et al, [30], in her study on an as cast CoCrMo alloy, also described triangular slip lines and intersecting slip lines on the edges of the scratches using an equivalent set up as the one described here. The coarse slip bands were attributed to the planar slip character which should be expected in a fcc Co-rich matrix of low stacking fault energy and to the SIT transformation. However, it was mentioned that "the phase transformation was just found around some of the highly deformed areas around the scratches due to the non-uniform force experienced by the material or due to the inhomogeneous nature of the crystal structure". There was an indication of crystal structure relationship with the deformation processes, but nothing else was investigated besides the triangular and/or rhombic grains observed at the edge of the scratches. They were related with an fcc crystal structure deformation pattern on the close-packed planes and directions which form a triangle in the (111) plane when the material is deformed forming a triangular and stepped structure (similar to the one described here in Chapter 6). In addition the subsurface damage was also investigated by FIB. Two regions were described: a constrained and an unconstrained area. The constrained area (or the area deformed below the indenter)

presented a nanocrystalline structured layer attributed to the cell formation/rotation under high strain fields, similar to the ones observed by some other authors in the subsurface of retrieved joints [73, 86, 271]. The unconstrained region, the sides of the scratch groove, showed a different microstructure where the slip and fracture lines intersected with the martensite transformation lines below the surface. In this study, no FIB was performed to evaluate the subsurface damage, but in addition to the triangular features, some other deformation mechanisms were observed and related to the specific grain orientations of the alloy. However, EBSD maps in Chapter 6 were unable to index the deformed region; therefore the fcc to hcp phase transformation was not possible to be identified. To confirm it further investigation with more accurate techniques such as XRD would be required, as explained in the Future Work Section.

The effect of crystal orientation on the deformation features has been described previously in other materials. Takagi et al [289], studied the static friction between Cu single crystals and described adhesion, shearing and deformation mechanisms for the (100) and (110) directions. In the case of friction experiments run parallel to the (100) plane direction, the deformed area grew in the form of an isosceles triangle while for the (110) plane the deformed track had a "rod" shape. The differences between the damage area were related to the friction coefficients showing higher values in the first case since the deformed contact area was more extensive than in the second one. Xia et al, [290], characterized single crystal Fe-Cr-Ni alloys with fcc and bcc structures, obtaining different slip trace deformation patterns around the indents depending on the plane in which they were made and the specific number of slip planes activated during indentation. Because fcc crystal structures only have one slip plane, (111), they cross-slip less and present straighter and coarser slip traces than bcc crystals structures.

7.2 Corrosion mechanisms

The corrosion mechanism dependency on crystal orientations has been described based on the theory that a densely packed crystallographic plane has a higher atomic coordination, tighter atomic bond, and thus a lower dissolution tendency than a loosely packed crystallographic plane because it has a lower free energy [61, 62, 284]. Due to the lower free energy values they tend to lose the fewest number of bonds per unit area when a new surface is formed. As a result, a loosely packed plane, e.g. (100), allows a higher accessibility of oxygen to the surface layer accelerating the reaction kinetics resulting in a rapidly oxidized surface film compared to close packed planes, e.g. (111), where the reactions are slower to occur. Faster oxidation rates produce thicker oxide layers resulting in lower currents for ion interchange.

Current density measurements from the dynamic scratch-corrosion experiments showed the following increasing trend depending on their grain orientations: Multiple grain oriented grains > (111) > (001). Considering current density as an indirect measurement of the thickness and or quality of the oxide layer formed on the metal substrate, the data suggests that grains with (111) form a thinner or less compact oxide layer compared to (001) oriented grains. This agrees with the trend found in the oxidation behaviour of Cu mono-crystals grown in different crystallographic orientations [283]. Cu crystals oriented in the (111) plane exhibited a higher resistance to oxidation, grew thinner layers and had higher currents than the crystals grown in the (100) plane which grew the thickest layers and produced the lower currents. The reason was (100) planes usually produce higher angle boundaries which act as pathways for metal ions to accelerate the oxidation process compared to the more densely packed planes (111) which have less free space for oxygen diffusion and thus produce a lower oxidation of the surface.

However, the work of Wang et al [62] conflicts with this. This study analysed the corrosion behaviour of a polycrystalline Al affirming the dissolution rate of grains with lowest surface free energy, (the highest close packed planes (111)), dissolved faster than the rest of the orientations because of the creation of new facets during the corrosion process. They discussed that the growth of new facets, their geometry, their angle and position with respect to the original surface and their higher free surface energy increased the dissolution rates for grains closer to a crystal orientation in the (111) planes.

The apparent contradiction between both studies is related first with the different samples tested, monocrystals in the Cu study and a polycrystalline Al alloy together with the environmental conditions since the Young study (Cu) studied the oxidation rates at different temperatures in dry conditions, while Wang reported the dissolution rate of the grains in NaCl and H_2SO_4 solutions.

7.3 Scratch-corrosion testing at the nano-scale

The scratch-corrosion synergy, as it was described in Section 2.5.4.4, has been evaluated in previous work according to any of these three approaches: synergistic approach, mechanistic approach and third body approach assuming there is always wear enhancing corrosion and corrosion enhancing wear. But what happens when a metallic surface is plastically deformed without loss of material? It is possible to have corrosion on the surface?

Unlike previous studies where the wear and corrosion processes were investigated, the new electrochemistry cell described in Section 3.7 produced single scratches deforming the surface without quantifiable if any removal of material, thus no wear

is consider to have occurred but transient currents were measured. This observation indicated corrosion can happen in the absence of wear and it was related with the 3D deformation features observed in Section 6.5.

Although the transient current densities generated by depassivation of the metal surfaces were dependent on the substrate grain orientation; the differences in the repassivation time kinetics for each of them can also be related to the variability in the oxide film regrowth, with different chemical composition, thickness or compactability, as suggested by Gilbert et al. [174] when comparing the oxide layers in CoCrMo and Ti alloys. This is supported by the static corrosion experiments in Chapter 4, where the Forged alloys presented higher corrosion densities than the three As Cast alloys, which indicate the oxide layers properties are different and supported by Paredes [291] and Milosev [28] who studied by XPS the composition of the oxide film growth in CoCrMo alloys under different potentials and environments, therefore affecting the reactions occuring on the metal surface and the liberation of metallic ions into the solution.

The scratch-corrosion experiments exhibited a different load onset at which the oxide layer of the alloys was fractured, see Figure 6.7. In some other studies this load has been also related with the mechanical strength of the oxide [32]. The Forged alloy despassivation occurred at a lower load than the As Cast alloys. This is due to two material specific variables. The first, is the small grain size of the Forged alloys and the increased number of grain boundaries interacted with the scratch. If grain boundaries are considered as anodic sites, then the values of the transient current will be expected to be higher under the same loading conditions than for a coarser grain size sample. The second, relates to the static corrosion experiments, Chapter 4, which showed that the oxide layer created on the samples after 3 hours immersion followed different kinetics, with a mixed mode for the As Cast samples and mass transfer with a limiting current for the Forged alloy. This indicates that As Cast samples can grow thicker and more stable oxide layers than Forged alloys. Therefore, if As Cast samples oriented in the (001) or (111) planes have a higher oxide adhesion resistance than Forged and As Cast multiple grain oriented samples, they will be more protective and the liberation of metallic ions will be minimised.

One would expect that a higher deformed area would produce a greater area of depassivated metallic surface to be oxidized. Hence the current transients produced in the Forged alloy should be the lowest of the alloys tested as it is the hardest and presented the lowest degree of deformation. However, this apparent contradiction can be explained by how the exposed area was calculated and how many grain boundaries were crossed by the indenter tip as mentioned in the paragraph above. When the scratch was produced on the materials surface, in addition to the displacement of material to the sides of the scratch groove, new 3D features were

created at the edges. These new features such as triangular slip lines, angular slip lines or micro-cutting are irregular making accurate calculation of the area difficult, as described in Section 2.5.4.2. The Forged alloy, where multiple grains were affected by the scratch, or As Cast alloys which produced more irregular patterns with a higher true damaged area prone to repassivation resulted in higher transient currents than the rest of the alloys.

In the scratch-corrosion experiments, the repassivation time estimates how long it takes for the oxide layer to regrow on the surface, with higher times suggesting slower kinetics and an increase of metal dissolution. The repassivation time constants obtained from fitting the transient current curves to a first order exponential decay equation as proposed by Goldberg [32] using a high fracture scratch experiment, followed the same decreasing trend as the current density values. Time constants were similar (30 ms in Gilberts work vs 40 ms in this study for an As Cast sample using similar contact conditions). Higher repassivation times were observed for the AC-multiple oriented grains and Forged alloys, followed by the AC-(111) and finally the AC-(001) grains. As with the current density values the crystallographic orientation affects the rate, with the (111) planes reforming the oxide slower than (001) planes as the atoms are more densely packed. Denser packed planes have fewer paths for metal oxidation due to the lack of space between the atoms, resulting into slower kinetic reactions and higher repassivation times.

For polycrystalline materials (Forged), corrosion will preferentially target any defect on the surface such as: phase boundaries (carbide-matrix), the presence and morphology of carbides, grain boundaries, precipitates on the grain boundaries, presence of stacking faults or slip lines etc, [56, 57, 62, 230]. The corrosive attack can also be accelerated due to the different orientation angles between neighbouring grains which will modify the interfacial energy between adjacent grains. In general defect sites act as diffusion paths for ions meaning the greater the number of defects the greater the oxidation rate. As a result of the smaller grain size of the polycrystalline structure, the repassivation times in the Forged alloys were three times higher. Slower repassivation kinetics resulted in higher liberation of metallic ions and worst corrosion behaviour, which in clinical terms may result in reaction to the implant and its revision [96].

To summarise: the new electrochemistry cell designed was able to monitor systematically transient currents as a consequence of the controlled plastic deformation damage under different loading conditions at the nano-scale. A new perspective was introduced in the understanding of the deformation-corrosion properties of the CoCrMo alloys under study. It was shown that at nano-scale, wear

(understood as a loss of material) is not necessary to produce corrosion and deformation and displacement of material are enough to enhance corrosion.

Deformation processes in dry conditions did not show significant differences between the four alloys, however closer analysis showed that at the nano-scale, the grain orientation played a significant role influencing the 3D deformation features around the scratch groove and therefore affecting the subjected areas undergoing the depassivation-repassivation processes.

Different grain sizes presented by the alloys caused differences in their hardness and yield stress. The finer grain size of the forged alloy provided a higher hardness, yield stress and resistance to plastic deformation. In contrast the As Cast alloys exhibited a coarser grain size and their deformation behaviour was linked to the specific crystal orientation of their grains. The close packed planes were more prone to move and glide and produced a higher deformed area than the ones with intermediate directions or in the basal plane with a higher resistance to deformation. In addition, the crystallographic orientation of the grain resulted in different deformation features at the edges of the scratches. These features directly impacted upon the current transient densities observed, as they produced new areas of the surface requiring repassivation, the area of which varied depending on the deformation feature. The repassivation process provided an estimate of the film growth rate and of the amount of metal dissolution. The faster kinetics presented by the As Cast samples will be beneficial for lower levels of metal dissolution and therefore higher corrosion resistance.

8

Conclusions and Future work

8.1 Conclusions

This study has developed a new electrochemistry cell to investigate the deformation-corrosion mechanisms in single asperity contacts between a diamond tip and the metallic surface of four CoCrMo alloys used in hip implants. The findings obtained during this work have result in a deeper knowledge of the relationship between the deformation and the corrosion processes which affect the liberation of metallic ions into the solution causing potential risk to the patients' health and shortening the implants life span. A detailed comparison of the surface deformation mechanisms under different contact conditions: fretting, reciprocating sliding and scratching experiments were assessed. The influence of the mechanical properties, microstructure and specific grain orientation of the Co-based alloys was linked to the deformation-corrosion processes identified during the experiments.

The conclusions from the thesis are summarised below:

8.1.1 Materials characterization

- For the first time, different alloy microstructures were compared under the same electrochemical experimental conditions. The forged alloy exhibited significantly different static corrosion behaviour to the As Cast alloys. An E_{corr} gap of ~130 mV was found between the Forged and the As

Cast alloys and between Forged samples with different grain sizes. This difference calls into question their use in combination in-vivo. The difference is big enough to establish a galvanic cell between components or areas of the same stem.

- The Forged alloy exhibited higher corrosion currents than the As Cast alloys indicating that the oxide film formed on the forged alloy was less protective than that of the As Cast alloy. In addition, the finer grain size, increased number of grain boundaries and oxidation paths in different samples from the Forged alloy resulted in the lowest corrosion resistance of the alloys tested.

8.1.2 Single asperity effect on the dry-deformation processes

- Higher significant differences were found in the plastic deformation resistance between the AC alloy and the other alloys when tested under reciprocating sliding conditions.

- The amount of particulate debris generated around the reciprocating wear scars was significantly higher for the AC-LC and the AC-TT alloys with respect to the Forged and the AC alloys.

- The Forged alloy exhibited dispersed energy values which were significantly higher than the As Cast alloys under 10 and 20 mN loads during the reciprocating-sliding experiments. In the same line, the Forged alloys during scratching experiments, showed statistically significant lower degree of penetration values than the AC alloys.

- COF values obtained from the nano-scratch experiments showed that the friction interfacial component was constant for all the alloys, while the ploughing component in the Forged alloys was significantly lower than in the As Cast alloys.

8.1.3 Scratch-corrosion testing at the nano-scale

- The novel electrochemical cell developed as part of this study was demonstrated to be able to assess the onset load at which the alloys were depassivated, monitor the transient currents generated and determine the oxide reformation kinetics.

- A new method was developed to calculate the depassivated areas, providing more accurate current density values and corrosion rates.

- The Forged alloys exhibited lower depassivation loads compared to the As Cast alloy indicating a less protective oxide film. This, in combination with higher transient currents and longer repassivation times increased the corrosion rates and therefore the liberation of metallic ions.

- For the first time, it was demonstrated that the deformation-corrosion mechanisms at the nano-scale were dependant on the specific grain orientation and the alloys microstructure, Forged or As Cast.

- Forged samples exhibited triangular slip line formation bands combined with irregular features on the edges of the groove while As Cast alloys presented several morphologies depending on their grain orientation. As Cast alloys oriented in the basal plane (001), produced angular slip lines along the side of the scratch, while alloys oriented in the denser closed-packed plane, (111), had triangular slip bands. Irregular accumulation of material on the sides of the scratch scar, with initiation of debris observed for the As Cast alloys whose orientation was closer to the edge plane (010) or with multiple oriented crystallographic systems.

- The highest transient currents and corrosion rates were found for the Forged and the As Cast samples with multiple oriented grains, as the deformation to the sides of the scratch resulted in a greater area of depassivated surface requiring repassivation.

- Multi-pass scratch experiments enlarged the area exposed to repassivation and increased the damage accumulated on the edges of the groove.

- The current transients monitored from subsequent passes in multi-pass scratch experiments were lower than those obtained during the first scratch. This indicated that the electrochemical reactions resulting from the interaction between the tip and the surface were different when the surface was previously deformed.

8.2 Future work

The novel results presented in this thesis represents just the tip of the iceberg with regards to what this new testing setup is capable of providing. During this work this single asperity contact was modelled using CoCrMo metallic samples in contact with a diamond tip to act as the hard radiopacifier particle embedded in the fixation cement in cemented hip implants using single scratch-corrosion experiments.

8.2.1 New alloys and electrolytes

To complete this study further work would require investigating the influence of proteins by substituting the NaCl electrolyte for a more representative one of the body environment such as PBS or Bovine Serum. In addition to CoCrMo alloys, some other metallic materials such as Titanium alloys or Stainless Steels can be added for a complete map of the deformation-corrosion mechanisms at the nano-scale.

8.2.2 Multiple scratch experiments

The influence on the corrosion parameters of multiple-pass scratch experiments over the same scratch track were briefly analysed in this work to simulate a trapped single asperity rubbing between two contact surfaces when motion occurs. The susceptibility of the repassivated surface to subsequent wear and corrosion processes is another interesting point to research more in depth together with the influence of loose debris trapped between the two contacting surfaces and how they affect the transient currents.

8.2.3 Oxide layer chemical characterization

The formation of the oxide layer and its specific characteristics such as chemical composition using XPS, thickness or porosity are closely related with the repassivation kinetics occurring on the surface. From preliminary fretting experiments in dry conditions, the characterized oxide layer was mainly formed by Co while previous studies in liquid environments reported that Co goes into the solution more than Cr because of its higher solubility, leaving Cr behind in the metal matrix. It would be interesting to study if in wet conditions the results would be similar to as reported before to understand the migration mechanisms of Co and Cr into the solution.

8.2.4 Analyse the fcc→ hcp SIT phase transformation

EBSD analysis performed during this project was not able to find if the areas around the edge scratches developed a fcc → hcp transformation. Since the high degree of plastic deformation meant that the technique was not able to index the data required to specify which phases were presented. XRD can be an alternative technique to find if the deformation process is influenced by the phase transformation and if there is any relation with the specific grain orientation of the alloys.

8.2.5 Calculate the real shear stresses below the indenter to know exactly which forces are interacting

In dry scratch-corrosion experiments characterized in depth in Chapter 7, lateral friction forces were monitored. When the 5 μm spherical tip was used the level of deformation was really high and the lateral friction force measured was related with the interaction of the material displaced on the sides of the scratches and in front of the tip. In this sense it would be interesting to calculate more accurately by finite element modelling (FEM) the deformed area and the stress and strain fields produced in front of the tip to analyse the role played by the shear stresses and how they influenced the deformation process.

The aims of the future work can be summarised as follows:

- Investigate the influence of protein on the deformation-corrosion mechanisms occurring on CoCrMo and Titanium alloys at the nano-scale.
- Understand the effect of multiple-scratch experiments on the corrosion kinetics on CoCrMo and Ti alloys and how their oxide layers reforms in a pre-deformed scratch groove.
- Examine the effects on the tribo-corrosion processes in metal on metal contacts under different environmental conditions and analyse mixed metal-metal contacts at the nano-scale by coupling Co and Ti alloys.
- Develop a full map describing the deformation-corrosion mechanisms at the nano-scale occurring in Co and Ti based alloys. The knowledge obtained from the work will be the basis to improve future metallurgical processes to develop new implants and understand the failure modes observed in implants retrieved from patients.

Appendix I: Publications and Awards

8.3 Journal papers

- Nano-scale wear characterization of CoCrMo biomedical alloys
  V.Martinez-Nogues, J.M. Nesbitt, R.J.K. Wood, .B.Cook.
  Journal: Tribology International, Volume: 93(2016) 563-572.
  http://dx.doi.org/10.1016/j.triboint.2015.03.037

- Specific grain orientation influence in the deformation-corrosion behaviour of CoCrMo biomedical materials
  V.Martinez-Nogues, R.J.K. Wood, R.B.Cook
  Intended to be submitted to Acta Biomateralia in the next months

8.4 Conference proceedings

- Nano-scale wear of CoCrMo alloys as biomedical materials: tribolayer characterization
  V.Martinez-Nogues, J.C.Walker, R.F.J Wood, J.M.Nesbitt, R.B.Cook
  20th International Conference on Wear of Materials.Toronto (Canada).
  12-16th April 2015.Contribution: Poster

- Nano-scale wear corrosion in hip implants: Why metallic biomaterials fail?
  SET for Britain Poster Competition 2015. House of Commons. London
  9th March 2015. Contribution: Poster

- Nano-scale fretting of biomedical materials: validation of a new nanointerferometer measurement system
  V.Martinez-Nogues, R.J.K. Wood, J.M. Nesbitt, C.Maul, R.B.Cook.

41st Leeds-Lyon Symposium on Tribology: Integrated Tribology.Leeds (UK). 7-9th September 2014. Contribution: Oral

- Nano-scale fretting of biomedical Materials: friction and plastic deformation measurements
  V.Martinez-Nogues, J.Wharton, R.J.K. Wood, R.B.Cook
  PGR Engineering Faculty Conference 2014. Southampton
  Contribution: Poster
- Nano-scale tribocorrosion of biomedical materials: preliminary results
  V.Martinez-Nogues, R.Alberts, M.Stolz, R.J.K.Wood, R.B.Cook
  PGR Engineering Faculty Conference 2013. Southampton
  Contribution: Oral

<u>Submitted: pending to be presented in 2016:</u>

- Influence of the manufacturing finishing on the nano-scale wear resistance of the taper-trunnion interface in hip implants
  V.Martinez-Nogues, J.C.Walker, R.B.Cook
  Submitted to 43rd Leeds-Lyon Symposium on Tribology.
  6-9th September 2016
- Analysis of the scratch corrosion behaviour of CoCrMo alloys at the nano-scale
  V.Martinez-Nogues, R.J.K. Wood, R.B.Cook
  Intend to be submitted to 3rd International Conference on Biotribology (ICoBT 2016). London (UK). 11-14th September 2016

8.5 Awards

- EPRSC Engineering and Physical Sciences Research Council Award
  May 2012
- Travel Grant "The Armourers and Brasiers Foundation" April 2014
- British Spanish Society Scholarship 2014. BUPA Bursary. April 2014
- Set for Britain Poster Competition. Engineering Finalist. March 2015

3rd Interantional Conference on Biotribology-ICoBT 2016

Influence of the grain orientation on the scratch-corrosion behaviour of CoCrMo alloys at the nano-scale

V.Martinez-Nogues[*1], J.Wharton[a], R.J.K. Wood[1], R.Cook[1]
[a] National Centre for Advanced Tribology, nCATS, Faculty of Engineering Sciences, University of Southampton. Southampton, University Road, SO17 1BJ, UK
Contact e-mail: vm1y11@soton.ac.uk

Hard radiopacifier particles (ZrO_2) embedded in the PMMA acrylic cement in cemented hip implants can act as single asperities causing abrasive wear on the metallic components due to micromotions at the interface. As a result the protective oxide layer is disrupted and the alloy is deformed generating metallic particles and ions which are known to produce severe reactions within the body and the failure of the implant. A novel electrochemistry cell was designed to understand the deformation-corrosion mechanisms affecting this interface at the nano-scale.

Single scratch experiments, 100 µm long, using a range load from 10 to 120 mN (14-33GPa) were performed in 4 CoCrMo alloys (Forged, As Cast, As Cast thermal treated and As Cast low carbon) using a 5 µm diamond spherical tip acting as a hard single particle in contact with the metal surface. Transient current densities were monitored during the test to calculate the repassivation kinetics. The affected area subjected to repassivation was determined by interferometric measurements and the specific 3D features created as a consequence of the deformation were observed by SEM. EBSD mapping was used to characterize the grain orientation for each alloy.

Specific deformation features (triangular slip lines, angular slip lines or micro-cutting), repassivation time constants (Figure 1) and the affected area (Figure 2) were correlated to the grain orientation of each sample as summarised in Figure 3. Forged samples and multiple grain oriented As Cast alloys showed repassivation times 50 % higher than As Cast alloys oriented in the easy glide or the basal plane.

From the detailed deformation-corrosion map developed, it was found that the crystallographic grain orientation and the grain size of the Co alloys under study play a decisive role governing the corrosion processes and therefore the liberation of metallic ions.

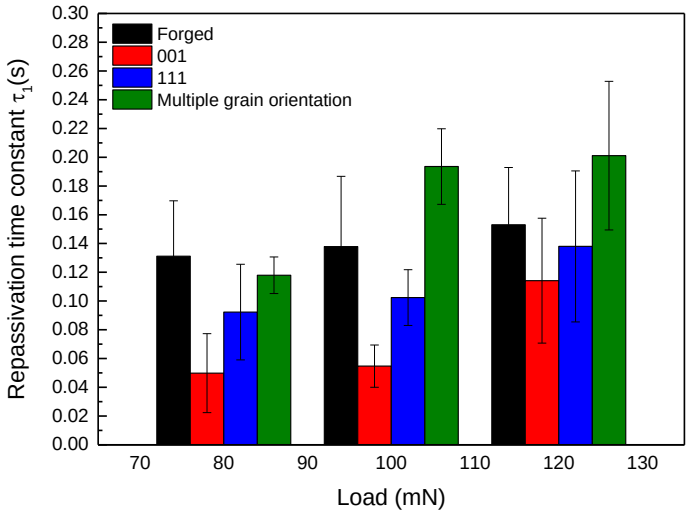

Figure 1. Repassivation time constants under 80, 90 and 120 mN load experiments for the four grain orientations found on the Co-based alloys.

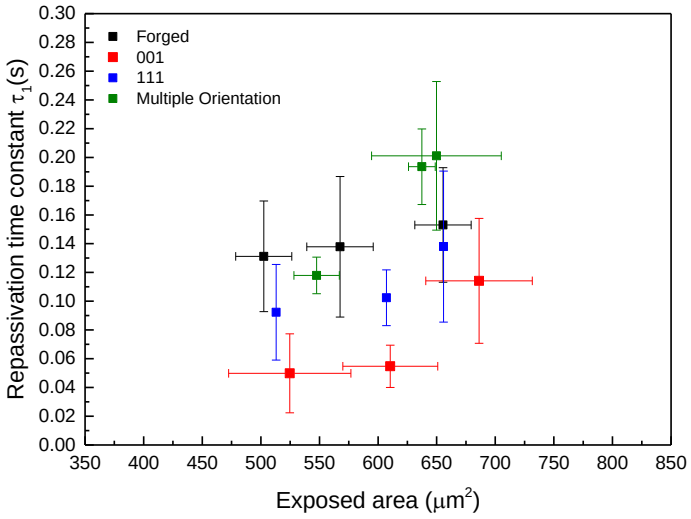

Figure 2. Repassivation time constant-exposed area correlation for the four grain orientations found on the Co-based alloys.

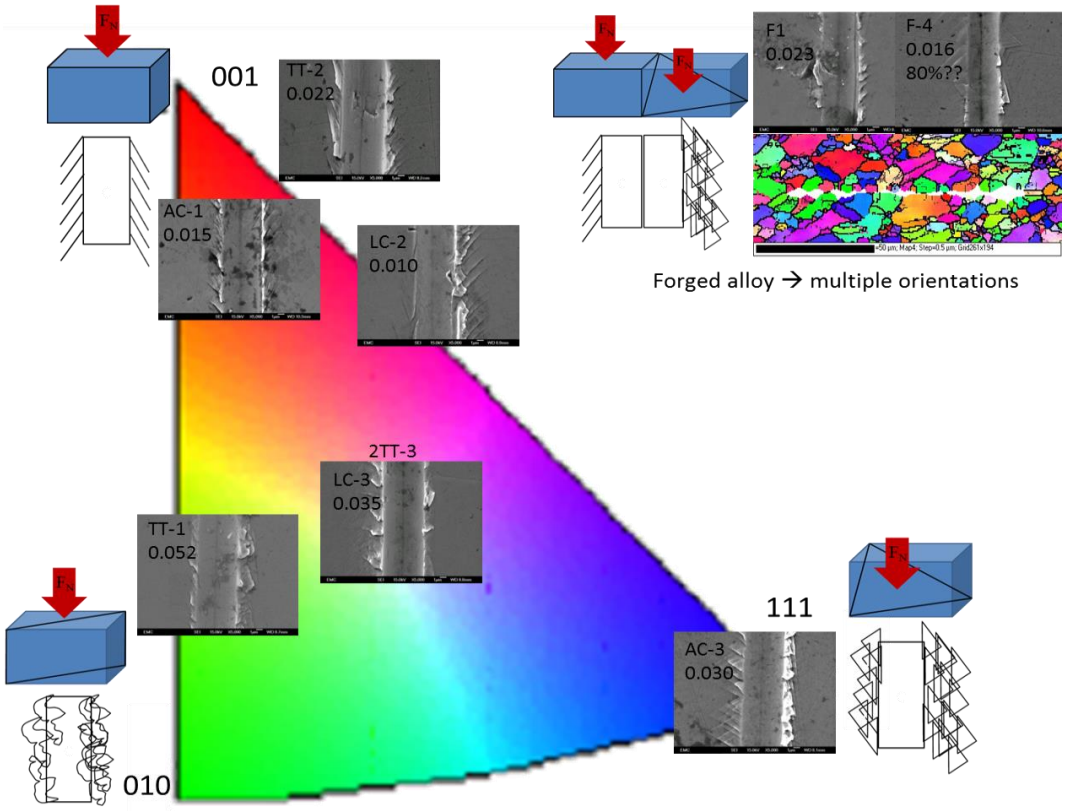

Figure 3. Scratch-corrosion summary map including: grain orientation related to transient corrosion currents values and specif deformation features found during the scratch-corrosion experiments at the nano-scale

43rd Leeds-Lyon Symposium on Tribology-2016

Influence of the manufacturing finishing on the nano-scale wear resistance at the taper-trunnion interface in hip implants

V.Martinez-Nogues[a], J.C.Walker[a] ,R.B. Cook[a]
[a] National Centre for Advanced Tribology, nCATS, Faculty of Engineering Sciences, University of Southampton. Southampton, University Road, SO17 1BJ, UK
Contact e-mail: vm1y11@soton.ac.uk

Introduction

Micromotions at the taper-trunnion interface result in wear and corrosion processes which produce damage resulting in the generation and release of metallic particles and ions into the body. These have been found to be responsible for triggering adverse reactions to the periprosthetic tissues, pain and the need to revise the implant. The influence of the surface finished at the taper-trunnion interface is investigated to analyse how it affects to the wear resistance at the nano-scale in three commercial systems.

Materials and methods

Three different taper surfaces were investigated, two female taper surfaces an as cast heat treated CoCrMo AC-TT alloy and a powder metallurgy GADS alloy and a trunnion surface made from forged-low carbon CoCrMo (FLC). Surface roughness and the metallurgical microstructure of the surfaces were investigated. The bulk material and the outer surfaces of the tapers and trunnion were mechanically characterised using nanoindentation and the wear resistance using nano-reciprocating sliding experiments at 5 and 10 mN loads using a 5 µm diamond tip.

Results and discussion

The roughness values were 0.54, 0.45 and 3.56 µm for the AC-TT, the GADS head and the FLC trunnion respectively, see Figure 1. A significant difference in hardness values, was found between the bulk and the edge locations for all samples 8 to 26 and 18 GPa for the GADS head and the CPT trunnion respectively, Figure 2a. The AC-TT head showed only a 2 GPa difference between the bulk and the edge locations. Plastic deformation values from reciprocating sliding experiments are shown in Figure 2b. Experiments under 5 mN loads did not show statistically significant differences between the three different alloys and between the two analysed locations.

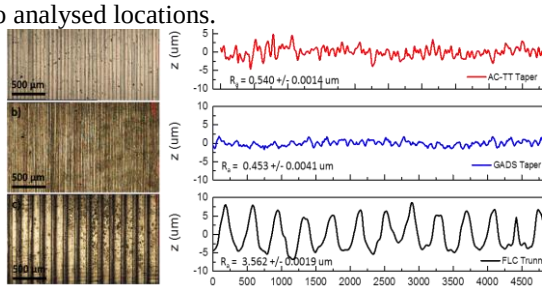

Figure 1. Characterisitic roughness profiles for the 3 alloys: a) AC-TT, b) GADS head and c) FLC

When a 10 mN load was applied, both the LC-TT and the GADS alloys did not show different plastic deformation values with 90 and 140 nm depths respectively. However, the FLC exhibited an edge depth 50 % higher than in the bulk material.

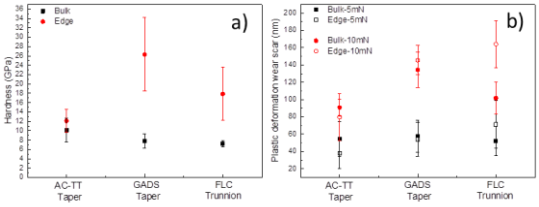

Figure 2. a) Hardness values and b) Plastic deformation at the bulk and edge locations for the 3 alloys

Conclusions

Results from the study indicates that manufacturing finishing differences affect the microstructure of the alloys at the edge of the sample resulting into a worse wear behaviour or the FLC alloy respect to the other two CoCrMo alloys under study.

Wear of Materials 2015

Nano-scale fretting characterization of biomedical materials

V.Martinez-Nogues*[1], R.Alberts[1], Christian Maul[2], R.J.K. Wood[1], R.Cook[1]
[a] National Centre for Advanced Tribology, nCATS, Faculty of Engineering Sciences, University of Southampton. Southampton, University Road, SO17 1BJ, UK
Contact e-mail: vm1y11@soton.ac.uk

Tribocorrosion processes at the taper-trunnion and cement-femoral stem interfaces of hip replacements result in the release of metal debris and ions which can trigger adverse local tissue reactions within the body resulting in serious complications and pain for the patient and the need for revision surgery. The origin of the release is micromotion between the surfaces, resulting in the removal of the oxide film from the metallic surfaces which contributes to material loss, but also depassivates the metal surfaces enabling corrosive attack.

The aim of the work is to establish a technique capable of reproducing the environment, contact pressures and micromotions seen in these interfaces. This paper presents the findings of the nanoscale fretting studies on three biomedical Cobalt Chromium Molybdenum (CoCrMo) alloys: forged, cast-thermal treated and cast double thermal treated. Nano-fretting experiments were performed at contact pressures from 0.7 to 2 GPa, during 18000 cycles at a frequency of 5Hz and a track length of 5µm. Friction coefficients and fretting scars depths were monitored during the experiments. Depth measurements were validated using a high performance white light interferometer with a lateral resolution of 0.8 µm and vertical resolution of 0.1 nm. (Figure 1 and 2).

Friction coefficients shown statistical differences between the alloys when low loads were applied. Dispersed energy values exhibited a linear relationship with the load, with the forged alloy having the highest energy per cycle, Figure

The study demonstrated the ability of the nano-fretting technique to determine the fretting resistance of the CoCrMo alloys and the white light interferometer capacity to characterize the fretting scars.

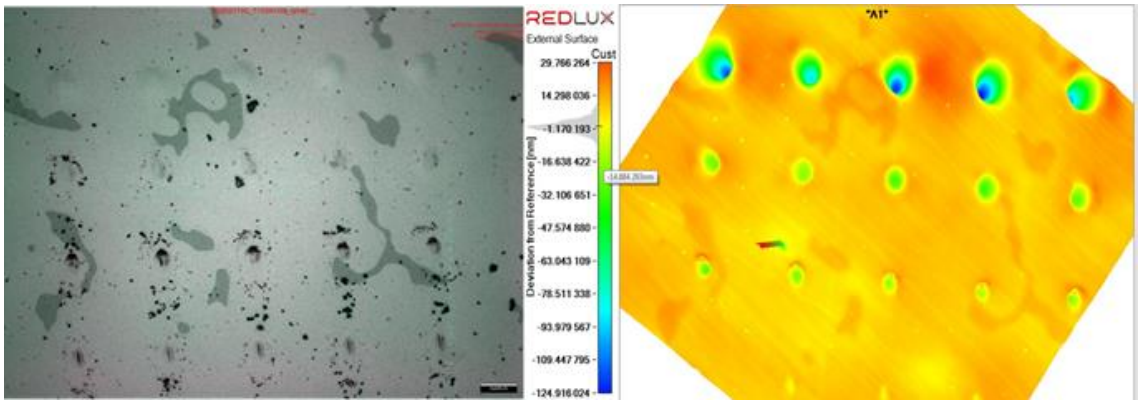

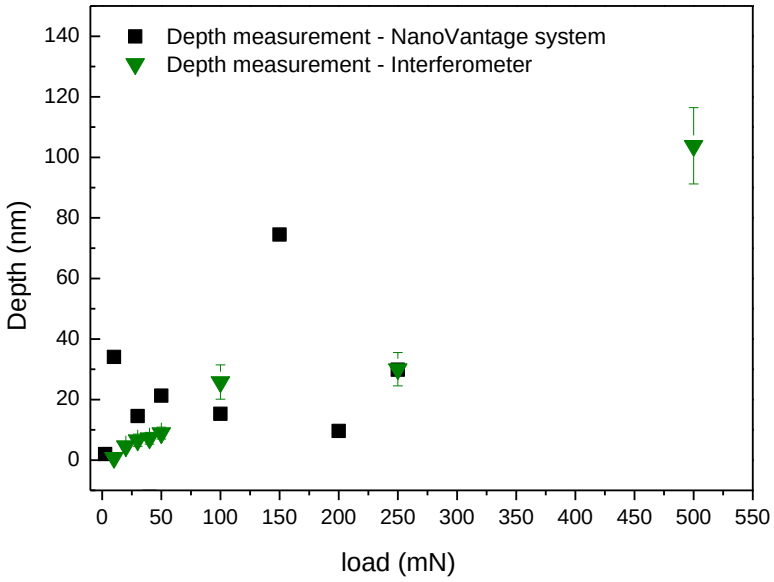
Depth measurement - NanoVantage system
Depth measurement - Interferometer
Depth (nm)
load (mN)
0
20
40
60
80
100
120
140
0
50
100
150
200
250
300
350
400
450
500
550

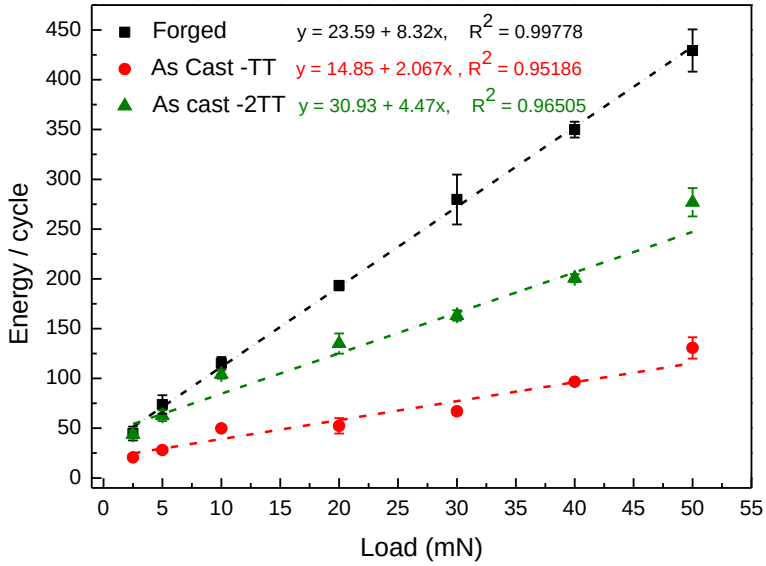
Forged
y = 23.59 + 8.32x, R2 = 0.99778
As Cast -TT
y = 14.85 + 2.067x , R2 = 0.95186
As cast -2TT
y = 30.93 + 4.47x, R2 = 0.96505
Energy / cycle
Load (mN)
0
50
100
150
200
250
300
350
400
450
0
5
10
15
20
25
30
35
40
45
50
55

SET for Britain Poster Competition

Nano-scale wear corrosion processes in total hip replacements: why metallic biomaterials fail?

Vanesa Martinez-Nogues, R.J.K. Wood, R. Alberts, R.B.Cook.
[a] National Centre for Advanced Tribology, nCATS, Faculty of Engineering Sciences, University of Southampton. Southampton, University Road, SO17 1BJ, UK
Contact e-mail: vm1y11@soton.ac.uk

Total hip replacement is one of the main surgical procedures in orthopaedics. It is a successful, safe and cost-effective medical treatment to restore functionality of the hip joint and to regain pain-free mobility in patients suffering from degenerative joint diseases, such as osteoarthritis, or trauma injuries. Business Wire reported that the Total Hip Replacement market is estimated to reach a value of $7.1 billion by 2019, due not only to the growth of the global elderly population, but also the climbing number of younger patients in need of the procedure. Despite this success, there is a growing concern about some designs and material pairings which presented high wear rates and corrosion problems, creating uncertainty about the safety and effectiveness of the artificial hip joints.

So far the main investigations in the field have mainly attributed these failures to implants were metal-metal interfaces were presented. However, the combination of wear and corrosion processes, known as tribo-corrosion, plays a significant role in the long-term performance and failure of a broader range of implantable materials such as ceramic femoral heads or cements used to fixed the devices to the bones. As part of an interdisciplinary team formed by mechanical engineers together with orthopaedic surgeons from the Southampton General Hospital, retrieved implants from patients have been analysed to confirm our hypothesis. The wear corrosion processes cause a particular damage which results from interactions at the nanoscale between contacting metallic and metal/non-metal interfaces in the artificial hip components such as the femoral stem-cement interface or the femoral head-taper connection. Micromotion between the roughness asperities of the surfaces causes deformation and destruction of the natural oxide layer leading to wear while at the same time increasing the corrosive attack.

In addition to the clinical data observations, a new state of the art laboratory technique has been developed to reproduce the extent of the tribo-corrosion damage which occurs between different pairs of implantable materials such as Cobalt alloys, Titanium alloys or ceramics at a level that had not been under study yet. Wear damage and chemistry alterations produced over the surface were analysed using high resolution optical techniques for a better understanding of the synergetic processes between wear and corrosion.

The results discovered so far provide a novel understanding of implant's failure modes which will optimize and improve the next generation of hip implants to benefit the patients, the national health systems and the orthopaedic industry. More reliable, free pain and longer-lasting artificial hip implants will reduce revision surgeries with lower health risks and economic costs due to potential long- term complications.

41rd Leeds-Lyon Symposium on Tribology-2014

Nanoscale Fretting of CoCrMo biomedical alloys>

V.Martinez-Nogues[a], R.J. K.Wood[a], J.Nesbitt[b], C.Maul[b] R.B. Cook[a]
[a] National Centre for Advanced Tribology, University of Southampton, Southampton University Road, SO17 1BJ, UK
[b] Redlux Ltd. 3/7 Avenger close, Chandlers Ford, Southampton, S053 4DQ
Contact e-mail: vm1y11@soton.ac.uk

Introduction

Fretting motion at the micro and the nano scale has been found to occur between the femoral stem and bone cement mantle, generating metallic and cement debris. The debris has been linked to bone osteolysis and subsequent aseptic loosening of the femoral component resulting in the implant failure.

Final surface roughness, pores and hard radio pacifier particles have been reported as the main reasons to influence the fretting processes on polished femoral stems [137, 138]. However, little is known about the role played by the alloys manufacturing processes or their microstructures. Initial findings on the nanofretting behaviour of four biomedical CoCrMo alloys are presented in this comparative study.

Materials and methods

A forged, as cast, a cast single thermal treated (as cast-TT) and a cast double thermal treated (as cast-2TT) alloys were used. Hardness and reduced modulus were calculated by nanoindentation techniques.

Nano-fretting tests were performed under loads from 1 to 30 mN (contact pressures from 6.6 to 20.70 GPa), using a 5 µm radius diamond spherical tip. The tests ran for 3000 cycles at a frequency of 7.5Hz and a track length of 10 µm. Tangential friction forces were continuously monitored during a number of the experiments and coefficients of friction were calculated from the ratio of tangential force to the normal force. Permanent plastic deformation of the fretting wear scars were measured in situ by the fretting system and compare with measurements performed by AFM and a scanning white-light interferometer microscope (Redlux Ltd, UK) with lateral resolution of 0.8 µm and vertical resolution of 0.1 nm.

Results and discussion

Coefficient of friction results didn't show statistical differences between the running-in and the steady state period for any of the alloys. Average µ value was 0.14 for the four materials (Figure 1a).

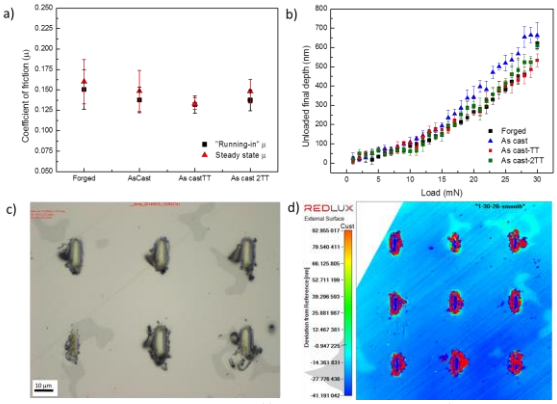

Figure 1.a) Friction coefficients.b) Unloaded final depth comparison, c) Optical microscope fretting scars image for the as cast sample, d) Interferometer fretting scars measurements

Fretting depth values at loads from 16 to 29 mN were significantly higher for the as cast alloy than for the other materials, see Figure 1b. In addition, the presence of carbides or thermal treatments influence the quantity of wear debris, see Figure 1c.

Conclusion

The initial findings indicate the nano-fretting wear resistance of CoCrMo alloys used for THR are influenced by manufacturing process and the applied thermal treatments which modified the alloy final microstructure.

PGR Conference 2014-Southampton

Nanoscale fretting of biomedical materials: friction and plastic deformation measurements

V.Martinez-Nogues[1], R.Alberts[1], M.Stolz[1], R.J. K.Wood[1], R. Cook[1]
[1]National Centre for Advanced Tribology, nCATS, Faculty of Engineering and the Environment, University of Southampton, UK

INTRODUCTION

Tribocorrosion plays a significant role in the performance and failure of implantable metallic devices. Damage caused by tribocorrosion has been reported previously in several implantable devices such as disk replacements [1], bone plates [2], interfaces between the cement and the femoral stem in cemented hip arthoplasties [3,4] and in the taper interfaces of hip replacements [5-7]. The production of metal debris and the liberation of metallic ions can result in allergic reactions within the body causing tissue necrosis, joint failure and the need for implant revision.

The tribocorrosion processes which occur have their origins at the nanoscale. Micromotions between the asperities of the contacting interfaces result in deformation and wear of the surfaces while at the same time depassivating them and opening nanscent metallic surfaces to corrosive attack.

The goal of that work is to establish a technique able to produce the tribocorrosion damage which would occur between biomedical material couples. For that purpose, the project will initially focus on the characterisation of the mechanical properties on their own and later an electrochemical cell will be attached to the system to study the electrochemical response produced by the different biomedical material pairings.

METHODOLOGY

Four different CoCrMo alloys were used in this study: forged, as cast, as cast single thermal treated and as cast double thermal treated. Micro Vickers hardness (Matzsuzawa Seiki Co.Ltd) and nanoindentation measurements were carried out on the alloys using a Nano Test Vantage system (Micro Materials) to calculate H_{IT} and E_R.

Nanofretting tests were conducted under two different experimental conditions. Track length was set to 10 μm, during 3000 cycles at 7.5 Hz. Experiments to analysed the frictional behaviour were carried out applying 5, 10 and 20 mN load which correspond to maximum contact pressures between 0.97 and 1.5 GPa. A spherical diamond tip of 200 μm was used. For the fretting behaviour resistance analysis the load range was set from 1 to 30 mN (6.6 to 20.70 GPa Hertzian pressure) and the tip radius was 5 μm. Coefficient of friction and fretting resistance of the four alloys were compared. Depth values were monitored in-situ by the Nanovantage system and post testing measurements were taken by AFM and nanointerferometry to validate the obtained results.

SEM and optical microscopy was used to analyse the fretting scar morphologies.

RESULTS AND DISCUSSION

The forged alloy exhibit the highest microindentation value, 5.8 GPa followed by the as cast alloy, 4.74 GPa. Thermal treatments produced a 7 and 11 % reduction in hardness compared to the non-treated as cast sample. Nanoindentation values allows assessment of the mechanical properties of the different phases (matrix and carbides), however the as cast and the as cast single thermal treated matrix values are higher than expected due to the influence of nearby and subsurface carbides within the indentation interaction volume. Reduced modulus followed the same trend as the hardness.

Running-in and steady state friction coefficients, see Figure 1a-b, didn't show significant differences between the samples, with values oscillating between 0.150 and 0.275 for the

different loads. Independently from the alloy the COF shows a systematic variation with load, where higher loads resulted in a lower COF; also the forged sample showed a higher dispersion than the as cast samples. The COF increment after the running–in period might be attributed to the tip increasing the contact surface with the sample producing more tangential forces and therefore the friction coefficient together with the production of metallic debris.

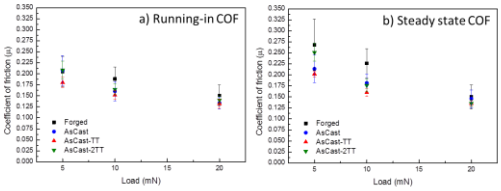

Figure 1.a) Running-in COF, b) Steady state COF

Depth values, Figure 2b, from the nanointerferometer fretting scars cross sections, Figure 2a, showed an increasing trend when load is raised. A significant higher plastic deformation was found on the as cast sample comparing with the rest of the alloys for loads over 17mN.

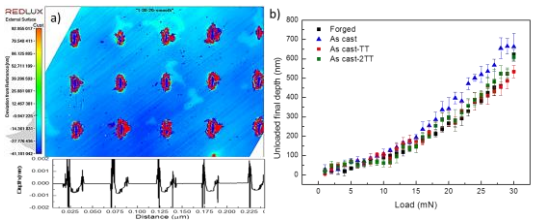

Figure 2: a) Interferometer fretting scars measurements.b) Unloaded final depth comparisonLinear correlations between the three measurement systems are shown in Figure 3. The Pearson's correlation values were 0.94 and 0.88, for the AFM and the nanointerferometer systems respectively.

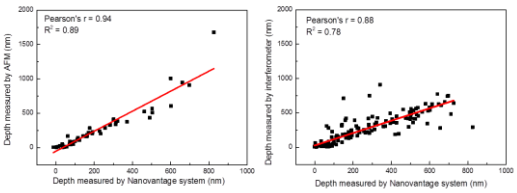

Figure 3. Depth measurement systems validation.

Morphological analysis of the fretting scars, presented severe plastic deformation which had produced pile up on the scar edges together with debris formation, more accentuated in the as cast double thermal treated alloy.

CONCLUSIONS AND FUTURE WORK

Nano-fretting experiments allow the comparison of the frictional and fretting resistance behaviour of the four CoCrMo alloys.

Future work will be focus on static corrosion experiments and the attachment of an electrochemical cell to understand the synergism between the corrosion and the fretting processes that occurs between different biomedical material pairings.

PGR Conference 2013-Southampton

Nanoscale tribocorrosion of biomedical materials: preliminary results

V.Martinez-Nogues[1], R.Alberts[1], M.Stolz[1], R.J. K.Wood[1], R. Cook[1]
[1]National Centre for Advanced Tribology, nCATS, Faculty of Engineering and the Environment, University of Southampton, UK

INTRODUCTION

Tribocorrosion plays a significant role in the performance and failure of implantable metallic devices. The damages caused by tribocorrosion have been reported previously in several joint implantable devices as disk replacements [1], bone plates [2], interfaces between the cement and the metallic stem in cemented hip arthoplasties [3,4] and moreover in the taper interfaces of hip replacements [5-7]. The production of metal debris and the liberation of metallic ions is the responsible of allergical reactions within the body causing in the long term the joint failure and the implant revision.

The origin of that tribocorrosion processes between the surfaces is produce at the nanoscale. Micromotions between the asperities of the contacting interfaces result in deformation and wear of the surfaces while at the same time depassivating them and opening nanscent metallic surfaces to corrosive attack.

The goal of that work is to establish a technique able to produce the tribocorrosion damage which would occur between biomedical material couples. In that way the tribological contact might be controlled and it would be possible to increase the lifespan of the materials used for joint implants. For that purpose, the project is focus first in the characterization of the mechanical conditions on their own and later an electrochemical cell will be attached to the system to study the electrochemical response produced by the different biomedical material pairings.

METHODOLOGY

The materials used in this study were three different CoCrMo biomedical alloys. The samples were obtained from a forged stem, an as cast acetabular cup component and a thermal treated stem. Different manufacturing processes provides each alloy with a specific microstructure and mechanical properties. The samples were polished to a roughness of 11 ± 2 nm. A mixture of 15ml HCl acid, 10 ml nitric acid and 10 ml acetic acid was used to reveal the microstructures by chemical etching immersing the samples during 5 minutes.

Nanoindentation measurements were carried out on the alloys using a Nano Test Vantage system (Micro Materials). The experiments were depth controlled applying a 500mN load using a Berkovich tip. Matrixes of 20 x 20 indents were programmed in the system to calculate the Young modulus, E, and the hardness, H.

The fretting behaviour of the CoCrMo alloys was characterised by nanofretting tests. The load applied was in the range between 1 and 10mN, using a diamond spherical tip of 200µm, which results into an initial contact pressure from 0.5 to 1.2GPa. The work frequency was 5Hz and the track length 5µm. Friction coefficients and depth of the fretting scars were recorded during 15000 cycles.

RESULTS AND DISCUSSION

The microstructures of the three CoCrMo alloys are shown in Figure 1. The forged sample, 1a, is characterised by a uniform equiaxed 20 µm sized grain microstructure while the as cast and the

thermal treated consists of a Co matrix with large columnar carbides, figures 1b and 1c. However, the carbides of the last one are coarser than in the as cast alloy, so more investigation should be carry out to determine the type of carbides and their exact composition.

Hardness values are shown in Figure 2. For the forged alloy it was obtained an average value of 7.11 ± 0.29 GPa, while for the as cast and the thermal treated ones the values are 6.60 ± 0.36 and 6.59 ± 0.26 GPa, respectively.

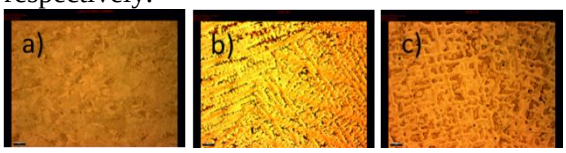

Figure 1:Microstructure for the three CoCrMo alloys. a) Forged, b)As cast, c) Thermal treated.

Maximum values of hardness were recorded for the carbides dispersed in the as cast matrix with a hardness around 9.40 ± 1.23 GPa.

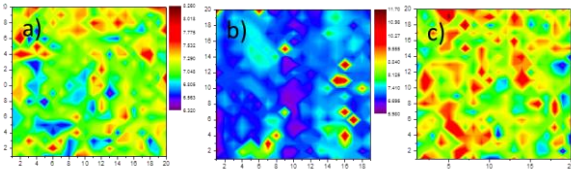

Figure 2: Hardness maps of the the different CoCrMo alloy: a) Forged alloy, b) As cast alloy, c) Thermal treated alloy.

The nanofretting behaviour of the samples is described by friction coefficient versus depth graphs, as is shown in Figure 3. In the case of the forged sample, the increase of load results in higher friction coefficients that vary from 0.25 when 1mN is applied, to 1 for the maximum load of 10mN.

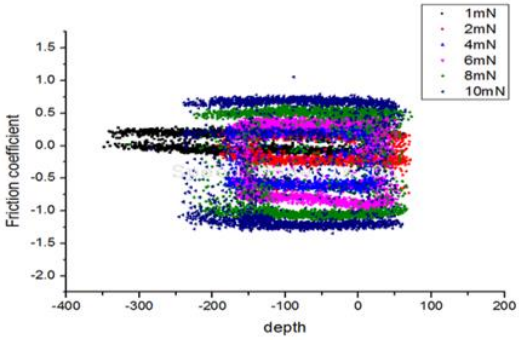

Figure 3: Friction coefficient versus wear track depth ofr the forged CoCrMo alloy obtained from the nanofretting tests applying a range of loads between 1 and 10mN.

CONCLUSIONS AND FUTURE WORK

Three different CoCrMo biomedical alloys were chemical etched to reveal their microstructures and observed the differences between them. Young Modulus and hardness were calculated by nanoindentation testing to provide a characterization of their mechanical properties.

Future work will be focus on characterised the nano fretting behaviour in dry and wet conditions, together with the developing of an electrochemical cell to provide information about the corrosion processes that occurs at the same time as the fretting processes are happening.

References

1. Board, N.E., *10th Annual Report 2013 National Joint Registry for England, Wales and Northern Ireland*, 2013.
2. Wood,L. *http://www.businesswire.com/news/home/20130829005601/en/Research-Markets-MediPoint-Total-Hip-Replacement--#.UxoWb_khDOE*. 2013 [cited 2013.
3. McKee, G.K. and J. Watson-Farrar, *Replacement of arthritic hips by the McKee-Farrar prosthesis.* The Journal of Bone & Joint Surgery 1966. **48 B**(2): p. 245-259.
4. Amstutz, H.C. and P. Grigoris, *Metal on metal bearings in hip arthroplasty.* Clin Orthop Relat Res, 1996(329 Suppl): p. S11-34.
5. Sharma, V., et al., *Revision Total Hip Arthroplasty for Ceramic Head Fracture: A Long-Term Follow-Up.* The Journal of Arthroplasty, 2010. **25**(3): p. 342-347.
6. Affatato, S., et al., *Comparative study on the wear behaviour of different conventional and cross-linked polyethylenes for total hip replacement.* Tribology International, 2008. **41**(8): p. 813-822.
7. Rieker, C.B., R. Schön, and P. Köttig, *Development and validation of a second-generation metal-on-metal bearing: Laboratory studies and analysis of retrievals.* The Journal of Arthroplasty, 2004. **19**(8, Supplement): p. 5-11.
8. Langton, D.J., et al., *Adverse reaction to metal debris following hip resurfacing: the influence of component type, orientation and volumetric wear.* J Bone Joint Surg Br, 2011. **93**(2): p. 164-71.
9. Pelt, C.E., et al., *Histologic, serologic, and tribologic findings in failed metal-on-metal total hip arthroplasty: AAOS exhibit selection.* J Bone Joint Surg Am, 2013. **95**(21): p. e163.
10. Elkins, J., J. Callaghan, and T. brown, *Are large heads and unqualified benefit for Metal on Metal Total Hip Replacement? Stability vs. "Trunnionosis" Wear*, in *American Society of Orthopaedic Surgeons. Annual Meeting.2013*2013: Chigago, Illionis. p. Poster P055.
11. Pastides, P.S., et al., *Trunnionosis: A pain in the neck.* World J Orthop, 2013. **4**(4): p. 161-6.
12. Bryant, M., et al., *Failure analysis of cemented metal-on-metal total hip replacements from a single centre cohort.* Wear, 2013. **301**(1–2): p. 226-233.

13. Howell, J.R., et al., *In Vivo surface wear mechanisms of femoral components of cemented total hip arthroplasties: the influence of wear mechanism on clinical outcome.* The Journal of Arthroplasty, 2004. **19**(1): p. 88-101.
14. Fricka, K.B., et al., *Metal-on-Metal Local Tissue Reaction Is Associated With Corrosion of the Head Taper Junction.* The Journal of Arthroplasty, 2012. **27**(8, Supplement): p. 26-31.e1.
15. Gilbert, J.L., C.A. Buckley, and J.J. Jacobs, *In vivo corrosion of modular hip prosthesis components in mixed and similar metal combinations. The effect of crevice, stress, motion, and alloy coupling.* Journal of Biomedical Materials Research, 1993. **27**(12): p. 1533-1544.
16. Hodgson, A.W., et al., *An analysis of the in vivo deterioration of Co-Cr-Mo implants through wear and corrosion.* Proc Inst Mech Eng H, 2007. **221**(3): p. 291-303.
17. Diomidis, N., et al., *Tribo-electrochemical characterization of metallic biomaterials for total joint replacement.* Acta Biomaterialia, 2012. **8**(2): p. 852-859.
18. Varano, R., et al., *The effect of microstructure on the wear of cobalt-based alloys used in metal-on-metal hip implants.* Proc Inst Mech Eng H, 2006. **220**(2): p. 145-59.
19. Valero-Vidal, C., et al., *Influence of carbides and microstructure of CoCrMo alloys on their metallic dissolution resistance.* Materials Science and Engineering: C, 2013. **33**(8): p. 4667-4676.
20. Escobedo, J., et al., *Effect of nitrogen on the microstructure and mechanical properties of a Co□Cr□Mo alloy.* Materials & Design, 1996. **17**(2): p. 79-83.
21. Band, T., *Materials and Metallurgy*, in *Modern Hip Resurfacing*, D.W. McMinn, Editor 2009, Springer London. p. 43-63.
22. Gupta, K.P., *The Co-Cr-Mo (Cobalt-Chromium-Molybdenum) System.* Journal of Phase Equilibria and Diffusion, 2005. **26**(1): p. 87-92.
23. Saldívar-García, A.J. and H.F. López, *Microstructural effects on the wear resistance of wrought and as-cast Co-Cr-Mo-C implant alloys.* Journal of Biomedical Materials Research Part A, 2005. **74A**(2): p. 269-274.
24. Henriques, B., et al., *Mechanical properties of hot pressed CoCrMo alloy compacts for biomedical applications.* Materials & Design, 2015. **83**: p. 829-834.
25. Ren, F., W. Zhu, and K. Chu, *Fabrication, tribological and corrosion behaviors of ultra-fine grained Co–28Cr–6Mo alloy for biomedical applications.* Journal of the Mechanical Behavior of Biomedical Materials, 2016. **60**: p. 139-147.
26. McMinn, D.J., *Development of metal/metal hip resurfacing.* Hip Int, 2003. **13**(1): p. 41-53.
27. Contu, F., B. Elsener, and H. Böhni, *Corrosion behaviour of CoCrMo implant alloy during fretting in bovine serum.* Corrosion Science, 2005. **47**(8): p. 1863-1875.
28. Milošev, I. and H.H. Strehblow, *The composition of the surface passive film formed on CoCrMo alloy in simulated physiological solution.* Electrochimica Acta, 2003. **48**(19): p. 2767-2774.
29. Virtanen, S., et al., *Special modes of corrosion under physiological and simulated physiological conditions.* Acta Biomater, 2008. **4**(3): p. 468-76.
30. Sun, D., J.A. Wharton, and R.J.K. Wood, *Micro and nano-scale tribocorrosion of cast CoCrMo.* Tribology Letters, 2011. **41**(3): p. 525-533.

31. Diomidis, N., et al., *A methodology for the assessment of the tribocorrosion of passivating metallic materials.* Lubrication Science, 2009. **21**(2): p. 53-67.
32. Goldberg, J.R. and J.L. Gilbert, *Electrochemical response of CoCrMo to high-speed fracture of its metal oxide using an electrochemical scratch test method.* J Biomed Mater Res, 1997. **37**(3): p. 421-31.
33. Swaminathan, V. and J.L. Gilbert, *Fretting corrosion of CoCrMo and Ti6Al4V interfaces.* Biomaterials, 2012. **33**(22): p. 5487-503.
34. Igual Muñoz, A. and S. Mischler, *Effect of the environment on wear ranking and corrosion of biomedical CoCrMo alloys.* Journal of Materials Science: Materials in Medicine, 2011. **22**(3): p. 437-450.
35. Yan, Y., et al., *Effect of metallic nanoparticles on the biotribocorrosion behaviour of Metal-on-Metal hip prostheses.* Wear, 2009. **267**(5–8): p. 683-688.
36. Muñoz, A.I. and S. Mischler, *Interactive Effects of Albumin and Phosphate Ions on the Corrosion of CoCrMo Implant Alloy.* Journal of The Electrochemical Society, 2007. **154**(10): p. C562-C570.
37. Milošev, I., *The effect of biomolecules on the behaviour of CoCrMo alloy in various simulated physiological solutions.* Electrochimica Acta, 2012. **78**: p. 259-273.
38. Mathew, M., J. Jacobs, and M. Wimmer, *Wear-Corrosion Synergism in a CoCrMo Hip Bearing Alloy Is Influenced by Proteins.* Clinical Orthopaedics and Related Research®, 2012. **470**(11): p. 3109-3117.
39. Valero Vidal, C. and A. Igual Muñoz, *Study of the adsorption process of bovine serum albumin on passivated surfaces of CoCrMo biomedical alloy.* Electrochimica Acta, 2010. **55**(28): p. 8445-8452.
40. Lucas, L.C., R.A. Buchanan, and J.E. Lemons, *Investigations on the galvanic corrosion of multialloy total hip prostheses.* Journal of Biomedical Materials Research, 1981. **15**(5): p. 731-747.
41. Collire, J.P., et al., *Corrosion at the Interface of Cobalt-Alloy Heads on Titanium-Alloy Stems.* Clinical Orthopaedics and Related Research, 1991. **271**: p. 305.
42. Schiff, N., et al., *Galvanic corrosion between orthodontic wires and brackets in fluoride mouthwashes.* The European Journal of Orthodontics, 2006. **28**(3): p. 298-304.
43. Bryant, M., et al., *Galvanically enhanced fretting-crevice corrosion of cemented femoral stems.* Journal of the Mechanical Behavior of Biomedical Materials, 2014. **40**: p. 275-286.
44. Ouerd, A., et al., *Reactivity of CoCrMo alloy in physiological medium: Electrochemical characterization of the metal/protein interface.* Electrochimica Acta, 2008. **53**(13): p. 4461-4469.
45. Espallargas, N., C. Torres, and A.I. Muñoz, *A metal ion release study of CoCrMo exposed to corrosion and tribocorrosion conditions in simulated body fluids.* Wear, 2015. **332-333**.
46. Hodgson, A.W.E., et al., *Passive and transpassive behaviour of CoCrMo in simulated biological solutions.* Electrochimica Acta, 2004. **49**(13): p. 2167-2178.
47. Lewis, A.C., et al., *Effect of synovial fluid, phosphate-buffered saline solution, and water on the dissolution and corrosion properties of CoCrMo alloys as used in orthopedic implants.* Journal of Biomedical Materials Research Part A, 2005. **73A**(4): p. 456-467.

48. Vidal, C.V. and A.I. Muñoz, *Effect of thermal treatment and applied potential on the electrochemical behaviour of CoCrMo biomedical alloy.* Electrochimica Acta, 2009. **54**(6): p. 1798-1809.
49. Sun, D., et al., *Microabrasion–corrosion of cast CoCrMo alloy in simulated body fluids.* Tribology International, 2009. **42**(1): p. 99-110.
50. Yan, Y., A. Neville, and D. Dowson, *Tribo-corrosion properties of cobalt-based medical implant alloys in simulated biological environments.* Wear, 2007. **263**(7–12): p. 1105-1111.
51. Valero Vidal, C. and A. Igual Muñoz, *Electrochemical characterisation of biomedical alloys for surgical implants in simulated body fluids.* Corrosion Science, 2008. **50**: p. 1954-1961.
52. Wood, R.J.K., et al., *Interpretation of electrochemical measurements made during micro-scale abrasion-corrosion.* Tribology International, 2010. **43**(7): p. 1218-1227.
53. Metikoš-Huković, M. and R. Babić, *Passivation and corrosion behaviours of cobalt and cobalt–chromium–molybdenum alloy.* Corrosion Science, 2007. **49**(9): p. 3570-3579.
54. Bettini, E., Eriksson, T., Bostrom, C., Pan, j., *Nature of Current Increase for a CoCrMo Alloy: "transpassive" Dissolution vs. Water Oxidation.* International Journal of Electrochemical science, 2013. **8**: p. 11791-11804.
55. Placko, H.E., S.A. Brown, and J.H. Payer, *Effects of microstructure on the corrosion behavior of CoCr porous coatings on orthopedic implants.* Journal of Biomedical Materials Research, 1998. **39**(2): p. 292-299.
56. Hiromoto, S., et al., *Microstructure and corrosion behaviour in biological environments of the new forged low-Ni Co–Cr–Mo alloys.* Biomaterials, 2005. **26**(24): p. 4912-4923.
57. Bettini, E., Eriksson, T., Bostrom, C., Pan, j., *Influence of grain boundaries on dissolution behavior of a biomedical CoCrMo alloy: in-situ electrochemical-optical, AFM and SEM/TEM studies.* Journal of The Electrochemical Society, 2012. **159**: p. 422-427.
58. Montero-Ocampo, C. and A. Salinas Rodriguez, *Effect of carbon content on the resistance to localized corrosion of as-cast cobalt-based alloys in an aqueous chloride solution.* Journal of Biomedical Materials Research, 1995. **29**(4): p. 441-453.
59. Bonfrisco, L.P. and M. Frary, *Effects of crystallographic orientation on the early stages of oxidation in nickel and chromium.* Journal of Materials Science, 2009. **45**(6): p. 1663-1671.
60. Schuh, C.A., K. Anderson, and C. Orme, *Rapid assessment of anisotropic surface processes: experiments on the corrosion of Inconel 600.* Surface Science, 2003. **544**(2–3): p. 183-192.
61. Song, G.-L. and Z. Xu, *Crystal orientation and electrochemical corrosion of polycrystalline Mg.* Corrosion Science, 2012. **63**: p. 100-112.
62. Wang, S., Wang, J., *Effect of grain orientation on the corrosion behavior of polycrystalline Alloy 690.* Corrosion Science, 2014. **85**: p. 183-192.
63. Mishra, A., Hamby,M.A, Kaiser, B., *Metallurgy, Microstructure, Chemistry and Mechanical Properties of a New Grade of Cobalt-Chromium Alloy Before and After Porous Coating*, in *Cobalt-Base Alloys for Biomedical Applications*, J.A. Disegi, Kennedy, R.L., Pilliar, R., Editor 1999, ASTM: West Conshocken, PA, usa.

64. Giacchi, J.V., et al., *Microstructural characterization of as-cast biocompatible Co–Cr–Mo alloys.* Materials Characterization, 2011. **62**(1): p. 53-61.
65. Giacchi, J.V., O. Fornaro, and H. Palacio, *Microstructural evolution during solution treatment of Co–Cr–Mo–C biocompatible alloys.* Materials Characterization, 2012. **68**: p. 49-57.
66. Guyard, C., et al., *Solidification path and phase equilibria in the liquid-solid range of cobalt-base alloy.* Journal of Materials Science. **16**(3): p. 604-612.
67. Narayan, R. and R.M. Pilliar, *Biomedical Materials- Chapter 2: Metallic Biomaterials*, ed. Springer2009: Springer.
68. Hughes, D.A., *Microstructure evolution, slip patterns and flow stress.* Materials Science and Engineering: A, 2001. **319–321**: p. 46-54.
69. Bay, B., et al., *Overview no. 96 evolution of f.c.c. deformation structures in polyslip.* Acta Metallurgica et Materialia, 1992. **40**(2): p. 205-219.
70. Rezvanian, O., M.A. Zikry, and A.M. Rajendran, *Statistically stored, geometrically necessary and grain boundary dislocation densities: microstructural representation and modelling.* Proceedings of the Royal Society of London A: Mathematical, Physical and Engineering Sciences, 2007. **463**(2087): p. 2833-2853.
71. Kocks, U.F., *A statistical theory of flow stress and work-hardening.* Philosophical Magazine, 1966. **13**(123): p. 541-566.
72. Hansen, N., *Hall–Petch relation and boundary strengthening.* Scripta Materialia, 2004. **51**(8): p. 801-806.
73. Wu, X., et al., *$\gamma \rightarrow \varepsilon$ martensite transformation and twinning deformation in fcc cobalt during surface mechanical attrition treatment.* Scripta Materialia, 2005. **52**(7): p. 547-551.
74. Salinas-Rodriguez, A. and J.L. Rodriguez-Galicia, *Deformation behavior of low-carbon Co-Cr-Mo alloys for low-friction implant applications.* Journal of Biomedical Materials Research, 1996. **31**(3): p. 409-419.
75. Rajan, K., *Phase transformations in a wrought Co-Cr-Mo-C alloy.* Metallurgical Transactions A, 1982. **13**(7): p. 1161-1166.
76. Rajan, K. and J. Sande, *Room temperature strengthening mechanisms in a Co-Cr-Mo-C alloy.* Journal of Materials Science, 1982. **17**(3): p. 769-778.
77. Saldívar García, A.d., A.M. Medrano, and A.S. Rodríguez, *Formation of hcp martensite during the isothermal aging of an fcc Co-27Cr-5Mo-0.05C orthopedic implant alloy.* Metallurgical and Materials Transactions A, 1999. **30**(5): p. 1177-1184.
78. Tolédano, P., et al., *Theory of the martensitic transformation in cobalt.* Physical Review B, 2001. **64**(14): p. 144104.
79. Pilliar, R.M., *Biomedical Materials. Chapter 2 : Metallic Biomaterials* Springer Science + Businees Media2009
80. Huang, P. and H.F. López, *Athermal ε-martensite in a Co–Cr–Mo alloy: grain size effects.* Materials Letters, 1999. **39**(4): p. 249-253.
81. Yamanaka, K., et al., *Local strain evolution due to athermal gamma-->epsilon martensitic transformation in biomedical CoCrMo alloys.* J Mech Behav Biomed Mater, 2014. **32**: p. 52-61.
82. López, H.F. and A.J. Saldivar-Garcia, *Martensitic Transformation in a Cast Co-Cr-Mo-C Alloy.* Metallurgical and Materials Transactions A, 2008. **39**(1): p. 8-18.
83. Huang, P. and H.F. López, *Strain induced ε-martensite in a Co–Cr–Mo alloy: grain size effects.* Materials Letters, 1999. **39**(4): p. 244-248.

84. Mani, A., R. Salinas, and H.F. Lopez, *Deformation induced FCC to HCP transformation in a Co–27Cr–5Mo–0.05C alloy.* Materials Science and Engineering: A, 2011. **528**(7–8): p. 3037-3043.
85. Barry, A.H., et al., *Microstructure and mechanical properties of bulk highly faulted fcc/hcp nanostructured cobalt microstructures.* Materials Characterization, 2014. **91**(0): p. 26-33.
86. Olson, G.B. and M. Cohen, *A mechanism for the strain-induced nucleation of martensitic transformations.* Journal of the Less-Common Metals, 1972. **28**: p. 107-118.
87. Salinas Rodrigues, A., *The Role of the FCC-HCP Phase Transformation during the plastic deformation of Co-Cr-Mo-C alloys for biomedical applications*, in *Cobalt-Base Alloys for Biomedical Applications, ASTM STP1365.*, A.S.f.T.a. Materials, Editor 1999: West Conshohocken, PA. p. 108-121.
88. ASME, *Surface Texture (Surface Roughness, Waviness, and Lay): An American National Standard*, 1996: New York.
89. ISO, *ISO 4288:1996-Geometrical Product Specifications (GPS) -- Surface texture: Profile method -- Rules and procedures for the assessment of surface texture*, 1996. p. 8.
90. ISO, *ISO 4287:2015-Geometrical Product Specifications (GPS) -- Surface texture: Profile method -- Terms, definitions and surface texture parameters*, 2015. p. 25.
91. Standardization, I.-I.O.f., *ISO 7206-2:2011 Implants for surgery -- Partial and total hip joint prostheses -- Part 2: Articulating surfaces made of metallic, ceramic and plastics materials*, 2011. p. 6.
92. Beake, B.D., A.J. Harris, and T.W. Liskiewicz, *Review of recent progress in nanoscratch testing.* Tribology - Materials, Surfaces & Interfaces, 2013. **7**(2): p. 87-96.
93. Dowson, D. *Tribological principles in metal-on-metal hip joint design*. in *Proceedings of the Institution of Mechanical Engineers. Part H: Journal of Engineering in Medicine* 2006.
94. Liu, F., et al., *Running-in wear and lubrication of metal-on-metal hip implants.* Journal of Bone & Joint Surgery, British Volume, 2006. **88-B**(SUPP III): p. 387.
95. Landolt, D., S. Mischler, and M. Stemp, *Electrochemical methods in tribocorrosion: a critical appraisal.* Electrochimica Acta, 2001. **46**(24–25): p. 3913-3929.
96. Mischler, S. and A.I. Muñoz, *Wear of CoCrMo alloys used in metal-on-metal hip joints: A tribocorrosion appraisal.* Wear, 2013. **297**(1–2): p. 1081-1094.
97. Yan, Y., A. Neville, and D. Dowson, *Biotribocorrosion of CoCrMo orthopaedic implant materials—Assessing the formation and effect of the biofilm.* Tribology International, 2007. **40**(10–12): p. 1492-1499.
98. Liao, Y., et al., *CoCrMo Metal-on-Metal Hip Replacements.* Physical chemistry chemical physics : PCCP, 2013. **15**(3): p. 10.1039/c2cp42968c.
99. Wood, R.J.K., *2.15 - Tribocorrosion A2 - Stott, Bob CottisMichael GrahamRobert LindsayStuart LyonTony RichardsonDavid ScantleburyHoward*, in *Shreir's Corrosion*2010, Elsevier: Oxford. p. 1005-1050.
100. Yan, Y. and A. Neville, *12 - Bio-tribocorrosion: surface interactions in total joint replacement (TJR)*, in *Bio-Tribocorrosion in Biomaterials and Medical Implants*2013, Woodhead Publishing. p. 309-340.

101. Jacobs, J.J., J.L. Gilbert, and R.M. Urban, *Current Concepts Review-Corrosion of Metal Orthopaedic Implants.* The Journal of Bone & Joint Surgery, 1998. **80**: p. 268-282.
102. Mansfeld, F., D.H. Hengstenberg, and J.V. Kenkel, *Galvanic Corrosion of Al Alloys I. Effect of Dissimilar Metal.* Corrosion, 1974. **30**(10): p. 343-353.
103. Papageorgiou, N. and S. Mischler, *Electrochemical Simulation of the Current and Potential Response in Sliding Tribocorrosion.* Tribology Letters, 2012. **48**(3): p. 271-283.
104. Wimmer, M.A., et al., *The acting wear mechanisms on metal-on-metal hip joint bearings: in vitro results.* Wear, 2001. **250**(1–12): p. 129-139.
105. Wimmer, M.A., et al., *Tribochemical reaction on metal-on-metal hip joint bearings: A comparison between in-vitro and in-vivo results.* Wear, 2003. **255**(7–12): p. 1007-1014.
106. Wimmer, M.A., et al., *Tribochemical Reactions in Metal-on-Metal Hip Joints Influence Wear and Corrosion*, in *Metal on Metal Total Hip Replacement devices*, ASTM, Editor 2013.
107. Wimmer, M.A., et al., *Wear mechanisms in metal-on-metal bearings: The importance of tribochemical reaction layers.* Journal of Orthopaedic Research, 2010. **28**(4): p. 436-443.
108. Rigney, D.A., *Transfer, mixing and associated chemical and mechanical processes during the sliding of ductile materials.* Wear, 2000. **245**(1–2): p. 1-9.
109. Rigney, D.A. and J.E. Hammerberg, *Unlubricated Sliding Behavior of Metals.* MRS Bulletin, 1998. **23**(06): p. 32-36.
110. Rigney, D.A. and J.E. Hammerberg, *Mechanical mixing and the development of nanocrystalline material during the sliding of metals*1999. Medium: X; Size: page(s) 465-474.
111. Odunuga, S., et al., *Forced Chemical Mixing in Alloys Driven by Plastic Deformation.* Physical Review Letters, 2005. **95**(4): p. 045901.
112. Pourzal, R., et al., *Micro-structural alterations within different areas of articulating surfaces of a metal-on-metal hip resurfacing system.* Wear, 2009. **267**(5–8): p. 689-694.
113. Pourzal, R., et al., *Subsurface changes of a MoM hip implant below different contact zones.* J Mech Behav Biomed Mater, 2009. **2**(2): p. 186-91.
114. Büscher, R., et al., *Subsurface microstructure of metal-on-metal hip joints and its relationship to wear particle generation.* Journal of Biomedical Materials Research Part B: Applied Biomaterials, 2005. **72B**(1): p. 206-214.
115. Papageorgiou, I., et al., *The effect of nano- and micron-sized particles of cobalt–chromium alloy on human fibroblasts in vitro.* Biomaterials, 2007. **28**(19): p. 2946-2958.
116. Varano, R., et al., *Effect of microstructure on the dry sliding friction behavior of CoCrMo alloys used in metal-on-metal hip implants.* J Biomed Mater Res B Appl Biomater, 2006. **76**(2): p. 281-6.
117. Kamali, A., et al., *Tribological performance of various CoCr microstructures in metal-on-metal bearings: the development of a more physiological protocol in vitro.* J Bone Joint Surg Br, 2010. **92**(5): p. 717-25.
118. Tipper, J.L., et al., *Quantitative analysis of the wear and wear debris from low and high carbon content CoCr alloys used in metal on metal total hip replacements.* Journal of Materials Science: Materials in Medicine, 1999. **10**: p. 353-362.

119. Buford, A. and T. Goswami, *Review of wear mechanisms in hip implants: Paper I – General.* Materials & Design, 2004. **25**(5): p. 385-393.
120. Wang, K., Wang, A.,Gustavson, L.J., *Metal-on-Metal Wear Testing of Co-Cr Alloys*, in *Cobalt-Base Alloys for Biomedical Applications*, J.A. Disegi, Kennedy, R.L., Pilliar, R., Editor 1999, ASTM: West Conshocken, PA, usa.
121. Dobbs, H.S., Robertson, J.L.M., *Heat treatment of cast CoCrMo for orthopaedic implant use.* Journal of Materials Science, 1983. **18**: p. 391-401.
122. Desai, V.M., et al., *Effect of carbide size on the abrasion of cobalt-base powder metallurgy alloys.* Wear, 1984. **94**(1): p. 89-101.
123. Sinnett-Jones, P.E., J.A. Wharton, and R.J.K. Wood, *Micro-abrasion–corrosion of a CoCrMo alloy in simulated artificial hip joint environments.* Wear, 2005. **259**(7–12): p. 898-909.
124. Sun, D., J.A. Wharton, and R.J.K. Wood, *Abrasive size and concentration effects on the tribo-corrosion of cast CoCrMo alloy in simulated body fluids.* Tribology International, 2009. **42**(11–12): p. 1595-1604.
125. Lewis, G., et al., *Influence of the radiopacifier in an acrylic bone cement on its mechanical, thermal, and physical properties: barium sulfate-containing cement versus iodine-containing cement.* J Biomed Mater Res B Appl Biomater, 2005. **73**(1): p. 77-87.
126. Ginebra, M.P., et al., *Mechanical performance of acrylic bone cements containing different radiopacifying agents.* Biomaterials, 2002. **23**(8): p. 1873-1882.
127. Wang, J.S., et al., *In vitro and in vivo biological responses to a novel radiopacifying agent for bone cement.* Journal of the Royal Society Interface, 2005. **2**(2): p. 71-78.
128. Caravia, L., et al., *The influence of bone and bone cement debris on counterface roughness in sliding wear tests of ultra-high molecular weight polyethylene on stainless steel.* Proc Inst Mech Eng H, 1990. **204**(1): p. 65-70.
129. Wimhurst, J.A., R.A. Brooks, and N. Rushton, *The effects of particulate bone cements at the bone-implant interface.* J Bone Joint Surg Br, 2001. **83**(4): p. 588-92.
130. Zhang, H.Y., et al., *The influence of bone cement type on production of fretting wear on the femoral stem surface: a preliminary study.* Clin Biomech (Bristol, Avon), 2012. **27**(7): p. 666-72.
131. Bryant, M., et al., *Fretting corrosion of fully cemented polished collarless tapered stems: The influence of PMMA bone cement.* Wear, 2013. **301**(1–2): p. 290-299.
132. Bryant, M., et al., *Fretting corrosion characteristics of polished collarless tapered stems in a simulated biological environment.* Tribology International, 2013. **65**: p. 105-112.
133. Bryant, M., et al., *Characterisation of the surface topography, tomography and chemistry of fretting corrosion product found on retrieved polished femoral stems.* Journal of the Mechanical Behavior of Biomedical Materials, 2014. **32**: p. 321-334.
134. Cook, R.B., et al., *The Mechanism and Magnitude of Tribocorrosion Damage at the Cement-Stem Interface*, in *2nd International Conference on BioTribology*, Elsevier, Editor 2014: Toronto, Canada.
135. Howell, J.R., Jr., et al., *In vivo surface wear mechanisms of femoral components of cemented total hip arthroplasties: the influence of wear mechanism on clinical outcome.* J Arthroplasty, 2004. **19**(1): p. 88-101.

136. Brown, L., et al., *Reproduction of fretting wear at the stem-cement interface in total hip replacement.* Proc Inst Mech Eng H, 2007. **221**(8): p. 963-71.
137. Zhang, H.Y., et al., *Femoral stem wear in cemented total hip replacement.* Proc Inst Mech Eng H, 2008. **222**(5): p. 583-92.
138. Blunt, L.A., et al., *What results in fretting wear on polished femoral stems.* Tribology International, 2009. **42**(11–12): p. 1605-1614.
139. Zhang, H., et al., *The contribution of the micropores in bone cement surface to generation of femoral stem wear in total hip replacement.* Tribology International, 2011. **44**(11): p. 1476-1482.
140. Mathew, M.T. and M.A. Wimmer, *13 - Tribocorrosion in artificial joints: in vitro testing and clinical implications A2 - Yan, Yu*, in *Bio-Tribocorrosion in Biomaterials and Medical Implants*2013, Woodhead Publishing. p. 341-371.
141. Cao, S., S. Guadalupe Maldonado, and S. Mischler, *Tribocorrosion of passive metals in the mixed lubrication regime: theoretical model and application to metal-on-metal artificial hip joints.* Wear, 2015. **324–325**: p. 55-63.
142. Liao, Y., et al., *New insights into Hard Phase of CoCrMo Metal-on-Metal Hip Replacements.* Journal of Mechanical Behaviour of Biomedical Materials, 2012. **12**: p. 39-49.
143. Hesketh, J., et al., *Biotribocorrosion of metal-on-metal hip replacements: How surface degradation can influence metal ion formation.* Tribology International, 2013. **65**: p. 128-137.
144. Hart, A.J., et al., *Cobalt from metal-on-metal hip replacements may be the clinically relevant active agent responsible for periprosthetic tissue reactions.* Acta Biomaterialia, 2012. **8**(10): p. 3865-3873.
145. Jacobs, J.J., et al., *Metal Degradation Products: A Cause for Concern in Metal-Metal Bearings?* Clinical Orthopaedics and Related Research, 2003. **417**: p. 139-147 10.1097/01.blo.0000096810.78689.62.
146. Maloney, W.J. and R.L. Smith, *Periprosthetic Osteolysis in Total Hip Arthroplasty: the Role of Particulate Wear Debris.* The Journal of Bone & Joint Surgery, 1995. **77**(9): p. 1448-1461.
147. Urban, R.M., et al., *Migration of corrosion products from modular hip prostheses. Particle microanalysis and histopathological findings.* J Bone Joint Surg Am, 1994. **76**(9): p. 1345-59.
148. Haynes, D.R., et al., *The differences in toxicity and release of bone-resorbing mediators induced by titanium and cobalt-chromium-alloy wear particles.* The Journal of Bone & Joint Surgery, 1993. **75**(6): p. 825-834.
149. Case, C.P., et al., *Widespread dissemination of metal debris from implants.* Journal of Bone Joint Surgery, 1994. **76**(5): p. 701-712.
150. Sargeant, A. and T. Goswami, *Hip implants – Paper VI – Ion concentrations.* Materials & Design, 2007. **28**(1): p. 155-171.
151. Dunstan, E., et al., *Chromosomal aberrations in the peripheral blood of patients with metal-on-metal hip bearings.* J Bone Joint Surg Am, 2008. **90**(3): p. 517-22.
152. Catelas, I. and M.A. Wimmer, *New insights into wear and biological effects of metal-on-metal bearings.* J Bone Joint Surg Am, 2011. **93 Suppl 2**: p. 76-83.
153. Williams, D.H., et al., *Prevalence of pseudotumor in asymptomatic patients after metal-on-metal hip arthroplasty.* J Bone Joint Surg Am, 2011. **93**(23): p. 2164-71.
154. Hanawa, T., *Metal ion release from metal implants.* Materials Science and Engineering: C, 2004. **24**(6–8): p. 745-752.

155. Alemón, B., et al., *Tribocorrosion behavior and ions release of CoCrMo alloy coated with a TiAlVCN/CNx multilayer in simulated body fluid plus bovine serum albumin.* Tribology International, 2015. **81**: p. 159-168.
156. Martin, E.J., et al., *Dominant role of molybdenum in the electrochemical deposition of biological macromolecules on metallic surfaces.* Langmuir, 2013. **29**(15): p. 4813-22.
157. Yan, Y., D. Dowson, and A. Neville, *In-situ electrochemical study of interaction of tribology and corrosion in artificial hip prosthesis simulators.* Journal of the Mechanical Behavior of Biomedical Materials, 2013. **18**: p. 191-199.
158. Yan, Y., Neville,A.,Dowson, D., Williams, S., Fisher J., *Tribofilm formation in biotribocorrosion-does it regulate ion release in metal-on-metal artificial hip joints?* Proceedings of the Institution of Mechanical Engineers, 2010. **224**: p. 997-2005.
159. Goldberg, J.R. and J.L. Gilbert, *In vitro corrosion testing of modular hip tapers.* J Biomed Mater Res B Appl Biomater, 2003. **64**(2): p. 78-93.
160. Geringer, J. and D.D. Macdonald, *Friction/fretting-corrosion mechanisms: Current trends and outlooks for implants.* Materials Letters, 2014. **134**: p. 152-157.
161. Royhman, D., et al., *Fretting-corrosion in hip implant modular junctions: New experimental set-up and initial outcome.* Tribology International, 2015. **91**: p. 235-245.
162. Gilbert, J.L., M. Mehta, and B. Pinder, *Fretting crevice corrosion of stainless steel stem-CoCr femoral head connections: comparisons of materials, initial moisture, and offset length.* J Biomed Mater Res B Appl Biomater, 2009. **88**(1): p. 162-73.
163. Casabán Julián, L. and A. Igual Muñoz, *Influence of microstructure of HC CoCrMo biomedical alloys on the corrosion and wear behaviour in simulated body fluids.* Tribology International, 2011. **44**(3): p. 318-329.
164. Böhni, H., T. Suter, and F. Assi, *Micro-electrochemical techniques for studies of localized processes on metal surfaces in the nanometer range.* Surface and Coatings Technology, 2000. **130**(1): p. 80-86.
165. Wang, X.Y. and D.Y. Li, *Application of an electrochemical scratch technique to evaluate contributions of mechanical and electrochemical attacks to corrosive wear of materials.* Wear, 2005. **259**(7–12): p. 1490-1496.
166. Liu, Y.-Z., et al., *Oxide structure and corrosion mechanism of ZrSnNbFeCrCu alloy studied with transmission electron microscopy and nano-indentation: Relation to corrosion kinetics.* Materials Chemistry and Physics, 2010. **122**(2–3): p. 408-416.
167. Zhao, T., et al., *Surface characteristics, nano-indentation and corrosion behavior of Nb implanted NiTi alloy.* Surface and Coatings Technology, 2011. **205**(19): p. 4404-4410.
168. Yan, Y., et al., *Study of the tribocorrosion behaviors of albumin on a cobalt-based alloy using scanning Kelvin probe force microscopy and atomic force microscopy.* Electrochemistry Communications, 2016. **64**: p. 61-64.
169. Sun, D., J.A. Wharton, and R.J.K. Wood, *Micro-abrasion–corrosion of cast CoCrMo—Effects of micron and sub-micron sized abrasives.* Wear, 2009. **267**(1–4): p. 52-60.
170. Ehrensberger, M.T. and J.L. Gilbert, *The effect of static applied potential on the 24-hour impedance behavior of commercially pure titanium in simulated*

biological conditions. J Biomed Mater Res B Appl Biomater, 2010. **93**(1): p. 106-12.
171. Haeri, M., S. Goldberg, and J.L. Gilbert, *The voltage-dependent electrochemical impedance spectroscopy of CoCrMo medical alloy using time-domain techniques: Generalized Cauchy–Lorentz, and KWW–Randles functions describing non-ideal interfacial behaviour.* Corrosion Science, 2011. **53**(2): p. 582-588.
172. Goldberg, J.R., et al., *Corrosion Testing of Modular Hip Implants*, in *Modularity of Orthopedic Implants, ASTM STP 1301*, D.E. Marlowe, J.E. Parr, and M.B. Mayor, Editors. 1997, American Society for Testing Materials.
173. Yan, Y., A. Neville, and D. Dowson, *Understanding the role of corrosion in the degradation of metal-on-metal implants.* Proc Inst Mech Eng H, 2006. **220**(2): p. 173-81.
174. Gilbert, J.L., Bai, Z, Bearinger, J.,Megremis, S, *The dynamics of oxide films on metallic biomaterials*, in *Medical Device Materials: Proceedings of the Materials and Processes for Medical Devices Conference*, S. Shrivastava, Editor 2004.
175. Ding, J., et al., *An Asperity-Contact Based Oxidation Model for Fretting Wear with the Presence of Debris*, in *Advanced Tribology*, J. Luo, et al., Editors. 2010, Springer Berlin Heidelberg. p. 346-347.
176. Geringer, J., et al., *Fretting corrosion with proteins: The role of organic coating on the synergistic mechanisms.* Thin Solid Films, 2013. **528**: p. 123-129.
177. Mischler, S., *Triboelectrochemical techniques and interpretation methods in tribocorrosion: A comparative evaluation.* Tribology International, 2008. **41**(7): p. 573-583.
178. Uhlig, H.H., *Mechanism of fretting corrosion.* Journal of applied mechanics-transactions of the ASME, 1954. **21**(4): p. 401-407.
179. Mischler, S., S. Debaud, and D. Landolt, *Wear-Accelerated Corrosion of Passive Metals in Tribocorrosion Systems.* Journal of The Electrochemical Society, 1998. **145**(3): p. 750-758.
180. Ponthiaux, P., et al., *Electrochemical techniques for studying tribocorrosion processes.* Wear, 2004. **256**(5): p. 459-468.
181. Mischler, S., et al., *Influence of passivity on the tribocorrosion of carbon steel in aqueous solutions.* Wear, 2001. **251**(1–12): p. 1295-1307.
182. Klarstrom, D., *Metallography and Microstructures of Cobalt and Cobalt alloys.ASM Handbook, Volume 9: Metallography and Microstructures.*, ed. G.F.V. Voort. Vol. 9. 2004.
183. Sun, D., J.A. Wharton, and R.J.K. Wood, *The Effects of Protein and pH on the Tribo-Corrosion Performance of Cast CoCrMo — A Combined Electrochemical and Tribological Study*, in *Advanced Tribology: Proceedings of CIST2008 & ITS-IFToMM2008*, J. Luo, et al., Editors. 2010, Springer Berlin Heidelberg: Berlin, Heidelberg. p. 825-826.
184. Holland, R.I., *Use of potentiodynamic polarization technique for corrosion testing of dental alloys.* European Journal of Oral Sciences, 1991. **99**(1): p. 75-85.
185. Materials, A.I.-A.S.f.T., *ASTM G-102-89(2015) Standard Practice for Calculation of Corrosion Rates and Related Information from Electrochemical Measurements*, in *e1*2015: West Conshohocken, PA.
186. ISO, B.S.-. *EN ISO 6507-1:2005 Metallic materials-Vickers hardness test.* , in *Part 1: Test Method*2005. p. 19.

187. Oliver, W.C. and G.M. Pharr, *An improved technique for determining hardness and elastic modulus using load and displacement sensing indentation experiments.* Journal of Materials Research, 1992. **7**(06): p. 1564-1583.
188. Fischer-Cripps, A.C., *A review of analysis methods for sub-micron indentation testing.* Vacuum, 2000. **58**(4): p. 569-585.
189. ISO, T.E.S.E., *Metallic materials - Instrumented indentation test for hardness and materials parameters. ISO 14577-1:2002,* in *Part 1: Test Method* 2002: Brussels.
190. Waterhouse, R.B., *Fretting wear.* Wear, 1984. **100**(1–3): p. 107-118.
191. Hoeppner, D.W. and V. Chandrasekaran, *Fretting in orthopaedic implants: A review.* Wear, 1994. **173**(1–2): p. 189-197.
192. Goldberg, J.R., et al., *A multicenter retrieval study of the taper interfaces of modular hip prostheses.* Clin Orthop Relat Res, 2002(401): p. 149-61.
193. Jauch, S.Y., et al., *Micromotions at the taper interface between stem and neck adapter of a bimodular hip prosthesis during activities of daily living.* J Orthop Res, 2013. **31**(8): p. 1165-71.
194. Fouvry, S., P. Kapsa, and L. Vincent, *Quantification of fretting damage.* Wear, 1996. **200**(1–2): p. 186-205.
195. Fouvry, S., P. Kapsa, and L. Vincent, *Description of fretting damage by contact mechanics.* ZAMM - Journal of Applied Mathematics and Mechanics / Zeitschrift für Angewandte Mathematik und Mechanik, 2000. **80**(S1): p. 41-44.
196. Liskiewicz, T.W., B.D. Beake, and J.F. Smith, *In situ accelerated micro-wear — A new technique to fill the measurement gap.* Surface and Coatings Technology, 2010. **205**(5): p. 1455-1459.
197. Mitchell, A. and P. Shrotriya, *Onset of nanoscale wear of metallic implant materials: Influence of surface residual stresses and contact loads.* Wear, 2007. **263**(7–12): p. 1117-1123.
198. Hokkirigawa, K., K. Kato, and Z.Z. Li, *The effect of hardness on the transition of the abrasive wear mechanism of steels.* Wear, 1988. **123**(2): p. 241-251.
199. Hokkirigawa, K. and K. Kato, *An experimental and theoretical investigation of ploughing, cutting and wedge formation during abrasive wear.* Tribology International, 1988. **21**(1): p. 51-57.
200. Dowson, D. and Z.M. Jin, *Metal-on-metal hip joint tribology.* Proc Inst Mech Eng H, 2006. **220**(2): p. 107-18.
201. G.F, V.V., *Specimen Preparation for Light Microscopy-Electropolishing*, in *Metallography. Principles and Practice*, A.I.T.M.I.S.M.S.a.E. Series, Editor 1999, ASM International: Illinois. p. 124.
202. Cawley, J., et al., *A tribological study of cobalt chromium molybdenum alloys used in metal-on-metal resurfacing hip arthroplasty.* Wear, 2003. **255**(7–12): p. 999-1006.
203. Montero-Ocampo, C., H. Lopez, and M. Talavera, *Effect of alloy preheating on the mechanical properties of as-cast CoCrMoC alloys.* Metallurgical and Materials Transactions A, 1999. **30**(3): p. 611-620.
204. Finkin, E.F., *Examination of Abrasion Resistance Criteria for Some Ductile Metals.* Journal of Lubrication Technology, 1974. **96**(2): p. 210-214.
205. Tsui, T.Y., et al., *Nanoindentation and Nanoscratching of Hard Carbon Coatings for Magnetic Disks.* MRS Online Proceedings Library Archive, 1995. **383**: p. null-null.

206. Weeton, J.W., Signorelli, R.A, *An investigation of lamellar structures and minor phases in eleven Cobalt-base alloys before and after heat treatment.* National Advisory Committee for Aeronautics, 1954.
207. Silverman, R., Arbiter, W., Hodi, F., *Effect of Sigma Phase on CoCrMo Base Alloys.* Trans A S M, 1957. **49**: p. 805-822.
208. Sims, C.T., *Contemporary view of cobalt-base alloys.* Journal of Materials Science, 1969. **21**: p. 27-42.
209. Caudillo, M., et al., *On carbide dissolution in an as-cast ASTM F-75 alloy.* Journal of Biomedical Materials Research, 2002. **59**(2): p. 378-385.
210. Ramírez-Vidaurri, L.E., et al., *Cooling rate and carbon content effect on the fraction of secondary phases precipitate in as-cast microstructure of ASTM F75 alloy.* Journal of Materials Processing Technology, 2009. **209**(4): p. 1681-1687.
211. Lippard, H.E., Kennedy, R.L., *Process Metallurgy of Wrought CoCrMo alloy*, in *Cobalt-Base Alloys for Biomedical Applications*, J.A. Disegi, Kennedy, R.L., Pilliar, R., Editor 1999, ASTM: West Conshocken, PA, USA.
212. Hall, E.O., *The Deformation and Ageing of Mild Steel: III Discussion of Results.* Proceedings of the Physical Society. Section B, 1951. **64**(9): p. 747.
213. Petch, N.J., *The Cleavage Strength of Polycrystals.* Journal of the Iron and Steel Institute, 1953. **174**: p. 25-28.
214. Saldivar-Garcia, A.J. and H.F. Lopez, *Microstructural effects on the wear resistance of wrought and as-cast Co-Cr-Mo-C implant alloys.* J Biomed Mater Res A, 2005. **74**(2): p. 269-74.
215. Stemmer, P., et al., *Microstructure of retrievals made from Standard Cast HC-CoCrMo Alloys*, in *Metal-On-Metal Total Hip Replacement Devices*, A.I.-S. 1960, Editor 2013.
216. Mancha, H., et al., *Effect of heat treatment on the mechanical properties of an As Cast ASTM F-75 Implant alloy.* Journal of Materials Synthesis and Processing, 1996. **4**(4): p. 217-226.
217. Yamanaka, K., M. Mori, and A. Chiba, *Effects of carbon concentration on microstructure and mechanical properties of as-cast nickel-free Co–28Cr–9W-based dental alloys.* Materials Science and Engineering: C, 2014. **40**: p. 127-134.
218. Kilner, T., et al., *Phase identification and incipient melting in a cast Co--Cr surgical implant alloy.* J Biomed Mater Res, 1982. **16**(1): p. 63-79.
219. Voyiadjis, G. and R. Peters, *Size effects in nanoindentation: an experimental and analytical study.* Acta Mechanica, 2010. **211**(1-2): p. 131-153.
220. Leyland, A. and A. Matthews, *On the significance of the H/E ratio in wear control: a nanocomposite coating approach to optimised tribological behaviour.* Wear, 2000. **246**(1–2): p. 1-11.
221. Musil, J., et al., *Relationships between hardness, Young's modulus and elastic recovery in hard nanocomposite coatings.* Surface and Coatings Technology, 2002. **154**(2–3): p. 304-313.
222. Mathew, M.T., et al., *Tribolayer formation in a metal-on-metal (MoM) hip joint: An electrochemical investigation.* Journal of the Mechanical Behavior of Biomedical Materials, 2014. **29**: p. 199-212.
223. Igual Muñoz, A., Mischler,S., *Inter-laboratory study on electrochemical methods for the characterisation of CoCrMo biomedical alloys in simulated body fluids*, ed. Wakefiled2011: Maney.
224. Pourbaix, M., *Electrochemical corrosion of metallic biomaterials.* Biomaterials, 1984. **5**(3): p. 122-34.

225. Pourzal, R., et al., *Investigation of the role of tribofilms in self-mating CoCrMo systems utilizing a quartz crystal microtribometer.* Tribology International, 2014. **72**: p. 161-171.
226. Petrov, Y.N., et al., *Influence of microstructural modifications induced by ultrasonic impact treatment on hardening and corrosion behavior of wrought Co-Cr-Mo biomedical alloy.* Materials Science and Engineering: C, 2016. **58**: p. 1024-1035.
227. Contu, F., B. Elsener, and H. Böhni, *Characterization of implant materials in fetal bovine serum and sodium sulfate by electrochemical impedance spectroscopy. II. Coarsely sandblasted samples.* Journal of Biomedical Materials Research Part A, 2003. **67A**(1): p. 246-254.
228. Kurz, S., Hodgson, W.E., Virtanen, S., Fervel, V., Mischler, S., *Corrosion characterisation of passive films on CoCrMo with electrochemical techniques in saline and simulated biological solutions.* European Cells and Materials, 2002. **3**(1): p. 26-27.
229. Schmuki, P., et al., *Electrochemical Behavior of Cr2 O 3 / Fe2 O 3 Artificial Passive Films Studied by In Situ XANES.* Journal of The Electrochemical Society, 1998. **145**(3): p. 791-801.
230. Bettini, E., et al., *Influence of metal carbides on dissolution behavior of biomedical CoCrMo alloy: SEM, TEM and AFM studies.* Electrochimica Acta, 2011. **56**(25): p. 9413-9419.
231. Vidal, C.V., et al., *Passivation of a CoCrMo PVD Alloy with Biomedical Composition under Simulated Physiological Conditions Studied by EQCM and XPS.* Journal of The Electrochemical Society, 2012. **159**(5): p. C233-C243.
232. Jacobs, J.J., et al., *The effect of porous coating processing on the corrosion behavior of cast Co–Cr–Mo surgical implant alloys.* Journal of Orthopaedic Research, 1990. **8**(6): p. 874-882.
233. Growcock, F.B. and R.J. Jasinski, *Time-Resolved Impedance Spectroscopy of Mild Steel in Concentrated Hydrochloric Acid.* Journal of The Electrochemical Society, 1989. **136**(8): p. 2310-2314.
234. Shearwood-Porter, N., M. Browne, and I. Sinclair, *Micromechanical characterisation of failure in acrylic bone cement: The effect of barium sulphate agglomerates.* Journal of the Mechanical Behavior of Biomedical Materials, 2012. **13**: p. 85-92.
235. Cook, R.B., et al., *Volumetric assessment of material loss from retrieved cemented metal hip replacement stems.* Tribology International, 2015. **89**: p. 105-108.
236. Meyer, J.N., et al., *Effect of Tribolayer Formation on Corrosion of CoCrMo Alloys Investigated Using Scanning Electrochemical Microscopy.* Analytical Chemistry, 2013. **85**(15): p. 7159-7166.
237. Maruyama, N., et al., *Friction-Wear Properties of Nickel-Free Co-Cr-Mo Alloy in a Simulated Body Fluid.* Materials Transactions. Special Issue on Medical, Healthcare, Sport and Leisure Materials., 2005. **46**(7): p. 1588-1592.
238. Wang, C.T., et al., *Effect of grain size on the micro-tribological behavior of pure titanium processed by high-pressure torsion.* Wear, 2012. **280–281**(0): p. 28-35.
239. Hanlon, T., et al., *Effects of grain refinement and strength on friction and damage evolution under repeated sliding contact in nanostructured metals.* International Journal of Fatigue, 2005. **27**(10–12): p. 1159-1163.

240. Huang, P., A. Salinas-Rodriguez, and H.F. López, *Tribological behaviour of cast and wrought Co–Cr–Mo implant alloys.* Materials Science and Technology, 1999. **15**(11): p. 1324-1330.
241. Woldman, M., et al., *The influence of abrasive body dimensions on single asperity wear.* Wear, 2013. **301**(1–2): p. 76-81.
242. Bowden, F.P. and D. Tabor, *The Friction and Lubrication of Solids. New York: Oxford University Press.* Science, 1951. **113**(2938): p. 443-444.
243. Swaminathan, V. and J.L. Gilbert, *Fretting corrosion of CoCrMo and Ti6Al4V interfaces.* Biomaterials, 2012. **33**(22): p. 5487-5503.
244. Lee, S.-H., et al., *Effect of carbon addition on microstructure and mechanical properties of a wrought CoCrMo implant alloy.* Materials Transactions. The Japan Institute of Metals, 2006. **47**(2): p. 287-290.
245. Beake, B.D. and T.W. Liskiewicz, *Comparison of nano-f`retting and nano-scratch tests on biomedical materials.* Tribology International, 2013. **63**: p. 123-131.
246. Ding, J., et al., *A multi-scale model for fretting wear with oxidation-debris effects.* Proceedings of the Institution of Mechanical Engineers, Part J: Journal of Engineering Tribology, 2009. **223**(7): p. 1019-1031.
247. Lombardi, A.V., et al., *Aseptic loosening in total hip arthroplasty secondary to osteolysis induced by wear debris from titanium-alloy modular femoral heads.* The Journal of Bone & Joint Surgery, 1989. **71**(9): p. 1337-1342.
248. Ahmed, R., et al., *Single asperity nanoscratch behaviour of HIPed and cast Stellite 6 alloys.* Wear, 2014. **312**(1–2): p. 70-82.
249. Tabor, D., *The Hardness of Metals, D. Tabor 1951, Oxford, p. 175, 15s.* Journal of the Japan Society of Mechanical Engineers, 1953. **56**(414): p. 592-593.
250. Milošev, I., et al., *Survivorship and Retrieval Analysis of Sikomet Metal-on-Metal Total Hip Replacements at a Mean of Seven Years.* The Journal of Bone & Joint Surgery, 2006. **88**(6): p. 1173-1182.
251. Bryant, M., et al., *The role of surface pre-treatment on the microstructure, corrosion and fretting corrosion of cemented femoral stems.* Biotribology, 2016. **5**: p. 1-15.
252. Bandyopadhyay, P., et al., *Effect of load in scratch experiments on soda lime silica glass.* Journal of Non-Crystalline Solids, 2012. **358**(8): p. 1091-1103.
253. Lahiri, D., et al., *Scratch induced deformation behavior of hafnium based bulk metallic glass at multiple load scales.* Journal of Non-Crystalline Solids, 2015. **410**: p. 118-126.
254. Paufler, P., *W. F. Hosford. The mechanics of crystals and textured polycrystals. Oxford University Press, New York–Oxford 1993. 248 Seiten, Preis £ 30,–. ISBN 0-19-507744-X.* Crystal Research and Technology, 1994. **29**(4): p. 532-532.
255. Gao, H. and Y. Huang, *Geometrically necessary dislocation and size-dependent plasticity.* Scripta Materialia, 2003. **48**(2): p. 113-118.
256. Ashby, M.F., *Deformation of plastically non-homogeneous materials.*Philosophical Magazine, 1970. **21**(170): p. 399.
257. Arsenlis, A. and D.M. Parks, *Crystallographic aspects of geometrically-necessary and statistically-stored dislocation density.* Acta Materialia, 1999. **47**(5): p. 1597-1611.
258. Nye, J.F., *Some geometrical relations in dislocated crystals.* Acta Metallurgica, 1953. **1**(2): p. 153-162.

259. Igual Muñoz, A. and N. Espallargas, *5 - Tribocorrosion mechanisms in sliding contacts*, in *Tribocorrosion of Passive Metals and Coatings*, D. Landolt and S. Mischler, Editors. 2011, Woodhead Publishing. p. 118-152.
260. Renner, E., et al., *Sensitivity of the residual topography to single crystal plasticity parameters in Berkovich nanoindentation on FCC nickel.* International Journal of Plasticity, 2016. **77**: p. 118-140.
261. Salehinia, I. and D.F. Bahr, *Mechanical behavior of FCC single crystals at finite temperatures in the presence of point defects.* Materials Science and Engineering: A, 2013. **588**: p. 340-346.
262. Salehinia, I. and D.F. Bahr, *Crystal orientation effect on dislocation nucleation and multiplication in FCC single crystal under uniaxial loading.* International Journal of Plasticity, 2014. **52**: p. 133-146.
263. Cleja-Ţigoiu, S. and R. Paşcan, *Slip systems and flow patterns in viscoplastic metallic sheets with dislocations.* International Journal of Plasticity, 2014. **61**: p. 64-93.
264. Pennycook, S.J., et al., *Atomic Structure and Properties of Dislocations and Grain Boundaries*, in *Reference Module in Materials Science and Materials Engineering*2016, Elsevier.
265. Shetty, H.R., T.H. Kosel, and N.F. Fiore, *A study of abrasive wear mechanisms using diamond and alumina scratch tests.* Wear, 1982. **80**(3): p. 347-376.
266. Shetty, H.R., T.H. Kosel, and N.F. Fiore, *A study of abrasive wear mechanisms in cobalt-base alloys.* Wear, 1983. **84**(3): p. 327-343.
267. Kosel, T.H., *Review of scratch test studies of abrasion mechanisms*1986. Medium: X; Size: Pages: 16.
268. Yamanaka, K., M. Mori, and A. Chiba, *Enhanced Mechanical Properties of As-Forged Co-Cr-Mo-N Alloys with Ultrafine-Grained Structures.* Metallurgical and Materials Transactions A, 2012. **43A**: p. 5243-5257.
269. Mori, M., et al., *Texture evolution and mechanical anisotropy of biomedical hot-rolled Co–Cr–Mo alloy.* Journal of the Mechanical Behavior of Biomedical Materials, 2015. **51**: p. 205-214.
270. Büscher, R. and A. Fischer, *The pathways of dynamic recrystallization in all-metal hip joints.* Wear, 2005. **259**(7–12): p. 887-897.
271. Chiba, A., et al., *Pin-on-disk wear behavior in a like-on-like configuration in a biological environment of high carbon cast and low carbon forged Co–29Cr–6Mo alloys.* Acta Materialia, 2007. **55**(4): p. 1309-1318.
272. Salinas Rodrigues, A., *The role of the FCC-HCP Phase Transformation During the Plastic Deformation of Co-Cr-Mo-C Alloys for Biomedical Applications*, in *Cobalt-Base Alloys for Biomedical Applications*, J.A. Disegi, Kennedy, R.L., Pilliar, R., Editor 1999, ASTM: West Conshocken, PA, usa.
273. Wu, X., et al., *Strain-induced grain refinement of cobalt during surface mechanical attrition treatment.* Acta Materialia, 2005. **53**(3): p. 681-691.
274. Lu, K. and J. Lu, *Nanostructured surface layer on metallic materials induced by surface mechanical attrition treatment.* Materials Science and Engineering: A, 2004. **375–377**: p. 38-45.
275. Holmberg, K., et al., *Tribological contact analysis of a rigid ball sliding on a hard coated surface: Part II: Material deformations, influence of coating thickness and Young's modulus.* Surface and Coatings Technology, 2006. **200**(12–13): p. 3810-3823.

276. Varano, R., Bobyn, J.D., Yue S., *Characterization of CoCrMo Alloys used in HIP Implant Articulating Surfaces.* MRS Proceedings, 1996. **441**(Thin Film-Structure and Morphology).
277. Sun, D., J.A. Wharton, and R.J.K. Wood, *Micro-abrasion mechanisms of cast CoCrMo in simulated body fluids.* Wear, 2009. **267**(11): p. 1845-1855.
278. Goldberg, J.R. and J.L. Gilbert, *The electrochemical and mechanical behavior of passivated and TiN/AlN-coated CoCrMo and Ti6Al4V alloys.* Biomaterials, 2004. **25**(5): p. 851-64.
279. Krishnan, J., Dumbre, S., Bhatt. S., Esther, T.,Akinlabi,T., Ramalingam, R., *Effect of Crystallographic Orientation on the Pitting Corrosion Resistance of Laser Surface Melted AISI 304L Austenitic Stainless Steel.* International Journal of Mechanical, Aerospace, Industrial, Mechatronic and Manufacturing Engineering, 2013. **7**(4): p. 650-653.
280. Jiang, Q., et al., *Anisotropy of the crystallographic orientation and corrosion performance of high-strength AZ80 Mg alloy.* Journal of Magnesium and Alloys, 2015. **3**(4): p. 309-314.
281. Gray, J.J., B.S. El Dasher, and C.A. Orme, *Competitive effects of metal dissolution and passivation modulated by surface structure: An AFM and EBSD study of the corrosion of alloy 22.* Surface Science, 2006. **600**(12): p. 2488-2494.
282. Cathcart, J.V., G.F. Petersen, and C.J. Sparks, *The Structure of Thin Oxide Films Formed on Nickel Crystals.* Journal of The Electrochemical Society, 1969. **116**(5): p. 664-668.
283. Young Jr, F.W., J.V. Cathcart, and A.T. Gwathmey, *The rates of oxidation of several faces of a single crystal of copper as determined with elliptically polarized light.* Acta Metallurgica, 1956. **4**(2): p. 145-152.
284. Wang, X., et al., *Influence of grain orientation on the incipient oxidation behavior of Haynes 230 at 900 °C.* Materials Characterization, 2015. **107**: p. 33-42.
285. Dyer, L.D., *Rolling friction on single crystals of copper in the plastic range.* Acta Metallurgica, 1961. **9**(10): p. 928-936.
286. Swadener, J.G., et al., *Crystal orientation effects in scratch testing with a spherical indenter.* Journal of Materials Research, 2010. **25**(05): p. 921-926.
287. Roa, J.J., et al., *Dependence of nanoindentation hardness with crystallographic orientation of austenite grains in metastable stainless steels.* Materials Science and Engineering: A, 2015. **645**: p. 188-195.
288. Steijn, R.P., *Friction and wear of single crystals.* Wear, 1964. **7**(1): p. 48-66.
289. Takagi, R. and Y. Tsuya, *Static friction between clean copper single crystal surfaces.* Wear, 1961. **4**(3): p. 216-227.
290. Xia, Y.Z., et al., *Synthesis, characterization, and nanoindentation response of single crystal Fe–Cr–Ni alloys with FCC and BCC structures.* Materials Science and Engineering: A, 2014. **611**: p. 177-187.
291. Paredes, V., et al., *Assessment and comparison of surface chemical composition and oxide layer modification upon two different activation methods on a cocrmo alloy.* Journal of Materials Science: Materials in Medicine, 2013. **25**(2): p. 311-320.